

UNIVERSITY OF Southampton



Fluid structure interaction testing, modelling and development of Passive Adaptive Composite foils

by

Laura Marimon Giovannetti

Ph.D. thesis

in the

Faculty of Engineering and the Environment

March 2017

Ph.D. Thesis

Laura Marimon Giovannetti.
L.Marimon-Giovannetti@soton.ac.uk
Faculty of Engineering and the Environment,
University of Southampton,
Southampton. SO16 7QF.
United Kingdom.

Abstract

High performance foiling catamarans are one of the fastest growing sectors in the sailing and sport industries, allowing athletes to perform in extremely fast and spectacular boats. These boats fly above the water with the aid of foils that not only provide horizontal side-force to counterbalance the aerodynamic forces from the sails, but also deliver vertical force that supports some or all of the mass of the boat. Exploring the possibility of using Passive Adaptive Composite (PAC) on the hydrofoils to control their pitch angle enables the boats to achieve a stable flight in a wide range of weather conditions.

This thesis presents an experimental and numerical evaluation of bend-twist elastic coupling in composite passive-adaptive structures. Due to the lack of experimental validation in Fluid Structure Interaction (FSI) investigations, a full-field deformation of an aerofoil-shaped section under wind loading is measured. Moreover, the influences of structure deflection on flow behaviour are investigated by looking at the changes in flow features evaluated on a transverse plane downstream of the trailing edge. The experimental analysis was carried out at the University of Southampton R. J. Mitchell wind tunnel and involved the use of full-field non-contact measurement techniques such as high speed three dimensional Digital Image Correlation (3-D DIC) and stereoscopic Particle Image Velocimetry (PIV). After assessing the validity and repeatability of the experiments, the research focuses on the development of a numerical FSI investigation that involves the use of a structural and a fluid solver to simulate the aero-elastic behaviour of composite tailored specimens with different internal structures. The numerical analysis is developed as a tool to allow the design of a new structure able to achieve a constant level of lift force (corresponding to the weight of the catamaran) in increased flow speed. During the research project it was proven that the efficiency of the foils can be improved by tailoring the internal structure to induce smart coupled bend-twist toward a wash-out (feather) or wash-in (stall) position under increased loading.

Academic Thesis: Declaration of Authorship

I, LAURA MARIMON GIOVANNETTI, declare that this thesis entitled “*Fluid structure interaction testing, modelling and development of Passive Adaptive Composite foils*” and the work presented in it are my own and have been generated by me as the result of my own original research.

I confirm that:

1. This work was done wholly or mainly while in candidature for a research degree at this University;
2. Where any part of this thesis has previously been submitted for a degree or any other qualification at this University or any other institution, this has been clearly stated;
3. Where I have consulted the published work of others, this is always clearly attributed;
4. Where I have quoted the work of others, the source is always given. With the exception of such quotations, this thesis is entirely my own work;
5. I have acknowledged all main sources of help;
6. Where the thesis is based on work done by myself jointly with others, I have made it clear what was done by others and what I have contributed myself;
7. Part of this work have been published as:
 - Banks, J., Marimon Giovannetti, L., Soubeyran, X., Wright, A. M., Turnock, S. R., Boyd, S. W., (2015) Assessment of Digital Image Correlation as a method of obtaining deformations of a structure under fluid load *Journal of Fluids and Structures*, Vol. 58, pp. 173-187.
 - Banks, J., Marimon Giovannetti, L., Taylor, J., Turnock, S. R. (2016) Assessing human-fluid-structure interaction for the international moth *in special issue: the Engineering of SPORT 11*, Procedia Engineering, Vol. 147, pp. 311-316.

- Marimon Giovannetti, L., Banks, J., Turnock, S. R., Boyd, S. W., (2017) Uncertainty assessment for fluid-structure interaction measurement by coupled Digital Image Correlation and Particle Image Velocimetry during wind tunnel experiments *Journal of Fluids and Structures*, Vol. 68, pp. 125-140.
- Marimon Giovannetti, L., Banks, J., Turnock, S. R., Boyd, S. W., (2017) Validation of a fully coupled FSI model of a Passive Adaptive Composite structure using experimental full-field synchronised fluid and structure response data (*ready for submission to the special issue of Journal of Computers & Structures*).

Signed:.....

Date:.....

Table of Contents

List of Figures	xi
List of Tables	xvii
Nomenclature	xix
Acronyms	xxiii
Acknowledgements	xxv
1 Introduction	1
1.1 Background	1
1.2 Motivation	4
1.3 Aim	6
1.4 Objectives	7
1.5 Novelty	8
1.6 Publications	9
1.6.1 Journal Papers	9
1.6.2 Conference Papers	9
1.7 Report Structure	10
2 Exploring Passive Adaptive Composites	13
2.1 Introduction	13
2.2 Composite Structures	13
2.3 Passive Adaptive Composites	15
2.3.1 Fluid Structures Interaction	17
2.3.2 Up-to-date Experimental Measures	29
2.4 Experimental Methodologies For PAC	30
2.4.1 Applications of Digital Image Correlation	30
2.4.2 Applications of Particle Image Velocimetry	33
2.4.3 DIC and PIV in Extreme Conditions	37
2.5 Numerical Methodologies For PAC	37
2.5.1 Finite Element Analysis	37
2.6 Summary of the Chapter	40
3 Experimental Methodology	43
3.1 Introduction	43
3.2 Development of a Simplified Foil	44
3.3 Digital Image Correlation	47
3.3.1 Measurement Accuracy	47

3.4 Set-up of the Experiment in Wind-Tunnel	58
3.5 Summary of the Chapter	64
4 Numerical Methodology	67
4.1 Introduction	67
4.2 Structural solver set-up	67
4.2.1 Simple Aluminium and Composite-Aluminium beam	68
4.2.2 Foam Aerofoil Structure	77
4.2.3 Mylar Outer-Skin Implementation	87
4.2.4 Final Full Structure	90
4.3 Coupled Fluid Structure Methodology	93
4.3.1 Moving Mesh	94
4.3.2 Coupling Algorithm	96
4.4 Flow solver set-up	101
4.5 Summary of the Chapter	107
5 Passive Adaptive Composite Performance	109
5.1 Introduction	109
5.2 Experimental Conventions	109
5.3 Experimental Coupled Systems	114
5.4 Ply Angle Investigation	119
5.5 Numerical Results	125
5.5.1 Finite Element Analysis Results	125
5.5.2 Computational Fluid Dynamics Results	127
5.5.3 Fluid Structure Interaction Results	129
5.6 Summary of the Chapter	133
6 Design & Test	135
6.1 Introduction	135
6.2 Design Development	137
6.3 Optimised Design For Bend-Twist Coupling	142
6.4 Manufacture & Test	151
6.5 Wind Tunnel Results	155
6.5.1 Quasi-Static Results	156
6.5.2 Dynamic Results	160
6.6 Summary of the Chapter	163
7 Conclusions	165
7.1 Contributions	167
7.1.1 Fluid Structure Interaction Experimental Methodology	167
7.1.2 Design Development of a Passive Adaptive Structure	168
7.2 Project Achievements	169
7.3 Further Work	169
7.3.1 Future Projects in Experimental FSI	169
7.3.2 Design of Real Hydrofoil Structure	170
References	171

List of Figures

1.1	<i>Bend-twist coupling (left) and extension-twist coupling (right) for beam structures (Fedorov, 2012).</i>	2
1.2	<i>Response of an aerofoil-shape structure with bend-twist coupling configuration.</i>	3
1.3	<i>Ben Ainslie Racing Team flying on the AC45 (Ben Ainslie Racing, 2015).</i>	4
1.4	<i>Catamaran sailing configurations.</i>	5
1.5	<i>NACRA Performance sailing catamarans.</i>	6
1.6	<i>Flow chart of the research project. The iterative process is associated with the possibility of designing new structures tailored to certain loads.</i>	8
2.1	<i>Study of composite materials from micro-mechanics (a) lamina level (b) and laminate level(c) (Barbero, 2008).</i>	14
2.2	<i>Bend-twist coupling under flexural loading for helicopter blade (Jung et al., 2002)</i>	22
2.3	<i>Inter-laminar shear strength effects on water soak at 100°C on different resins (Gurit, 2012c).</i>	25
2.4	<i>Change in pitch due to hydrodynamic pressure load on a non-deformed and a pre-deformed propeller blade (Lee and Lin, 2004).</i>	26
2.5	<i>Author sailing a NACRA 17 “flying” on the left hand side and the sudden “crash” (“wheelie”) of the crew out of the boat due to instabilities in foiling conditions.</i>	28
2.6	<i>Digital Image Correlation measurement diagram (LaVision, 2012).</i>	31
2.7	<i>High Speed and Ultra-High Speed imaging technology (Reu and Miller, 2008).</i>	33
2.8	<i>Particle Image Velocimetry vector calculation in cross-correlation mode (LaVision, 2016).</i>	34
2.9	<i>Scheimpflug criterion, where image, lens and object plane are collinear (Prasad and Jensen, 1995).</i>	35
2.10	<i>Object, lens and image planes intersecting at a common line (Mottelet et al., 2012).</i>	36
2.11	<i>Bar representation in FEA modelling as described by Barbero (2008).</i>	38
2.12	<i>One-, two- and three-dimensional element types in FEA modelling (Madenci and Guven, 2006).</i>	39
3.1	<i>Tested specimen showing the load-carrying carbon-aluminium beam, the foam rib structure and the Mylar sheet as well as the principal dimensions. Experimental specimen measurement accuracy ± 10 mm.</i>	44
3.2	<i>PAC beam sandwich structure manufacturing process.</i>	45
3.3	<i>R. J. Mitchell wind tunnel working section showing the aerofoil and equipment position.</i>	46

3.4	<i>Longitudinal and transverse alignment of the DIC high-speed cameras.</i>	47
3.5	<i>Static out-of-plane displacement accuracy including the influence of the magenta filters applied to the LED lights.</i>	49
3.6	<i>Histogram comparison between white light image and the addition of magenta filters.</i>	50
3.7	<i>Differences in transmission between white-light and magenta filters.</i>	51
3.8	<i>Percentage error comparison for Near- and Far-end depths of field rigid body motions of 0.5 and 1 mm.</i>	52
3.9	<i>Measurement of accuracy in dynamic motions. Graph shows the pure out-of-plane displacement over time.</i>	52
3.10	<i>Accuracy of DIC measurements in rotation.</i>	53
3.11	<i>Influence of double-glazed window in DIC results.</i>	54
3.12	<i>Influence of glass in DIC results for a given rigid body motion.</i>	55
3.13	<i>Assessment of DIC measures for three different calibration procedures and changing the image resolution.</i>	56
3.14	<i>Assessment of DIC measures for three different calibration procedures and changing the image resolution.</i>	57
3.15	<i>DIC and PIV setup in the wind tunnel showing the principal dimensions and the components used.</i>	60
3.16	<i>An angular-displacement stereo PIV arrangement, where the two cameras are further rotated tilting the image plane with respect to the orientation of the camera lens and light sheet according to the Scheimpflug criterion.</i>	62
3.17	<i>Synchronisation diagram for the DIC-PIV-Aerodynamic measures.</i>	63
3.18	<i>Wind tunnel set-up.</i>	64
4.1	<i>Mesh convergence study for isotropic aluminium beam under bending loading.</i>	69
4.2	<i>Wall-clock time increase with mesh density.</i>	70
4.3	<i>Sandwich PAC beam ply angle $\phi = -30^\circ$, 21 integration points.</i>	72
4.4	<i>Young's modulus over density for a range of different materials (Ashby, 1992).</i>	73
4.5	<i>Experimental PAC beam under bending load.</i>	74
4.6	<i>Tip deflection and twist angle variations for a range of ply angles.</i>	75
4.7	<i>Young's modulus and stress ratio for a range of different ply angles (Clyne, 2014).</i>	76
4.8	<i>PAC sandwich beam laminate material properties.</i>	77
4.9	<i>Aerofoil flexible structure made of PAC beam ($\phi = -30^\circ$) and full-foam aerodynamic part.</i>	78
4.10	<i>Aerofoil flexible structure made of PAC beam ($\phi = -30^\circ$) and rib-foam aerodynamic part.</i>	79
4.11	<i>Foam test specimens for tensile, compressive and shear testing.</i>	79
4.12	<i>ASTM D1623 standard dimensions for tensile type A specimen. All dimensions are in millimetre.</i>	80
4.13	<i>Foam specimen loaded in tension at beginning and end of test.</i>	81
4.14	<i>Stress-strain curves from tensile foam tests.</i>	81
4.15	<i>Foam specimen loaded in compression.</i>	83
4.16	<i>Stress-strain curves from compressive foam tests.</i>	83
4.17	<i>Foam specimen loaded in shear, in compression direction.</i>	85

4.18	<i>Shear stress-shear strain curves from shear foam tests.</i>	85
4.19	<i>Foam micro-mechanical cellular structure of a compression sample prior to the compression-test.</i>	86
4.20	<i>Mesh interaction between PAC beam and foam cut-through.</i>	87
4.21	<i>Shell element directions and definitions for the Mylar sheet.</i>	88
4.22	<i>Tensile test for Mylar sheet.</i>	89
4.23	<i>Aerofoil flexible structure made of PAC beam ($\phi = -30^\circ$), rib-foam part and Mylar sheet.</i>	90
4.24	<i>Mesh of the whole FEA tested model showing the parts forming the assembly in different colours.</i>	92
4.25	<i>Boundary conditions and static FEA loads.</i>	93
4.26	<i>Mapping model between finite element mesh to finite volume mesh (Starccm+, 2015).</i>	95
4.27	<i>Implicit and explicit coupling algorithms for fluid-structure interaction problems</i>	97
4.28	<i>Comparison of different FSI coupling methods and time-steps for benchmark cases.</i>	99
4.29	<i>FSI model shown in the numerical wind-tunnel domain. The internal structure, as well as the part of the beam fixed above the wind tunnel ceiling, are presented. The blue region represents the interface surface.</i>	100
4.30	<i>CFD mesh of the flexible aerofoil.</i>	104
4.31	<i>Percentage error difference between the numerical and the experimental values at three different mesh densities.</i>	105
4.32	<i>Change in wing shape with angle of attack detected by DIC cameras.</i>	106
5.1	<i>Calibration image number 1 viewed from left-hand camera.</i>	110
5.2	<i>Surface height for two different angles of attack as seen from DIC cameras.</i>	110
5.3	<i>Displacement length for two different angles of attack at $V_S = 25 \text{ ms}^{-1}$.</i>	111
5.4	<i>Images from the two high-speed DIC cameras, mapped image deriving from the calibration procedure and histogram comparison of the images coming from the two cameras for $\alpha = 15^\circ$ and $V_S = 25 \text{ ms}^{-1}$.</i>	112
5.5	<i>DIC tip region and twist line conventions.</i>	113
5.6	<i>Angle conventions for the structural specimens.</i>	113
5.7	<i>Frequency response for structural and aerodynamic data.</i>	114
5.8	<i>Comparison of structural tip displacement between one set of DIC-only data and coupled DIC-PIV data and aerodynamic loads for $\alpha = 15$ degrees and a range of wind speeds. Differences between tip displacement and vortex position.</i>	115
5.9	<i>Structural response comparison for the change in angle of attack between DIC only data and coupled DIC-PIV data. The Figure shows the change in twist angle for a range of wind speeds at three different locations in the span-wise direction for $\alpha = 15$ degrees.</i>	117
5.10	<i>Time-averaged axial velocity distribution relative to the free stream velocities. The in-plane velocity field is represented as vectors. The vortex centre calculated from the mean velocity field is represented by a white circle.</i>	118

5.11 Aerodynamic forces acting on the flexible aerofoil for the three different internal structures. Full line: $\phi = 0^\circ$, dotted line: $\phi = -30^\circ$ and dot-dash line: $\phi = 2 \times 30^\circ$	120
5.12 Tip displacement comparison for the three PAC beams at a range of wind speeds and angles of attack. Full line: $\phi = 0^\circ$, dotted line: $\phi = -30^\circ$ and dot-dash line: $\phi = 2 \times 30^\circ$	121
5.13 Twist angle comparison for the three PAC beams at a range of wind speeds and angles of attack. Full line: $\phi = 0^\circ$, dotted line: $\phi = -30^\circ$ and dot-dash line: $\phi = 2 \times 30^\circ$	122
5.14 Non-dimensional displacement and twist for the three different internal structures.	124
5.15 Tip deflection magnitude over angle of attack for two different wind speeds. The solid lines represent $\phi = 0^\circ$ and the dotted lines represent $\phi = -30^\circ$ measured in the experiments. The markers represent the FEA results for both $\phi = 0^\circ$ (light-colours) and $\phi = -30^\circ$ (dark colours).	126
5.16 Change in angle of attack for different wind speeds and set-angles of attack. The solid lines represent $\phi = 0^\circ$ and the dotted lines represent $\phi = -30^\circ$ measured in the experiments. The markers represent the FEA results for both $\phi = 0^\circ$ and $\phi = -30^\circ$	126
5.17 First five mode frequencies of the flexible areofoil. Scale factor 10.	127
5.18 Axial velocity distribution relative to the free stream velocity of 25 m/s in wind tunnel axis system. The in-plane velocity field is represented as vectors. The vortex centre detected by the VORTFIND algorithm is represented by a white circle.	128
5.19 Tangential velocity for CFD numerical model and PIV measures for $\alpha = 15^\circ$ and $V_S = 25$ m/s.	129
5.20 Deflection and lift force (L) over time for wind tunnel measurements (i.e. deflection measured with DIC and lift by the forces balance) and FSI numerical simulations.	130
5.21 Aerofoil deflection as measured with DIC and as simulated in the numerical environment for $V_S = 14.95$ m/s, $\alpha = 9.97^\circ$ and $\phi = 0^\circ$	131
5.22 Twist angle comparison between DIC and FSI numerical simulations at three different span-wise locations.	132
5.23 Displacement magnitude along the aerofoil span at the leading and trailing edges. Wind speed $V_S = 14.95$ m/s and angle of attack $\alpha = 9.97^\circ$	132
5.24 Velocity streamlines and nodal deflection shown in the numerical wind tunnel working section. Wind speed $V_S = 14.95$ m/s and angle of attack $\alpha = 9.97^\circ$	133
 6.1 Ideal lift over velocity profile for a hydrofoil section.	136
6.2 Foiling catamaran configuration. In the transverse plane it is possible to change the cant-angle, and in the longitudinal plane the rake, which adjusts the pitch angle.	136
6.3 Change in aerofoil internal design. Design 1 shear centre location moved 10% toward the trailing edge. Design 2 oriented plies moved 30% away from the neutral axis. The internal spar of Design 3 is a C-beam, which presents a shear centre location forward of the one of Designs 1 and 2 and maximum distance between the oriented plies and the neutral axis.	138

6.4	<i>Differential Stiffness Bend-Twist coupling for a closed box-beam section with different stiffness of the webs as presented by Raither et al. (2012).</i> 139
6.5	<i>CFD pressure and position of shear centres and centre of pressure (CoP) on aerofoil section for Design 0 and Designs 1, 2, 3 and 4.</i> 140
6.6	<i>Comparison of twist levels between the four different designs.</i> 142
6.7	<i>Change in twist angle with wind speed for a range of angles of attack, as calculated by the analytical model and as measured in the wind tunnel.</i> 143
6.8	<i>Section shape of a real hydrofoil tip and of a NACA 2412 aerofoil.</i> 143
6.9	<i>Design 4 technical drawing showing the different section shapes and the principal dimensions. All the dimensions shown are in millimetres.</i> 144
6.10	<i>Lift over velocity profile for Design 0 and Design 4 at $\alpha = 5^\circ$.</i> 145
6.11	<i>Lift coefficient curves for cambered and symmetric sections. The arrows show the influence of using PAC composites that change the angle of attack, and the change in section shape that can be achieved with multi-elements foils or flaps.</i> 146
6.12	<i>Ply orientation reference systems for the C-beam internal spar. The plies are oriented around axis 1 and stacked along axis 3.</i> 147
6.13	<i>CFD boundary layer mesh at the tip of Design 4.</i> 148
6.14	<i>Lift and drag coefficients over a range of angles of attack for $V_S=15\text{ m/s}$.</i> 149
6.15	<i>Fluid-structure interaction response of Design 4 compared to Design 0.</i> 150
6.16	<i>Design 4 C-beam internal spars composite lay-up process.</i> 152
6.17	<i>Design 4 aerodynamic structure made of foam and Mylar.</i> 152
6.18	<i>Wind tunnel and equipment set-up.</i> 154
6.19	<i>Transmission of red filters on DIC high-speed cameras.</i> 155
6.20	<i>Lift force over wind speed for $\alpha = 10.02^\circ$: analytical, numerical FSI and wind tunnel results.</i> 156
6.21	<i>Aerodynamic lift force acting on the flexible aerofoil over wind speed for the two different internal structures. Solid line: carbon spar, dotted line: glass-carbon spar.</i> 157
6.22	<i>Tip displacement comparison for the two internal structures at a range of wind speeds and angles of attack. Solid line full markers: carbon spar, dotted line open markers: glass-carbon spar and X: FSI response of the carbon spar as modelled numerically.</i> 158
6.23	<i>Change in angle of attack for different wind speeds and set-angles of attack at 90% of aerofoil span. The solid lines represent the carbon spar and the dotted lines represent the glass-carbon spar as measured in the wind tunnel. For $\alpha=20.04^\circ$ the closed marker indicates the carbon beam and the open marker the glass-carbon beam. The green markers presented for $\alpha=10.02^\circ$ show the FSI twist for the modelled aerofoil with a carbon spar.</i> 158
6.24	<i>Non-dimensional displacement and twist for the two internal structures materials compared to the Design 0 $\phi = 2 \times 30^\circ$.</i> 159
6.25	<i>Lift coefficient over angle of attack for two different wind speeds - Glass PAC.</i> 160
6.26	<i>Change in angle of attack in a dynamic run from $\alpha = 10.02^\circ$ to $\alpha = 28^\circ$ as measured with DIC for $V_S=10\text{ m/s}$.</i> 161
6.27	<i>Lift force, displacement magnitude and relative tip vortex movement over recording time for $\alpha = 10.02^\circ$.</i> 162

6.28 <i>Natural frequency response of both internal spars as measured in an impact test.</i>	162
7.1 <i>The International Moth class shown when sailed and its hydrofoil configurations (Sheahan, M., 2015).</i>	170

List of Tables

3.1	PAC structure dimensions.	46
3.2	DIC performance table showing the equipment and the setting used, as well as the speckle pattern characteristics.	58
3.3	PIV performance table showing the equipment and the setting used. . . .	61
4.1	PAC sandwich beam dimensions.	71
4.2	Tensile tests on foam specimen results.	82
4.3	Compression tests on foam specimen results.	84
4.4	Shear tests on foam specimen results.	86
4.5	Tensile modulus for Mylar film for a gauge length of 250 mm and for the actual gauge length for each specimen.	90
4.6	Material properties used in the FEA model.	91
4.7	CFD numerical settings within Star-CCM+.	107
5.1	First five mode natural frequencies of the flexible aerofoil in wind tunnel and numerical analyses.	127
6.1	PIV performance table showing the equipment and the setting used. . . .	153

Nomenclature

Symbols are defined in the text at the first point of usage. All symbols used in multiple sections are included in the nomenclature. Where a symbol has dual meaning, this is explicitly stated in the text. In general, bold typeface represents a **vector**.

symbol	description	units
A	Area	[m ²]
A_{ij}	In-plane stiffness [A]	
AR	Aspect ratio of a foil element	
AoA	Angle of Attack	[deg]
B	Strain displacement matrix	
B_{ij}	Bending-extension coupling [B]	
C	Asymmetric aerofoil constant	
c	Aerofoil chord	[m]
c_b	Circle of blurr	[pixels]
C_D	Drag coefficient	
C_F	Friction coefficient	
C_L	Lift coefficient	
C_Z	Vertical coefficient	
D	Drag force	[N]
D	Stress displacement matrix	
D_{ij}	Bending stiffness [D]	
D_F	Distance from camera to far limit of depth of field	[mm]
DoF	Depth of field	[mm]
D_N	Distance from camera to near limit of depth of field	[mm]
d_x	x displacement	[mm]
d_y	y displacement	[mm]
d_z	z displacement	[mm]
E	Young's Modulus	[MPa]
F	Force	[N]
F_N	Normal force	[N]
f	Force vector	
f	Focal length	[mm]
G	Shear Modulus	[MPa]

I	Second moment of area	[mm ⁴]
I	Turbulence intensity	[%]
J	Advance ratio	
J	Torsional constant	[mm ⁴]
K	Element stiffness matrix	
K	Lift curve slope	
k	Element stiffness matrix	
k	Number of layer	
k	Element	
k	Turbulent energy	[J/kg]
$k_{x,y,xy}$	Laminate curvature	
<i>l</i>	Specimen length	[m]
l	Turbulence scale length	[m]
L	Lift force	[N]
M	Magnification	
M_{ij}	Moments per unit length applied to the laminate	
M_Y	Yaw moment	[Nm]
N	Number of layers in the laminate	
N	Shape function	
N_f	<i>f-number</i>	
N_{ij}	Forces applied to the laminate	[N]
n	face centroid	
P	Force applied on FEA node	[N]
Q_{ij}	Stiffness matrix components	
<i>r</i>	Radius	[m]
R_e	Reynolds number	$\left[\frac{V_s \times c}{\nu_{air}} \right]$
<i>s</i>	Specimen distance to camera	[mm]
T_n	Shape function interpolant	
t	Layer thickness	[mm]
t_i	Co-simulation time step	[mm]
u	Displacement vector	
<i>u</i>	x-direction flow velocity	[ms ⁻¹]
$\overline{u'_i u'_j}$	Reynolds stress tensor	
u_τ	Friction velocity	[m/s]
<i>v</i>	y-direction flow velocity	[ms ⁻¹]
\overline{v}	Turbulent viscosity	[m ² /s]
V_s	Wind speed	[ms ⁻¹]
y	First prism layer	[m]
y^+	y-plus value	
z	Layer distance from the reference plane	[mm]
α	Angle of attack	[deg]

α_c	Coupling coefficient	
γ_{xy}	Shear strain	
Δt	Exposure time PIV camera	$[\mu s]$
Δt_c	Coupling step size	
δ	Displacement	[mm]
δ'	Non-dimensional displacement	
δ_{gg}	Boundary layer thickness	[m]
$\frac{\partial \alpha}{\partial L}$	Bend-twist coupling term	
ϵ	Strain	
ϵ	Effective angle of attack	[deg]
η	Element computational coordinate 2	
θ	Twist angle	[deg]
θ'	Non-dimensional twist angle	[deg]
$\frac{\mu_t}{\mu}$	Eddy viscosity ratio	
ν	Poisson's ratio	
ν_{air}	Kinematic viscosity of fluid (air or water)	$[ms^{-1}]$
ξ	Element computational coordinate 1	
ρ	Density	$[kgm^{-3}]$
σ	Stress	[MPa]
τ_{xy}	Shear stress	[MPa]
τ_w	Wall shear stress	[Pa]
ϕ	Ply angle	[deg]
χ	Element computational coordinate 3	
ψ	Stereo angle	[deg]
ω	Frequency	[Hz]
ω	Specific dissipation rate	[1/s]

Subscripts

subscript	description
1	Along composite ply axes
2	Transverse to composite ply axes
3	Through thickness composite ply axes
e	FEA Element
i	Along flow axes
j	Transverse flow axes
k	Through flow axes
x	Along laminate or global axes
y	Transverse laminate or global axes
z	Through thickness laminate axes or global axes

∞

Free-stream velocity

Acronyms

abbreviation	description
ALE	Arbitrary Lagrangian Eulerian method
CAS	Circumferential Asymmetric Stiffness
CFD	Computational Fluid Dynamics
CLT	Classical Laminate Theory
DIC	Digital Image Correlation
DoF	Depth of field
DSBT	Dirrential Stiffness Bend-Twist
FEA	Finite Element Analysis
FFT	Fast Fourier Transform
FSI	Fluid Structure Interaction
LSS	Laminate Stacking Sequence
PAC	Passive Adaptive Composites
PIV	Particle Image Velocimetry
RANS	Reynolds-Averaged Navier-Stokes

Acknowledgements

These past three years have been an amazing journey, I have really enjoyed being able to research into a field that corresponds to my passion: sailing. This was possible only thank to my supervisors Dr Steve Boyd and Prof. Steve Turnock, who have always been extremely supportive of me both as a student and as a sailor. They have helped me understand what the word “research” means and I really hope I can continue to work with them as I have really loved being their student. Alongside my supervisors I would like to acknowledge the EPSRC for funding my research under the grant number EP/I009876/1.

The bond between sailing and research surely helped me to enter as an intern in FSI at Land Rover Ben Ainslie Racing. I really would like to thank Dr Rodrigo Azcueta and Matteo Ledri (and all the rest of the team) for welcoming me at BAR since day one. For all the experimental work I would like to thank Dr Dave Marshall and Mike in the wind tunnel. Dr Andy Robinson in the TSRL and Dr Dave Hollis and Dr Alex Nila from LaVision.

One big thank you goes to Dr Joe Banks: without him I would have not been able to cope with all the stress involved in the tests. He has always been there, working side by side with me (even at weekends) and sharing the passion for cakes and coffee!

My Ph.D. path would have not been possible without my parents and my brother, who always thought I was good enough to be able to do research and pursue my dreams. I really hope they were right...

The final thank you goes to Simone, who followed this journey from the beginning. He shared with me all the emotional moments that came along in those three years, the happy and sad ones, and he was the one that made me smile on all occasions.

”Considerate la vostra semenza:
fatti non foste a viver come bruti,
ma per seguir virtute e canoscenza”

Divina Commedia, Inferno, Canto XXVI by Dante Alighieri.

1

Introduction

1.1 Background

The recent developments in composite materials led to their application to a wide variety of different structures, from the aircraft industry, to renewable energy devices, to high performance sports applications and marine components. Composite materials are formed of two or more materials which together can produce mechanical properties different from the properties of the constituents alone. Fibre-reinforced composite materials, formed of a high strength and high modulus fibre in a matrix material, are used because of their excellent specific strength, stiffness and fatigue resistance. These characteristics are provided by the load-carrying fibre and by the action of the matrix that keeps the fibres together and isolates them from the surrounding environment. Composite materials can be studied at different levels, from micro-mechanics to macro-mechanics. Depending on the fibre and matrix selected, they provide different material properties such as modulus, strength and thermal coefficients. In composite design, not only would the type of material change the laminate material properties, but also the orientation of the fibres inside the laminate. Due to the atomic bonding within a laminate, the material is stronger in one direction, which is usually aligned with the load direction. Composite structures are therefore usually designed to achieve their maximum stiffness, and mostly to provide similar properties in all the directions, as isotropic materials. However, it is possible to design composites also by increasing their strength, resulting in flexible

structures. This can be achieved by taking advantage of the anisotropic nature of composites, tailoring the material properties of a laminate to achieve a desired deformation response. Due to the interactions between the bending-twist and extension-twist within the stiffness matrices of the composite laminates (as shown in Figure 1.1), it is possible to maximise the performance of a given structure, leading to the possibility of exploring design techniques that account for the internal flexibility of the composite laminates.

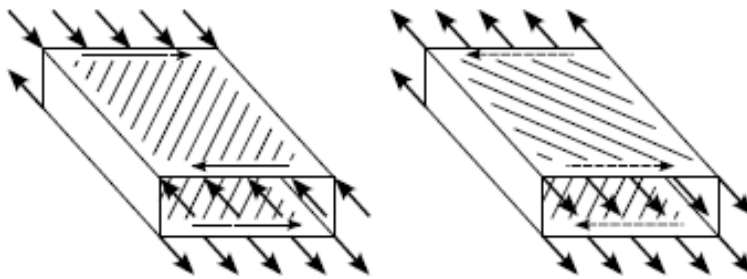


FIGURE 1.1: *Bend-twist coupling (left) and extension-twist coupling (right) for beam structures (Fedorov, 2012).*

As shown in Figure 1.1, in order to have a bend-twist coupling in the structure, the fibres at the opposite sides of the laminate shear centre should be oriented in the same direction. This arrangement, when a beam is subject to bending loading, allows the top face to be in compression and the bottom face to be in tension.

This research mainly focuses on the applications of composite materials to high-performance sailing foils. The research can also be applicable to renewable energy blades (such as wind turbine and tidal turbine blades) and general foil structures. These structures can be designed, using the bend-twist and extension-twist interactions, to change their structural behaviour according to the applied load. In order to correctly understand the structural response of these components, and therefore to design an optimised structure, it is necessary to investigate how they deform under fluid-loading. The new design process needs to account for the different deformation given by diverse laminate structures that could ultimately lead to a performance improvement. For aerofoil-shaped structures, the design paradigm can develop structures with internal composite lay-up that can change the angle of attack for certain fluid-loading cases. The structure under load can either decrease its effective angle of attack, in a position toward feather, or increase it, toward stall, as can be seen in Figure 1.2.

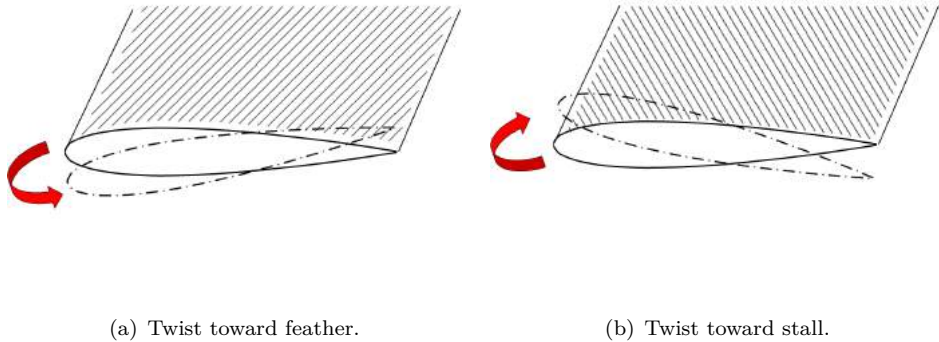


FIGURE 1.2: *Response of an aerofoil-shape structure with bend-twist coupling configuration.*

Under fluid loading, the forces and moments experienced will be related to the strains at laminate level (i.e. in a macro-mechanics approach) as:

$$\begin{bmatrix} N_x \\ N_y \\ N_{xy} \\ M_x \\ M_y \\ M_{xy} \end{bmatrix} = \begin{bmatrix} A_{11} & A_{12} & A_{16} & B_{11} & B_{12} & B_{16} \\ A_{12} & A_{22} & A_{26} & B_{12} & B_{22} & B_{26} \\ A_{16} & A_{26} & A_{66} & B_{16} & B_{26} & B_{66} \\ B_{11} & B_{12} & B_{16} & D_{11} & D_{12} & D_{16} \\ B_{12} & B_{22} & B_{26} & D_{12} & D_{22} & D_{26} \\ B_{16} & B_{26} & B_{66} & D_{16} & D_{26} & D_{66} \end{bmatrix} \begin{bmatrix} \epsilon_x \\ \epsilon_y \\ \gamma_{xy} \\ k_x \\ k_y \\ k_{xy} \end{bmatrix} \quad (1.1)$$

where N_x , N_y , N_{xy} are the fluid forces, M_x , M_y , M_{xy} are the fluid moments, ϵ_x , ϵ_y , γ_{xy} are the laminate strains and k_x , k_y , k_{xy} are the laminate curvatures and

$$A_{ij} = \sum_{k=1}^N (\bar{Q}_{ij})_k t_k; \quad i, j = 1, 2, 6$$

$$B_{ij} = \sum_{k=1}^N (\bar{Q}_{ij})_k t_k \bar{z}_k; \quad i, j = 1, 2, 6$$

$$D_{ij} = \sum_{k=1}^N (\bar{Q}_{ij})_k \left(t_k \bar{z}_k^2 + \frac{t_k^3}{12} \right); \quad i, j = 1, 2, 6$$

where $(\bar{Q}_{ij})_k$ are the coefficients in the global coordinates of the plane-stress stiffness matrix, A_{ij} represents the in-plane stiffness of the laminate (and presents values also for symmetric and balanced lay-ups), B_{ij} represents the bending-extension coupling (i.e. the coupling term between moments and direct strains, and forces and curvature) and D_{ij} the bending stiffness of the component. It has to be noted that the material properties defined by $(\bar{Q}_{ij})_k$ are not a function of the distance from the reference centre of the laminate, but are unique for each layer.

In order to correctly design tailored composite materials, it is necessary to account for the B_{ij} matrix, as this gives the coupling terms for bending-twist from the fluid-loads

to the laminate structure.

1.2 Motivation

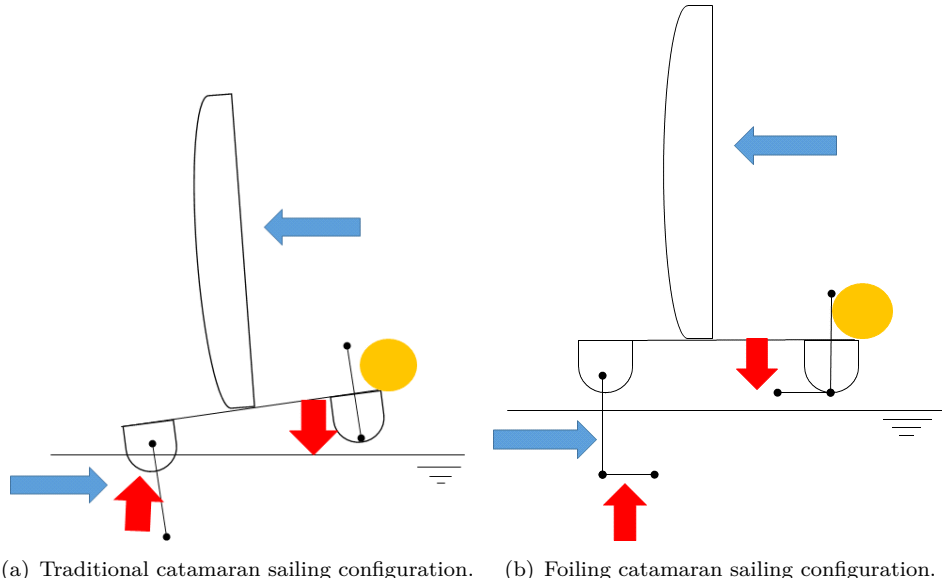
One composite structure that needs optimising nowadays is a sailing daggerboard. The design and construction of high speed sailing catamarans is going through a very innovative period. Since 2007 a large number of catamarans have been built and research and innovation are of primary importance for the new sailing community. These boats have the power to attract the interest of the media, because of their speed and the athletic skills that the crew must have. The first catamaran to sail a world series event was the Extreme 40, in 2007.

Since 2007 the America's Cup team BMW Oracle has developed the 90 foot trimaran that won the 2010 cup. After the America's Cup in San Francisco in 2013, also won by BMW Oracle, sailed with the AC72, a number of different teams are now racing the *foiling* AC45F (Figure 1.3) in the America's Cup world series to improve their "flying" skills.



FIGURE 1.3: *Ben Ainslie Racing Team flying on the AC45 (Ben Ainslie Racing, 2015).*

These new catamarans are designed to avoid sailing in a normal catamaran configuration, Figure 1.4(a), always sailing in a foiling configuration, Figure 1.4(b). The foiling configuration, which entails the boat "flying" with both hulls above the water, greatly reduces the wetted area of the hulls, allowing reduction of the drag associated with the hull when immersed in the water. Therefore, for the crews and design teams it is necessary to enhance this condition in order to improve the hydro-dynamic performances.

FIGURE 1.4: *Catamaran sailing configurations.*

The 2013 America’s Cup, sailed in San Francisco Bay, experienced very reliable and steady wind conditions. However, for the next event hosted in Bermuda in June 2017 it is crucial to acquire the knowledge needed to sail the catamarans in the fastest way in all wind conditions, as the weather, and therefore the wind intensity, can vary greatly throughout the racing week. Therefore, the possibility of tailoring the daggerboard structure to change the angle of attack depending on the flow speed should be investigated.

Another type of catamaran where the possibility of tailoring the composite lay-up can be useful is the 2016 Olympic-class catamaran NACRA 17. NACRA Performance sailing has produced two high performance catamarans in the last five years. The NACRA F20c sails in the F20 class with a heavyweight all-male crew, and the NACRA 17 was chosen in 2012 over a wide range of other catamarans as being the new class in the Rio 2016 Olympics and is sailed by a mixed gender crew. Both of these have two foil daggerboards, as can be seen in Figure 1.5.

The regulations of Olympic classes do not permit active devices to change the angle of attack of the C-foil while sailing, however they do permit the enclosure of the foils within the daggerboard case which can change the incidence angle. This allows the slight control of the angle of attack and the angle of pitch. Moreover, the possibility of tailoring the foils can be explored in order to have a control on the structural behaviour under hydro-dynamic loadings while sailing. If the laminate fibre directions are designed in such a way as to change the angle of attack, and the pitch angle in increased boat speed, the crew might benefit, as they should be able to sail more comfortably and for longer periods in the down-wind legs in foiling configuration. This performance gain can be achieved if the structure is tailored toward feather as the daggerboards, due to the



(a) Author sailing a NACRA 17 down-wind. (b) NACRA F20 sailing upwind (The Foiling Week, 2015).

FIGURE 1.5: *NACRA Performance sailing catamarans.*

dynamic nature of sailing, stall when the crew weight is on the stern and the gennaker down-wind sail has higher loads in the top part.

The stiff nature of the NACRA C-foils, leads to the necessity of investigating both experimentally and numerically a more flexible aerofoil. The use of a flexible aerofoil, permits the investigation of large structural deformations, changes in angle of attack due to shifts in the centre of pressure of the foil with increased aerodynamic loading, and therefore, large tip vortex motions. Being able to assess the response of an aerofoil under fluid-load enables the creation of a design tool applicable to a large variety of structures in general, and foil-shaped structures in particular.

The performance evaluation that needs to be investigated in the present project is therefore the possibility of reducing the angle of attack at high fluid loads, while still maintaining a constant lift value (ideally of the weight of the boat) in increased boat speed, thereby increasing the performance range of the aero/hydro-foil sections. This response can be achieved using Passive Adaptive Composite (PAC) structures that are tailored to a certain design take-off speed. The evaluation needs to be achieved knowing the structural response of composite materials under fluid loading, and therefore a complete Fluid Structure Interaction (FSI) investigation is needed in both experimental and numerical environments.

1.3 Aim

Based on the discussion presented in Sections 1.1 and 1.2, this work is aimed at utilising both experimental and numerical tools to develop an aero/hydrofoil section able to passively adapt its pitch angle to achieve a constant lift value in increased flow-speeds.

A significant knowledge gap exists within the fluid-structure interaction field regarding an accurate, robust and repeatable experimental methodology able to represent the

structural deformation under fluid-load, and vice-versa the changes in flow-features given by the structural response.

Therefore, two main aims were considered in the current research:

- To develop an experimental methodology capable of accurately describing the structural response of a full-scale aerofoil under fluid-load, together with the flow features that are affected by the deformation and twist of the aerofoil
- To design and develop an aerofoil structure tailored to decrease its lift coefficient by means of increased flow-speed

1.4 Objectives

In order to achieve the above aims the following objectives were set:

1. to develop a method for accurate measurement of the full-field deformation of a structure subject to fluid loading;
2. to develop a methodology for synchronising structural deformation measurements with laser-based fluid measurements;
3. to quantify the uncertainty values associated with the experimental measures;
4. to develop a Finite Element Methodology for modelling a generic foil structure with passive-adaptive capabilities;
5. to undertake a coupled Fluid Structure Interaction numerical model that accurately describes both the flow features and the structural deformation of a PAC structure;
6. to validate the Fluid Structure Interaction numerical model using the full-field experimental results;
7. to understand the influence of passive adaptive layers on the internal structure of an aero/hydrofoil;
8. to apply the numerical method to a new design, understanding the bend-twist response of the structure;
9. to finally manufacture and test the new design capable to achieve a given response.

A flow chart of the research is summarised in Figure 1.6. The project was initiated testing the NARA F20 C-foil. Throughout the research two new structures were simulated, manufactured and tested to achieve the possibility of building a new hydrofoil that could passively adapt to help a high-performance boat to foil more easily in a wider range of weather conditions.

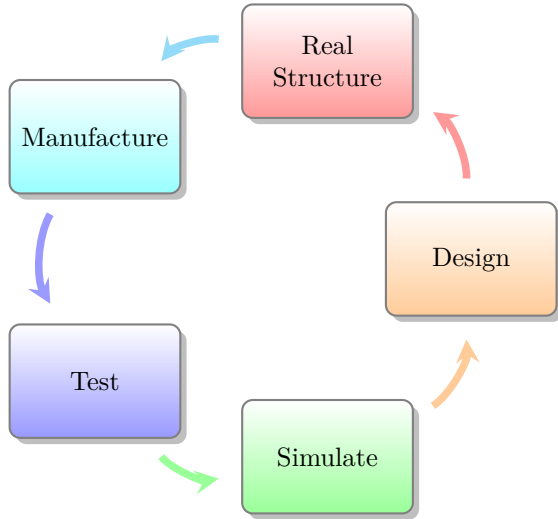


FIGURE 1.6: *Flow chart of the research project. The iterative process is associated with the possibility of designing new structures tailored to certain loads.*

1.5 Novelty

A large number of studies has been performed on aero-elastic structures during the past twenty years, investigating the possibility of designing composite structures for their strength, tailoring the properties for a desired purpose. However, the large majority of these studies still does not account for the complexity of the Fluid Structure Interaction (FSI) coupled problem, where the structural response affects the flow behaviour and vice-versa.

The lack of experimental validation cases for FSI investigations triggered the necessity to provide the scientific community with a complete FSI experiment that can describe the structure and the fluid behaviour of a generic structure simultaneously. This experimental case for a simple generic-aerofoil can provide validation cases for in-house numerical simulations as all the structural details and the uncertainties associated with the measures are described.

Moreover, a numerical coupled FSI analysis on the generic aerofoil structure and a comparison with the experimental results gives enough confidence on how to couple structural and fluid solvers in the numerical environment. Therefore, another contribution to the scientific knowledge is associated with the design of a structure that passively adapts its response to aerodynamic load, changing only the internal composite plies orientation. This will improve the performance range of aero-hydrofoil sections, especially tailored for catamaran foils.

1.6 Publications

This report represents a research contribution within Fluid Structures Interaction problems, especially contributing in the field of FSI experimental methodologies and in design developments of passive-adaptive structures.

1.6.1 Journal Papers

1. Banks, J., Marimon Giovannetti, L., Soubeyran, X., Wright, A. M., Turnock, S. R., Boyd, S. W., (2015) Assessment of Digital Image Correlation as a method of obtaining deformations of a structure under fluid load *Journal of Fluids and Structures*, Vol. 58, pp. 173-187.
2. Banks, J., Marimon Giovannetti, L., Taylor, J., Turnock, S. R. (2016) Assessing human-fluid-structure interaction for the international moth *in special issue: the Engineering of SPORT 11*, Procedia Engineering, Vol. 147, pp. 311-316.
3. Marimon Giovannetti, L., Banks, J., Turnock, S. R., Boyd, S. W., (2016) Uncertainty assessment for fluid-structure interaction measurement by coupled Digital Image Correlation and Particle Image Velocimetry during wind tunnel experiments *Journal of Fluids and Structures*, Vol. 68, pp. 125-140.
4. Marimon Giovannetti, L., Banks, J., Turnock, S. R., Boyd, S. W., (2017) Validation of a fully coupled FSI model of a Passive Adaptive Composite structure using experimental full-field synchronised fluid and structure response data (*ready for submission to the special issue of Journal of Computers & Structures*).

Two more journal papers should be produced on the new passive-adaptive design. The former will focus on the design developments based on passive adaptive layers. The latter will focus on the unsteady response of the aerofoil in near-stall conditions, especially looking at the tip vortex strength and position and at the deformation of the structure.

1.6.2 Conference Papers

1. Marimon Giovannetti, L., Banks, J., Turnock, S. R., Boyd, S. W. (2014) Data-rich experimental fluid structures interaction of composite structures under wind loading *Marine Technology Postgraduate Conference*, 9-10 June, Newcastle, UK.
2. Banks, J., Marimon Giovannetti, L., Turnock, S. R., Boyd, S. W. (2014) Developing tools for assessing bend-twist coupled foils *NuTTS '14: 17th Numerical Towing Tank Symposium*, 28-30 September, Marstrand, Sweden.

3. Marimon Giovannetti, L., Banks, J., Turnock, S. R., Boyd, S. W. (2015) Fluid Structures Interaction of High Performance Catamaran C-Foils Under Load *Proceedings of the 5th High Performance Yacht Design conference*, 8 - 12 March, Auckland, New Zealand.
4. Marimon Giovannetti, L., Banks, J., Turnock, S. R., Boyd, S. W. (2015) Developing tools for assessing bend-twist coupled foils *NuTTS '15: 18th Numerical Towing Tank Symposium*, 28-30 September, Cortona, Italy.
5. Marimon Giovannetti, L., Banks, J., Turnock, S. R., Boyd, S. W. (2016) Developing tools for assessing the Fluid Structure Interaction of Passive Adaptive Composite foils *The Sixth International Conference on Structural Engineering, Mechanics and Computation*, 5-7 September 2016, Cape Town, South Africa.

1.7 Report Structure

The structure of the thesis presents a number of stages of work undertaken toward the development of a reliable design optimisation method for PAC structures.

The report of the project presents an extended critical literature review, firstly introducing the concept of composite materials, especially focusing on the introduction of Passive Adaptive Composites (Chapter 2). The advantages of their applications and the drawbacks that need to be accounted for in the new researches are discussed. The experimental techniques that can be used in FSI experiments are also presented. The range of different applications of full-field measurement techniques, both in laboratory and extreme environments, are discussed. Finally, Finite Element Analysis methodology applicable to composite passive-adaptive structures is presented, describing the advantages and disadvantages associated with utilising some modelling techniques.

The new experimental methodology is described in Chapter 3, explaining the full-field measurement techniques involved and the positions of the equipment. In this chapter the assessment of the experimental methodology accuracy is described in detail, as well as the techniques used to couple the measurement tools to be able to conduct a FSI experiment. The uncertainty values associated with the experimental measures are also outlined.

Chapter 4 provides an outline of the numerical method used to simulate the fluid-structure response of the flexible aerofoil. In this chapter the numerical model is described in all its aspects, looking at the selection of the elements for the mesh, at the material properties and at how to correctly couple the Finite Element Analysis and the Computational Fluid Dynamic software.

The results for the experimental and the numerical analyses are provided in Chapter 5. A discussion of the results can be found in the same chapter, explaining the robustness of the experimental technique carried out and a critical assessment of the numerical outcomes.

Chapter 6 presents the design challenge of building a hydrofoil that could adapt its pitch angle to reach a constant value of lift force. The design development by means of analytical, numerical and finally experimental results is outlined and the outcomes of the design optimisation are discussed.

Finally, overall conclusions are given in Chapter 7. This includes an overview of the research carried out, the discussion of the contributions to the field and recommendations for future work.

2

Exploring Passive Adaptive Composites

2.1 Introduction

This chapter presents a review of composite materials, and their potential of bend-twist and bend-extension couplings are presented. The wide range of applications of Passive Adaptive Composites (PAC) is described, looking not only at marine structures but also at applications in different fields. Composite structures designed for their strength rather than for their stiffness are investigated, and in particular an analysis of the influence of ply orientation on the properties of the material and their response. In addition, a review of the background related to the experimental methodologies used, Digital Image Correlation (DIC) and Particle Image Velocimetry (PIV), is presented. For both experimental methods, a range of different applications is discussed, in particular describing the current level of understanding and their limitations. Their applications in synchronised or extreme conditions are described. Moreover, the Finite Element Analysis (FEA) numerical methodology is presented, describing the differences deriving from choosing a two- or three-dimensional representation of a physical problem and changing the shape interpolation function.

2.2 Composite Structures

Composite materials are defined as being made up of two or more constituent parts. Two materials are used to generate a new material with properties that are different to

the properties of the constituents on their own (Reddy, 2003).

The study of composite materials follows different levels, as can be seen in Figure 2.1.

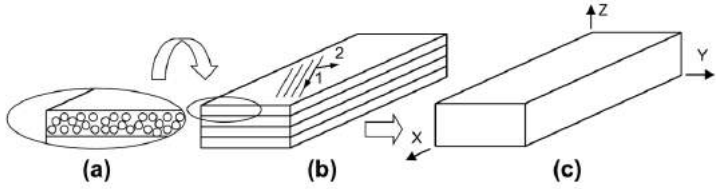


FIGURE 2.1: *Study of composite materials from micro-mechanics (a) lamina level (b) and laminate level(c) (Barbero, 2008).*

In order to understand the elastic behaviour of anisotropic materials as well as the coupling between bending-twist and extension-twist within a laminate, the Laminate Stacking Sequence (LSS) needs to be investigated. The material properties of the laminate are a function of the stacking sequence of the various layers. In order to obtain the material properties of a laminate, the Classical Laminate Theory (CLT) and the first-order shear deformation plate theory were developed, and are currently used as approximations to obtain material properties analytically knowing the staking sequence and the thickness of the layers. These two approaches are derived from three-dimensional elasticity theory and rely on assumptions regarding the kinematics and the deformations through the thickness of the laminate, as described by Reddy (2003). These assumptions allow reduction from a 3-D to a 2-D problem, and are the same used when modelling composite materials in FEA analyses with shell elements, as they follow the *Kirchhoff* assumptions:

- straight lines perpendicular to the mid-plane remain perpendicular after deformation;
- the transverse normals do not experience elongation;
- the transverse normals rotate in such a way that they remain perpendicular to the mid-plane after deformation.

Further assumptions are made in order to analytically determine the material properties of a laminate:

- each lamina in the stack is homogeneous and orthotropic, i.e. the void content within the lamina must be small;
- the laminate is thin compared to its overall dimensions;
- the laminate and lamina are in a state of plane stress;

- displacements are small compared to the thickness;
- displacements are continuous throughout the laminate;
- in-plane displacements vary linearly through the thickness of the laminate;
- ϵ_z is very small compared to ϵ_x and ϵ_y .

Composite structures, designed to maximise their stiffness are mostly symmetric laminates with fibres located at 0° , 45° and 90° , therefore presenting quasi-isotropic material properties, as the major loading modes are counteracted by the fibres positioned at those three characteristic angles. However, if the laminate is not symmetric and it is designed for its strength, allowing flexibility in the structure, the interactions between bending-extension coupling must be considered (Barbero, 2008). Using the anisotropy of the material, it is possible to design components presenting elastic couplings that will enhance the performance of the whole structure (Fedorov, 2012; Veers *et al.*, 1998). This can be achieved by manufacturing the components to vary the lay-up of the composite fibres according to the expected load.

In those structures, the relationship of the stresses and strains must take into consideration the complete stiffness matrix as the stresses (σ and τ) and strains (ϵ and γ) are coupled to σ_1 and/or σ_2 in the two principal directions, leading to:

$$\begin{bmatrix} \sigma_x \\ \sigma_y \\ \tau_{xy} \end{bmatrix} = \begin{bmatrix} \bar{Q}_{11} & \bar{Q}_{12} & \bar{Q}_{16} \\ \bar{Q}_{12} & \bar{Q}_{22} & \bar{Q}_{26} \\ \bar{Q}_{16} & \bar{Q}_{26} & \bar{Q}_{66} \end{bmatrix} \begin{bmatrix} \epsilon_x \\ \epsilon_y \\ \gamma_{xy} \end{bmatrix} \quad (2.1)$$

where \bar{Q}_{ij} represents the stiffness matrix in principal axis. Changing the ply angle in each lamina influences the stiffness matrix \mathbf{Q} , as the material axis is not aligned with the laminate axis.

This design of structures with fibres off the three principal loading axes has been investigated in the last thirty years, nevertheless the advantages deriving from designing a component at its structural level are yet to be completely understood because of the complexity of interactions occurring in each laminate.

2.3 Passive Adaptive Composites

In the past two decades, the trend of investigating the potential applications of composite structures has widely increased. Composite materials not only present a high stiffness to weight ratio, but also a better fatigue resistance compared to metallic components (Lin and Lai, 2010). A large number of studies involve the investigation into the behaviour of passive adaptive composite (PAC) structures. These are manufactured

as smart structures that control the aeroelastic deformation under aerodynamic loadings, therefore affecting both the aerodynamic and the structural performance of the foil (Shirk *et al.*, 1985). Wind turbine blade design and adaptivity were investigated during the 70_s and 80_s. The efficiency of wind-turbine blades was improved, both changing the blade design (Ahmed, 2012) and trying to adapt the pitch angle to the inflow. The effect of pitch change to regulate the power output was investigated by Corbet and Morgan (1992). The aim was to achieve a flat power curve in high varying winds, avoiding load fluctuations that would affect the fatigue response of the blade. Wind turbine blades as well as helicopter blades, aircraft wings and tidal turbine blades, all aim at increasing the flutter speed (i.e. the speed at which resonant condition is achieved because of the phasing between the aerodynamic load fluctuations and the elastic deformation) and decreasing the divergence (i.e. the condition at which the increase in load caused by the deformation further increases the perceived load, exceeding the maximum blade load capacity), (Veers *et al.*, 1998). These two conditions occur for opposing angles of attack configurations. It is therefore necessary to achieve a blade design that does not exceed the maximum flutter or divergence speeds but can maximise the performances of the structure, allowing a larger lift contribution to the tangential force, which aids the rotation of the foil (Ahmed, 2012; Veers *et al.*, 1998). Designing toward feather position (also known as wash out) would reduce the aerodynamic loads on the blade, decreasing the possibility of achieving divergence; conversely, increasing the angle of attack toward stall (wash in) would increase the flutter speed, (Lobitz and Veers, 1997). Alongside these problems, the strength of the component should be maintained, therefore a large number of different configuration should be investigated to achieve a design that can produce an optimised power output, (De Goeij *et al.*, 1999).

The first to introduce the concept of passively adapting the blades using different laminate lay-up were Karaolis *et al.* (1988). In this research the possibility of introducing off-axis fibres, oriented at 20 degrees to the span-wise direction of the blade, showed that twist could be produced by loading the structure in bending, still maintaining the required strength in the blade. Karaolis predicted that introducing aeroelastic tailoring techniques to the blades could create a change in angle of attack (i.e. inducing twist under flexure load) up to one degree per span metre, utilising the limits of maximum strain of the structure. It is however important to note, as is well described by De Goeij *et al.* (1999), that the fatigue limits of the blades must be respected to achieve the required lifetime in operation. Therefore, it is necessary not only to design accounting for the inherent flexibilities of composites, but also looking at their requirements and stiffness limits to avoid fatigue damage.

The following section will present a review of the literature and the studies produced regarding passive adaptive composite structures. This will account for different applications of passive adaptive composites and the benefits from the induced twist parameter will be investigated. The conditions of maximised performances and efficiency with two

different angles of attack change (i.e. toward feather and toward stall) will be reported for the extended literature review up to date. Additionally, the experimental measures present up-to-date are outlined as well as the problems associated with those methods.

2.3.1 Fluid Structures Interaction

A number of studies on aeroelastic structures have been carried out over the past twenty years. Most of them only looked at simplified box-beam components or just structural or aerodynamic analysis. The majority of the research still does not account for the complexity of the Fluid Structure Interaction (FSI) coupled problem. The motion and deformation of the structures depend on the flow speed, and the flow pattern depends on the motion and deformation of the structures. Without a coupled FSI model, the modelling of structural behaviour or of flow features can not be realistic, as an unsteady aerofoil deformation, for example, affects the aerodynamic efficiency and the noise associated with it (de Borst *et al.*, 2013). The following sections will identify the different approaches used for PAC structures in a number of diverse applications.

Aircraft Wings

Shirk *et al.* (1985) viewed aeroelastic tailoring as the way to maximise the performance of aerofoil structures. After giving a definition of aeroelastic tailoring used in most of the subsequent research, a review of flexible aircraft is presented, describing the response of different tailored wings to dynamic flutter, showing an optimisation process that meets the twist and strength requirements. A number of existing flexible aircraft are investigated, using both two Rockwell computer codes and a finite element analysis method, showing the benefits of aeroelastic tailoring on wings while maintaining the operation requirements. A study on the effect of tailoring on swept-forward wings is described by Patil (1998). This study assesses the best lay-up configuration necessary to avoid divergence problems. Both the structural and the aerodynamic responses are simplified into two-dimensional problems with the addition of 1-D beam analysis that uses the cross-sectional stiffness calculated in the combined 2-D results. Theodorsen's theory is used to obtain the unsteady forces along the span for a circumferentially uniform stiffness (CUS) beam configuration, and the results show the possibility of changing the response by tailoring the wing components. Another study on aircraft wings is described by Guo (2007). The fibre orientations of both the wing skin and spar were investigated to achieve a weight optimal design as well as increasing the flutter speed. The composite wing and different lay-up configurations are compared to its metallic counterpart, and weight savings up to 40% were achieved. This research was based on an FEA model coupled with the aerodynamic forces calculated with lifting surface theory for incompressible flows. In the paper the relationship between bending moment and torque and transverse and twist deflection at the ends of the anisotropic thin walled closed-section beam are given,

showing the interaction of the coupling terms in the stiffness matrix. The optimisation on the lay-up orientation was assessed in (Thuwis *et al.*, 2009) using an existing programme (i.e. ASTROS) to study the optimum weight and the percentage needed of the assessed fibres to satisfy strength and increase the flutter speed. Haghigat *et al.* (2012) investigated the effect of the control system during manouvre and wind gusts to achieve a sound design for the aircraft wing. This would maximise the endurance of the aircraft using active control system. In this research the aerodynamic forces are calculated with a vortex-lattice panel method and the structure is modelled as a beam structure in FEA. It is important to note, as described in (Chattopaghyay and Jha, 1996), that the classical laminate theory (CLT) equations and assumptions should be changed to account for the through thickness shear deformation given by the asymmetry of the lay-up. This is not always accounted for and most papers reviewed still assume CLT to work in a Circumferential Asymmetric Stiffness (CAS) structure. A panel code method is used to evaluate the unsteady aerodynamic forces to investigate the effects of composite passive adaptivity on the aeroelastic stability and structural characteristics of the aircraft wing under investigation.

Wind Turbine Blades

A large number of studies have been carried out on wind turbine blades, analysing bend-twist coupling effects with analytical (De Goeij *et al.*, 1999; Lin and Lai, 2010; Lobitz and Veers, 1997; Maher *et al.*, 2007; Veers *et al.*, 1998), numerical (Fedorov, 2012; Fedorov *et al.*, 2009; Kenway and Martins, 2008; Lee *et al.*, 2012; Maher *et al.*, 2007; Park *et al.*, 2011) and experimental works (De Goeij *et al.*, 1999; Fedorov, 2012; Fedorov *et al.*, 2009). These studies all aim at enhancing the power generation or the power regulation of wind turbines. A design factor of absolute importance is to take into consideration the remoteness of most of the wind farms, leading to a component that permits a long operational life with very low maintenance intervention needed, hence considering the fatigue limit of the composite structures.

The works that use an analytical structural approach are based on Euler-Bernoulli, Timoshenko or St Venant's beam theories. The former is the most simple approach and is widely used for thin-walled beams. However, it is not particularly appropriate for composite asymmetric lay-ups as it does not take into consideration the transverse shear (i.e. planes normal to the axis of the beam remain plane and normal to the axis after the load is applied). The second approach (Timoshenko beam theory) assumes that the planes normal to the axis remain plane but not normal to the axis when loaded, accounting for shear and rotatory inertia, (Kennedy *et al.*, 2011). This assumption therefore can be used in a numerical approach to beam composite elements. St Venant torsion analysis is based on the unconstrained warping assumption, therefore the effect of the end constraints are limited to a small portion close to the edges.

In most of the analytical approaches described in literature a theoretical analysis is compared or implemented by a more complex Finite Element model that calculates the material stiffness components (i.e. the stiffness matrix elements). Moreover, the wind turbine blade performance prediction should account for an aerodynamic load or a pressure load distribution to be coupled with the structural solver. The combined solution to this problem gives the aeroelastic response of the wind turbines, possibly accounting for the rotation of the blades and not only for one blade shape.

Elastic coupling is used, as described by Lin and Lai (2010), to improve the stability of the components. The research is based on the assessment of a 5 metre long blade, considered as a uniform beam model in the commercial software ABAQUS. The stiffness matrix is then calculated combining the matrix of each beam element and the displacements could be calculated assuming a fixed end at the root of the blade. The FEA model is based on thin-walled assumption, not accounting for shear deformation (i.e. using Euler-Bernoulli's approach). Three different loading conditions are considered, namely point load, uniform load and triangular load (with increased load at the tip). The twist angle response is investigated for different lay-up configurations, showing that the maximum interaction parameter occurs with off-axis fibres arranged at 20°, as described also by Karaolis *et al.* (1988). This paper shows all the coupling terms in the stiffness matrix and how they are affected in the different blade sections, however it lacks the fluid force input, so it is therefore difficult to correctly understand the real implications of the angle of attack change in rotating blades.

The effects of different lay-up techniques and orientations in angles of attack changes (i.e. toward feather and toward stall) are well summarised by Veers *et al.* (1998). In this article previous research is reported, explaining the effects of tailoring in both better power production, and vibration and load alleviation. Both active and passive pitch control devices are described, discussing the advantages of passive adaptive composites, that change the response to fluctuating loads allowing for an increase in energy production, minimising the disturbances on the stiffness and the manufacturing costs. The concept of varying angles of attack configurations is introduced, showing an improvement in pitch controlled rotor if the first 40% of the blade span from the root twists toward feather and the remaining part of the span (i.e. approaching the tip) presents a configuration toward stall as the wind speed increases, (Veers *et al.*, 1998). The effects of the coupling coefficient (α_c) are shown in the response of flutter and divergence, highlighting that twisting toward feather in response to an increase in wind will reduce the dynamic loading on the blade (i.e. a divergence problem). Finally, as for the above-mentioned research, the off-axis ply angle of 20° is found as the angle at which the maximum coupling is achieved. It is however mentioned by Veers *et al.* (1998) that this angle configuration is not taking into consideration the off-axis strength and toughness requirements. The results presented by Veers *et al.* (1998) include also the research developed at Sandia National Laboratory on HAWT blades described by Lobitz and Veers (1997).

Some innovative research was developed at the Technical University of Denmark by Fedorov on the effects of bend-twist couplings on wind turbine blades, (Fedorov, 2012; Fedorov *et al.*, 2009). He assessed the behaviour of a full scale blade in a comprehensive FEA analysis as well as involving the use of 3-D Digital Image Correlation to assess the deflection of the foil under three different loading conditions, namely bending, torsion and coupled bending-torsion. These loads are applied by a hydraulic system to the tip of the blade. The FEA model of the PhD thesis (Fedorov, 2012) comprises solid beam elements modelled in ANSYS (i.e. BEAM 185) to represent the thick walls of the aerofoil. The solid model has been proven (for both the full length blade and test-case beams) to better represent the composite structure, especially under torsion, than the shell elements tested (from ANSYS and ABAQUS), (Fedorov *et al.*, 2009). The problem with the shell elements is that they cannot represent the smooth surface of the blade, creating discontinuities in the design. The above-mentioned research includes all the results to be expected from a passive adaptive composite investigation, however it lacks the aerodynamic forces, as the only load encountered by the blade and the beams is a hydraulic load applied at the tip, not accounting for unsteady forces or true wind loads, which are modelled in the present project.

The effects of specific wind loadings are assessed by Kenway and Martins (2008). In this article two different wind turbines, as well as their locations, are investigated. The probability of encountered winds for both off-shore and inland wind turbines are assessed, and therefore a shape optimisation in the post-stall power generation is developed. The goal of the research was to maximise the annual energy production. The structure of the blade was modelled with an in-house FE software (pyFEA) whereas the aerodynamic loads were simulated in XFOIL. The two blades are designed with constraints in yield strength of the material, cost of the blade and maximum power capacity. The approach of this article only regards the shape of the blade and its effects on energy production, but it would be of interest for the current research to look at the effects of passive adaptivity on the different locations to see if the optimum off-axis fibre orientation changes with different wind speeds.

The design parameters, such as the amount of elastic couplings, are investigated by Maher and Isikveren (2009). A design software is presented to assess the benefits that can be achieved through inserting in a wind turbine a passive adaptive blade, comparing the results with respect to a metallic conventional blade. Additionally, the adaptivity of the blades allows an increase or decrease along the span on operational loading, increasing the possibilities of energy capture with no increment in load, or decreasing the load without losing any of the amount of power gained.

Recently, after a large number of studies that focused their attention on simplified FEA models, a full wind turbine blade was numerically assessed by Lee *et al.* (2012) in the commercial software ABAQUS and the aerodynamic loads were calculated with Blade Element Method and XFOIL, and integrated along the span of the blade. The results

show that blades exhibit rotation in the foil sections as well as flap-wise deformation. An important finding of this research is that the displacement varies linearly with the applied load. The paper proposes three suggestions for the improvement of wind turbine efficiency. The first regards pre-twisting the geometry of the blades. Moreover, the pitch angle, as already discussed, should be corrected for the varying wind conditions. Finally, the fibres orientations should be adjusted to enhance the twist, where appropriate. A similar approach was previously found by Maher *et al.* (2007) to increase the wind turbine performance.

The literature surveyed up to now mostly reviews the possibility of passively adapting the wind turbine blades without taking into consideration the fatigue limits during operation. In (De Goeij *et al.*, 1999) not only is the lay-up that gives the maximum flexibility described (i.e. $\phi = 25^\circ$ with respect to the span axis for carbon reinforced plastics), but, more importantly, the stiffness and fatigue limits are investigated. De Goeij *et al.* (1999) show that the design that gives a substantial increase in twist angle toward post-stall operation is not satisfying the stiffness requirements, therefore the paper suggests investigating ply-orientation arrangements that could improve the performance by decreasing the angle of attack. This research not only presents a theoretical approach, but also a FEA model is compared to experimental results for bend and twist deformation of composite asymmetric beams. Nevertheless, the conclusions of the article summarise that it is possible to passively adapt a wind turbine blade tailoring only the internal spar and leaving the outer skins as a transfer of the aerodynamic loading on the internal structure.

Helicopter Blades

Aeroelastic tailoring on helicopter and wind turbine blades are similar, but their final aims are different. For helicopter blades, the aeroelasticity is needed to improve the stability of the ride and decrease the vibration as well as increasing the fatigue life. As for wind turbine blades and aircraft wings, the ply-angle orientation on helicopter blades is investigated.

The study of composite helicopter blades was initiated at the end of the 70s in a series of studies developed to separate the blades' natural frequencies from the aerodynamic forcing frequencies. The studies on the effects of composite couplings were initiated and conducted by Chopra *et al.* (Ganguli and Chopra, 1995; Hong and Chopra, 1985, 1986; Smith and Chopra, July 1993). The initial studies did not take into account the shear deformation and the warping effects, which have been added in more recent studies. The coupling of pitch angle and aerodynamic load, if correctly analysed, may change the frequency response of the blade, leading to an altered flap response, (Smith and Chopra, July 1993). Hong and Chopra (1985, 1986) presented the potential of improving the aeroelastic stability reducing the vibration using composite rotor blades that

couple bending-torsion effects. Similarly to wind turbine applications initial methods were simplified to flat plates and composite thin-walled beams. Both analytical and FEA models were applied to the box-beam like composite structures. An aeroelastic optimisation was carried out in (Ganguli and Chopra, 1995) showing that significant changes can be made to the elastic stiffness and the coupling of the composite rotor blade by means of varying few ply angles in the box-beam walls. Comparing these results with a baseline-non coupled blade a reduction up to 50% in blade vibration is achieved.

Jung *et al.* (2002) carried out the analysis of a method to capture the non-classical behaviour of composite flexures as well as the investigation of coupling effects of composite flexures on the aeroelastic stability. The coupling effect of bending and rotation can be seen in Figure 2.2. The behaviour of the helicopter blade beam-like structure is investigated using a finite element method (in ABAQUS). The negative pitch-lag coupling (i.e. lag back/pitch-up condition) introduces a strong stabilising effect on the lag mode damping. Moreover, the pitch-flap coupling (i.e. flap up/pitch-up condition) stabilises the lag motion. Therefore the lag mode can be substantially improved via aeroelastically tailoring the blades.

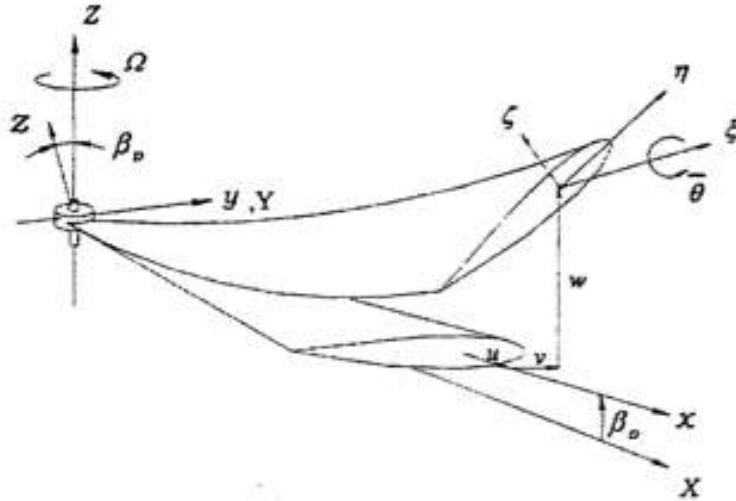


FIGURE 2.2: *Bend-twist coupling under flexural loading for helicopter blade (Jung et al., 2002)*.

Vibration responses to dynamic loading were investigated by Friedmann *et al.* (2009). These were assessed with different FEA methodologies and compared with experimental values for four revolutions of the hub, showing a very good agreement. The fundamental rotating natural frequencies in forward flight are considered as the vibration-stabilising factors. It is shown that the bending of the blade is minimised using an anti-symmetric layup.

Murugan *et al.* (2008) assessed the effects on uncertainty in the composite material properties on the cross-sectional stiffness properties, the natural frequencies and the aeroelastic response of the rotor blades. The material properties (i.e. Young's modulus and Poisson's ratio) were considered random variables with a variation of 4% and the aeroelastic analysis was carried out with a Monte Carlo simulation. A composite thin-walled box-beam was analysed with a symmetric lay-up, as most helicopter blades still rely on symmetric designs (Murugan *et al.*, 2008). The conclusions on the effects of random material properties show that the flap natural frequencies are less sensitive to material uncertainty than the lag and torsional frequencies.

The research developed on helicopter blades helps the author of the present study to understand the behaviour of lifting surfaces under unsteady dynamic forces that might arise from increased loading conditions. It is therefore necessary to perform a modal analysis of the investigated composite foil to correctly represent its behaviour in experimental and numerical studies.

Marine Applications

The concept of passively tailoring composite materials can be applied also to marine structures such as tidal turbines (Nicholls-Lee *et al.*, 2009; Nicholls-Lee, 2011), propeller blades (Khan *et al.*, 2000; Lee and Lin, 2004; Lin *et al.*, 2009; Young and Motley, 2011), hydrofoils (Ducoin and Young, 2013; Ducoin *et al.*, 2012a) and more recently to high performance sailing boat lifting foils (Findlay and Turnock, 2008; Lothode *et al.*, June 2013; NACRA International, 2014).

Composite materials not only present lightweight and high strength advantages when compared to metallic structures, but also high corrosion resistance. This feature is particularly attractive in marine environments.

Corrosion, usually enhanced by seawater, can therefore be significantly reduced using composite materials. If a composite structure is built to operate in a marine environment, a sound manufacturing process should be carried out, in order to reduce the void content. More importantly water resistance epoxy resins should be employed so as to prevent water absorption. In a marine environment, moisture uptake affects the mechanical properties of a composite, as these are dominated by the matrix or fibre-matrix interface. Therefore, inter-facial shear strength and inter-laminar tensile strength, due to the weakening of the fibre-matrix bond, swelling of matrix material and plasticising of the matrix can occur when composite structures are subjected to a seawater environment (Wang and Chung, 2012). The selected matrix in marine components should be epoxy, as hydrolysis has a noticeable effect on the matrix-dominated mechanical properties (Selzer and Friedrich, 1997). Water penetration may occur due to diffusion through the polymer matrix and movement by capillary action through the micro-channels formed

along imperfectly bonded polymer-fibre interfaces (Tsenoglou *et al.*, 2006). Another disadvantage in marine composites may be the development of blisters, due to two possible causes, the creation of defects during fabrication and osmotic penetration during service. Defects can present themselves within components in the form of air pockets and entrapped liquids, such as water, solvents or oils, which may expand during service (Rocket and Rose, 1987). Coatings, usually applied to reduce fouling and alleviate the effects of the aggressive environment, are also investigated. A number of tests have been conducted using various coatings and methods of application. It was found that while most coatings, such as epoxy and polyurethane, presented blistering at some point, and with varying degrees of severity, a simple polyester top coat with no additional surface treatments presented no measurable blistering (Eric Greene Associates, 1999). A simple polyester outer gel coat, therefore, would be beneficial in reducing the risk of blistering due to osmotic penetration. Looking at the applications of composites in a marine environment the main fibres used are E-glass and carbon fibres. Contrary to air-applications, where glass fibres are mostly used (i.e. in wind turbines), carbon fibres should be chosen in marine structures over glass, not only for their better mechanical properties (i.e. highest specific modulus for low density) but also because of the operating environment. Marine components need to account for water absorption, a serious problem for glass-reinforced composites, as the seawater is absorbed by the structure, degrading the matrix and hence affecting the fibre performance. Water absorption, therefore, not only lowers the mechanical properties of the component but also increases its weight in prolonged exposure to a seawater environment, (Kootsookos, 2001). Epoxy resins should be preferred over other resins such as Vynilester and Polyester because of their better mechanical properties and lower shrinkage porosity. Epoxy resins present excellent ageing properties in the marine environment, as can be seen in Figure 2.3, as after an accelerated degradation period they retain 90% of their inter-laminar shear strength, (Gurit, 2012c).

Having described the main advantages and disadvantages of composites in a marine environment, it should be noted that in recent years they have been preferred over the metallic components, thanks also to their tailoring capacities, and because of their lightness, which enables, if necessary, an easier replacement procedure.

Regarding tidal turbine applications, the anisotropy of composite materials should result in a change in induced twist such as the one analysed for wind turbines, maximising the twist for a minimum bend (Nicholls-Lee *et al.*, 2009; Nicholls-Lee, 2011). In previous research conducted at the University of Southampton, Nicholls-Lee assessed numerically and experimentally the lay-up of the internal spar and the outer-ply that could give the maximum change in blade pitch angle for a reduced bending (Nicholls-Lee, 2011). The number of mid layer plies was investigated and, as expected, she showed that a significant level of twist can be achieved with a reduced number of plies (Nicholls-Lee *et al.*, 2009). In her final Ph.D. thesis, Nicholls-Lee describes the beam structure on which

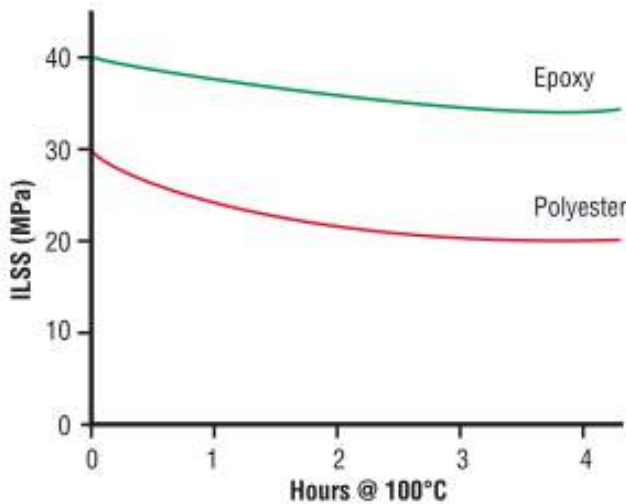


FIGURE 2.3: *Inter-laminar shear strength effects on water soak at 100° C on different resins (Gurit, 2012c).*

she performed the numerical and experimental analysis. The inner lay-up was formed of plies at 45° and 20° and the outer rovings were positioned at 60°. This arrangement gave the maximum bend-twist coupling, minimising the displacement of the beam (Nicholls-Lee, 2011). Furthermore, she showed that the deflection at a given distance from the fixed end varies linearly with the applied load. The results were obtained from an FEA model in the commercial software ANSYS Mechanical, using shell elements (SHELL281) and an experimental set-up that permitted calculation of the displacement and the twist angle, using laser pointers positioned at the beam edges. From these results, it is possible to continue the fluid structure interaction research on passive adaptive composites, comparing new numerical models to the existing one and applying pressure distributions calculated with Computational Fluid Dynamic techniques, and also experimentally.

Recent studies have developed the optimisation of marine propellers. The ability to change the pitch angle with different ship speeds makes composite materials particularly attractive in the building of marine propellers, as they can improve their efficiency. In propeller design it is particularly important to achieve a pitch angle similar to the inflow angle at the design speed. Initial studies presented by Lee and Lin (2004) and Khan *et al.* (2000) did not achieve a satisfactory bend-twist coupling by only adjusting the ply orientation and using symmetric lay-ups. A research by Lee and Lin (2004) presents the possibility of having a decreased pitch angle at low advance coefficients (J) with a pre-deformed blade. As can be seen in Figure 2.4, the pre-deformed blade twists toward a wash-out position when a higher hydrodynamic pressure is encountered, enabling a more efficient propeller at a larger range of ship speeds.

Lin *et al.* (2009) presented numerical and experimental results for composite unbalanced propellers. For the optimised asymmetric lay-up the pitch angle is reduced when the

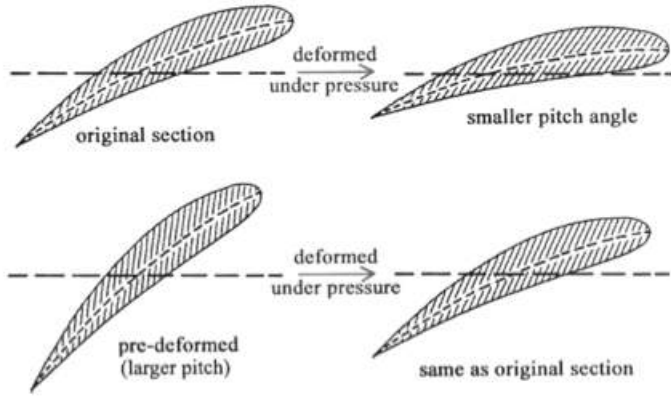


FIGURE 2.4: *Change in pitch due to hydrodynamic pressure load on a non-deformed and a pre-deformed propeller blade (Lee and Lin, 2004).*

inflow angle is low, therefore the efficiency of the propeller is increased. The experimental work was carried out in a cavitation tank and the deflection was assessed by means of photographic inspection. The numerical analysis was performed in ABAQUS to solve the structural model and in PSF2 (a software designed at the Massachusetts Institute of Technology) to solve the hydrostatic pressure with lifting-surface theory. The results for both experimental and numerical analysis show a similar trend. The pitch of the optimized propeller decreases as the ship speed decreases, reducing the torque and increasing the efficiency. The pitch angle with an unbalanced stacking sequence automatically changes with the inflow angle. Composite propellers are yet to be used in commercial applications as they still need to be regulated by classification societies, however they can significantly change the propeller performance improving their efficiency. It is important to correctly assess all the ply-angles as design variables in a correct FSI investigation in order to avoid material uncertainties under varying loads (Young and Motley, 2011).

Composite propellers can also be relevant in an assessment of hydrofoils, as the behaviour given by an unbalanced layup can be used to design new active control surface rudders. Ducoin *et al.* (2012a) investigated a flexible hydrofoil experimentally in a hydrodynamic water tunnel tunnel to assess the response to pitching motions in cavitating and non-cavitating flows. The structural response of the tip displacement was assessed with a high speed video camera, and the surface velocity fluctuations and transition points were analysed with a laser doppler vibrometer. It is important to understand the hydroelastic instabilities of flexible foils, as they may suffer from cavitation and possible flutter, which is associated with hydroelastic instability, and may rise from cavitating flow if the random loading fluctuations become a significant fraction over the average force. The research principally focuses on experimental results, as there is a need for experimental data in FSI applied to lifting bodies in hydrodynamic applications. The results show that when the hydrofoil pitches, the structural response evolves linearly

with the hydrodynamic loading, and that it is governed by the effect of viscosity. From the experiments, the transition from laminar to turbulent region can be clearly seen. This experimental set-up is of interest for the author of the current research as experimental analysis of vortex strength will be carried out using Particle Image Velocimetry (PIV). The research presented by Ducoin *et al.* (2012a) is further developed by Ducoin and Young (2013). Here, the hydroelastic response and the stability of the hydrofoil are assessed in viscous flow using a numerical CFD solver, and a simple 2 degrees of freedom system to simulate the tip deflection and torsion. The numerical results show that the flexible hydrofoil under hydrodynamic loading undergoes a wash-in motion (toward stall) about its elastic axis. When the flow is fully turbulent, the effective angle of attack changes non-linearly, with initial angle of attack and flow speed, as the centre of pressure shifts toward the leading edge of the foil. The non-linear effect stops when the foil stalls, therefore a major finding of the research is that the viscous effects associated with stall help to delay the static divergence. These conditions can however enhance fluttering or resonance of the foil, due to the fluctuations in pressure which constantly causes the leading edge to stall, and producing periodic vortex sheddings.

The possibility of passively adapted composite materials is particularly interesting in the context of the latest developments in high performance sailing boats. Since the first appearance in 1998 of the hydro-foiling dinghy moth (Moth International, 2014), there has been a rapid increase in technologies, and of interest in sailing boats with only the support of rudder and centerboard, drastically decreasing the wetted surface area, and therefore the frictional drag, of the boat (Findlay and Turnock, 2008).

After the last America's Cup sailed in monohulls (in 2007), a large number of catamarans have been built, and the most interesting ones present a foil configuration (i.e. C-foils or L-foils). Following the 2010 America's Cup, the AC45 and the AC72 were designed and built, and the larger part of the research was based on the development of the wing-sail and of the foils. The evolution carried out on the foils by Oracle Team USA during the final races of the 34th America's Cup, held in September 2013 in San Francisco bay, led to the astonishing victory over Emirates Team New Zealand. The leader of the CFD team from Team Oracle (Mario Caponnetto) explained in (Caponnetto, 2014) how they tried to constantly optimise the position of the foils to reduce the cavitation of the appendages, thus increasing the boat's speed.

The recent increased interest in high speed catamarans led to the designation of the NACRA 17 as the new Olympic class, entering the Olympic event for the first time in Rio 2016. This catamaran presents curved (C-foils) daggerboards. These foils, used up to now in off-shore trimarans (Lothode *et al.*, June 2013), not only give the right amount of horizontal side force but, advantageously, deliver a vertical force that supports some or all of the mass of the boat. Moreover, they increase the longitudinal stability and shift the underwater centre of effort forward, so as to prevent pitch-pole in downwind conditions (NACRA International, 2014).

It is important to know that the America's Cup boats, as well as the moths, have two foiling surfaces - the rudders and the daggerboards - and therefore they can sail lifted on two locations. The NACRA 17, on the other hand, has only the C-foil, which produces the vertical force that lifts the boat off the water, therefore the foiling condition (which is encountered only in downwind) is extremely unstable and dependent on the angle of attack (pitch angle) of the foil. The foil lift increases in accordance with the square of the velocity, and when it lifts the hulls off the water, it may stall or be subjected to a "wheelie" condition. Moreover, being a one-design class, the Olympic class rules forbid the active alteration of the incidence angle of the foils while sailing. It is therefore a major concern of the crews to find an optimal angle that allows the steadiest possible lifting of the boat. Figure 2.5 shows the immediate instability created by a boat lifted just by the daggerboards. The present research aims at finding an optimal stacking sequence that permits bending-twist coupling of the NACRA 17 foil to passively tailor the incidence angle, so as to keep the catamaran off the water, thus minimising the wetted surface area, for as long as possible. This can be achieved by changing the amount of lift force generated by the daggerboards, steadily decreasing the pitch angle in increased boat speed.

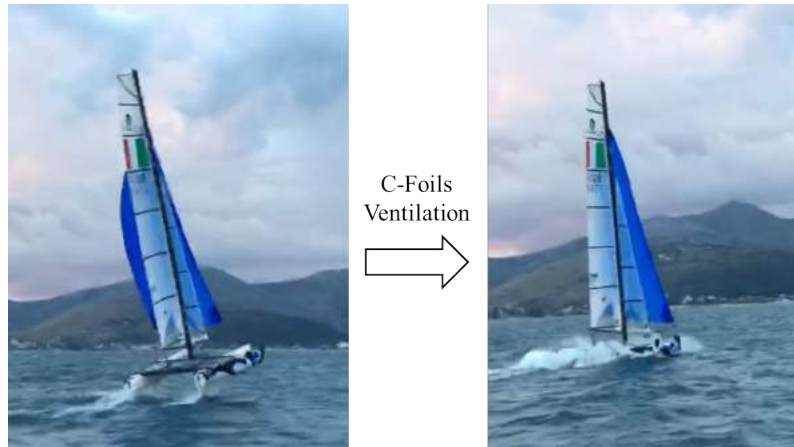


FIGURE 2.5: *Author sailing a NACRA 17 “flying” on the left hand side and the sudden “crash” (“wheelie”) of the crew out of the boat due to instabilities in foiling conditions.*

Other Applications of Flexible Components

Passive adaptive structures and flexible airfoils were investigated in recent years also for the application of Micro Air Vehicles (MAV). The effects of chord-wise flexure amplitude were investigated on the generated thrust and the propulsive efficiency of the MAV (Miao and Ho, 2006). Experimental analyses to assess the transient behaviour of the vortex and the turbulent flow on the flexible airfoils were carried out using high performance Particle Image Velocimetry (PIV) (Hu *et al.*, 2008; Tamai *et al.*, 2008) and numerical simulations (Tamai *et al.*, 2008). At the University of Florida, a research project pioneered the use

of Digital Image Correlation (DIC) in wind tunnel experiments (Albertani *et al.*, 2007). However, their studies were mostly looking at the aerodynamic coefficients and the strains of the flapping aerofoils, rather than a full-field FSI investigation.

It is also worth mentioning that the use of passive adaptive structures may be employed in F1 applications as the rear wing flap, as reported by Thuwis *et al.* (2009). The techniques used to tweak the regulations that might be used for the NACRA foils can be applicable in order to optimise the performances of F1 cars in straight courses by decreasing the induced drag aeroelastically tailoring the rear wing, without the need to use active systems not permitted by the class rules.

2.3.2 Up-to-date Experimental Measures

Analytical solutions do not exist for most FSI problems (de Borst *et al.*, 2013; Hou *et al.*, 2012). Likewise, it has proved challenging to acquire experimental measures of dynamic coupling between applied fluid loading and a structure response. As a result, research in this area has mainly focused on coupled Computational Fluid Dynamics (CFD) and structural Finite Element Analysis (FEA) simulations, as described in the previous section. Even though numerical studies have been extensive, especially in recent years with the increase in computer power, there is a lack of experimental validation cases for FSI problems and, for the limited cases that there are, the uncertainty in measurements is often unknown.

The advent of composite structures provides the designer with the potential to tune the response of the structure to the load applied. Fedorov (2012) presents a numerical and experimental approach where the effects of loads on a composite bend-twist full-scale wind turbine blade are measured. In particular they measured deflection and twist using Digital Image Correlation (DIC), however the uncertainty is not stated. It also lacks the dynamic coupling from the aerodynamic forces, as a known hydraulic load was applied whereas the aerodynamic force will actually change due to fluid-induced deformation and twist.

High speed cameras and laser Doppler vibrometers were employed to measure the pitch motion of a flexible hydrofoil and the areas of cavitation (Ducoin *et al.*, 2012b). These experiments present the displacement and pitch angle for the tip section of a two-dimensional hydrofoil under real flow conditions. This study provides useful validation material for cavitation simulations, including structural deformation, but does not provide the hydrodynamic forces or flow field information to assess non-cavitating CFD models. Malijaarsl and Kaminski (2015) present a review of the published studies on flexible propellers. The possibility of using composite propellers to reduce cavitation

problems is addressed, but they identify a need for experiments to validate the hydro-elastic numerical simulations, as well as measurements of the deformed shape of flexible propellers.

To assess the validity of numerical FSI simulations we require the ability to measure the influence of fluid load on the structural response. It is important that this is conducted in a controlled manner, to provide data with known uncertainties for comparison with numerical FSI simulations. CFD is often validated in isolation using flow field data captured with Particle Image Velocimetry (PIV) and measured aero-hydrodynamic forces (Jones *et al.*, 2008). Similarly FEA models can be validated against full-field deformation measurements acquired using DIC (Siddiqui, 2014). The present work aims also to quantify the uncertainty associated with a wind tunnel based experimental method that couples both DIC and PIV.

2.4 Experimental Methodologies For PAC

In order to fully capture the behaviour of a structure or a fluid under investigation without interfering with it, full-field non-contact measurement techniques can be used. These techniques have been employed extensively in the last two decades, as described by Raffel *et al.* (2007), Rastogi and Hack (2012), and Grediac and Hild (2012), and are capable of recording the data necessary to describe the surface's structural behaviour or the flow surrounding an object without modifying the nature of the structure or of the flow itself. These capabilities, which are beneficial with respect to point measurement techniques, together with the recent developments in sensor cameras and computer power, has permitted an increase in use of Digital Image Correlation and Particle Image Velocimetry in recent years.

Particle Image Velocimetry (PIV) and Digital Image Correlation (DIC) are both full field, non-contact, light based optical techniques and have been extensively used in a wide variety of experiments separately since the 1980s (Chen *et al.*, 2013; Wieneke, 2014).

2.4.1 Applications of Digital Image Correlation

Digital Image Correlation (DIC) is a measurement technique used to analyse problems in solid mechanics. It is a white light full-field non-contact measurement technique (Tang *et al.*, 2012) which involves the use of CCD digital cameras that register a series of images of a surface on which a randomised speckle pattern is applied. From these images, the displacement, the strain, and the stress of the specimen can be measured, using a correlation algorithm, tracking the motion of each speckle within the field of view (Rastogi and Hack, 2012). The speckle pattern is applied to the surface, providing

a grey-level distribution which should be adequately illuminated in order to achieve a smooth histogram. This technique has been used for different scale problems, from high magnification (Crammond *et al.*, 2013) to large scale structures (McCormick, 2012). Within the DIC software, the speckle pattern is mapped to calculate its deformation, allowing the displacements and strains of the underlying structure to be measured, as can be seen in Figure 2.6.

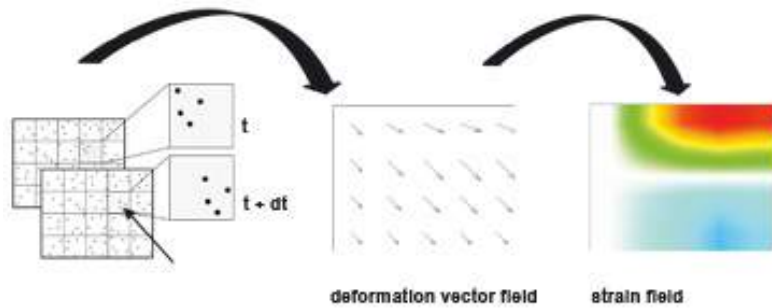


FIGURE 2.6: *Digital Image Correlation measurement diagram (LaVision, 2012).*

The accuracy of the measurements is increased as the number of pixels and speckles in the interrogation area is increased, as described by Sutton (2009). To obtain the maximum amount of independent data, the area of interest should be minimised, decreasing the subset size and increasing the spatial resolution. The subset size specifies the sizes of the local reference and target subsets between which the displacements are sought. The subsets must contain enough unique and identifiable features to achieve a reliable and accurate displacement determination. It is well known that the subset size has a significant impact on the accuracy of the displacement measurements in DIC (Pan *et al.*, 2008).

Crammond *et al.* (2013) describe the relationship between the size and the density of the speckles within a pattern. Analysing different magnification problems involves choosing an appropriate trade-off between spatial resolution and introduction of noise in the measures. Moreover, the quality of the speckle pattern influences the correlation function values, therefore the distribution, size and density of the speckle should be optimised for each measure, depending mainly on the camera resolution and the stand-off distance. A previous study conducted at the University of Southampton by Soubeyran (2013) investigated the effect of different speckle patterns on displacement error for a DIC set-up with stand-off distances close to those encountered in the wind tunnel experiments. Instead of manually generating the speckle pattern using spray-paint or airbrush techniques, generally used in solid mechanics measures, the speckles were generated using a computer programme ImageJ, where the density and the size of the speckles could be accurately determined. A range of speckle sizes and densities were compared in a laboratory environment by providing a known out-of-plane displacement and assessing

the error in the DIC displacement. A high-density pattern with a speckle size of approximately 6.3 pixels was found to minimize the error in displacements below 5 mm, whilst little difference was observed for larger displacements.

The use of a single camera allows for the measurement of deformation in a single plane normal to the camera, i.e. 2D DIC. The use of two cameras, in a stereo configuration, allows for the measurement of deformations both in the plane normal to the camera and out of plane, i.e. 3D DIC. For 3D DIC the angle between the cameras, stereo angle, controls the measurement accuracy of the out of plane deformation (Rastogi and Hack, 2012; Reu, 2013; Schreier *et al.*, 2009; Sutton *et al.*, 2009; Tang *et al.*, 2012). In full-field measurements involving the use of cameras it is extremely important, in order to obtain correct results from an experiment, to assess the quality of the pictures obtained and the most appropriate camera set-up for given stand-off distances. In white light imaging, and more specifically in DIC, the quality of the results depends entirely on the layout of the experiment. This relies not only on the choice of camera and lenses, but also on the correct amount of diffused light on the specimen, on the speckle pattern size and distribution, and on the alignment of the specimen with respect to the camera. It is crucial to consider the set-up process as the main focus of the experiment in order to obtain a good set of results, and to adjust the settings according to the fixed distances outlined by the experimental apparatus.

DIC has been widely used and validated for two-dimensional and three-dimensional analysis of small specimens, as described by Helm *et al.* (1996), Rastogi and Hack (2012), and Tang *et al.* (2012). These are mostly assessed using small stereo angles (ψ up to 17°) as this increases the in-plane resolution (Ke *et al.*, 2011; Reu, 2013). Three-dimensional DIC for a wide range of stereo angles and lenses are presented by Ke *et al.* (2011); Reu (2013); Wang *et al.* (2011), and deflections and strains are compared with experimental values, showing the possibility of increasing the stereo angle up to $\psi = 60^\circ$ for large out-of-plane deformations, allowing an optimum trade-off between in-plane and out-of-plane accuracy at $\psi \approx 45^\circ$.

In order to fully capture the structural response of a specimen, it is necessary to acquire the DIC images with high-speed cameras in a stereo configuration. High-Speed DIC has been used in many experiments, including modal analysis, impact testing and explosive events (Reu and Miller, 2008; Schmidt *et al.*, 2004; Trebuna and Hagara, 2014). A review of the available high-speed and ultra-high speed cameras can be seen in Figure 2.7.

While DIC was initially developed for quasi-static full-filed analysis, with 1-15 frames per second, the possibilities of capturing the dynamic displacements of a specimen allows us to measure simultaneously with two cameras the same amount of data acquired with thousands of point measurements, as described by Schmidt *et al.* (2004). However, high-speed cameras present a lower resolution compared to low-speed ones and a higher intensity of white light is required due to the short exposure time (Reu and Miller, 2008).

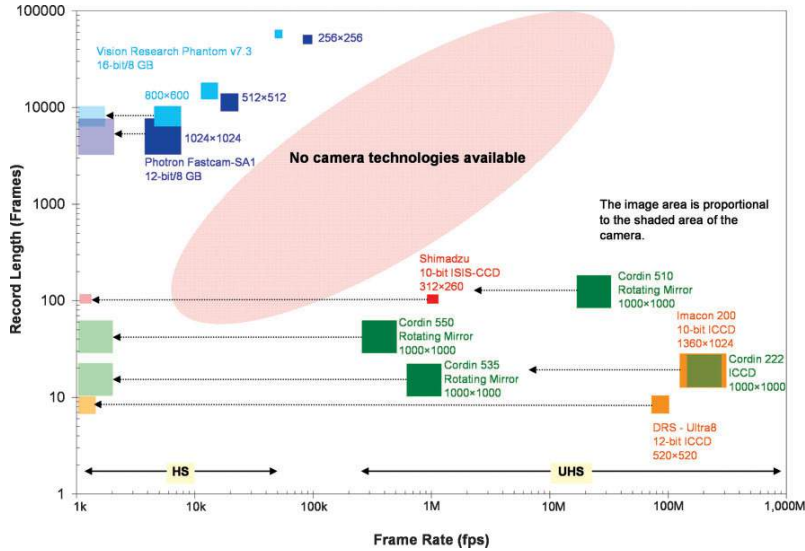


FIGURE 2.7: *High Speed and Ultra-High Speed imaging technology (Reu and Miller, 2008).*

Moreover, the speckle size must be adjusted to the camera, as a lower resolution camera would require larger speckles to achieve the same pixel size.

2.4.2 Applications of Particle Image Velocimetry

Particle Image Velocimetry (PIV) is a laser light, full-field, non-contact measurement technique that involves the use of CCD digital cameras. This technique is very similar to DIC except that PIV tracks a laser-illuminated pattern within the flow field surrounding an object at a given plane of interest. The pattern is generated by the inclusion of small oil-based seeding particles in the flow. A camera records two images in rapid succession (with a given time delay, Δt) so that the same seeding particles are seen in both images and their motion can be tracked (i.e. $f(V_s, \text{laser sheet width})$) (Raffel *et al.*, 2007). The displaced tracer particles that move due to the flow velocity between the two images describe the flow behaviour. For each set of pictures the flow velocity components u , v , and, in the case of stereo PIV, w , where u and v are in the plane of the camera detector and w is normal to the camera detector plane. The displacement of particles in the time between the laser pulses is recorded as either a single image exposed twice, or as a pair of two single exposure images. The main difference between these two methods is that with the former image, the picture does not retain information on the temporal order, leading to directional ambiguity in reconstructing the velocity vector (Raffel *et al.*, 2007). The recorded particle displacement field is measured locally across the whole field of view of the images, scaled by the image magnification and then divided by the known laser-pulse separation, to obtain flow velocity at each point (LaVision, 2016). The aim of the cross-correlation, where the scattered light from the first and second exposure of the particles is recorded in two different images, is to find the distance that the particle pattern has

moved during the inter-image time, and translate this into a velocity measurement. The relationship between the velocities \mathbf{u} and the particle displacements \mathbf{d} follows:

$$u = \frac{d}{M\Delta t} \quad (2.2)$$

where M is the magnification and Δt is the inter-image time.

The displacement vector for the images of the seeding points of the first and second illumination is determined for each interrogation cell (i.e. the area on which the spatial resolution is defined) by means of statistical methods, assuming that all the particles within one interrogation area have moved homogeneously between the two illuminations Raffel *et al.* (2007).

The cross-correlation function is not calculated on the whole images but on the interrogation areas, see Figure 2.8. The cross-correlation produces a peak, as can be seen from the figure, corresponding to the average displacement vector of the particles inside the interrogation areas. Therefore, one interrogation cell results in one velocity vector. This leads to an investigation of the correct number of interrogation cells to correctly represent the flow features.

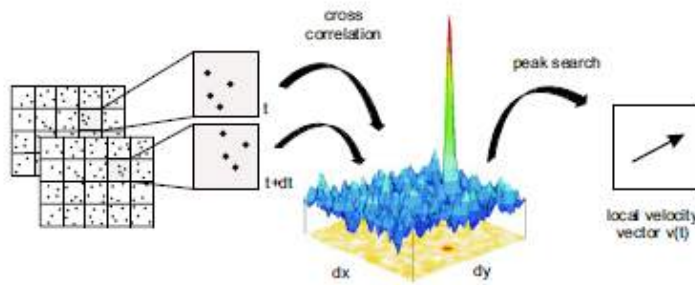


FIGURE 2.8: *Particle Image Velocimetry vector calculation in cross-correlation mode (LaVision, 2016).*

Being a full-field measurement technique, PIV allows the recording of an extended region, therefore the spatial resolution is very large; however, due to technological restraints in CCD cameras, laser frequency, and data transfer speed, the temporal resolution is still limited compared to point measurement techniques such as hot wires and pressure probes (Giuni, 2013).

Stereoscopic PIV, involving the use of two or more cameras, is capable of evaluating all three components of the velocity vector from a two-dimensional slice of the flow field. This method generally employs at least two imaging systems to record simultaneous but distinct off-axis views of the same region of interest. Two pairs of images are recorded at the same time by the two cameras. Each pair is analysed independently to derive two in-plane velocity fields. Knowing the perspective angles between the imaging systems and the measuring plane, the cross flow velocity component can be derived, as described

by Lawson and Wu (1997), and Raffel *et al.* (2007). Moreover, stereoscopic PIV is also known to produce more accurate measurements of the in-plane velocity components in the flow field than conventional PIV, as described by Prasad and Jensen (1995). This is because significant errors can be observed if the optical axis of the camera is not perpendicular to the laser sheet. Unavoidable errors can also be introduced by out-of-plane particle motions observed as in-plane motions due to the perspective transformation. By using two cameras in a stereoscopic system the out-of-plane motion can be used to determine all the three velocity components on the laser sheet plane.

In stereo PIV the two cameras are positioned so that their optical axes intersect at the midpoint of the field of view (Prasad and Jensen, 1995). However, in order to allow a good focus over the entire field of view the use of the Scheimpflug condition is required (Prasad, 2000). The Scheimpflug adaptors correct the limited depth of field, given by the stereo and the pitch angles of the cameras, additionally tilting the image plane to align with the plane of the laser sheet, in accordance with the Scheimpflug criterion which requires that the object plane, the lens plane, and the image plane are collinear, as shown in Figure 2.9 and described by Prasad (2000) and Prasad and Jensen (1995).

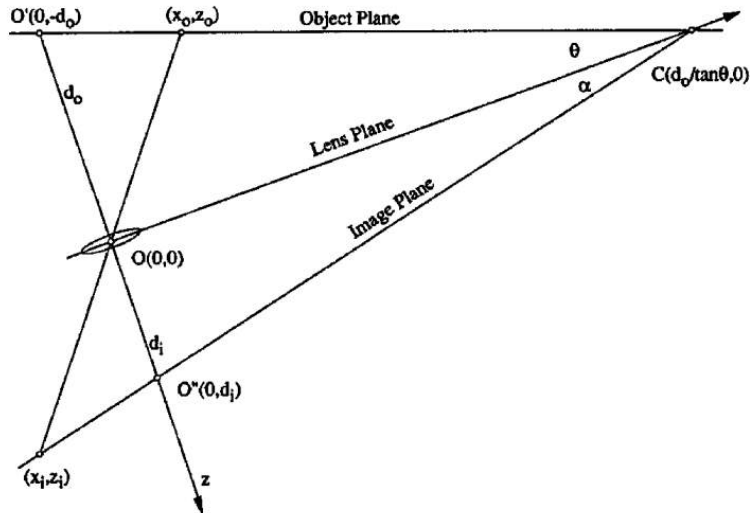


FIGURE 2.9: *Scheimpflug criterion, where image, lens and object plane are collinear (Prasad and Jensen, 1995).*

Therefore, for the Scheimpflug rule, if the object plane is in focus, the image, lens and object planes intersect on a common line, i.e. the Scheimpflug line, as can be seen in Figure 2.10.

The PIV measurements can be used to describe the turbulence statistics and the vortex structure in the wake flow over a time period (Zhang *et al.*, 2012). The stereo PIV system provides sufficient information to extract the out-of-plane component of the velocity and corrects the misalignment errors that might arise in standard 2D PIV configurations.

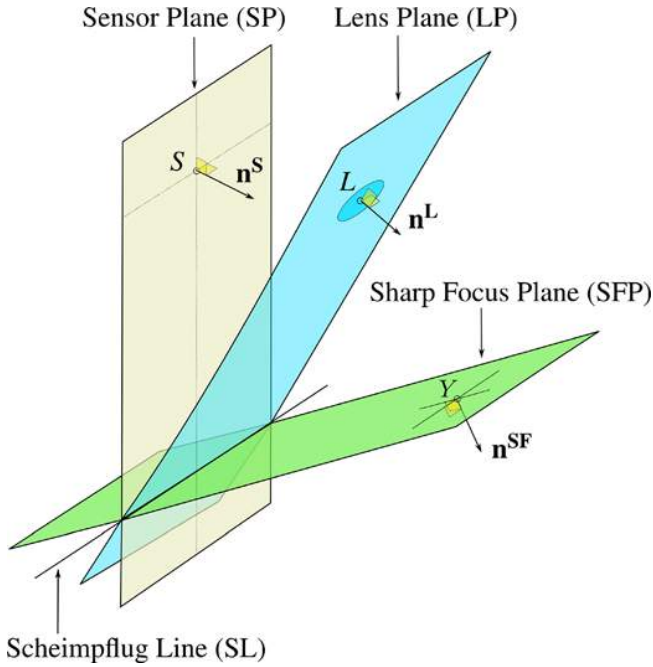


FIGURE 2.10: *Object, lens and image planes intersecting at a common line (Mottelet et al., 2012).*

The accuracy of the velocity vectors from PIV measurements can depend on many different factors. Systematic (or bias) errors can be caused by limitations of the correlation algorithm, calibration errors and particle images of one pixel or less causing peak locking. Residual (or random) errors can be typically caused by camera noise, high background image intensity reducing the contrast of particle images, defocused particle images, seeding density, particle image shift and out-of-plane motion reducing particle image pairs from one frame to the next (Sciacchitano *et al.*, 2015). Historically these uncertainties could only be assessed if the velocity field being measured is already known or by using synthetic data. Recently, however, different approaches have been proposed for *a posteriori* uncertainty quantification. The correlation statistics method was proposed by Wieneke (2015) and is implemented within the commercial PIV software DaVis (LaVision, 2016). This approach uses the converged solution of the displacement field to de-warp the second image back onto the first image. If an exact displacement field was calculated, each particle image would be mapped directly onto its position in the first image, creating a symmetric correlation peak. Any differences between the de-warped image and the first image are due to errors in the displacement field and create a non-symmetric correlation peak. A statistical analysis of how each pixel contributes to the correlation peak shape allows the vector uncertainty to be determined. This method was shown to accurately determine various sources of error in synthetic data including: out-of-plane motion, seeding density, particle image size, velocity gradients across interrogation windows and image noise. A comparison of different *a posteriori* uncertainty quantification techniques concluded that the correlation statistics approach was

the most accurate method assessed, typically reproducing real experimental error with 85% accuracy (Sciacchitano *et al.*, 2015).

2.4.3 DIC and PIV in Extreme Conditions

A number of studies have been carried out on the accuracy of DIC measures of specimens subject to high temperatures and extreme lighting conditions. In these cases it is necessary to combine bandpass filters with monochromatic light to be able to correctly capture the deflection of the specimen (Grant *et al.*, 2009; Guo *et al.*, 2014; Pan *et al.*, 2012). Those findings are therefore brought together in the current research to be able to accurately measure the deflections of a specimen with a fixed speckle size and density under varying lighting conditions.

Similarly, PIV has been used in literature for simultaneous measurements of temperature and different flow components using different light sources and the corresponding bandpass filters (Funatani *et al.*, 2004; Post *et al.*, 1994). Those applications are particularly interesting in the simultaneous measurements of DIC and PIV proposed in the current investigations, due to the need to isolate different optical systems.

2.5 Numerical Methodologies For PAC

In order to correctly represent a passive-adaptive structure, it is important to model correctly the structural response of a specimen with different ply lay-ups. This can be achieved accurately by modelling the structure numerically, using finite-element methods and in particular by investigating the best-element formulations for composite structures.

2.5.1 Finite Element Analysis

The Finite Element Analysis (FEA) method was introduced by Turner *et al.* (1956) to calculate the stiffness influence coefficients of complex structures. FEA has become nowadays a very powerful tool to simulate the physical phenomenon in different engineering disciplines, varying from structural to bio-mechanical engineering (Madenci and Guven, 2006). FEA modelling relies on decomposing a structure (or domain) into a finite number of sub-domains (elements). In each element an approximate solution is constructed varying with different interpolation functions, defined at specific points (nodes) located at the edges of the elements. The elements are therefore connected together at the nodes' locations. The variables at the nodes are the degrees of freedom of the elements and are dictated by the physical nature of the problem, i.e. structural problems have displacement and rotation degrees of freedom to resolve a mechanical forces

vector (Madenci and Guven, 2006). So FEA mathematically models representations of real problems, as can be seen in Figure 2.11.

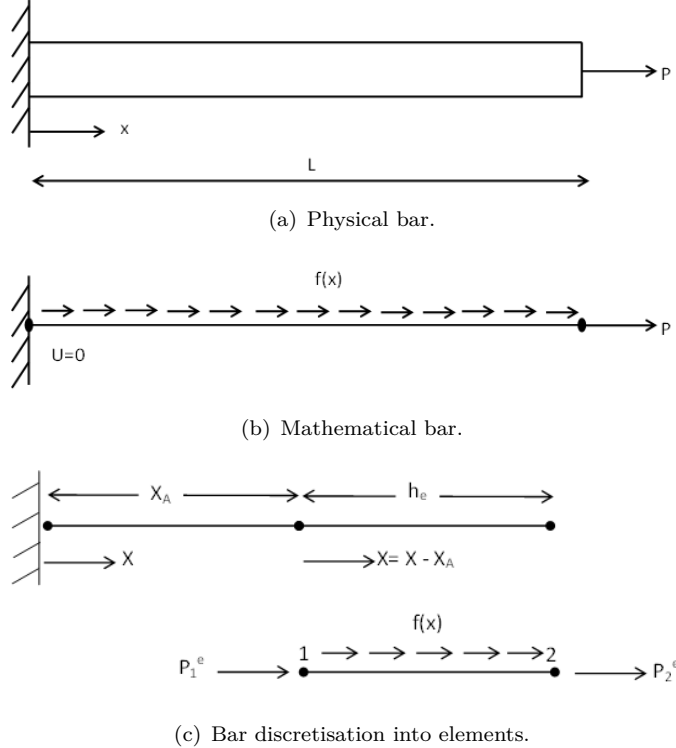


FIGURE 2.11: *Bar representation in FEA modelling as described by Barbero (2008).*

Considering a simple one-dimensional problem of a linear spring system with stiffness k and two nodes, each of which is subject to axial loads f_1 and f_2 , the displacement results as being:

$$u = u_1 - u_2 \quad (2.3)$$

which is related to the forces acting at each node by:

$$f_1 = ku = k(u_1 - u_2). \quad (2.4)$$

For equilibrium of forces

$$f_2 = -f_1 = k(u_2 - u_1) \quad (2.5)$$

therefore combining Equation (2.4) and (2.5) in matrix form yields:

$$\begin{bmatrix} k & -k \\ -k & k \end{bmatrix} \begin{Bmatrix} u_1 \\ u_2 \end{Bmatrix} = \begin{Bmatrix} f_1 \\ f_2 \end{Bmatrix} \quad (2.6)$$

or

$$\mathbf{k}^{(e)} \mathbf{u}^{(e)} = \mathbf{f}^{(e)} \quad (2.7)$$

where $\mathbf{k}^{(e)}$ is the element stiffness matrix, $\mathbf{u}^{(e)}$ is the nodal unknowns of displacements and $\mathbf{f}^{(e)}$ is the force vector. The superscript (e) denotes the element under investigation.

This simple formulation can be applied to more complex structures with different stiffness matrices and forces summing the different stiffness and the applied forces for all the representing nodes (Madenci and Guven, 2006).

Each element, depending on the complexity of the structure, can be represented as a one-, two- or three-dimensional element (as can be seen in Figure 2.12). Within each element the unknown displacements are calculated at each node and are interpolated within the elements with linear or polynomial interpolation functions. The interpolation functions are related to the number of nodes in the elements, and selecting a higher number of nodes per element implies a higher level of accuracy and less need for a fine mesh, at the expense of a higher computational cost (Barbero, 2008).

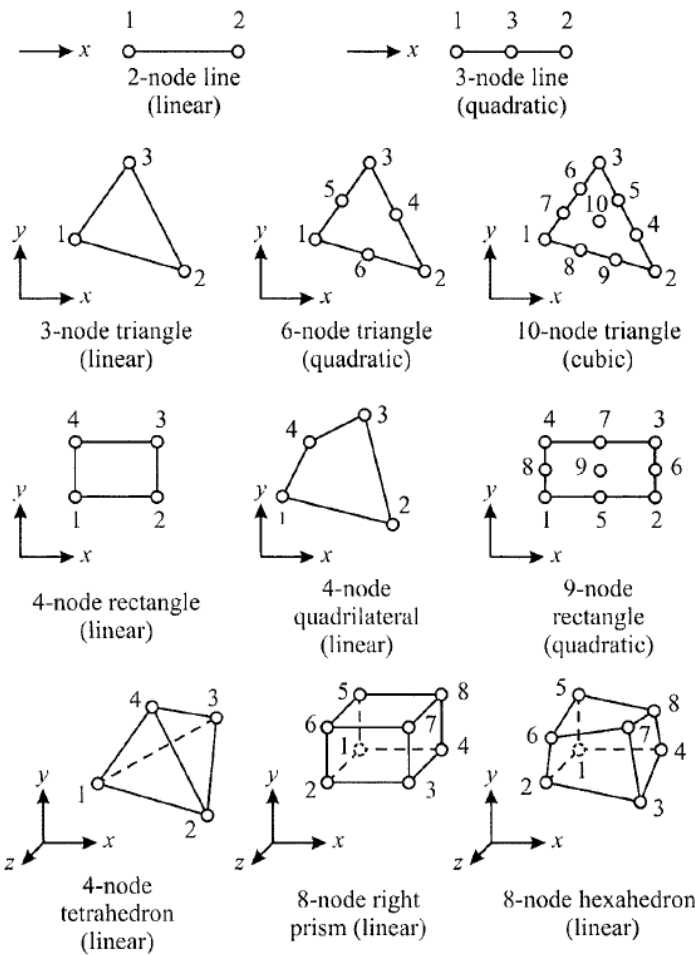


FIGURE 2.12: One-, two- and three-dimensional element types in FEA modelling (Madenci and Guven, 2006).

Therefore, in order to correctly model a complex physical problem in FEA it is not only necessary to select the appropriate element type, but also the interpolation functions need to be accounted for. Within connecting elements and common nodes it is necessary to ensure a continuous behaviour and compatibility between the interpolation functions.

Furthermore, the nodal displacements and their derivatives need to be represented with constant variations throughout the elements, thus satisfying the degrees of freedom of the elements (i.e. rotation and translation). Strain (ϵ), for example, is directly computed from the known displacements inside the element as:

$$\epsilon_x = \frac{du}{dx} = \sum_{j=1}^2 u_j^e \frac{dN_j^e}{dx} \quad (2.8)$$

where N represents the chosen interpolation function, and if it is linear the strains is constant over the entire element (Barbero, 2008). The stress values are then computed from the strains through the constitutive equations, knowing the stiffness matrix and the material properties of each element.

In FEA programmes it is possible to select accurately the type of element that best describes the characteristics of a problem. The element type determines the number of degrees of freedoms as well as the interpolation functions. In general, complex problems are modelled with solid or shell elements. Those elements can describe two- or three-dimensional problems. Three-dimensional problems might be reduced to two-dimensional problems using shell elements; however, shell elements are not able to represent the curvature through the thickness of deflected cross-sections. Moreover, the thickness of the shell remains unchanged as the shell deforms, and sandwich structures with a soft core cannot be modelled in shell elements, since the stiffness within a shell must not differ by more than two orders of magnitude.

Each element in the FEA model needs material properties and, in case of anisotropic materials, a local orientation must be associated to the elements. The possibility of defining local orientations for each element is particularly important when analysing composite structures, as the ply angle will cause the laminate material properties to vary.

2.6 Summary of the Chapter

A comprehensive literature review has been covered in this chapter. Composite structures were initially presented. The most common two-dimensional theories were described. Then the possibility of changing the ply angles and their influence on material properties of the laminate were discussed. This led to the formulation of PAC, for which a number of applications was presented. For each application the major advantages of using passive-adaptive structures were described. A wide focus was used in describing the possible use of PAC in marine components, also exploiting their applications in high-performance sailing boats.

Nevertheless, it is important to note that the state of art of tailored foils still needs a complete FSI validation, by the means of a robust and reliable experimental set-up and a systematic numerical research on an optimised bend-twist stacking sequence. This research project aims at implementing those models that might be applied in future work as validation procedures.

The applications as well as the drawbacks of full-field experimental techniques were then described. Following a literature study on the experimental techniques it was therefore possible to understand the important features to be assessed while conducting the experiments. Being able to analyse the histogram distribution of the speckle pattern was discovered as being one of the major aspects in measuring a structural behaviour with DIC. Moreover, it was possible to understand that changing the spatial resolution and the number of data-points within a DIC analysis can affect the measures results, therefore a careful assessment of the correct settings needs to be developed in order to achieve a physical representation of the deflected shape. In what concerns PIV, not only are the seeding level and the inter-image time of extreme importance when measuring flow features, but also the Scheimpflug criterion needs to be fully understood to correctly align the lens and the image planes with the object plane. If these three planes are not collinear, the seeding particles at the edges of the images will be spurious.

Finally, the FEA method was described, paying particular attention to the formulation of element types and interpolation functions. These two parameters are of crucial importance when trying to model a structural response numerically, as choosing the wrong elements and interpolation functions can result in erroneous numerical answers; even if the number of elements is increased, the numerical results might be described with an oscillatory convergence, leading to wrong results and very lengthy computational times.

3

Experimental Methodology

3.1 Introduction

This chapter describes the design of a new experimental methodology to test a representative aerofoil in a wind tunnel and accurately measure its response to aerodynamic load. As described in Chapter 2, in the literature to date there is a lack of experimental validation cases for fluid-structure interaction problems and, for the limited cases that there are, the uncertainty in measurements is often unknown. The experimental equipment used for the Digital Image Correlation and Particle Image Velocimetry and their implementation in the wind tunnel are introduced. In addition, the measurement accuracy and the uncertainties deriving from coupling the two techniques are described and discussed.

The current chapter therefore presents an experimental technique that can be used to assess the structural response as well as the fluid behaviour and the aerodynamic response of an aerofoil simultaneously under fluid loading. The presented experimental set-up describes the optimised technique used to investigate the Passive Adaptive Composite (PAC) flexible structure in December 2014.

3.2 Development of a Simplified Foil

The aerofoil under investigation is a NACA0015 section containing a load-carrying beam, an aerofoil-shaped foam-rib structure and a layer of Mylar to transfer the aerodynamic loading to the foam and the beam, see Figure 3.1.

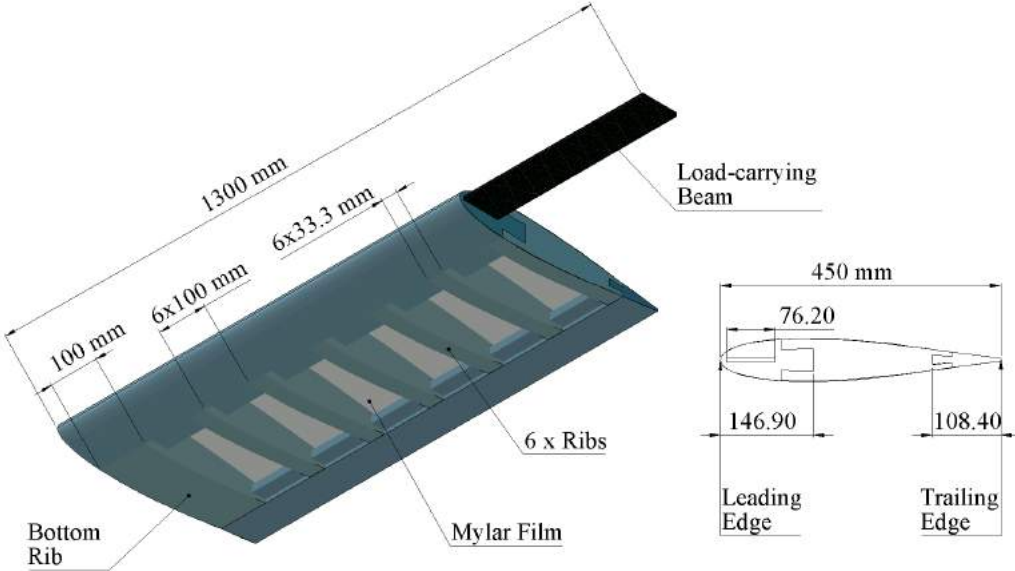
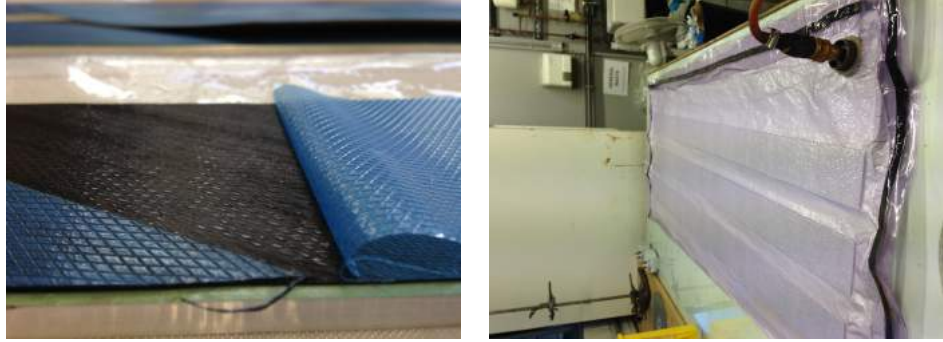


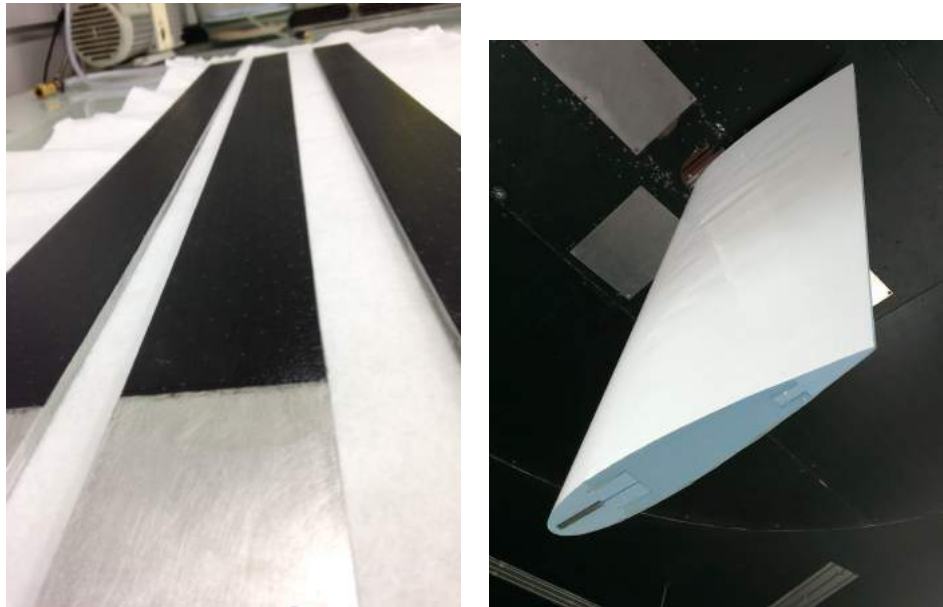
FIGURE 3.1: *Tested specimen showing the load-carrying carbon-aluminium beam, the foam rib structure and the Mylar sheet as well as the principal dimensions. Experimental specimen measurement accuracy ± 10 mm.*

The load-carrying beam was made of a sandwich structure (where the two skins are unidirectional carbon fibre and the core is aluminium 6082), see Figure 3.2. The manufacturing process of the sandwich structure involved the use of unidirectional (UD) prepreg carbon fibre (SE 84LV (Gurit, 2012a)) and a toughened epoxy adhesive film (SA 80 (Gurit, 2012b)) to fully bond the carbon skins to the 6082 aluminium. The manufacturing process was carried out by laying-up the UD carbon fibres at the desired ply angle, as shown in Figure 3.2(a). Three different sandwich beams were manufactured. Following a numerical study on the response of a number of different passive adaptive beams (from $\phi = 0^\circ$ to $\phi = 90^\circ$ in increments of ten degrees), the chosen investigated ply angles were $\phi = 0^\circ, -30^\circ$ and $2 \times 30^\circ$. The ply angle of zero does not induce any bend-twist coupling and its response follows the aerodynamic load. The PAC beams under investigation of $\phi = -30^\circ, 2 \times 30^\circ$ present the same ply-direction in the two sides of the shear centre. The opposite sign of the two beams will result in contrasting responses for what concerns the twist angle.

The sandwich beams were then cured under vacuum at 2 bar and 120°C for one hour, see Figure 3.2(b) and 3.2(c). Figure 3.2(d) shows the sandwich beam inserted in the Mylar-foam aerofoil structure in the wind tunnel.



(a) Laying-up process of the UD carbon fibres
for a ply angle of -30° . (b) PAC sandwich beams in vacuum prior to
curing process.



(c) PAC beams with three different lay-up configurations after curing cycle. (d) Sandwich beam inserted into the aerodynamic foam model in the wind tunnel.

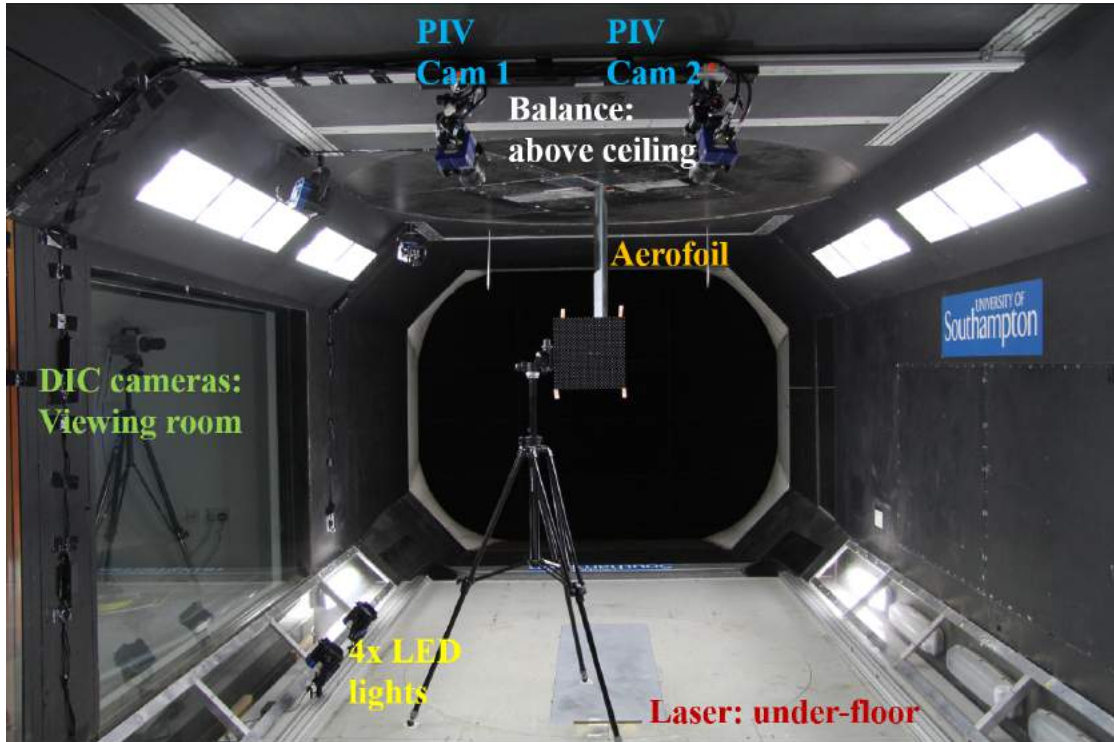
FIGURE 3.2: *PAC beam sandwich structure manufacturing process.*

The aerodynamic aerofoil foam structure manufacturing process was carried out using the hotwire technique to cut the foam to the desired shape. All the foam parts were joined together by means of a two-component epoxy adhesive and the Mylar was added to the structure. The aerofoil dimensions are described in Table 3.1. The structure was designed to be able to deflect more than 10% of its span length and to withstand the wind tunnel aerodynamic loadings for a Reynolds Number (R_e) of 750,000.

TABLE 3.1: PAC structure dimensions.

Parameter	Value
Chord	450 [mm]
Span	900 [mm]
Aspect Ratio	2
Thickness	67.5 [mm]
Area	40500 [mm ²]

The aerofoil structure was attached to the overhead balance of the R. J. Mitchell wind tunnel, as described in Section 3.4, through the load-carrying beam by means of a mounting frame designed with aluminium Rexroth® components. The load-carrying beam was therefore fixed to the dynamometer for 350 mm. The beam was then exposed in the wind tunnel working section for 50 mm before being inserted into the aerofoil structure for the following 900 mm. This arrangement allowed the transfer of the aerodynamic loading directly onto the dynamometer through the beam, so that it was possible to assess the influence of the ply orientation in the aerodynamic results directly. The set-up of the aerofoil within the working section of the wind tunnel can be seen in Figure 3.3.

FIGURE 3.3: *R. J. Mitchell wind tunnel working section showing the aerofoil and equipment position.*

3.3 Digital Image Correlation

In order to fully capture the structural response of the aerofoil, it was necessary to acquire the DIC images with high-speed cameras in a stereo configuration. The stereo angle between the two cameras controls the measurement accuracy of the out-of-plane deformation (Schreier *et al.*, 2009; Tang *et al.*, 2012). This was very important in the present research, as out-of plane was the major mode of deformation, and it was carefully considered with respect to the dimensional constraints of the wind tunnel (Reu, 2012; Wang *et al.*, 2011). Given the fixed dimensions of the wind tunnel and the level of accuracy needed for relatively large out-of-plane deflections, a stereo angle (ψ) of 41° was selected.

The acquisition frequency varied between 0.1 to 1 kHz depending on the length of recorded time. The high-speed camera trigger was monitored via the LaVision PT9 high-speed controller, and the shutter of the cameras was output to the forces and moments balance to measure the exact force to displacement ratio over time.

3.3.1 Measurement Accuracy

A number of tests of the accuracy of the DIC measures were carried out to overcome the limitations outlined in Chapter 2.4.1. The alignment of the two DIC High-speed cameras was carefully assessed, as can be seen in Figure 3.4.

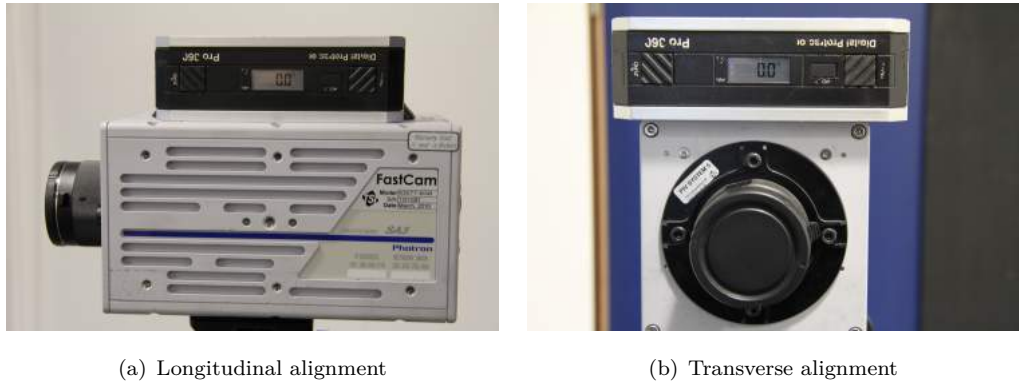


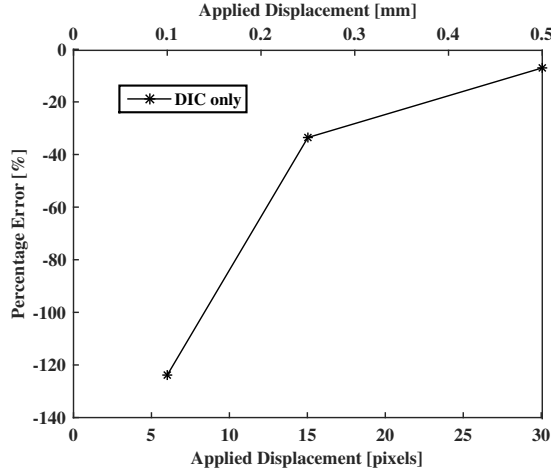
FIGURE 3.4: *Longitudinal and transverse alignment of the DIC high-speed cameras.*

The accuracy of the DIC was quantified against high-precision motorised stages in both translation (8MT175-50 motorised linear stage) and rotation (8MR174-11 motorised rotation stage) in static and dynamic conditions. The motorised translation stage has an accuracy of 2.5 μm and can travel at a speed of 5 mm/s. In static conditions the DIC out-of-plane accuracy was tested for a range of translations from 0.1-50 mm, as can be seen in Figure 3.5. The percentage error is calculated between the measured values of

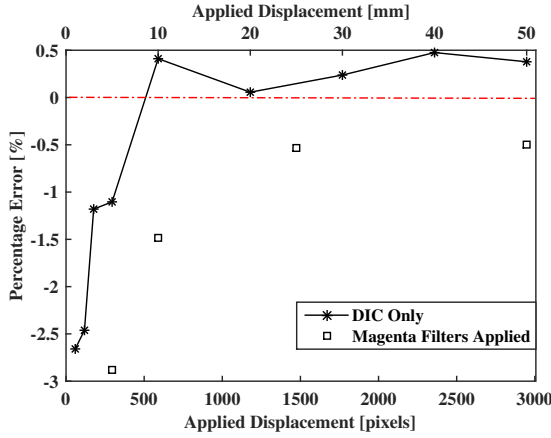
the DIC and the motions input to the motorised stage as:

$$\%_{error} = \left| \frac{DIC_{measure} - Stage_{translation}}{Stage_{translation}} \right| \times 100. \quad (3.1)$$

The results are presented in pixel shift as well as mm offset to enable comparison with results obtained from cameras of different resolutions. The accuracy of the results for small out-of-plane deflections (i.e. 0.1-0.25 mm) presents large errors due to the chosen stereo angle. The stereo angle provides a trade-off in accuracy for in-plane and out-of-plane translations (Reu, 2012; Wang *et al.*, 2011). In order to decrease the error in relatively small out-of-plane rigid body motions, the stereo angle should be increased. However, accuracy at these small out-of-plane deformations is not relevant to the present research as the foil has been designed to produce large deformations and Figure 3.5(b) shows that for deformations greater than 0.5 mm the error is less than 3% with a stereo angle of 41°. The physical constraints of the wind tunnel prevent very large stereo angles.



(a) 0.1 to 0.5 mm rigid body motion



(b) 0.5 - 50 mm rigid body motion

FIGURE 3.5: *Static out-of-plane displacement accuracy including the influence of the magenta filters applied to the LED lights.*

From Figure 3.5(b) it can be seen that the addition of the magenta gel filters on the LED lights shifts the percentage error without changing its trend. This phenomenon is due to the change in the greyscale histogram of the acquired images (Figure 3.6). As the exposure time and the lens aperture are not varied while the two measurement systems are captured, the histogram captured by the high-speed cameras for the same speckle pattern shows a shift toward the black end of the scale (i.e. 0 pixel intensity) and a lower pixel count. This produces the percentage error shift shown in Figure 3.5(b).

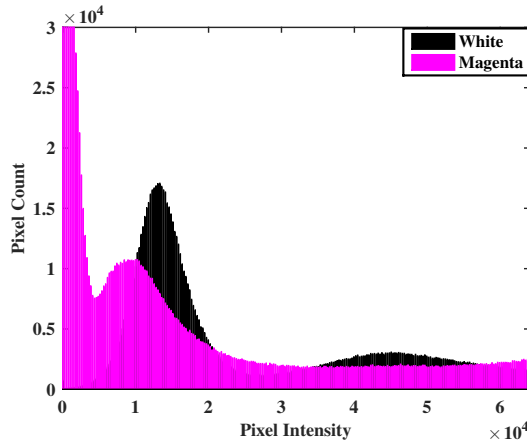


FIGURE 3.6: *Histogram comparison between white light image and the addition of magenta filters.*

The magenta filters applied to the LED lights allow transmission of blue and red light, with zero-transmission in the green-wavelength region, that corresponds to the PIV laser wavelength, as can be seen in Figure 3.7(a). The zero-transmission area is necessary for synchronising the DIC and PIV systems ensuring optical isolation between the two measurement tools. The addition of magenta filters changes the intensity profile of the speckle pattern as viewed by the cameras, as can be seen by the differences between Figure 3.7(b) and 3.7(c). Figure 3.7(c) captures the speckle pattern on the specimen well, however the image is darker than Figure 3.7(b). This results in a decrease in contrast between the speckles. Analysing the intensity levels along the line marked A-B in the figures, it was possible to see that the intensity decreases by approximately $\frac{1}{3.4}$ with the addition of the filters.

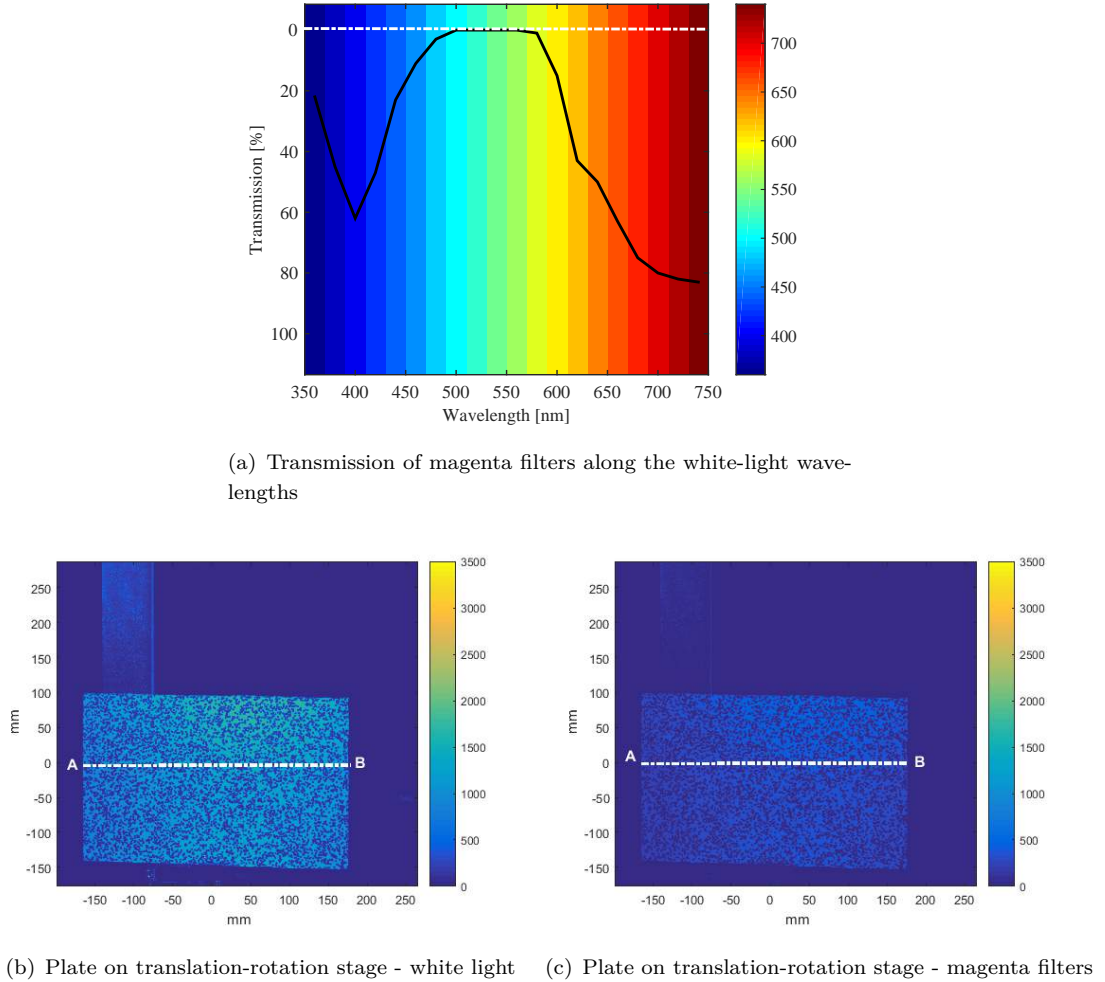


FIGURE 3.7: *Differences in transmission between white-light and magenta filters.*

In order to correctly assess the measurement accuracy in translation, the relative displacement error is also measured. For a base-applied deflection of 49 mm, the DIC accuracy is investigated for rigid body motions of 0.5-1 mm (i.e. yielding a total displacement of 49.5 and 50 mm). The percentage errors for the two applied displacements at the far-end of the depth of field (49 mm away from the calibration image) can be seen in Figure 3.8, compared to the small displacement captured at the near-end of the depth of field. For both cases, it can be seen that a rigid body motion of 1 mm yields a smaller percentage error. Moreover, it can be seen that the percentage error captured 49 mm away from the calibration plane is larger for both motions. This phenomenon might be due to the decrease in the relative stereo angle given by the larger out-of-plane distance of the specimen to the cameras. Nonetheless, the DIC accuracy has been shown to be consistent for small displacements in the whole depth of field (DoF) range.

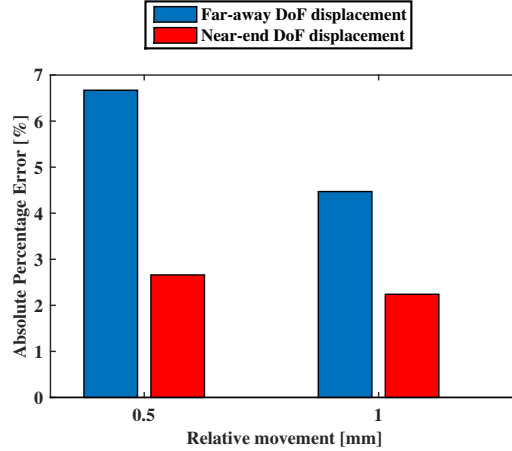


FIGURE 3.8: Percentage error comparison for Near- and Far-end depths of field rigid body motions of 0.5 and 1 mm.

Figure 3.9 shows the assessment of the DIC accuracy for dynamic motions. The known rigid body motion corresponds to 5 mm/s and the DIC measurement shows a rate of 4.97 mm/s, where the R^2 value calculated for the linear fit is 0.9999. Being the dynamic motion of 25 Hz and the DIC acquisition frequency of 100 Hz, the DIC displacement presents constant values between one motion step and the next.

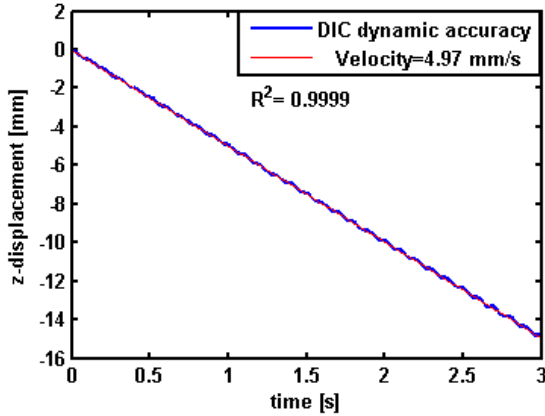
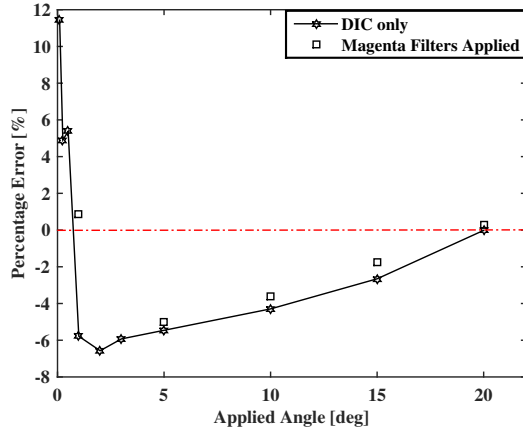


FIGURE 3.9: Measurement of accuracy in dynamic motions. Graph shows the pure out-of-plane displacement over time.

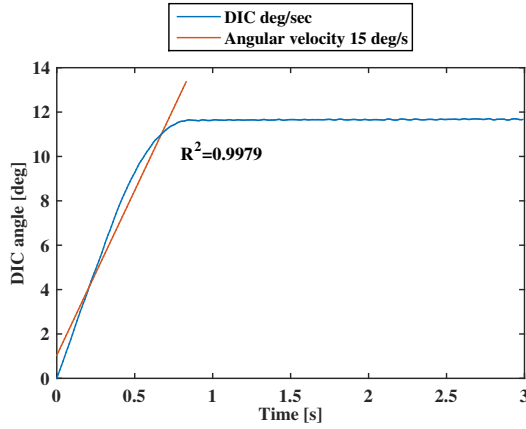
The accuracy of the DIC system is also assessed in rotation. The motorised rotation stage has an accuracy of ± 0.1 degrees and can rotate at a speed of $15^\circ/\text{s}$. The applied rotation varied from 0.1° to 20° . This represents a realistic range of change in effective angle of attack of the aerofoil due to aerodynamic loading. Figure 3.10(a) presents the rotation measurement accuracy with and without the influence of the magenta gels on the DIC lights. As detected for the translation, the percentage error shifts with respect to the pure white light DIC, but the trend is consistent, showing that for larger applied

angles the percentage error decreases. Comparing Figure 3.5(b) with Figure 3.10(a) it is possible to see that the error in rotation is decreased with respect to the white light image. This phenomenon can be seen as the rotation results take into consideration only two-point measures at the sides of the specimen, where the intensity level change is smaller. In translation response, on the other hand, the results are averaged over the entire field of view of the image. The percentage errors captured in rotation lie within the accuracy of the rotation stage.

The transient response of the rotation is also assessed. Figure 3.10(b) shows the response captured by the high-speed DIC cameras for a change in angle of $15^\circ/\text{s}$. The end of the rotation scale range is reached after 0.85 s. The angular velocity measured with the DIC system is $14.42^\circ/\text{s}$.



(a) Comparison of pure white light and the magenta gels statistically



(b) DIC transient rotation accuracy over time

FIGURE 3.10: Accuracy of DIC measurements in rotation.

Prior to the set of experiments conducted on the PAC flexible aerofoil, a number of investigations were carried out to assess the best DIC configuration to use during the experiments. The accurate motorised translation and rotation stage were not yet available, therefore a manual translation Vernier micrometer, with an accuracy of 0.1 mm, was used. In addition, the DIC E-lite cameras were used in this investigation. Their maximum resolution is 2448×2050 pixels and the sensor size is 8.5×7.1 mm.

The main concern about the DIC accuracy was raised by the presence of the double-glazed window, which separated the viewing room from the wind tunnel working section. The glass sat between the camera sensors and the specimen and it was not possible to measure the distance between the panes as the area was inaccessible. Therefore, different configurations were assessed. An aerofoil-shaped section was mounted on the Vernier micrometer. The experiment was conducted in the wind tunnel, reproducing the distances from the cameras to the specimen. Figure 3.11 shows the DIC results for a test case for a rigid body motion of 25 mm without the glass, with the influence of glass, and moving the camera closer to the specimen.

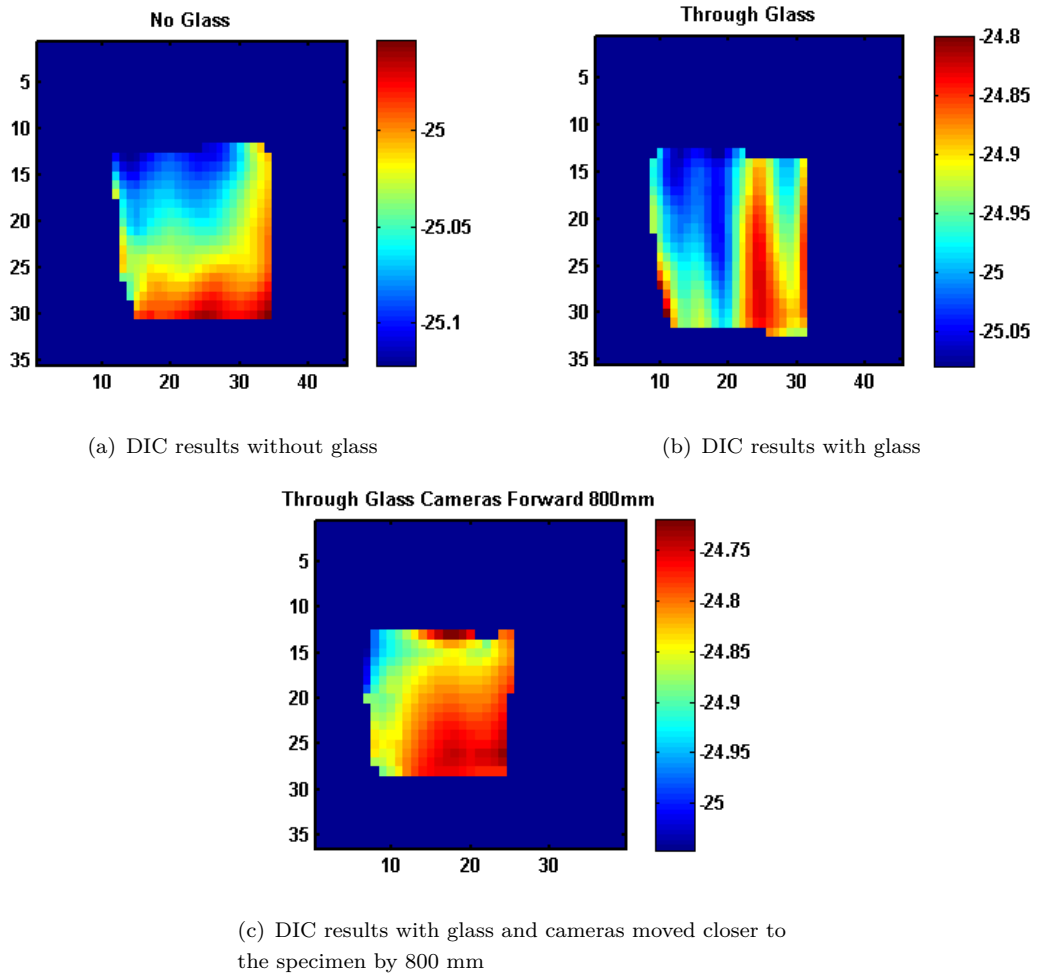
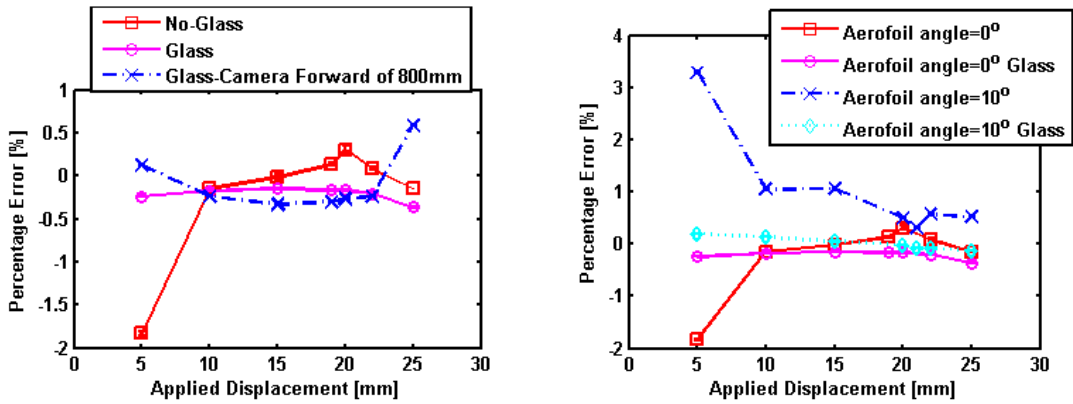


FIGURE 3.11: *Influence of double-glazed window in DIC results.*

From Figure 3.11 it can be seen that the addition of the glass introduces a waviness in the individual measures, as a result of the refractive index. Increasing the stereo angle while moving the camera closer to the specimen reduces the influence of the waviness as the accuracy for very small displacements is decreased (Figure 3.5). The purpose of the research is to look at average values on the specimen to assess its deflection and twist; therefore, as can be seen in 3.12, the addition of the glass smooths the percentage error value in a range of applied body motions. Figure 3.12(b) shows the influence of glass when an angle of attack of 10 degrees is added to the aerofoil.

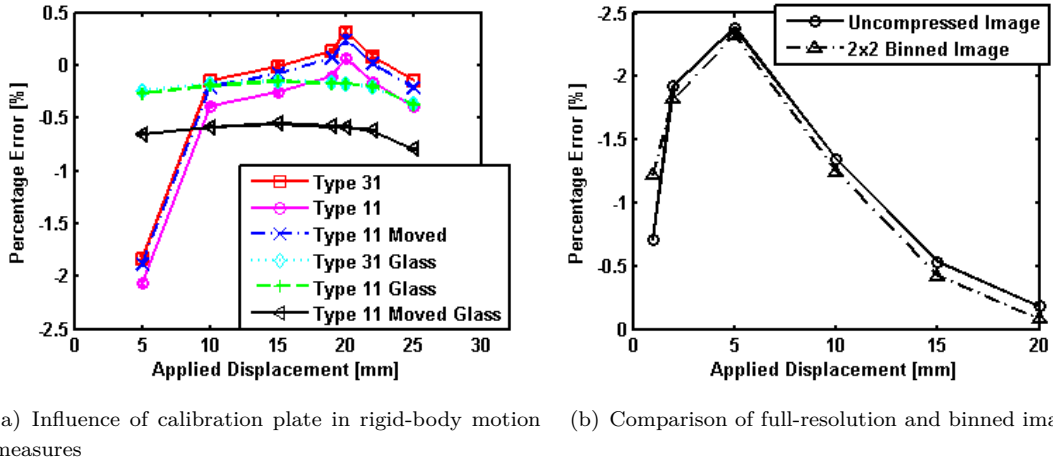


(a) Percentage error comparison without glass, with glass and moving the camera forward (b) Percentage error comparison between two aerofoil configurations (i.e. $\alpha = 0^\circ, 10^\circ$) with and without glass

FIGURE 3.12: *Influence of glass in DIC results for a given rigid body motion.*

From Figure 3.12 it can be seen that the average value measured through the glass appears to be closer to the applied displacement.

In addition, two different calibration plates were compared, as can be seen in Figure 3.13(a), and the influence of using a low-resolution high speed camera is investigated (Figure 3.13(b)). Two calibration plates from LaVision were compared: i.e. type 11 and type 31, the former being 106×106 mm and the latter being 309×309 mm. Type 11 calibration plate only covers a small part of the PAC aerofoil, therefore a calibration taken moving the plate in the entire field of view was assessed. The results from Figure 3.13(a) show a good agreement between all the calibrations. However, while using the high speed camera, which has a lower resolution compared to the E-lite camera, the pixel-shift of the dots diameter of the Type 11 plate was too small to be used. The influence of resolution on induced displacements can be seen in Figure 3.13(b). The full-resolution image from the E-lite camera is binned in the two dimensions by a factor of two, thus reducing the image resolution to the high-speed camera resolution level. This procedure permits a comparison of the results from the E-lite cameras with the expected results from the SA3 Photron High-speed cameras. The resulting values show a very similar trend between them, therefore it is possible to use a low-resolution high-speed camera to assess the out-of-plane displacement of an aerofoil under fluid load.



(a) Influence of calibration plate in rigid-body motion (b) Comparison of full-resolution and binned image measures

FIGURE 3.13: *Assessment of DIC measures for three different calibration procedures and changing the image resolution.*

Finally, the spatial resolution (subset-size) and the number of data point (step-overlap) was investigated also taking into consideration the CPU time taken to post-process the images, as can be seen in Figure 3.14. The subset size specifies the size of the local reference and target subsets between which the displacements are sought. The subsets must contain enough unique and identifiable features to achieve a reliable and accurate displacement determination. It is well known that the subset size has significant effects on the accuracy of displacement measurement in DIC (Pan *et al.*, 2008). The spatial resolution can be changed by varying the subset-size (i.e. the interrogation area on which each single displacement vector is calculated) (LaVision, 2012). Varying the subset size influences the accuracy of the results, as increasing the subset size reduces the noise in the image (allowing a larger area smooths the results) but also it decreases the accuracy of the displacement peaks. From the results in Figure 3.14(a) the larger subset size is giving the smallest error. The main reason of a higher accuracy for a large interrogation area (i.e. subset size of 121×121 pixels) is given by the full-field displacement of the aerofoil, that comprises of a rigid body motion, leading to a smooth deflection along the whole specimen, not occurring in peaks (which may occur if looking at strains of joints of small component failure loadings). The largest subset size is chosen because its low spatial resolution greatly reduces the CPU time (Figure 3.14(c)) both in terms of post-processing and analysing the results. This feature is particularly significant when analysing the large number of DIC images from the coupled DIC-PIV experiments (i.e. 3000 images). An overlap of 50% is chosen from Figure 3.14(b) as increasing the overlap also smooths the results and increases the number of data-point.

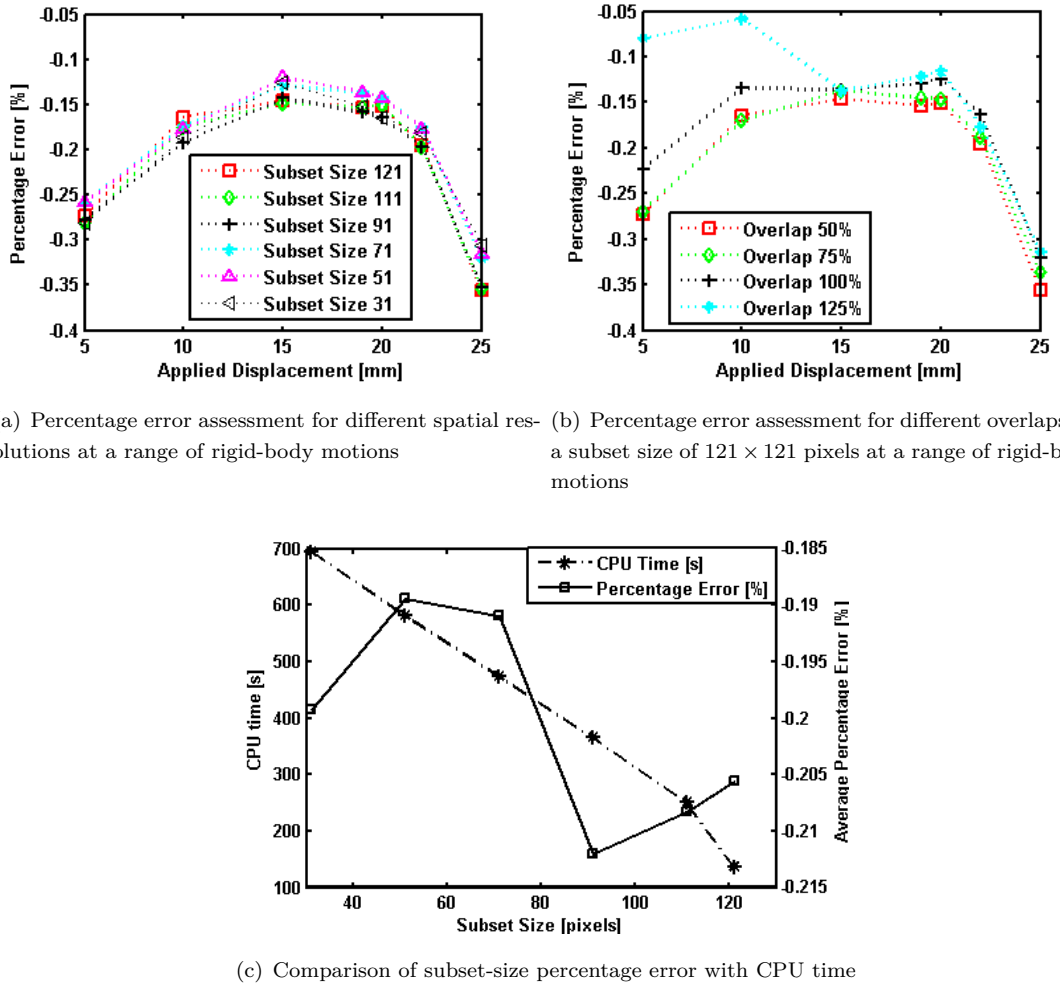


FIGURE 3.14: *Assessment of DIC measures for three different calibration procedures and changing the image resolution.*

3.4 Set-up of the Experiment in Wind-Tunnel

The experiments were conducted in the 3.5 m x 2.4 m R. J. Mitchell closed-circuit wind tunnel at the University of Southampton. Its turbulence intensity levels are less than 0.2% (Castro, 2001).

The aerodynamic forces on the NACA0015 foil were measured via a six component Nuntem load cell balance, mounted on a turntable in the roof of the wind tunnel. The aerodynamic data was acquired at a sampling frequency of 1 kHz. A number of repeats were measured in order to assess the repeatability and the robustness of the aerodynamic results.

High-speed three-dimensional DIC was used to capture the structural response of the foil. Details of the set-up and equipment used are provided in Table 3.2. The acquisition frame rate varied between 0.1 to 1 kHz. Two high speed SA3 Photron cameras were placed in the viewing room of the wind tunnel to avoid aerodynamic loading and vibration on the cameras. All the mean DIC results are averaged over a large number of pictures, varying from 100 to 3000 images. In addition, 30 second recordings at 0.1 kHz were captured to be able to describe the structural and fluid behaviour in the coupled DIC-PIV measurements.

Four high-powered LED lights (NILA Zaila) were mounted in the wind tunnel ceiling and floor to provide the required level of light to the DIC cameras. The greyscale histogram of the applied speckle pattern was assessed to achieve the correct level of diffused light (Crammond *et al.*, 2013).

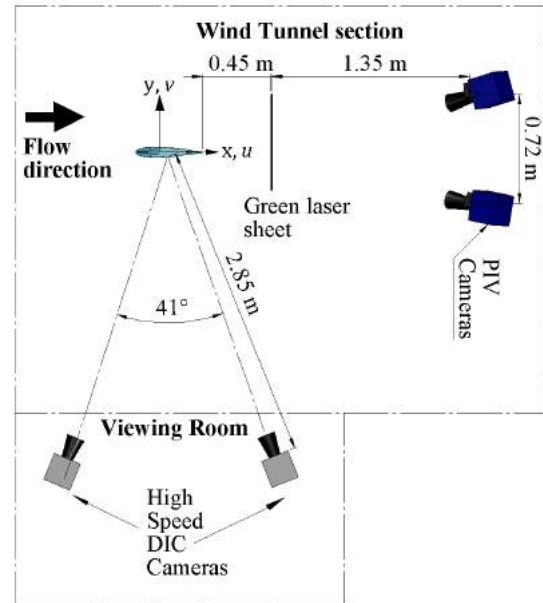
TABLE 3.2: DIC performance table showing the equipment and the setting used, as well as the speckle pattern characteristics.

Equipment	Set-up
Camera	2 high speed SA3 Photron
	Sensor size: 17.4×17.4 mm
	Pixel size: $17 \mu\text{m}$
	Resolution (max): 1024×1024 pixels
	Exposure time: $2000 \mu\text{s}$
Lens	Frame rate: 0.1-1 kHz
	Tokina 100 mm f2.8
Speckle pattern	Aperture: $f-16$
	Speckle size: approx. 7 pixels
	Dimensions: 450×450 mm

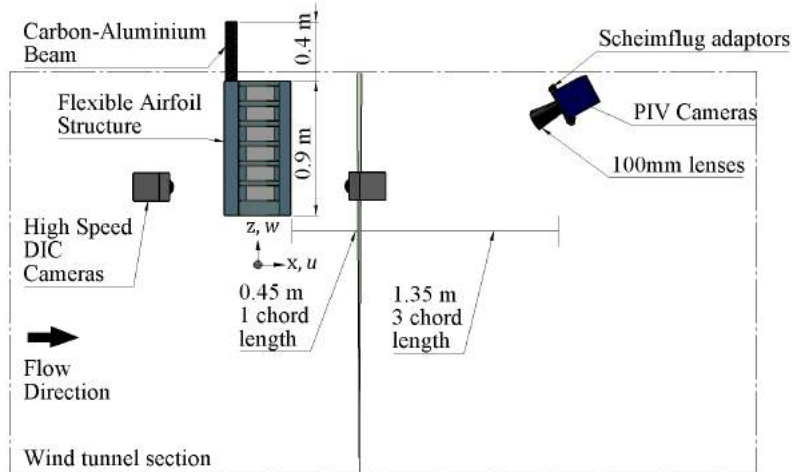
Table 3.3 describes the set-up and the equipment used in the PIV system. The accuracy of the PIV system is described by Marimon Giovannetti *et al.* (2016) and is measured

a posteriori. Two high-resolution LaVision Imager LX 29M PIV cameras were mounted on the wind tunnel ceiling 4 chords downstream of the trailing edge of the specimen for the PIV measurements. The acquisition frame rate for the PIV images was set to 2 Hz and the time between the two cross-correlation frames was adjusted for each wind speed, to provide a constant particle displacement of approximately 1/4 of the laser sheet thickness. The Litron Bernoulli Laser was mounted 1 chord downstream of the trailing edge, below the wind tunnel working section, with a 90 degree mirror and laser sheet optics to provide a 4 mm thick in-focused sheet 1.3 m above the tunnel floor, i.e. corresponding to the location of the tip of the foil.

Figure 3.15 shows a schematic set-up of the two full-field measurement systems in the wind tunnel. The reference point, about which the forces and moments are measured, was added and provides the coordinate system for the PIV data, presented in the tunnel axis system.



(a) Plan view



(b) Side view

FIGURE 3.15: *DIC and PIV setup in the wind tunnel showing the principal dimensions and the components used.*

The reference point is located on the tunnel centreline 1.26 m below the tunnel ceiling, 0.31 m below the tip of the unloaded foil and 0.09 m downstream of the unloaded leading edge. The stereo angle accuracy was $\pm 0.5^\circ$ and the linear measures accuracy was ± 2.5 mm.

TABLE 3.3: PIV performance table showing the equipment and the setting used.

Equipment	Set-up
Camera	2 ImagerLX 29M (LaVision) Sensor size: 36.3×24.2 mm Pixel size: $5.5 \mu\text{m}$ Resolution (max): $(6.4 \times 4.4) \times 10^3$ pixels Exposure time: $1/500 \mu\text{s}$ Frame rate: 2 Hz Stereo angle: ≈ 27 deg. Pitch angle: ≈ 25 deg. $\Delta t = 100-50-40 \mu\text{s}$ for $V_s = 10-20-25 \text{ m/s}$
Lens	Tokina 100 mm f2.8 Aperture: $f/4$ Depth of field: 16 mm
Laser	Litron Bernoulli Nd: YAG PIV Laser Wavelength: 532 nm Output energy: 200 mJ
PIV processing	Software: DaVis 8.2 Area of interest: Y(-260 to 140 mm) Z(25.5 to 145.5 mm) Digital resolution: 9.8 px mm^{-1} Initial interrogation area: $64 \times 64 \text{ px}$ Final interrogation area: $48 \times 48 \text{ px}$ (75% overlap)

To ensure that the areas of interest in both systems (i.e. the speckle pattern for DIC and the seeding particles for PIV) remained in focus during the experiments, it was necessary to calculate the expected depth of field for the chosen lenses, as presented by Jacobson *et al.* (2000):

$$DoF = D_F - D_N = \frac{2f^2 s^2 N c_b}{f^4 - s^2 N^2 c_b^2}. \quad (3.2)$$

In equation (3.2) D_F is the distance from the camera to the far limit of the depth of field, D_N is the distance to the near limit, s is the specimen distance from the camera, c_b is an assumed blur circle of 2 pixels, f is the focal length and N the f -number (Jacobson *et al.*, 2000). For the DIC high-speed camera the depth of field was calculated to be ≈ 635 mm and for the high-resolution PIV system $DoF \approx 16$ mm.

In order to correctly focus the stereo PIV cameras, two Scheimflug adaptors were mounted on the PIV cameras. These adaptors correct the limited depth of field, as described in section 2.4.2, given by the stereo and the pitch angles of the cameras, additionally tilting the image plane to align with the plane of the laser sheet, in accordance

with the Scheimpflug criterion (Prasad, 2000). The arrangement adopted during the experiments can be seen in Figure 3.16.

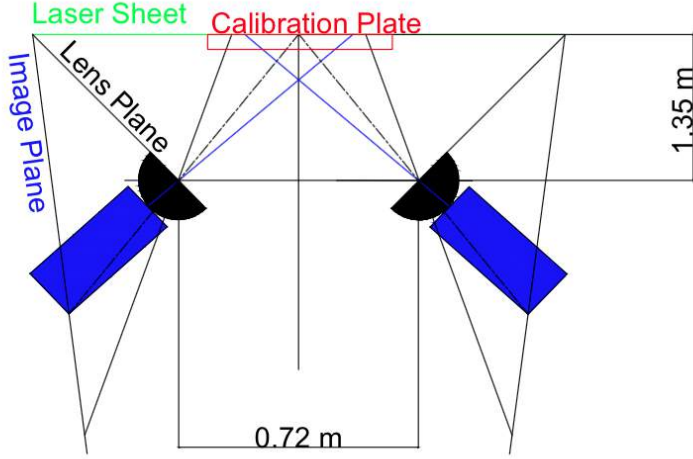


FIGURE 3.16: *An angular-displacement stereo PIV arrangement, where the two cameras are further rotated tilting the image plane with respect to the orientation of the camera lens and light sheet according to the Scheimpflug criterion.*

Both DIC and PIV systems were calibrated using a LaVision type-31 calibration plate that covers the whole field of view of the two systems. The Scheimpflug adaptor adjustment was performed during the PIV calibration process. This procedure increased the focus area to the whole calibration plate, allowing the cameras to detect the shift of sharply focused seeding particles in the entire field of view.

The trigger signal generated by the shutter of each of the four cameras from the DIC and PIV systems were fed into the Nuntem force and moment balance data acquisition system to relate the aerodynamic loading to each recorded full-field image, as can be seen in Figure 3.17.

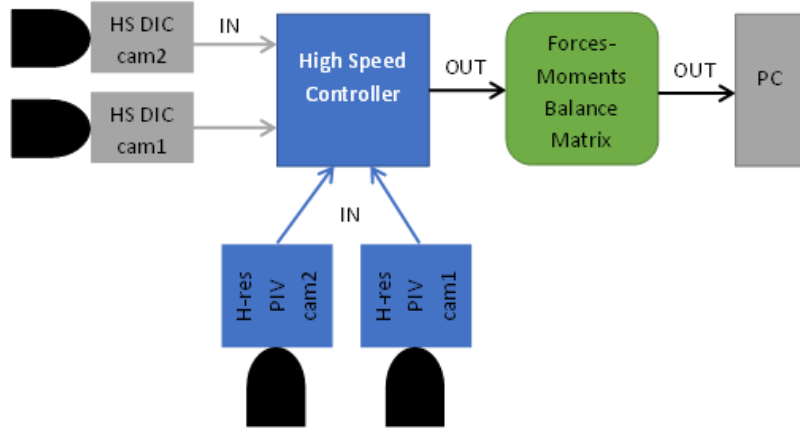
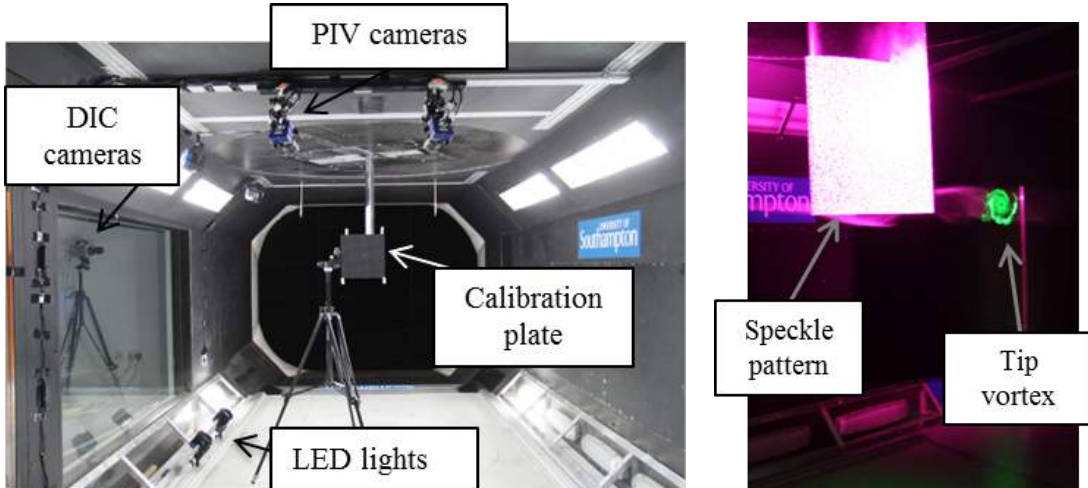


FIGURE 3.17: *Synchronisation diagram for the DIC-PIV-Aerodynamic measures.*

In order to correctly synchronise the two systems, not only did the camera shutter signals need to be related to forces and moments balance data, but it was also necessary to ensure optical isolation between the two full-field measurement techniques: the white light DIC and the laser illuminated PIV. Therefore, two low-pass $532\text{ nm} \pm 10\text{ nm}$ filters were applied to the PIV high resolution cameras to allow them to only capture the laser wavelength.

In addition, the LED lights were covered with magenta gel filters to allow the high-speed DIC cameras to only detect two-thirds of the white light histogram, cutting off the laser wavelength, as described in Figure 3.7(a). The adopted method provided enough light for the aperture and exposure settings of the cameras to not need to be adjusted. This ensured that the comparison of the results between DIC or PIV in isolation and synchronised DIC/PIV includes the introduction only of errors deriving from the addition of the filters (increase of <1%). Figure 3.18 shows pictures from the wind tunnel working section during the calibration process and during a coupled DIC-PIV run.

Given the high shutter speed and the short exposure time, a close inspection of the coupled DIC-PIV images showed that the PIV seeding particles are not affecting the image quality of the DIC when the two measuring systems are synchronised.



(a) Wind tunnel section during the PIV calibration process

(b) Coupling of DIC and PIV systems in the wind tunnel working section

FIGURE 3.18: *Wind tunnel set-up.*

3.5 Summary of the Chapter

The lack of experimental data for aeroelastic problems triggered the necessity to provide a repeatable and robust experimental method that can be reproduced. The experimental methodology presented in this chapter uses synchronised DIC and PIV within a wind tunnel environment to accurately describe the structural deformations and fluid response. The impact of coupling the two optical systems on measurement uncertainty has been assessed.

The fluid dynamic and structural response of a flexible aerofoil can therefore be measured in the controlled environment of a wind tunnel utilising this technique. This was achieved for a complete FSI experiment that was never presented in literature. Another source of novelty in FSI experiments is the understanding and quantification of sources of error in the measuring systems.

It has been shown that by suitable experimental design the accuracy of the DIC system is not significantly affected by the addition of the PIV to the methodology and vice-versa. The maximum error for DIC measures both in translation and rotation for static and dynamic motions is always less than 5%. For structural deformation measures, the influence of glass-effects on the cameras is studied as well as the spatial resolution and overlap. The optimised settings are therefore described.

By demonstrating and quantifying the relationship between structural and fluid response, the presented experimental methodology has the potential to investigate the influence of changing the internal design of a structure to evoke deformations that have a positive effect on fluid response. Therefore, this technique will be relevant to a large

range of applications not only as an experimental method, but also to provide valuable validation cases for numerical FSI investigations.

4

Numerical Methodology

4.1 Introduction

A numerical model of the simplified foil structure described in Section 3.2 is developed. The aim is to provide a numerical prediction of this structure to fluid loading validated through experiments. The numerical analysis has been approached systematically, firstly assessing the validity of the Finite Element Analysis (FEA) model from a simple beam, building the geometry complexity to its final shape, containing the foam-rib structure as well as the Mylar sheet. The validity of the flow solver is assessed alongside the experimental results, comparing the forces and the tip vortex position measured in the experiments and simulated. Finally, the coupling technique between the FEA and the Computational Fluid Dynamic (CFD) solvers is investigated. The software used are ABAQUS 6.14 for the structural solver and Star-CCM+ 11.0.2 for the fluid solver.

4.2 Structural solver set-up

The finite element model of the aerofoil section represents the wind tunnel specimen. The material properties of the carbon, foam and Mylar were tested independently at the University of Southampton and the results of a systematic approach to FEA numerical modelling is herein described.

4.2.1 Simple Aluminium and Composite-Aluminium beam

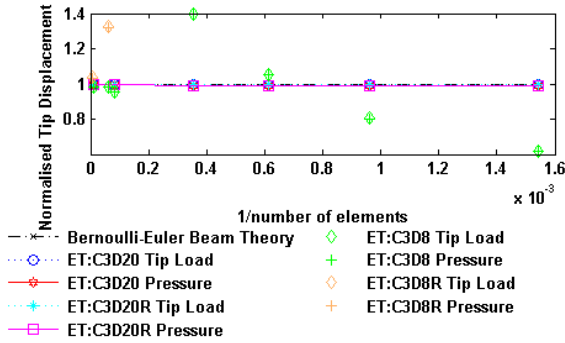
To build up the accuracy level needed in the FEA model, the first model investigated was a homogeneous aluminium beam. Applying a static loading to it, it was possible to assess the different elements of the mesh and compare them with respect to the known analytical solution, as can be seen in Figure 4.1.

Taking into consideration a simple isotropic aluminium beam under bending and comparing the numerical results with the analytical solution, it was possible to assess the behaviour of different element types and to reach a level of accuracy on the FEA mesh that could be used subsequently in the wind tunnel simulations.

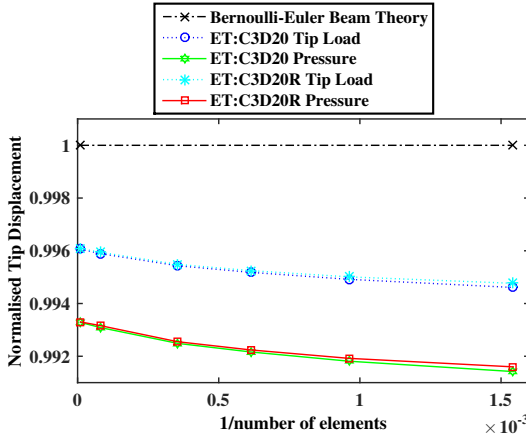
The first analyses were conducted with first-order and first-order-reduced integration elements, C3D8 and C3D8R respectively. However, it was found that first-order elements, whilst greatly reducing the computational cost, are subject to *shear locking* and *hourgassing* effects. Shear locking occurs in first-order fully integrated elements (i.e. such as C3D8) that are subject to bending, as the investigated loading condition. The numerical formulation of the elements give rise to shear strains that do not exist in reality (i.e. parasitic shear), as described in (ABAQUS Simulia, 2013). This element therefore results in having an artificially increased stiffness in bending, in particular if the element length is the same order of magnitude as, or greater than, the wall thickness. C3D8 element was therefore discarded as an element to be used, as in composite sections the element thickness needs to match the wall thickness, as each element contains the number of plies defined in the section (ABAQUS Simulia, 2013). Hourgassing occurs in first-order-reduced integration elements (i.e. as C3D8R) in stress-displacement analysis. Since this type of element has only one integration point, it is possible for these elements to distort in such a way that the strains calculated at the integration point are all zero, which leads to a distortion of the mesh. The reduced integration elements have only one Gauss point: these are the points at which the constitutive matrix C is evaluated and where the most accurate values of strains and stresses are obtained (Barbero, 2008).

Second order elements, such as C3D20 and C3D20R, provide a higher accuracy than first order elements for smooth problems that do not involve severe element distortion (in such cases they can fail in volumetric locking). Volumetric locking occurs in fully-integrated elements when the material behaviour is almost incompressible (i.e. poisson's ratio approaching 0.5). In such a case spurious pressure stresses develop at the integration points, causing the element to behave too stiffly for deformations that should cause no volumetric changes. In the case under investigation the materials involved in the formulation of the aerofoil specimen did not involve incompressible materials, so it was possible to choose the second order elements without any issues of volumetric locking. Furthermore, second order elements are very effective in bending-dominated problems such as the one under investigation (ABAQUS Simulia, 2013).

Figure 4.1 shows the convergence study conducted on the mesh for the aluminium isotropic beam under tip and pressure loadings. For both cases the 1300 mm beam is fixed for 350 mm at the root. In the tip load case a point load of 98.6 N is applied at the centre of the free-end of the beam. In the pressure load case, a pressure is uniformly distributed along the span and width of the beam. The results are presented as normalised tip displacement over the 1/number of nodes. It is possible to see from Figure 4.1(a) that while the mesh was coarse, the results for the first-order element type (C3D8 and C3D8R) are greatly underestimated, whereas reaching a finer mesh density the results are over-estimated until they reach steady values for a very fine grid. Figure 4.1(b) only presents the results for the second-order element types (C3D20 and C3D20R). It can be seen how these elements accurately capture the bending of the beam from a coarse to a finer grid, as Figure 4.1 shows the numerical results compared with the known Bernoulli-Euler analytical beam theory for a tip load case.



(a) Mesh convergence study for first- and second-order element types compared to analytical solution



(b) Mesh convergence study for second-order element types compared to analytical solution

FIGURE 4.1: *Mesh convergence study for isotropic aluminium beam under bending loading.*

Furthermore, it was possible to analyse the increase of computational cost associated with the increase in mesh density, as can be seen in Figure 4.2.

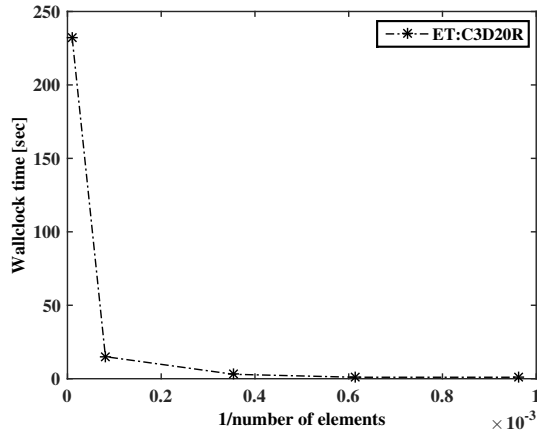


FIGURE 4.2: *Wall-clock time increase with mesh density.*

Following this study, an appropriate element size of 8 mm for the composite section PAC beam was chosen, corresponding to 6.13×10^{-4} 1/number of elements. This size provides a correct representation of the beam under bending while having only one element through the thickness of the beam. Therefore it was possible to use this element size also in the composite analyses.

The same beam response was modelled as a composite section, and the influence of changing the material orientation was assessed for deflection and twist while analysing the laminate material properties. It has to be noted, as described earlier, that only one element in the through thickness direction needs to be used in a composite layup, as each element contains the number of plies defined in the section (ABAQUS Simulia, 2013). Recent studies have shown that quadratic solid elements are able to capture the stress distributions and the deflections with just one element through the thickness, as presented by Young (2008). Moreover, failure criteria are shown to be best captured with one element through the thickness of the composite rather than for one layer per thickness, as presented by Arafath *et al.* (2007); Svard (2012).

Following those studies, in order to increase the accuracy in the results, the number of integration points was increased to allow a smooth stress and strain distribution to be captured for each ply in the through thickness direction. Generally, in a composite element, at least one Gauss integration point per layer is required to capture the effects of different layer properties Arafath *et al.* (2007). According to the FEA models for a beam bending problem, the displacement is defined at the nodes and the stresses and strains are calculated at the integration points, following Equations (4.1-4.4). In a typical composite laminate that involves a number of different layers, the number of integration points per layer should be sufficient to integrate the higher order terms

accurately, without increasing the run time excessively.

$$[k] = \int \mathbf{B}^T \mathbf{D} \mathbf{B} d(vol) \quad (4.1)$$

$$\{P\} = \{K\} \{\delta\} \quad (4.2)$$

$$\{\epsilon\} = \mathbf{B} \{\delta_e\} \quad (4.3)$$

$$\{\sigma\} = \mathbf{D} \{\epsilon\} \quad (4.4)$$

where

$$\{\epsilon\} = \{\epsilon_x \epsilon_y \epsilon_z \gamma_{xy}\}$$

and

$$\{\sigma\} = \{\sigma_x \sigma_y \sigma_z \tau_{xy}\}$$

where δ is the nodal displacement, δ_e is the element displacement, \mathbf{B} is the strain displacement matrix, \mathbf{D} is the stress displacement matrix, P is the load applied on the node and K is the element stiffness matrix (ABAQUS Simulia, 2013; Barbero, 2008).

The PAC composite beams under investigation present two configurations, as described in Section 3.2; therefore Table 4.1 presents the dimensions of the composite beams for both cases (i.e. one ply at each side of the aluminium core or two plies at each side of the core - for $\phi = 2 \times 30^\circ$ -).

TABLE 4.1: PAC sandwich beam dimensions.

Parameter	Value
Length	1300 [mm]
Width	76.2 [mm]
Aluminium thickness	6.38 [mm]
Thickness 2 composite plies	7.51 [mm]
Thickness 4 composite plies	8.146 [mm]
I 2 composite plies	2095.12 [mm ⁴]
I 4 composite plies	2646.89 [mm ⁴]

In Figure 4.3 the beam, its plies orientations and material definitions are presented, as well as the integration Gauss points (blue dots in Figure 4.3(b)). From the figure it is possible to see that, as in the experimental beam, the carbon skins are attached to the aluminium core through the use of the toughened epoxy adhesive SA80 (Gurit, 2012b).

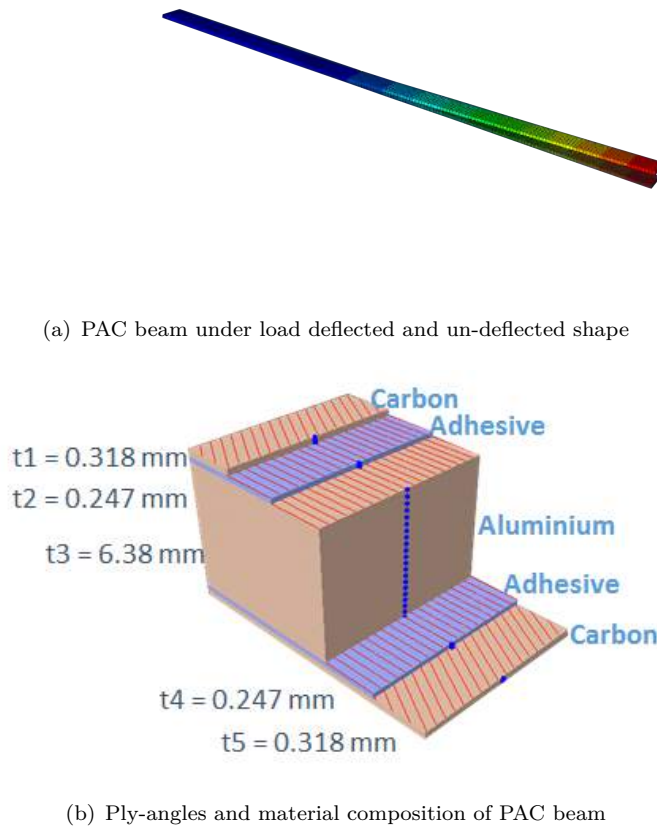


FIGURE 4.3: *Sandwich PAC beam ply angle $\phi = -30^\circ$, 21 integration points.*

The most important aspect in FEA modelling is to correctly model the material properties of the elements, especially if comparing the results with experiments. Most of the materials are presented to customers with their engineering properties; however, when closely inspecting them, *book* values are sometimes different from true engineering constants. Therefore, it is very important to test the materials accurately, in order to be able to input the correct values into the FEA models. Figure 4.4 presents a log-plot of typical engineering properties for a range of different materials, including the ones under investigation in the present project.

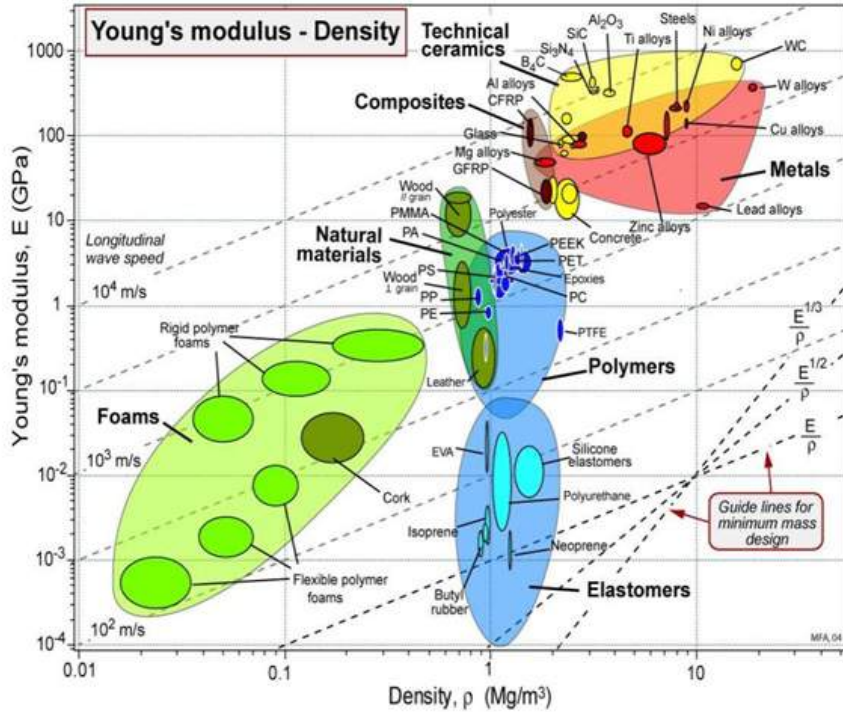


FIGURE 4.4: *Young's modulus over density for a range of different materials (Ashby, 1992).*

The initial simulations were performed with *book* values for both the aluminium and the carbon; however, after having compared the results with some experiments conducted at the University of Southampton on composite sandwich (aluminium-carbon) beams (Note, 2014), the mechanical properties of these two materials were changed. The carbon SE 84LV fibres were tested at the University of Southampton by Nicholson (2015) and the engineering constants were changed from $E_1 = 110000$ MPa and $E_2 = 9000$ MPa to $E_1 = 117940$ MPa and $E_2 = 7840$ MPa. In addition, the 6082 aluminium properties were changed, comparing the results of a beam-bending case between the FEA, the analytical, and the experimental results, from $E = 67000$ MPa to $E = 55000$ MPa. The tip deflection result from the experiments, as shown in Figure 4.5, was set into the analytical formula, Equation (4.5), to find the Young's modulus value, knowing all the other constants.

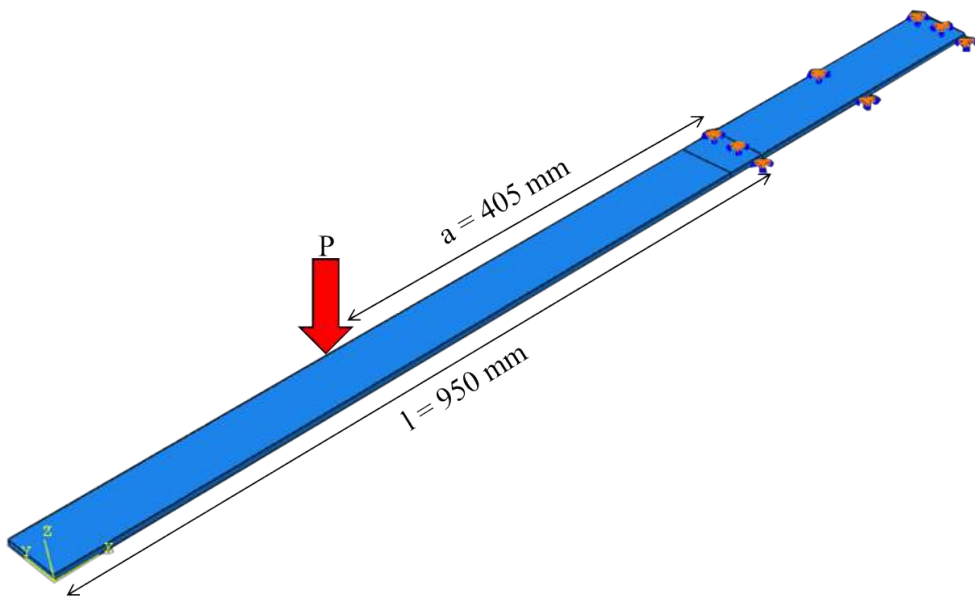


FIGURE 4.5: *Experimental PAC beam under bending load.*

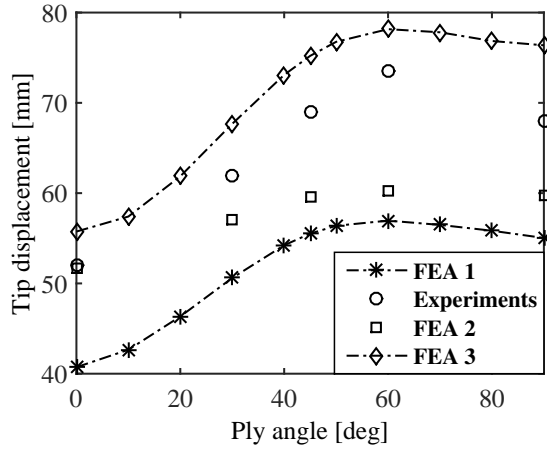
$$\delta_{max} = \frac{Pa^2}{6EI} \times (3l - a) \quad (4.5)$$

Figure 4.6 shows the deflection and twist angle values obtained comparing the experimental results with three different numerical configurations. The experiments were conducted by Note (2014) at the end of a set of wind tunnel tests, fixing the PAC beams for 350 mm and applying a load to the side of the beam at 405 mm from the fixed end. It has to be noted that the PAC beams used for this set of experiments experienced a large amount of de-lamination of the composite skins, therefore the experimental results might be larger than expected. The numerical approaches that modelled the beam as a solid composite section made of an isotropic core and the two carbon skins, were:

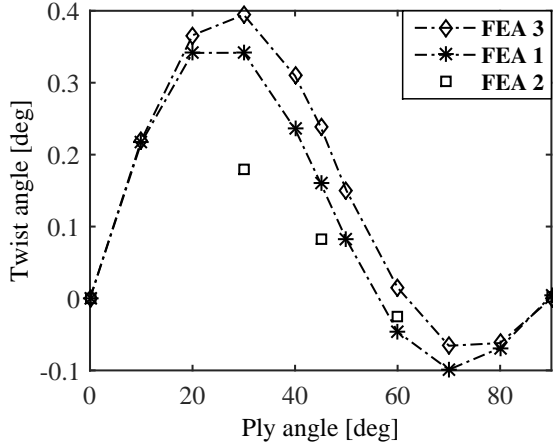
1. FEA1: Correct boundary conditions, fixing in translation and rotation the first 350 mm of the beam and load applied at 405 mm from the end of the fixed part on the edge of the beam, $E_{1carbon} = 110000$ MPa, $E_{2carbon} = E_{3carbon} = 9000$ MPa and $E_{Aluminium} = 67000$ MPa
2. FEA2: Correct boundary conditions, fixing in translation and rotation the first 350 mm of the beam and load applied at 405 mm from the end of the fixed part on the edge of the beam, $E_{1carbon} = 117940$ MPa, $E_{2carbon} = E_{3carbon} = 7840$ MPa and $E_{Aluminium} = 55000$ MPa

3. FEA3: Only one end of the beam fixed in translation and rotation and load applied at 405 mm from the end on the edge of the beam , $E_{1carbon} = 110000$ MPa, $E_{2carbon} = E_{3carbon} = 9000$ MPa and $E_{Aluminium} = 67000$ MPa.

From Figure 4.6(a) it is possible to see that decreasing the Young's modulus of the aluminium and increasing the engineering constants of the carbon makes the beam more flexible in deflection, but stiffer in twist and in rate of deflection change while changing the ply orientation (from FEA1 to FEA2). Comparing Figure 4.6(a) and Figure 4.6(b) it is possible to note that the highest $\frac{twist}{displacement}$ ratio occurs for $\phi = 30^\circ$. This configuration presents the smallest deflection for the highest twist values. Therefore, in the present research a ply angle of 30° was chosen in its positive and negative form to assess the effects of sign rotation on the twist response of the structure.



(a) Tip deflection values for different ply angles

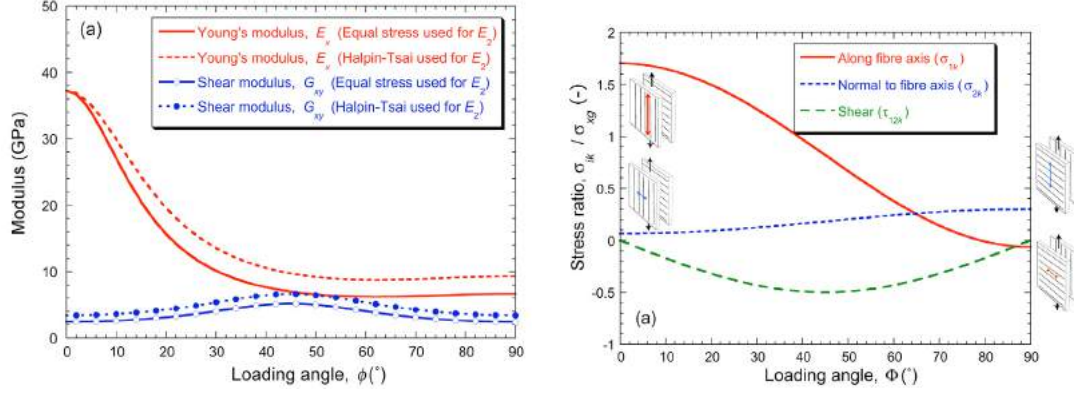


(b) Twist angle values for different ply angles

FIGURE 4.6: Tip deflection and twist angle variations for a range of ply angles.

Furthermore, Figure 4.6(a) shows that in all the analysed cases, the maximum deflection is occurring at $\phi = 60^\circ$. This phenomenon can be explained because, while the Young's

modulus E_1 reaches a steady value at $\phi = 45^\circ$ and remains constant until $\phi = 90^\circ$, for a single ply, at $\phi = 60^\circ$ there is a maximum stress ratio (i.e. $\frac{\sigma_{ik}}{\sigma_{xy}}$) for the stress normal to the fibre axis, as can be seen in Figure 4.7, and there is a larger interaction between shear strain γ_{xy} and the normal strain ϵ_x (Clyne, 2014).



(a) Modulus for a single ply over a range of loading angles

(b) Stress ratio over a range of loading angles

FIGURE 4.7: *Young's modulus and stress ratio for a range of different ply angles (Clyne, 2014).*

In order to correctly describe the sandwich laminate properties, the beam was analysed with a macro-mechanics Classical Laminate Theory (CLT) to derive the sandwich engineering constants. The **ABD** matrices were calculated for each orientation angle, knowing the ply thickness of both the carbon and the aluminium components. Having calculated the inverse matrix of **A**, it was possible to calculate the material properties for each PAC configuration following Equations (4.6-4.11).

$$E_x = \frac{1}{(\mathbf{A}^{-1}(1,1) \times (h))} \quad (4.6)$$

$$E_y = \frac{1}{(\mathbf{A}^{-1}(2,2) \times (h))} \quad (4.7)$$

$$G_{xy} = \frac{1}{(\mathbf{A}^{-1}(3,3) \times (h))} \quad (4.8)$$

$$\nu_{xy} = -\frac{\mathbf{A}^{-1}(1,2)}{\mathbf{A}^{-1}(1,1)} \quad (4.9)$$

$$\nu_{yz} = -\frac{\mathbf{A}^{-1}(1,2)}{\mathbf{A}^{-1}(2,2)} \quad (4.10)$$

$$G_{yz} = \frac{E_y}{(2 \times (1 + \nu_{yz}))}. \quad (4.11)$$

It was therefore possible to plot the laminate material properties, as can be seen in Figure 4.8. From Figure 4.8(a) it is also possible to see that the laminate E_x reaches a

minimum value at $\phi = 60^\circ$, better explaining the PAC beam response encountered in the experiments and numerical simulations.

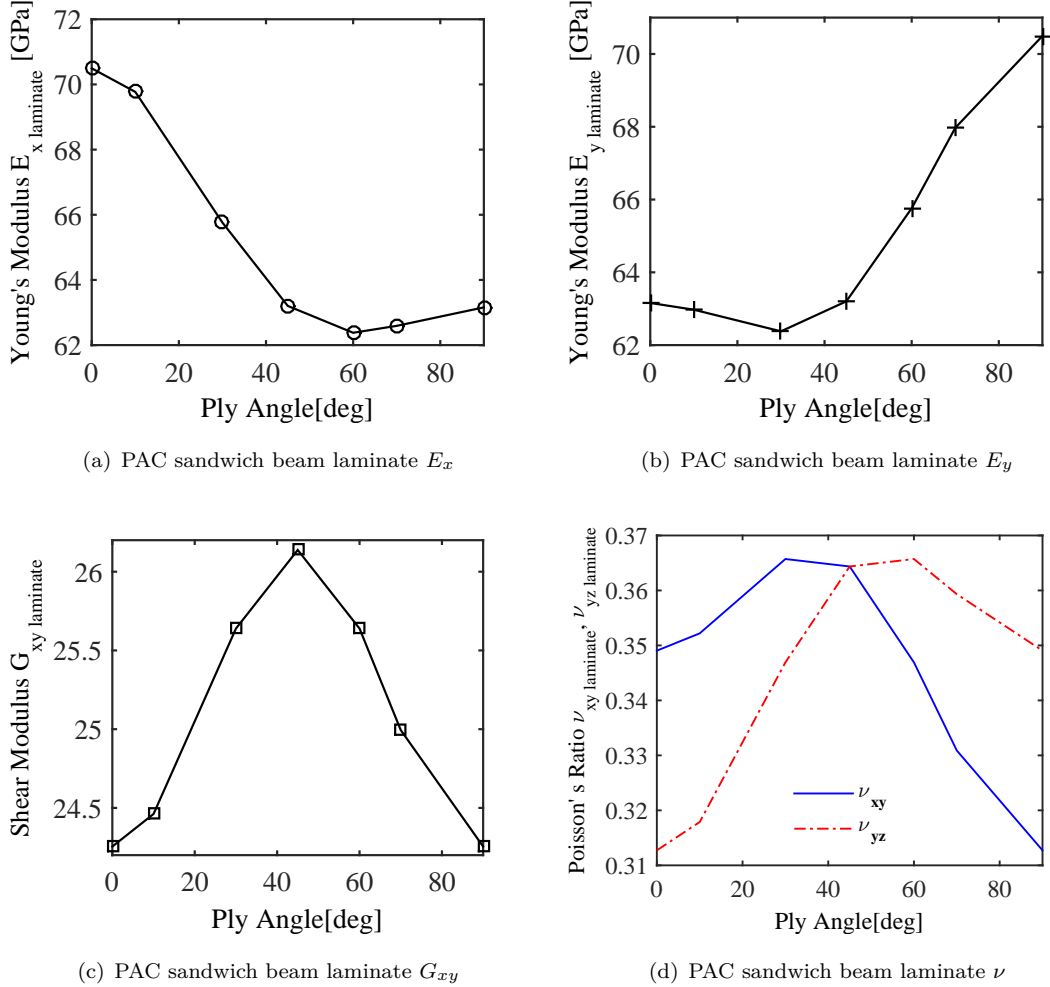


FIGURE 4.8: *PAC sandwich beam laminate material properties.*

4.2.2 Foam Aerofoil Structure

The complexity of the geometry was then increased, adding a full-foam structure to the assembly. The foam aerofoil structure presented a cut-through of the same width and thickness of the PAC beams. The cut was positioned in the same location as in the wind tunnel experiments. The addition of the aerofoil structure not only increased the geometrical complexity, but also added the necessity of the correct modelling of the material of the foam. Then, with the addition of the full-foam aerofoil part, it was possible to start the coupling between the FEA and CFD solvers. The contact region between the beam and the foam structure was modelled as a tie constraint, that bound the two separate regions together so that there was no relative motion between them. The constraint was modelled as a surface-to-surface constraint, using

as a *master* surface the four regions of the PAC beam, and the cut-through regions of the aerofoil as a *slave* surface. Surface-to-surface discretisation was chosen over node-to-node discretisation, as it provides a more accurate stress distribution when the geometry is well represented, as it enforces contact conditions in an average sense over regions in proximity to slave nodes, rather than only at individual slave nodes (ABAQUS Simulia, 2013). The averaging regions were approximately centred on slave nodes, so each contact constraint predominantly considered one slave node but also considered adjacent slave nodes. Figure 4.9 presents a view of the full-foam geometry represented in ABAQUS.



FIGURE 4.9: *Aerofoil flexible structure made of PAC beam ($\phi = -30^\circ$) and full-foam aerodynamic part.*

The geometry of the foam was added as in the wind tunnel tests, consisting of leading and trailing edges that run though the whole span of the aerofoil (i.e. 900 mm), a tip rib of 100 mm and six ribs of 33.3 mm. The ribs were separated from each other by 100 mm. The leading edge region presents the cut-through where the beam was inserted. All the parts in contact were modelled as tie-constraints. The first tie constraint was given by the *master* surface of the four regions of the PAC beam and the *slave* surface of the cut-through regions of the leading edge part. The leading edge insert was modelled as a *master* surface for the leading-edge parts of the various ribs (i.e. *slave* surfaces). Finally, the trailing-edge parts of the ribs were modelled as *master* surfaces of the trailing edge insert. This configuration allowed the deflection to be propagated and controlled through the PAC beam. Figure 4.10 presents a view of the rib-foam geometry represented in ABAQUS.

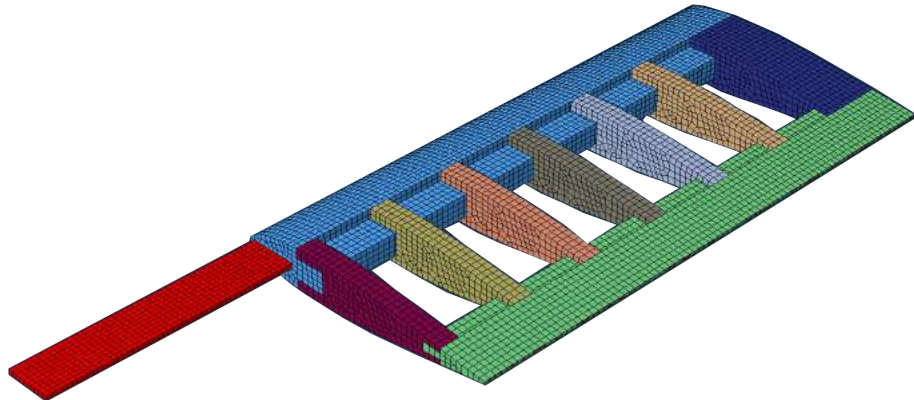


FIGURE 4.10: *Aerofoil flexible structure made of PAC beam ($\phi = -30^\circ$) and rib-foam aerodynamic part.*

Having chosen the numerical arrangement from FEA2 (Figure 4.6) to be the most accurate in describing the material behaviour of the PAC beam, it was necessary to investigate the material properties of the foam. Extruded polystyrene was designed to transmit the aerodynamic loading to the PAC beam providing as little strength as possible to the assembly model. The foam was therefore tested in tension, compression and shear to obtain the correct material properties to use in the FEA analysis. A number of foam samples were manufactured to be tested under the respective ASTM test standards, i.e. ASTM D1623, ASTM D1621 and ASTM C273 (ASTM International, 2003, 2004, 2007). Three of the tested samples can be seen in Figure 4.11.

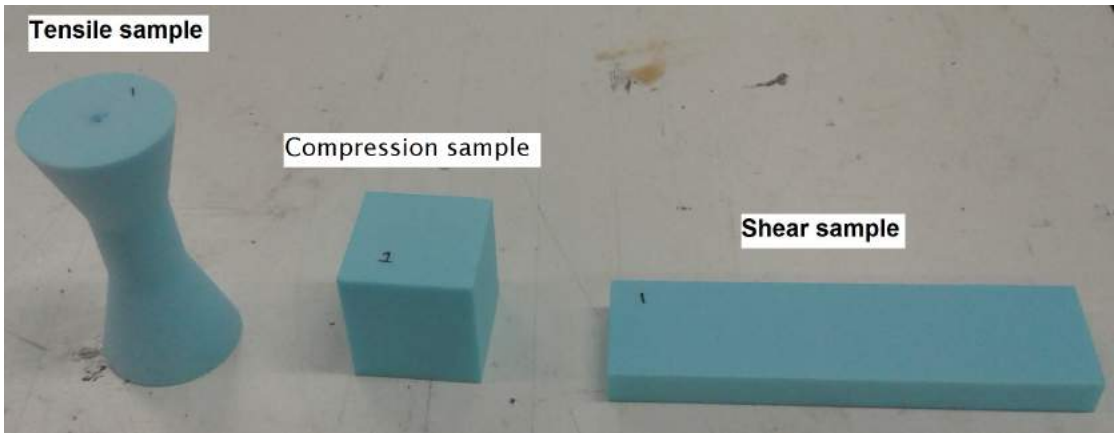


FIGURE 4.11: *Foam test specimens for tensile, compressive and shear testing.*

All the dimensions of the specimens were checked against the tests standards. Compressive and shear samples were manufactured using a hot wire foam cutter. Tensile test specimens were manufactured using a lathe. It is important to recognise that the

properties of the foam materials can vary significantly from one batch to another, therefore all the samples were cut from the same batch that was used for the wind tunnel experiments.

Tensile Test

Tensile testing of the foam was carried out according to ASTM D1623. The test machine used for this testing was an Instron 5569 servo-mechanical test machine. The foam specimens were accurately cut with the hot-wire technique and shaped with a lathe according to the dimensions prescribed in ASTM D1623 and shown in Figure 4.12.

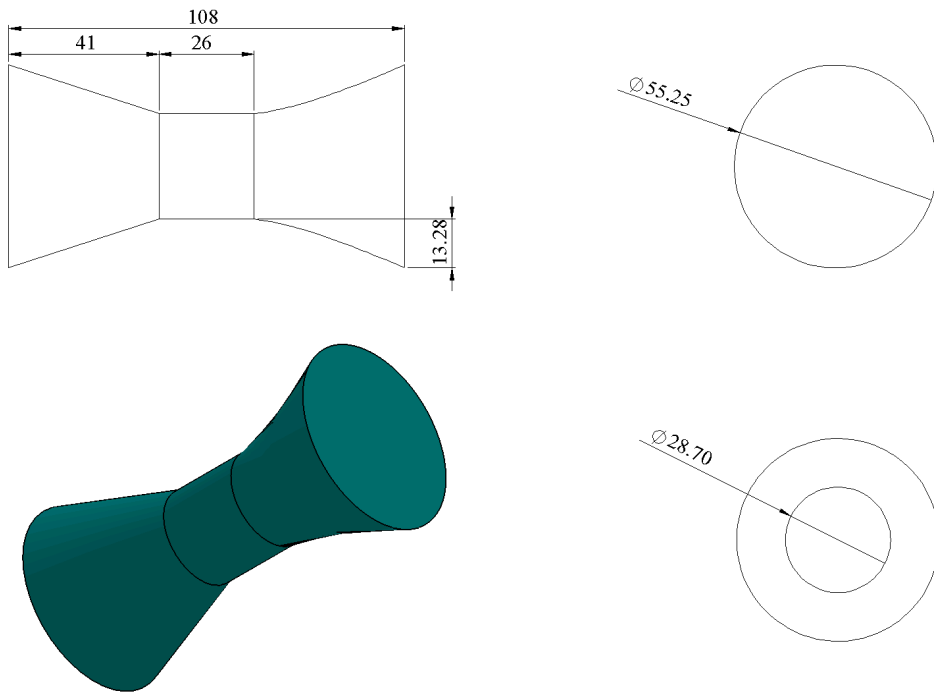
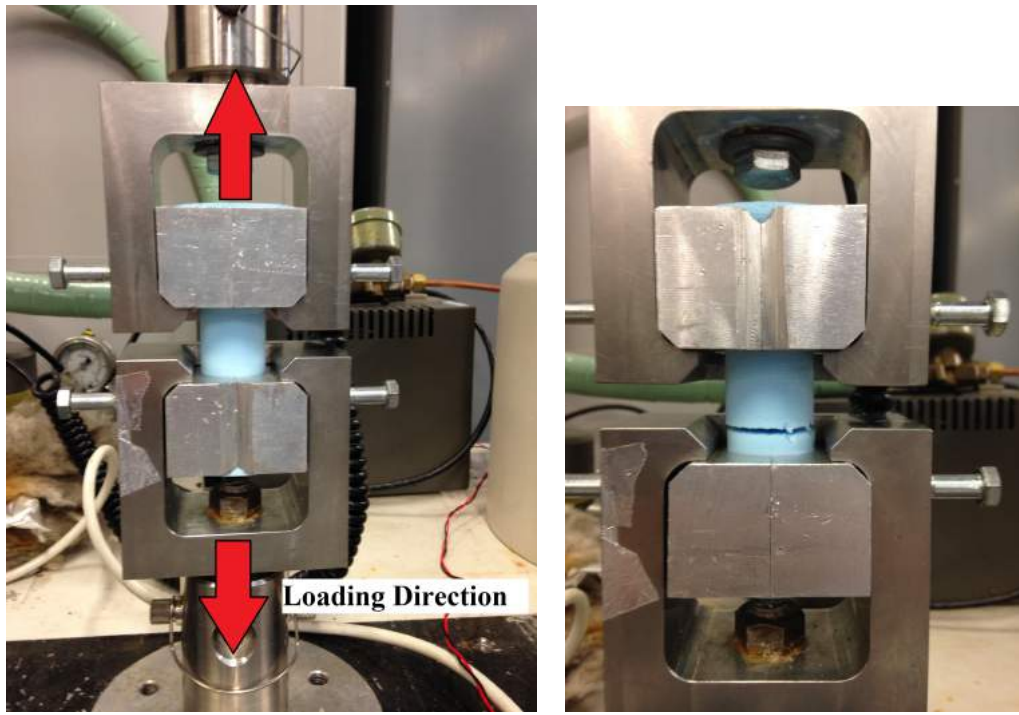


FIGURE 4.12: *ASTM D1623 standard dimensions for tensile type A specimen. All dimensions are in millimetre.*

A custom-made rig was used to distribute the tensile load and avoid crushing the foam in the jaws. An image of the tensile test can be seen in Figure 4.13. The foam was loaded at a cross-head displacement rate of 1.3 mm/min, as described in the standard. Figure 4.13(b) shows the specimen at the end of a test. It can be seen that in order to achieve correct results the breakage of the specimen should occur at the centre of the gauge length, avoiding cracks initiated at the jaws.



(a) Foam tested specimen loaded in tension in the Instron 5569 machine (b) Foam specimen loaded in tension at the end of test

FIGURE 4.13: *Foam specimen loaded in tension at beginning and end of test.*

Figure 4.14 shows the stress-strain curves from the tensile tests of eight specimens. From the figure it is possible to note that the initial slope changes from specimen to specimen. This is due to an initial misalignment, or a difference in contact point between the rig and the foam specimens. The initial necking of the cell walls is represented by the initial steep increase in stress.

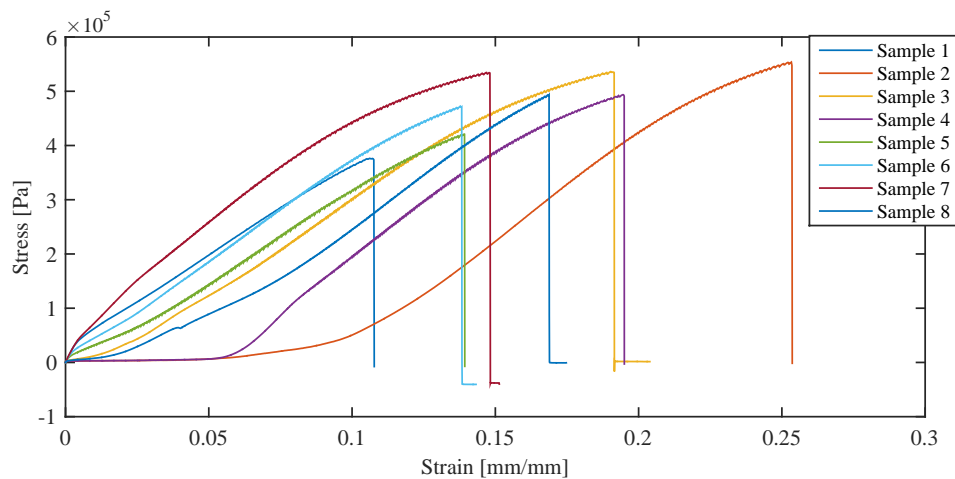


FIGURE 4.14: *Stress-strain curves from tensile foam tests.*

Thus the material properties were calculated from the linear sections of the stress-strain curves, following the initial 5% of the curves. The average tensile modulus was found to be 3.64 MPa and the mean ultimate tensile strength to be 485 kPa. Full results are given in Table 4.2.

TABLE 4.2: Tensile tests on foam specimen results.

Sample	Tensile Modulus[MPa]	Tensile Strength [kPa]
1	3.33	376
2	3.82	554
3	3.51	536
4	3.83	494
5	3.37	421
6	3.54	472
7	3.84	535
8	3.86	493
Mean	3.64	485
Standard deviation	0.22	61

It should be noted that, due to their internal cellular structure, foam materials are known to be difficult to test accurately, and therefore material properties obtained are unreliable. This is particularly true for tensile properties, due to their cellular and anisotropic internal structure. The anisotropic nature of these materials means that the strain distribution is not constant throughout the material. This causes a multi-axial stress state to develop, which in turn affects the calculated Young's modulus and Poisson's ratio values.

Compressive Test

A compressive testing of the foam was carried out in accordance with ASTM D1621. The test machine used for the test was the same used for the tensile tests, i.e. Instron 5569, but with a different rig to put the specimens into contact with the servo-mechanical test machine. Flat plates with cylindrical joints were fitted in the rig and the samples were loaded centrally in compression, as can be seen in Figure 4.15. Given the geometry of the rig and the specimens, an even loading of the compressive force across the specimen is expected. A compressive load was applied with a cross-head displacement rate of 2.5 mm/min, as described in the ASTM standard. Two sets of compression tests were carried out to investigate the anisotropic behaviour, placing the specimen in the y and z directions and comparing the results obtained for the two cases.

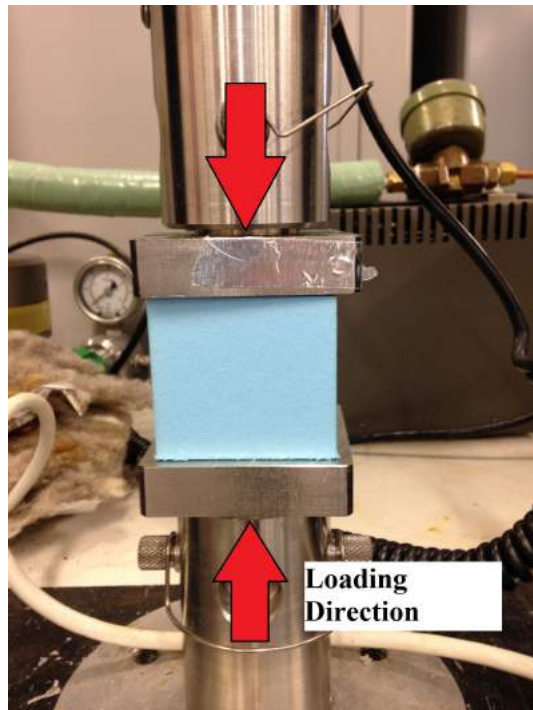


FIGURE 4.15: *Foam specimen loaded in compression.*

Figure 4.16 shows the compressive stress-strain curves for foam samples. It is clear from these results that the foam has anisotropic properties, depending on the orientation of the samples. Samples 5 and 6 (which were orientated in the through-thickness direction) give an average compressive modulus of 21.3 MPa and an average compressive strength of 434 kPa. Those values are almost double the values obtained from the remaining samples, loaded in the y – *direction*, that present an average compressive modulus of 10.4 MPa and average compressive strength of 241 kPa.

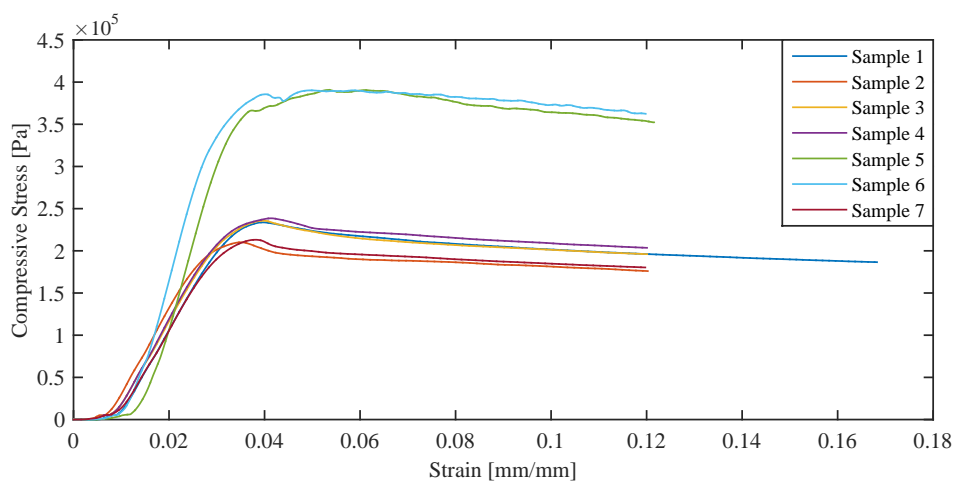


FIGURE 4.16: *Stress-strain curves from compressive foam tests.*

The test results are presented in Table 4.3

TABLE 4.3: Compression tests on foam specimen results.

Sample	Compressive Modulus[MPa]	Compressive Strength [kPa]
1	10.4	252
2	10.8	227
3	10.7	255
4	10.9	256
5	20.7	431
6	21.8	437
7	9.5	212
Mean $z - dir$	21.3	434
Mean $y - dir$	10.4	241

The anisotropic material behaviour is due to the manufacturing method used to produce the different blocks of foam, made from extrusion. It should be noted that the compressive modulus found for the foam varies greatly from the tensile modulus, with an average tensile value of 3.64 MPa and compressive value of 10.4 MPa or 21.3 MPa depending on sample orientation. It is generally accepted that there is no logical reason for the tensile and compressive modulus of a material to be different. Therefore, the wide difference in moduli can be attributed to the difficulties associated with testing foam materials in tension, and to errors in tensile testing results due also to the lack of extensiometer readings (Gibson and Michael, 1988).

Shear Test

Finally, shear tests of the foam were carried out in accordance with ASTM C273. The samples were initially bonded to steel plates with a two-part Araldite adhesive and were placed in the servo-mechanical Instron 5569 as shown in Figure 4.17. The specimens were loaded for shear in compression at a cross-head displacement rate of 2.5 mm/min. It has to be noted that the cross-head touched the specimens before failure occurred. The test was stopped just prior to the contact point between the cross-head and the steel plates. Therefore, whilst the shear modulus was measured, the shear strength could not be evaluated.

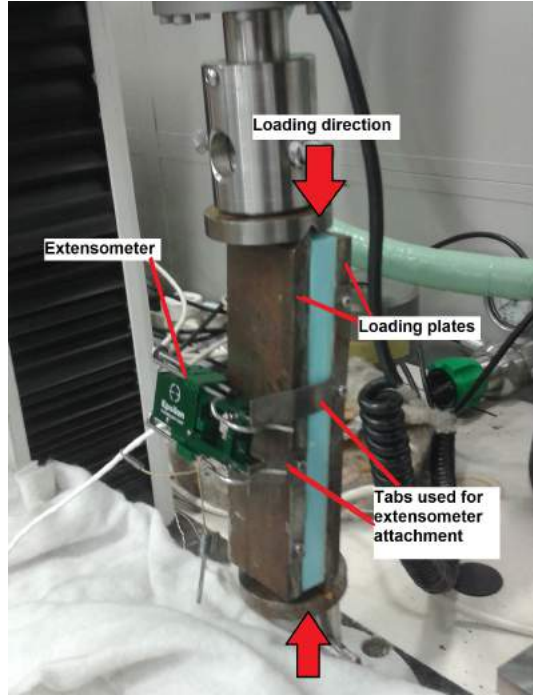


FIGURE 4.17: *Foam specimen loaded in shear, in compression direction.*

Figure 4.18 shows the shear stress over the shear strain curves for six samples. It can be observed from Figure 4.18 that the results show very little variation in slope of the tested samples. Moreover, it can be noted that there is a rise in shear stress when the shear strain reaches 0.32. This phenomenon is caused by the contact point between the cross-head and the loading plates.

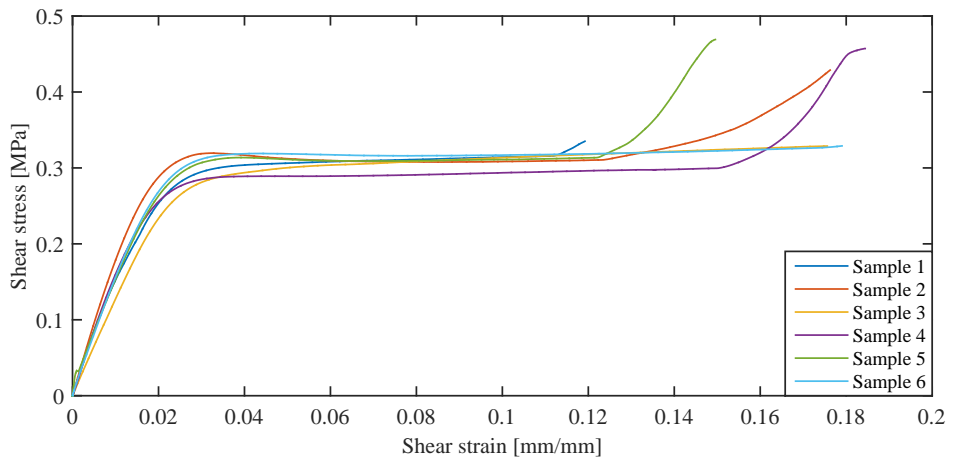


FIGURE 4.18: *Shear stress-shear strain curves from shear foam tests.*

The shear modulus was calculated according to the ASTM standard with Equation 4.12

$$G = \frac{(\frac{\Delta P}{\Delta u})t}{Lb} \quad (4.12)$$

Where G represents the shear modulus, $\frac{\Delta P}{\Delta u}$ is the slope of the force-displacement curve in Nmm^{-1} from 0.002 to 0.006 engineering strain, t is the thickness of the sample, L is the length of the sample and b is the width of the sample. The results for the shear modulus are summarised in Table 4.4.

TABLE 4.4: Shear tests on foam specimen results.

Sample	Shear Modulus [MPa]	Shear Strength [kPa]
1	10.289	335.136
2	11.967	428.825
3	8.397	328.767
4	10.929	457.262
5	9.352	469.106
6	9.911	328.988
Mean	10.141	391.347
Standard deviation	1.241	67.469

FEA Modelling of Foam Structure

Having analysed the results from the material tests, the values were inserted in ABAQUS 6.13 using a *hyperfoam* model, that allows the modelling of elastomeric compressible foams at finite strains. The modelled foam is made up of polyhedral cells that pack in three dimensions as closed cells, as can be seen in Figure 4.19.

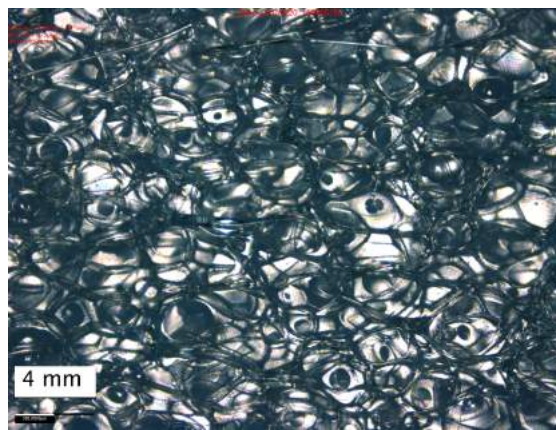


FIGURE 4.19: *Foam micro-mechanical cellular structure of a compression sample prior to the compression-test.*

The foam properties varied in the different principal dimensions. The shape anisotropy is affected by the elongation or the buckle of the cell walls in the different loading conditions. In order to correctly model the anisotropy of the material, the engineering constants have been inserted for the three dimensions in the FEA analysis.

The assembly mesh was then developed. In order to be able to create an adaptive mesh, the foam was modelled with free second-order tetrahedral mesh elements (C3D10). However, the free mesh was constrained at all the edges to be able to control the mesh size, especially close to the intersection between the foam and the PAC beam. In the cut-through region, the number of elements were chosen to match the beam elements, as can be seen in Figure 4.20. This configuration allows a smooth transition of the displacements, stresses and strains between the aerodynamic loadings and the sandwich beam.

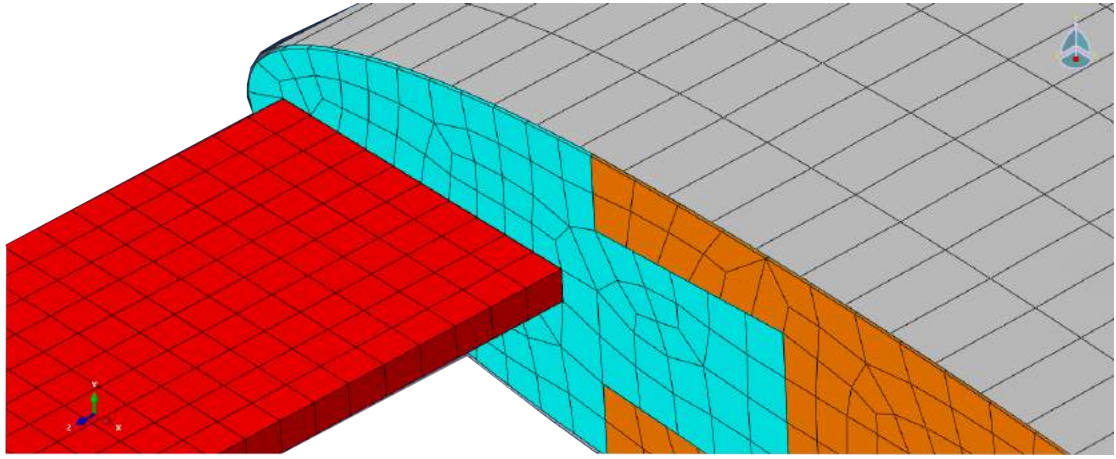


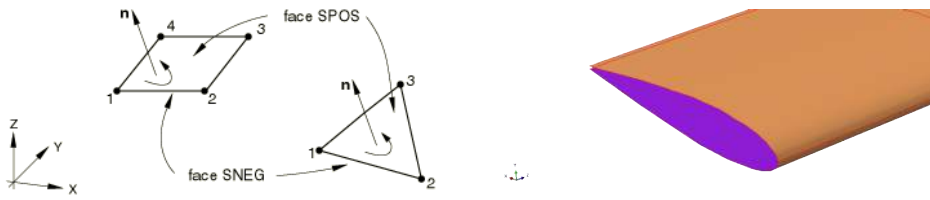
FIGURE 4.20: *Mesh interaction between PAC beam and foam cut-through.*

4.2.3 Mylar Outer-Skin Implementation

Both the beam and the foam parts were modelled as solid sections, the former as a composite solid and the latter as a homogeneous solid. However, the Mylar sheet, needed to complete the wind tunnel model, was modelled as a shell section. Shell elements are used in structures in which the thickness dimension is significantly smaller than the other dimensions. This is the case for a thin Mylar sheet. The thickness of the Mylar sheet is given while defining the section. In ABAQUS the conventional shell elements represent the geometry of the surface. The elements are therefore discretised over the surface and have six degrees of freedom. In order to correctly represent the Mylar sheet, shell elements also allow the representation of surface wrinkles, as recorded in the wind tunnel experiments. As described by Tessler *et al.* (2003) a robust shell model is able to capture the wrinkling in sheet materials. Therefore, a thick second-order element shell is chosen to represent the transverse shear flexibility resulting in a smooth displacement

field. The Mylar sheet is meshed as quadratic shell quadrilateral elements (S8R) with six degrees of freedom.

For all the geometric parts, it was important to define the local orientation. The PAC beam, for instance, was set to have a local orientation with the *z-axis* in the through-thickness direction and the rotation angle about it. For the Mylar sheet shell elements, the positive normal direction needed to be defined, so that pressure loads could be assigned in their positive or negative direction. The *top* surface of a conventional shell element is the surface in the positive normal direction and is referred to as the positive face (SPOS) for contact definition (i.e. shown as brown in Figure 4.21(b)). The *bottom* surface is in the negative direction along the normal and is referred to as the negative face (SNEG) for contact definition (i.e. shown as purple in Figure 4.21(b)). Positive and negative are also used to designate top and bottom surfaces when specifying offsets of the reference surface from the shell's mid-surface (ABAQUS Simulia, 2013). Figure 4.21 presents the positive and negative surfaces as well as the normal shell direction for conventional shell elements (Figure 4.21(a)) and for one surface of the Mylar sheet (Figure 4.21(b)).



(a) Positive and negative surfaces and normal (b) Positive and negative shell faces for the My-
shell direction for conventional shell elements lar sheet surface of the aerofoil
(ABAQUS Simulia, 2013)

FIGURE 4.21: *Shell element directions and definitions for the Mylar sheet.*

The Mylar sheet thickness is defined as being 0.15 mm. The Mylar part is paired in a tie constraint as a slave surface to the trailing edge region. Within the tie-constraint a shell to solid coupling is created allowing both solid and shell elements to be modelled.

Given the large variability in tensile modulus seen in the literature ($\pm 15\%$ changes in modulus as described in Blachut and Stainer (2012); Byrd (2012); Potes (2012); Tessler *et al.* (2003)), it was necessary to experimentally test the Mylar to obtain its properties in order to model it correctly numerically.

The tensile test was carried out according to ASTM D882, testing 10 samples from the same roll of Mylar sheet as used in the wind tunnel.

The gauge length specified in the ASTM standard was 250 mm and the specimens were carefully placed in the jaws at the marked location, as shown in Figure 4.22. In order to increase the jaw grip, four pieces of sand paper were placed in each side of the two jaws facing the Mylar sheet.



(a) Specimen alignment

(b) Marked gauge length

FIGURE 4.22: *Tensile test for Mylar sheet.*

However, once the specimens were stretched, it was possible to see that the gauge length had increased slightly both at the top and at the bottom location, due to the stretching of the film. Therefore, the new gauge length was inspected while analysing the tensile modulus data, as can be seen in Table 4.5. The tensile modulus is measured in the elastic region, excluding the first toe region, which is artificially created by the slack of the jaws. The stress-strain curve for each specimen was repeatable both in the elastic and the plastic region, as can be seen also by the relatively small standard deviation values in Table 4.5.

The values measured during the tests lie within the error in tensile modulus found in the literature and are smaller than the values given by the Mylar manufacturer.

TABLE 4.5: Tensile modulus for Mylar film for a gauge length of 250 mm and for the actual gauge length for each specimen.

Sample	Gauge E [MPa]	Max E [kPa]
1	2110.3	2282.5
2	2000.8	2151
3	2098.9	2260.1
4	1983.1	2117.5
5	2013	2185.3
6	2006.4	2198.4
7	2048.4	2214.3
8	2024.3	2169.7
9	2118.6	2254.8
10	2018	2146
Mean	2042.18	2197.96
Standard deviation	49.41322	54.61396

4.2.4 Final Full Structure

The geometry tested in the wind tunnel was initially produced in SolidWorks and all the connection points were created to assess the validity of the assembly and the possibility of changing the beam during the experiments. In order to correctly reproduce the tested geometry in ABAQUS 6.13 it was necessary to model the contact surfaces appropriately, joining them so that there was no relative motion between them (ABAQUS Simulia, 2013). The 3D model also needed to have a high level of accuracy in order to create a smooth mesh along the different parts of the assembly.

Figure 4.23 presents a view of the complete wind tunnel geometry represented in ABAQUS.

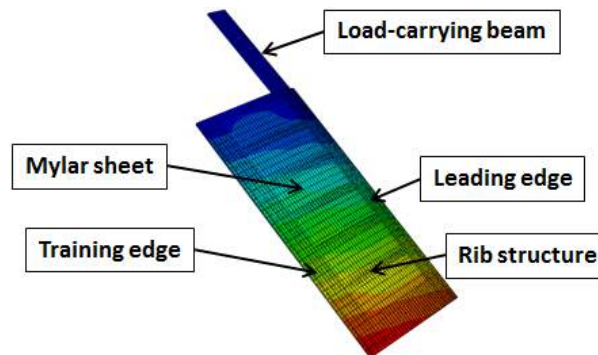


FIGURE 4.23: Aerofoil flexible structure made of PAC beam ($\phi = -30^\circ$), rib-foam part and Mylar sheet.

A summary of the material properties used in the FEA analysis is found in Table 4.6. It has to be noted that all the units have been selected to be consistent units in the SI(mm) system.

TABLE 4.6: Material properties used in the FEA model.

Material	Property	Value
Aluminium	ρ	$2.7 e^{-9}$ tonne mm $^{-3}$
	E	55000 MPa
	ν	0.35
Carbon	ρ	$3 e^{-9}$ tonne mm $^{-3}$
	E_1	117940 MPa
	E_2	7840 MPa
	E_3	7840 MPa
	ν	0.25
	G_{12}	4400 MPa
	G_{13}	3600 MPa
	G_{23}	4400 MPa
	ρ	$3.6 e^{-12}$ tonne mm $^{-3}$
Foam	E_1	10.4 MPa
	E_2	10.4 MPa
	E_3	10.4 MPa
	ν	0.3
	G_{12}	10.14 MPa
	G_{13}	10.14 MPa
	G_{23}	10.14 MPa
Mylar	ρ	$2 e^{-9}$ tonne mm $^{-3}$
	E	2042.18 MPa
	ν	0.38
SA80	ρ	$2.75 e^{-9}$ tonne mm $^{-3}$
	E	2500 MPa
	ν	0

The final mesh for the complete wind tunnel FEA model can be seen in Figure 4.24. The final total number of nodes was 108,597 and the total number of elements was 56,671.

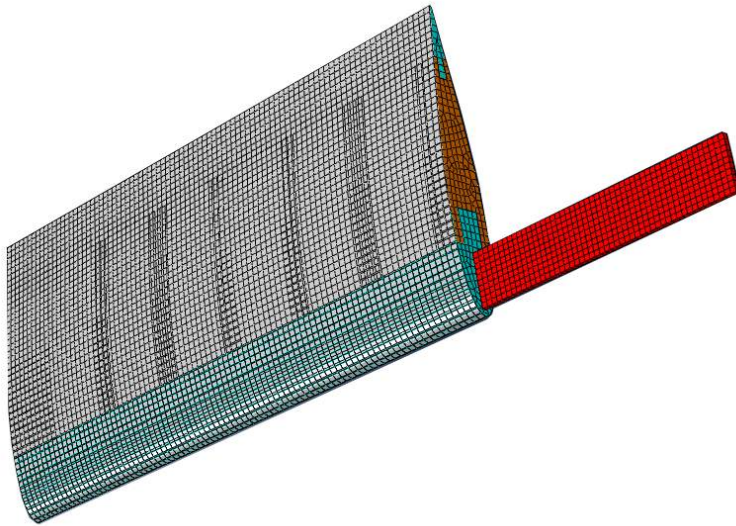
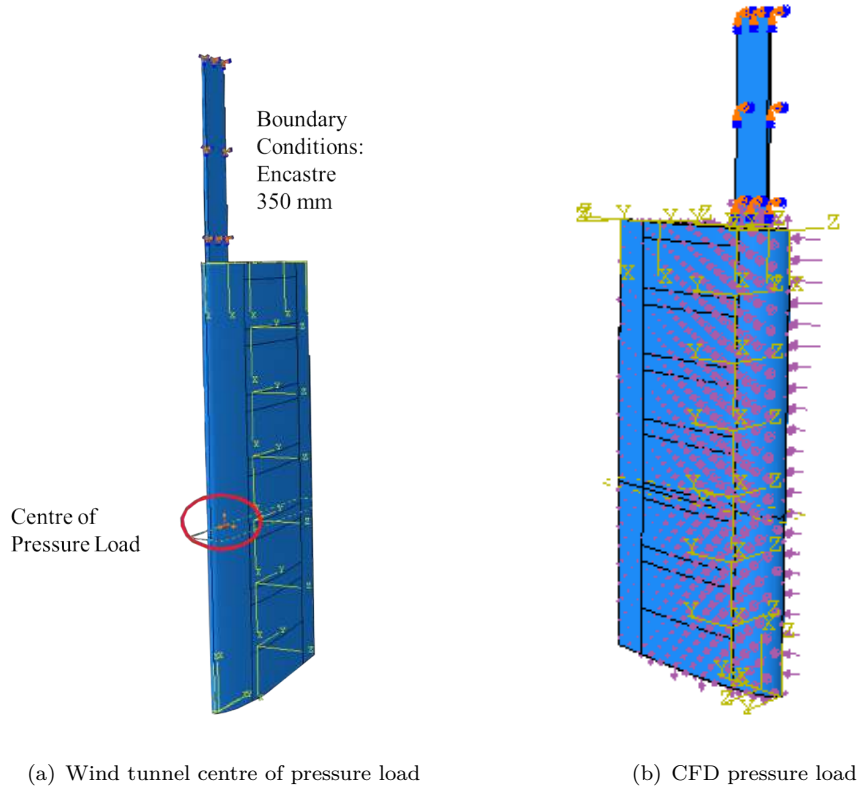


FIGURE 4.24: *Mesh of the whole FEA tested model showing the parts forming the assembly in different colours.*

In order to correctly model the tested conditions, it was necessary to apply the same boundary conditions and loads encountered during the wind tunnel experiments. In the wind tunnel, the PAC beam was fixed for 350 mm from the root. The beam was then exposed in the wind tunnel working section for 50 mm before being inserted into the aerofoil structure for the following 900 mm. The same conditions were replicated in the FEA model, as the beam was constrained with an *encastré* boundary condition, constraining the elements in rotation and translation for all the degrees of freedom, as can be seen in Figure 4.25. The described boundary conditions are applicable, for a dynamic implicit solution (i.e. coupled with the CFD solver), for a static general case and for a frequency analysis.

To assess the validity of the FEA model, the initial analysis of the full FEA model was performed applying the forces obtained in the wind tunnel to the centre of pressure location. Figure 4.25 shows two investigated load-cases, one with a point load applied at the centre of pressure, describing the wind tunnel load in the three dimensions, and one with a pressure load obtained by a CFD-only numerical simulation. The pressure-load magnitude was assessed and validated against the pressure magnitude obtained in the wind tunnel experiments.

FIGURE 4.25: *Boundary conditions and static FEA loads.*

4.3 Coupled Fluid Structure Methodology

In a typical single-field mechanics problem, such as a fluid-only or structure-only problem, the simulation starts with a set of governing differential equations in the domain, and a set of boundary conditions on the domain boundary (de Borst *et al.*, 2013). The situation is more complicated in a FSI problem such as the one encountered in the simulation of the wind tunnel conditions. The sets of differential equations and boundary conditions associated with the fluid and structure domains must be satisfied simultaneously. To simulate the wind tunnel experiments, a Fluid Structure Interaction (FSI) coupling is needed, where ABAQUS solves the structural domain and STAR-CCM+ solves the fluid domain. The two domains are interconnected using the SIMULIA Co-Simulation Engine (CSE). The co-simulation between ABAQUS 6.13 and Star-CCM+ permits the creation of an interaction between the two domains through a common physical interface surface. The interface conditions are the compatibility of the kinematics and tractions at the fluid-structure interface. The structure domain is in motion and its motion follows the material properties of the PAC beam.

4.3.1 Moving Mesh

Modelling the structural part in motion is known as the Lagrangian description of the structural motion. As the structure moves through space, the shape of the fluid sub-domain changes to conform to the motion of the structure. The motion of the fluid mechanics domain needs to be accounted for in the differential equations and boundary conditions. One of the most well-known methods used to capture the interaction between the structures and fluid is the Arbitrary Lagrangian Eulerian method (ALE) developed by Donea *et al.* (1982). ALE allows arbitrary motion of grid/mesh points with respect to their frame of reference by taking the convection of these points into account. In case of an FSI problem, the fluid points at the fluid-solid interface are moved in a Lagrangian way (Star-ccm+, 2015). ALE combines the Langrangian formulation, standard framework for structural dynamics, and the Eulerian formulation, adapted to fluid-dynamics. With the Eulerian formulation, the equation of motion is written in a spatial domain so that the system moves through a fixed grid. In the Lagrangian formulation, the equation of motion is written in a material domain, therefore the motion is tracked by a grid which deforms while the system moves. ALE combines both formulations following the equation of motion in a moving frame. This allows a control of the mesh geometry independently from the material geometry (Sigrist, 2015). In Star-ccm+ an automatic moving mesh scheme is generated to move the model points where the motions of the internal nodes is determined by solving the structural equations of elasticity (Star-ccm+, 2015). The objective, in order to maintain a good mesh geometry, is to stiffen the smaller elements, which are typically placed near the solid surfaces, more than the larger ones. The large elements are indeed located in areas where the solution is not expected to exhibit complex behaviour, therefore they can be altered to adapt to the newly-deformed shape.

On the interface surface the data are mapped from the fluid-solver to the structural solver and vice-versa. In the CSE a shape function interpolation is used. In this configuration, shown in Figure 4.26, the data from the vertices of the blue source mesh are mapped to the faces of the red target mesh using shape function interpolation. The face centroid n lies within the element k . The shape functions of element k are used to interpolate data to the point n .

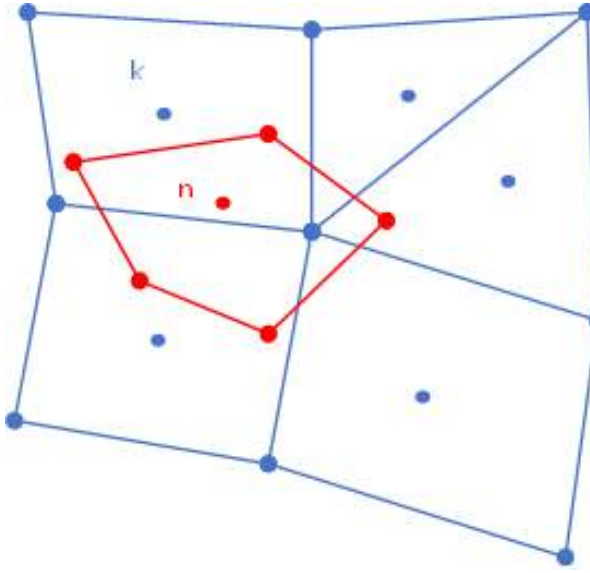


FIGURE 4.26: *Mapping model between finite element mesh to finite volume mesh (Star-ccm+, 2015).*

The general form of the shape function interpolant is:

$$T_n = \sum_{l \in N(k)} T_l N_l(\xi_n, \eta_n, \chi_n) \quad (4.13)$$

where N is the shape function for the specific element type and (ξ_n, η_n, χ_n) are the computational coordinates of the point n in the element k .

For a three-node isoparametric triangle in 3D, the shape function at each node is:

$$N_1(\xi, \eta) = \frac{(1 - \xi)(1 - \eta)}{4} \quad (4.14)$$

$$N_2(\xi, \eta) = \xi \quad (4.15)$$

$$N_3(\xi, \eta) = \eta. \quad (4.16)$$

Fields are mapped between a boundary on the fluid grid and a surface on the structural mesh. A separate mapping is done for each type of exchange field (displacement versus traction) and each direction of mapping (imported versus exported). For fields extrapolated to ABAQUS, the fluid boundary acts as a source, and the surface acts as a target. For fields imported from ABAQUS, the structure surface acts as surface and the fluid boundary acts as a target (Star-ccm+, 2015).

4.3.2 Coupling Algorithm

In order to correctly approach a FSI problem its time discretisation needs to be understood thoroughly. The fluid behaviour depends on the fluid-domain movement, therefore, the larger the domain deformation is, the more different the flow field will be from its un-deflected shape. The structural deformation on the other hand depends strongly from the material properties, therefore, in this case, on the PAC response to load, and on the magnitude of the applied forces, depending on the flow. Therefore, in some cases it is necessary to choose different time-steps for different FSI solutions in order to have equilibrium in both the structure and the fluid (Sieber, 2002; Turnock and Wright, 2000).

Fluid-structure interaction problems can be solved in several ways, and the implications for changing the coupling algorithm depends mostly on the problem itself. At the boundary between fluids and solids, the fluid-structure interface, information for the solution of the problem is shared between the flow and structural solver. The amount of information exchanged is dependent on the coupling method (Benra *et al.*, 2011). One-way coupling is used in problems where the fluid forces have an impact on the structure, but the structure is rigid enough to affect the flow motion only marginally. This method exhibits a very efficient computational time, however it does not guarantee energy conservation at the interface, therefore the stability of the results is affected. Two-way coupling methods are divided between explicit and implicit coupling algorithms, also known as weakly and strongly coupled methods respectively. In two-way interactions the fluid motion and pressure affect the displacement and deformation in the structure, and the response of the structure has a significant effect on the flow field (Star-ccm+, 2015). A schematic view of the two two-way coupling can be seen in Figure 4.27.

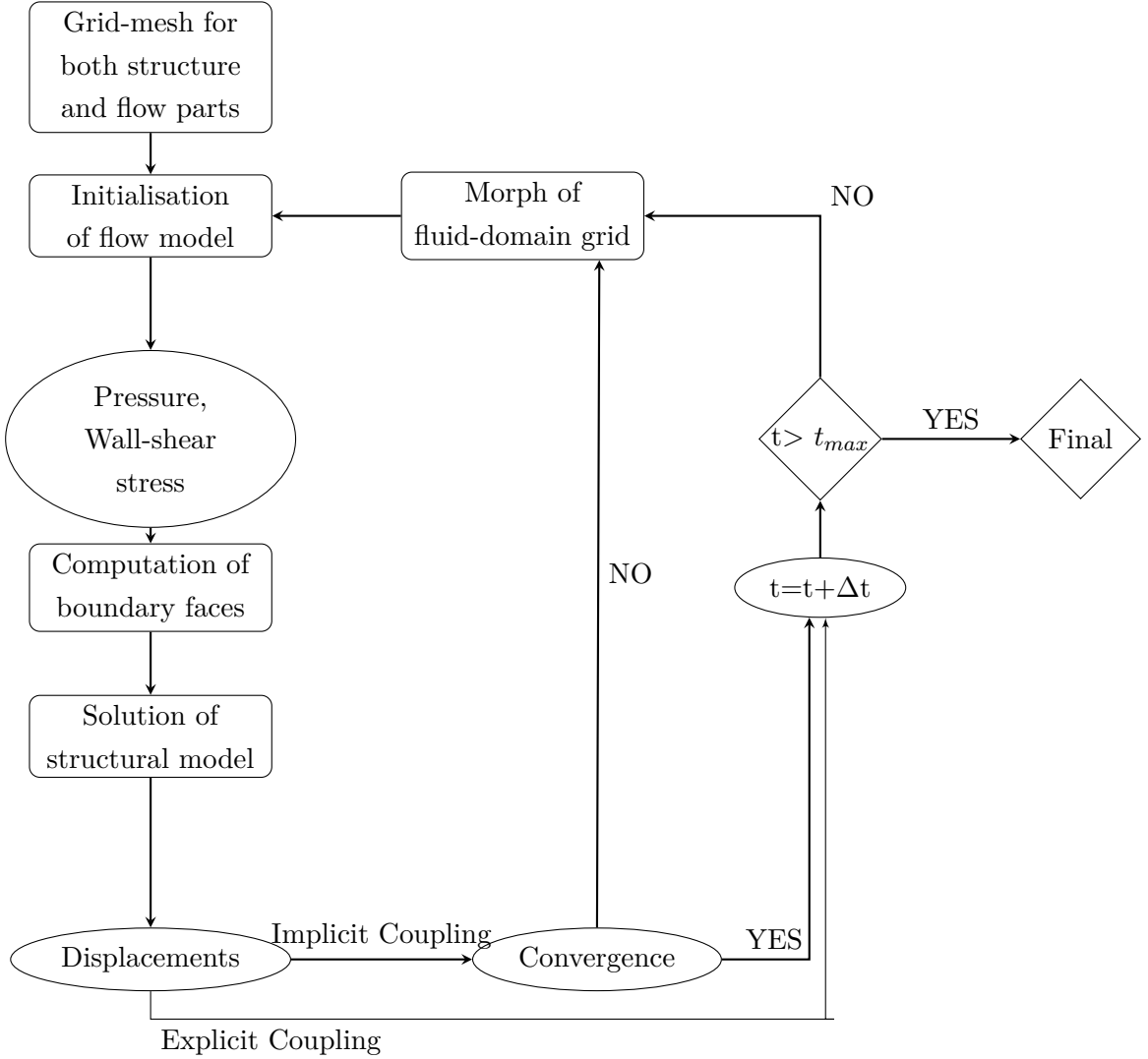


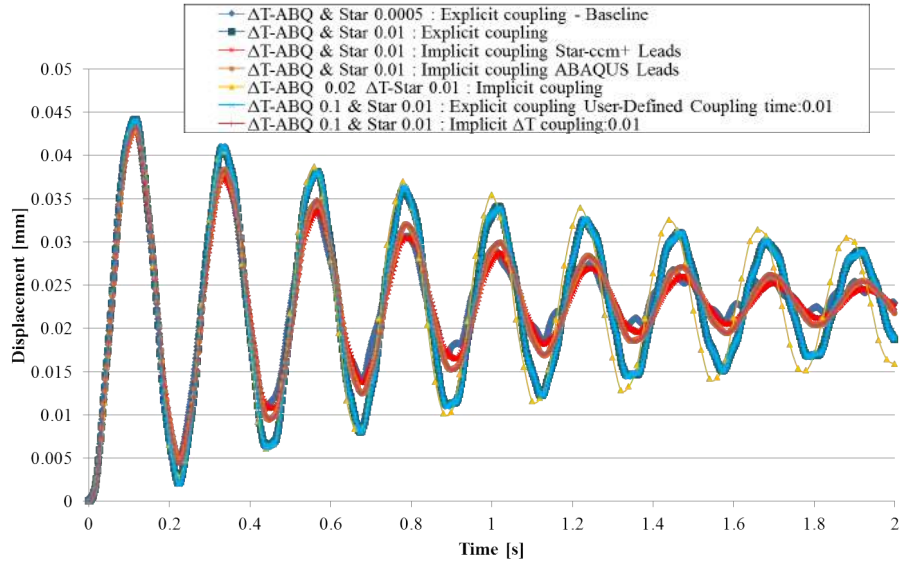
FIGURE 4.27: *Implicit and explicit coupling algorithms for fluid-structure interaction problems*

In the strong coupling method (implicit coupling) within one time-step, a converged solution for the flow field is required to provide the forces acting on the body. After interpolating the forces from the fluid mesh to the surface mesh of the structure, a converged solution of the structural dynamics needs to be achieved under the effects of the acting forces. The response of the structure to the load represents a displacement of the structural grid nodes. The displacements at the boundary between the structure and the fluid are interpolated to the fluid mesh, through the mapping process, which leads to the deformation of the mesh through morphing. This process closes one inner loop of the simulation. All these steps are repeated until the changes in displacements and flow forces fall below a prescribed threshold. Afterwards a new time-step is started (Benra *et al.*, 2011).

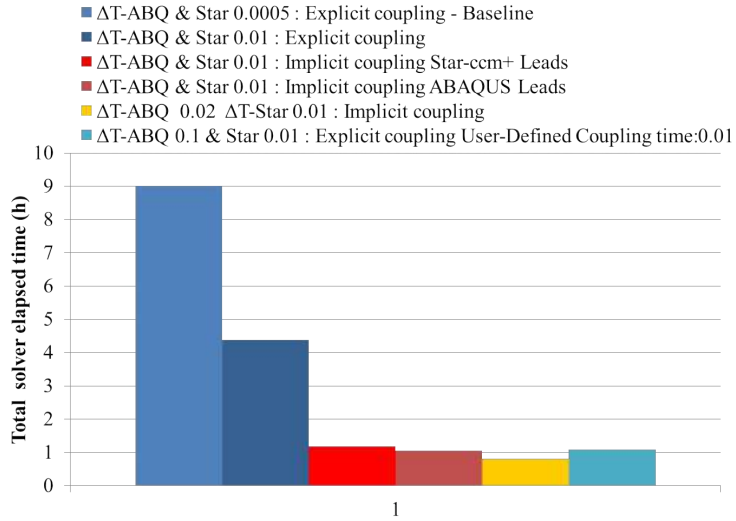
In weak coupling, the convergence at the boundary between the structure and the fluid is not considered, and the new step is launched directly, as can be seen in Figure 4.27. This

approach could lead to more efficient computational time; however, the inertia effects are neglected and the two solvers are not achieving convergence at the same point in time.

It is possible to investigate the differences in response and simulation times rising from the two approaches, as can be seen in Figure 4.28. Those responses are simulated for simple cases of a flexible isotropic plate subject to aerodynamic loading. The simplicity of the problem aids the investigation of the differences arising from the two-coupling methods. Figures 4.28(a) and 4.28(c) show the amplitude and frequency changes using the implicit (strong) or the explicit (weak) coupling methods. It can be observed that the amplitudes of motions are in both cases greater when using an explicit coupling method, unless the time-step size chosen is extremely small. Therefore, in order to have an accurate solution for the explicit coupling method, the time-step needs to be small and the computational cost is increased substantially, when compared to an implicit solution with a larger time-step, Figure 4.28(b).



(a) Displacement change over time



(b) Computational cost

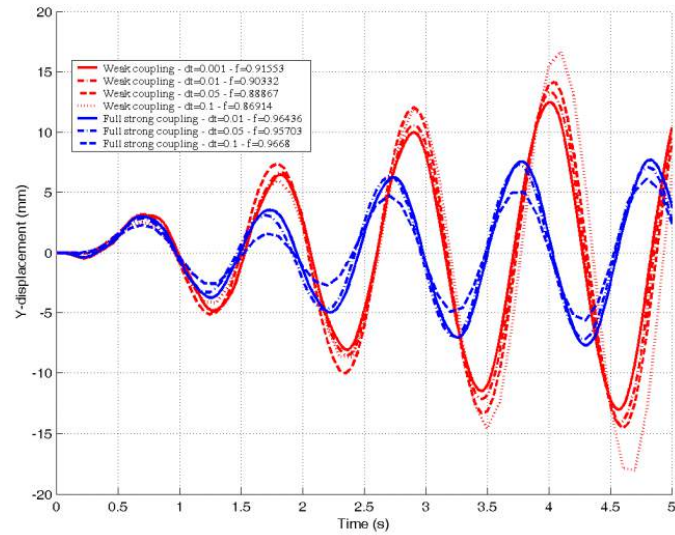
(c) Displacement over time (Vaassen *et al.*, 2010). Blue lines: implicit coupling, red lines: explicit coupling

FIGURE 4.28: Comparison of different FSI coupling methods and time-steps for benchmark cases.

The increase in response amplitude depends on a convergence problem associated with explicit coupling methods because of the explicit treatment of the fluid grid (Sieber, 2002). If a larger time step is used in explicit coupling, the fluid programme predicts the new flow field based on an approximation of the structural position without considering the movement of the structure caused by the fluid forces. However, the structure will change its position due to the fluid actions. Hence, the fluid forces are over-predicted by the flow solver and the energy is not conserved in the fluid grid if large deformations are encountered.

Therefore, the approach chosen to model the FSI coupling between the structure and the aerodynamic loading for the wind-tunnel model is a dynamic implicit solution, as there is a strong physical coupling deriving from the highly flexible specimen. In the implicit iterative approach, the fields are exchanged multiple times per coupling step until an overall equilibrium is achieved prior to advancing to the next coupling step.

In the co-simulation the Mylar sheet surface, as well as the tip of the aerofoil and 50 mm of the PAC beam exposed to the wind, are chosen as interface regions, as can be seen in Figure 4.29. The same surface must be present and defined with the same name in the two solvers. The nodal position and the element topology information define the co-simulation interface and a mapping between dissimilar surface meshes is performed. In this region the displacements are exported into the global coordinate systems from the FEA solver, and the pressures normal to the element surfaces are imported back (ABAQUS Simulia, 2013).

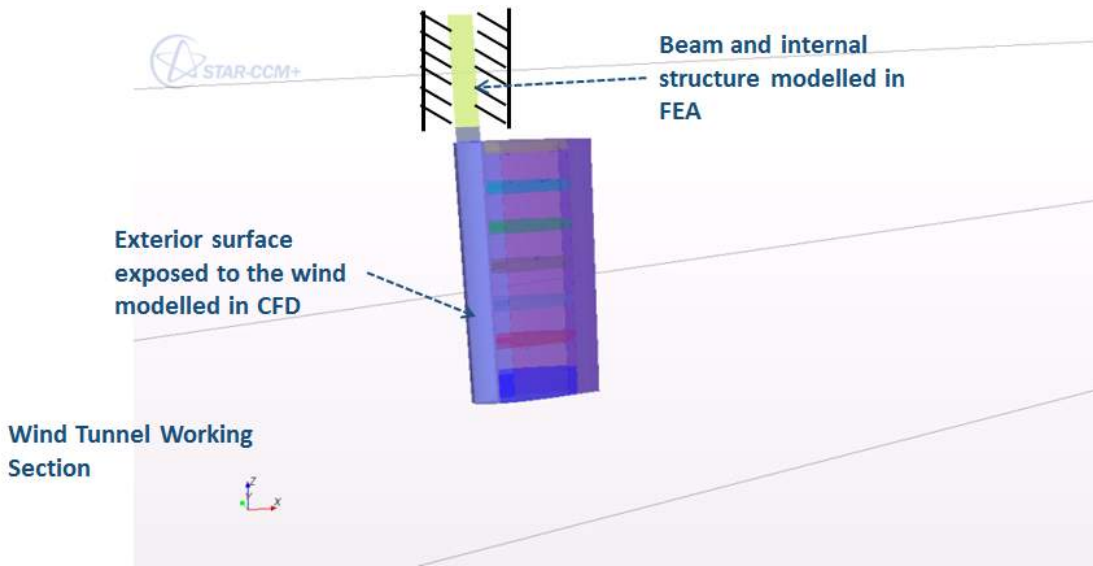


FIGURE 4.29: *FSI model shown in the numerical wind-tunnel domain. The internal structure, as well as the part of the beam fixed above the wind tunnel ceiling, are presented. The blue region represents the interface surface.*

As previously discussed, it is important to correctly define the co-simulation controls both in ABAQUS and in Star-CCM+. These define the sequence of exchanges between the analysis programmes. The iterative coupling scheme allows one analysis to lead (in this case the fluid solver) while the other analysis lags the co-simulation (ABAQUS Simulia, 2013). As seen in Figure 4.27 multiple exchanges per coupling steps are performed until the termination criteria are met. The coupling step sizes need to be specified in the two solvers and define the period between the two consecutive exchanges, and therefore the frequency of exchange between the analyses. The coupling step size is established at the beginning of each coupling step and is used to compute the target time (i.e. the time when the next synchronisation exchange occurs).

Using a constant coupling size allows both analyses to advance while exchanging data at set target points according to:

$$t_{i+1} = t_i + \Delta t_c$$

where Δt_c is a value that defines the coupling step size to be used throughout the coupled simulation, t_{i+1} is the target time and t_i is the time at the start of the coupling step, in this case 0.0025 s set in both solvers.

In ABAQUS the pressure loads are applied to the surface of the solid structure. In Star-CCM+ the displacements are used as an input to the mesh morpher. As discussed in Section 4.3.1 a moving mesh, and therefore the mesh morpher, allows the fluid mesh to deform in response to the imported nodal displacements from ABAQUS.

Finally, in order to correctly exchange the nodal position and pressure loads it is important to set up consistent units throughout both solvers, paying particular attention to the units in ABAQUS, as it does not have a built-in system of units.

4.4 Flow solver set-up

The solution of the fluid is based on the continuity equation and the Navier-Stokes equation. The Navier-Stokes equation is summarised in equation (4.17)

$$\rho \frac{\partial u_i}{\partial t} + \rho \left(\frac{\partial u_i u_j}{\partial x_j} \right) = - \frac{\partial p}{\partial x_i} + \eta \frac{\partial}{\partial x_j} \left(\frac{\partial u_i}{\partial x_j} + \frac{\partial u_j}{\partial x_i} - \frac{2}{3} \frac{\partial u_k}{\partial x_k} \delta_{ij} \right) \quad (4.17)$$

A solution of this equation requires a discretisation in time and space. In order to reduce the computational effort the solution variables are divided into mean (\bar{u}) and fluctuation (u') values, as shown in equation (4.18)

$$u = \bar{u} + u'. \quad (4.18)$$

This division leads to the creation of Unsteady Reynolds Averaged Navier Stokes equation (URANS):

$$\rho \frac{\partial \bar{u}_i}{\partial t} + \rho \left(\frac{\partial \bar{u}_i \bar{u}_j}{\partial x_j} \right) = - \frac{\partial \bar{p}}{\partial x_i} + \eta \frac{\partial}{\partial x_j} \left(\frac{\partial \bar{u}_i}{\partial x_j} + \frac{\partial \bar{u}_j}{\partial x_i} - \frac{2}{3} \frac{\partial \bar{u}_k}{\partial x_k} \delta_{ij} \right) - \rho \left(\frac{\partial}{\partial x_j} \bar{u}'_i \bar{u}'_j \right) \quad (4.19)$$

In this equation $\bar{u}'_i \bar{u}'_j$ is the Reynolds stress tensor. Its value is calculated with the $k - \omega$ SST model. In order to correctly replicate the flow-properties of the wind tunnel, the values for the turbulent models were calculated. The turbulence intensity levels (I) of the wind tunnel with fixed floor are less than 0.2% (Castro, 2001) for speeds between 15 and 38 m/s.

The mesh was generated as a structured mesh with 8 prism layers. The first prism layer thickness was set to $y = 0.00167$ m assuming a turbulent y-plus value $y^+ = 50$ for a base wind speed $V_S = 25$ m/s, following Equations (4.20-4.23).

$$y = \frac{y^+ \mu_{air}}{\rho_{air} u_\tau} \quad (4.20)$$

$$u_\tau = \sqrt{\frac{\tau_\omega}{\rho}} \quad (4.21)$$

$$\tau_\omega = C_F \frac{1}{2} \rho V_S^2 \quad (4.22)$$

$$C_F = [2 \log(R_e) - 0.65]^{-2.3} \quad (4.23)$$

Next, knowing the number of prism layers and assuming a growth rate of 1.4, it was possible to calculate the boundary layer thickness to be $\delta_{gg} = 0.018$ m. Moreover, it was possible to calculate the turbulence scale (i.e. the size of the large energy-containing eddies in a turbulent flow) as $l = 0.4 \delta_{gg} = 0.0072$ m. Therefore, the turbulent viscosity, the turbulent energy, the specific dissipation rate and the eddy viscosity ratio could be calculated respectively following Equations (4.24-4.27)

$$\bar{v} = \sqrt{\frac{3}{2}} (u_\infty l) \quad (4.24)$$

$$k = \frac{3}{2} (u_\infty l)^2 \quad (4.25)$$

$$\omega = \frac{\sqrt{k}}{l} \quad (4.26)$$

$$\frac{\mu_t}{\mu}. \quad (4.27)$$

In this case, the continuity equation and the Navier-Stokes equations are solved using a finite volume approach. Looking at the integral form of the continuity equation (4.28), it is possible to see that it is formed of three terms, the first describing the change in

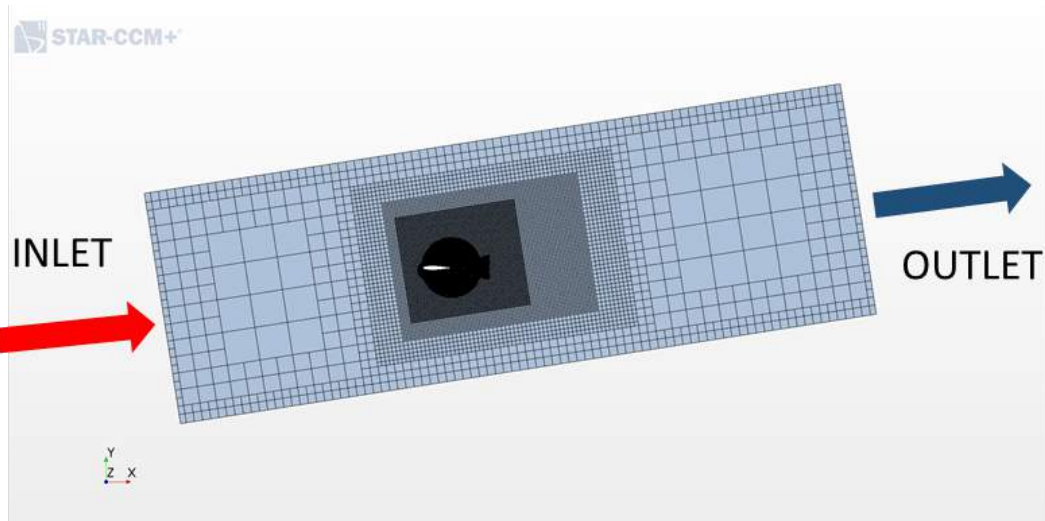
mass in control volume, the second the mass flux through the control volume and the third the change of the control volume through the mesh deformation (morph following ALE motions)

$$\frac{d}{dt} \int_V \rho dV + \int \rho U_j dn_j + \int_S \rho W_j dn_j = 0. \quad (4.28)$$

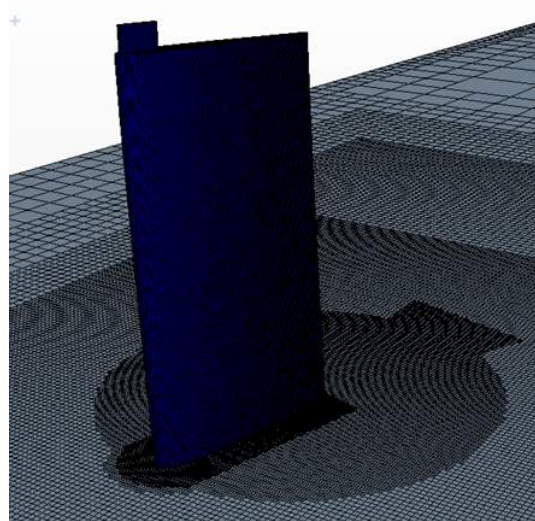
To correctly represent the wind tunnel environment the γRe_θ transition model was used to capture the transition-turbulent boundary layer near the leading edge of the aerofoil (Malan, 2009). It was necessary to use a transition model, as during the wind tunnel test the foil boundary layer was not forced to be turbulent.

The flexible aerofoil geometry is imported in Star-CCM+ and the co-simulation surface is subtracted from the fluid domain. The fluid domain was set as a box-section $10.7 \times 3.5 \times 2.6$ m replicating the wind tunnel dimensions to correctly capture the fluid behaviour. The aerofoil was positioned 4 metres downstream of the inlet, attached to the domain roof and centred in the cross-domain direction, as in the working section during the experiments.

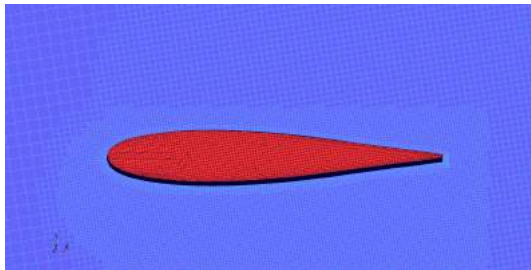
In order to have the interface surface aligned in the two solvers and the inlet-outlet always constant, the aerofoil was kept centred in the domain and the domain boundaries were rotated when different angles of attack were investigated. In order to improve the flow resolution around the aerofoil the mesh was aligned with the flow direction, as can be seen in Figure 4.30(a). Figure 4.30 presents the CFD mesh showing the areas of refinement near the aerofoil and along the wake and the boundary layer mesh.



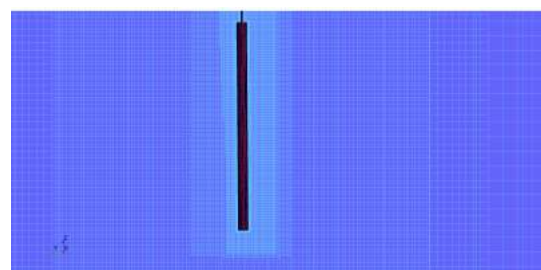
(a) Structured trimmed mesh along the whole CFD domain



(b) Structured trimmed mesh on the specimen-interface surface



(c) CFD grid-mesh of top-plane and aerofoil sections, showing the boundary layer prisms



(d) CFD grid-mesh of front-plane and aerofoil sections, showing the boundary layer prisms along the aerofoil and the beam

FIGURE 4.30: *CFD mesh of the flexible aerofoil.*

The validity of the mesh density and the physical properties of the CFD simulations was investigated looking at the differences in lift and drag force produced by the wing in the

numerical and experimental environments. It was possible to compare the numerical and the experimental values using a deflected shape as a wall in the CFD domain. The deflected shape was imported into Star-CCM+ from ABAQUS as an *.stl* mesh file. Using an accurate deflected shape enables a close comparison of the results from the experiments and the numerical simulations without the necessity of developing the CFD domain in a two-way FSI coupling, which would be computationally expensive. Three different mesh densities were analysed, shown in Figure 4.31. While analysing the CFD results it was possible to see that changing the mesh density in a well-structured mesh (with a good level of refinement near the body and along the wake) did not influence the results. Therefore, the set angle of attack detected by the DIC cameras was investigated, as the major source of error in the experimental method was given by the error in angle of attack (i.e. error of $\pm 1^\circ$). Looking at the shape detected by the DIC cameras (Figure 4.32) it was possible to see that there was an error of approximately 2-5% between the angle of attack set in the wind tunnel and the actual angle of attack of the aerofoil. Figure 4.31 presents the angle of attack at which the wind tunnel was set (i.e. 5.1°), the angle detected by the camera (i.e. 4.98°) and the angle detected by the camera minus 1 degree (due to misalignments of the aerofoil in the cross-flow direction during the experiments).

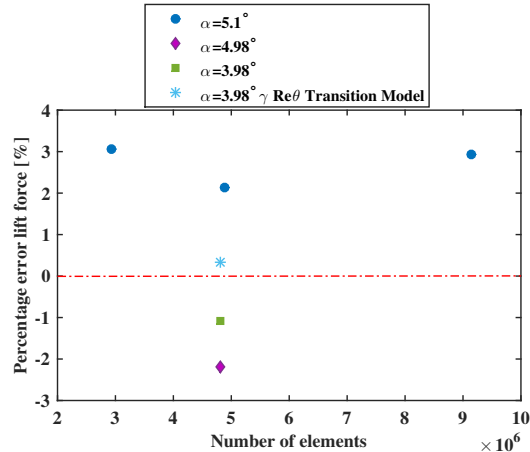


FIGURE 4.31: *Percentage error difference between the numerical and the experimental values at three different mesh densities.*

The error of 0.3% between the simulation and the experimental results achieved with a mesh of approximately 4.8 million cells and the transition model was considered to be representative of a good numerical model to solve the flow field in FSI simulations.

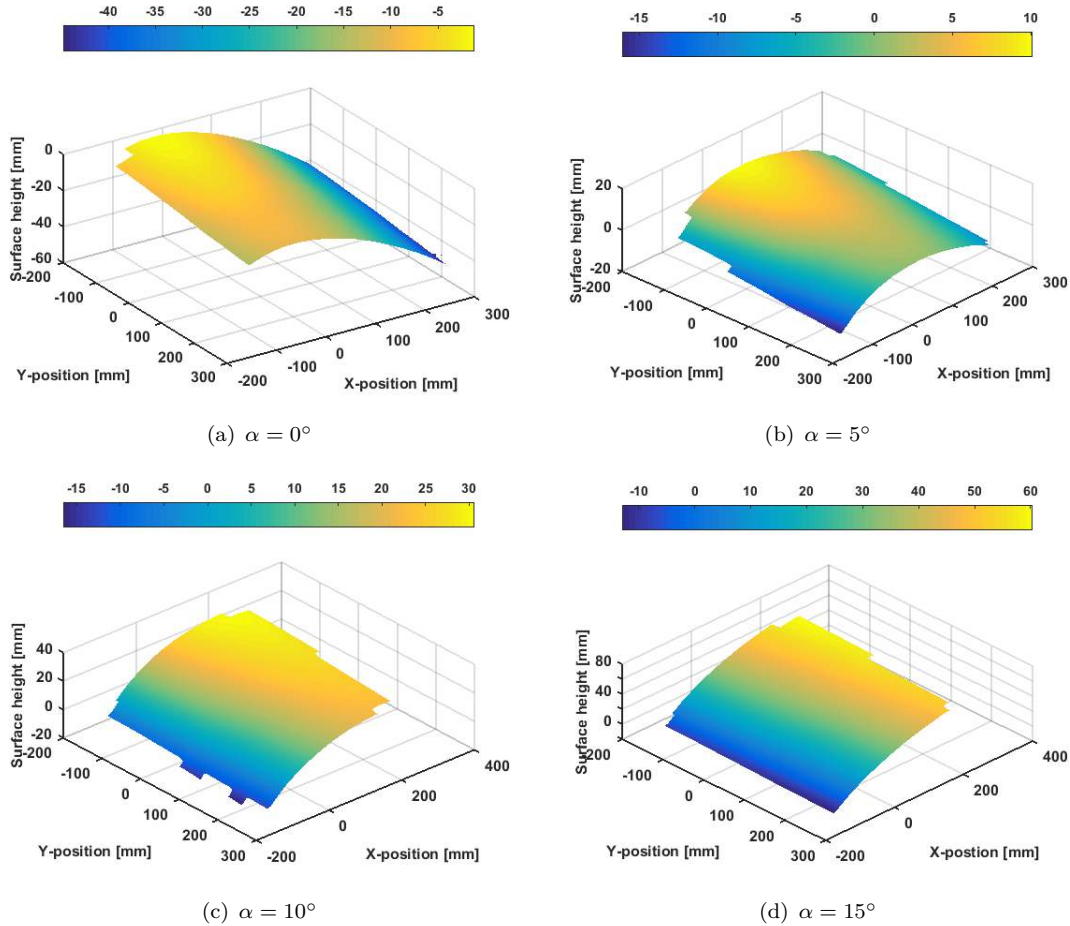


FIGURE 4.32: Change in wing shape with angle of attack detected by DIC cameras.

These simulations were achieved by carefully choosing the boundary conditions for the numerical set-up. The aerofoil is modelled as a wall, where the boundary layer is represented by prism layers. The wind tunnel ceiling is modelled as a wall without a boundary layer to avoid an excessive number of elements. The inlet is simulated as a velocity inlet, where the velocities in the three directions can be set with different angles of attack, the outlet is modelled as a pressure outlet, and the bottom and side walls as symmetry planes.

The CFD settings used are summarised in Table 4.7.

TABLE 4.7: CFD numerical settings within Star-CCM+.

Simulation item	Set-up
Type of mesh	Trimmer Surface remesher Prism layer mesher
No. of elements	4.8 million
y^+ on aerofoil	>50
Boundary layer thickness	0.018 m
Turbulence intensity	0.002
Turbulent viscosity ratio	34
Domain physics	k- ω SST fully turbulent model γRe_θ transition model ABAQUS co-simulation
Solver	Implicit unsteady
Coupling step time	0.0025 s
Morpher solver	Morph from zero
Inlet	Velocity inlet
Outlet	Pressure outlet
Bottom and sides walls	Symmetry plane
Top wall	Wall free stream velocity
Aerofoil + beam	Wall no slip condition

4.5 Summary of the Chapter

In this chapter the numerical set-up was extensively described, from the initial models through the progression of an accurate reproduction of the wind tunnel conditions. Since the research focuses on optimising a lay-up stacking sequence for a PAC specimen, great care was taken to develop a reliable FEA model. The FEA mesh was therefore analysed thoroughly, looking in particular for the best element formulation for composite beam-bending problems. In addition, the material properties of all the aerofoil parts were investigated to allow the FEA solver to correctly capture the deflection under fluid load. The FSI methodology used was explained and compared to the other coupling algorithms available in literature. Finally, the numerical simulations for the flow field were analysed and the accuracy of the numerical method was compared to the accuracy of the experimental settings. It was shown that the major cause of error detected in the experiments was in the setting of the angle of attack of the aerofoil. This led to a careful investigation of the exact position of the aerofoil within the wind tunnel, possible thank to the measured values from the DIC experiments. The approach used in setting up both

the FEA and the CFD simulations systematically ensured that the FSI simulations could achieve a high level of fidelity compared to the experimental measures.

Validating a numerical tool against robust experiments enables to understand the implications of different structures on a FSI response. This allows in further developments to use the numerical set-up to design new geometries for a number of aero-hydroelastic applications.

5

Passive Adaptive Composite Performance

5.1 Introduction

Previous chapters have focused on accurately describing the set-up of both the experimental and the numerical analyses. In this chapter the results from the experimental tests on the NACA0015 aerofoil are presented and discussed, both assessing the influences of synchronising the systems together and investigating the influence of passive adaptivity in the internal structures of the aerofoil.

These experimental results are also compared to the numerical simulations. This procedure ensures an accurate response in the simulations, not only for quasi-isotropic structures, but also for structures with oriented plies. The validation process is necessary in order to use the numerical simulations as new-design tools for structures subject to aero/hydro-dynamic loads.

5.2 Experimental Conventions

Having accurately measured the precision of the DIC system, as described in section 3.3.1, it was possible to set up the DIC high-speed cameras in the viewing room of the wind tunnel. The calibration procedure was carried out by means of the Type-31 calibration plate from LaVision, comparing eight images of the calibration plate positioned at different angles. This procedure reveals the shape of the aerofoil, as the

cameras can map their own position with respect to the specimen for different locations in space. In order to fix the PAC load-carrying beam as a reference plane, the first image of the calibration is always taken when the calibration plate is resting on the beam, as can be seen in Figure 5.1.

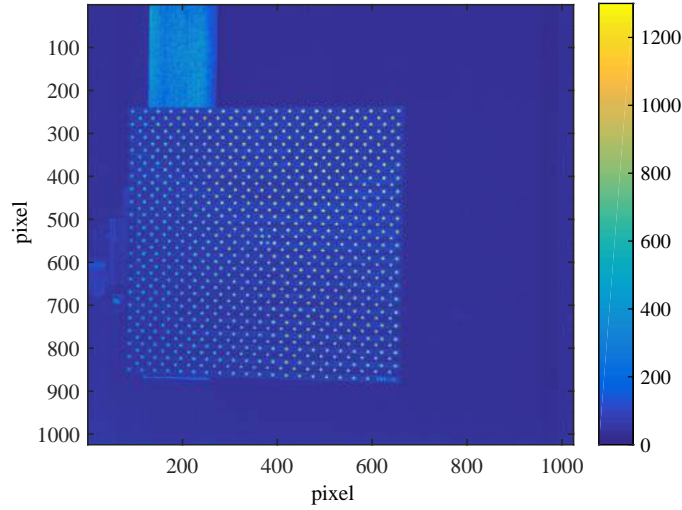


FIGURE 5.1: *Calibration image number 1 viewed from left-hand camera.*

Particular care was taken to ensure that none of the images processed in the calibration procedure presented any saturation point, thus leading to spurious results. Therefore, the standard deviation of fit for all the calibrations was achieved as being as low as ≈ 0.2 pixels. A single calibration was used for each beam configuration, therefore the same calibration was applied to different angles of attack and wind speeds. This leads to a change in analysed shape of the aerofoil when investigating different angles of attack. Figure 5.2 presents two surface plots of the same aerofoil at $\alpha = 0^\circ$ and $\alpha = 15^\circ$.

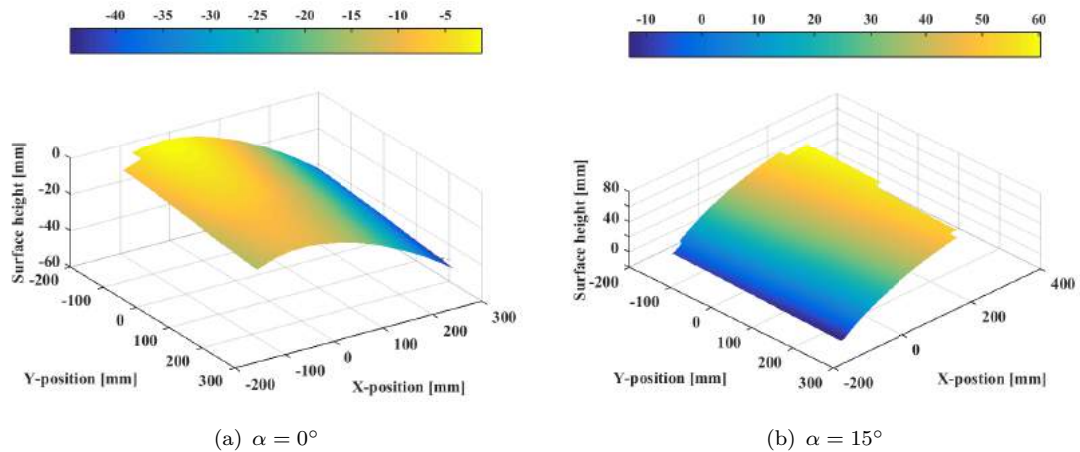


FIGURE 5.2: *Surface height for two different angles of attack as seen from DIC cameras.*

From Figure 5.2 it is possible to see that the trailing edge of the aerofoil, when the angle of attack is increased, moves toward the cameras (i.e. from negative to positive values). The change in shape is well represented, and even at extreme angles of attack it is possible to capture the whole chord of the aerofoil, making possible to analyse the effective changes in angles of attack by investigating the \tan^{-1} of the difference in displacements at the leading and trailing edges.

Figure 5.3 presents two surface plots of the displacement length at $\alpha = 10^\circ$ and $\alpha = 15^\circ$ for $V_S = 25 \text{ ms}^{-1}$. From the figure it is possible to see that the lowest displacements are occurring at the root of the field of view (i.e. 450 mm from the tip, where the span is zero) and at the leading edge (where the chord is $\approx 5 \text{ cm}$), as expected.

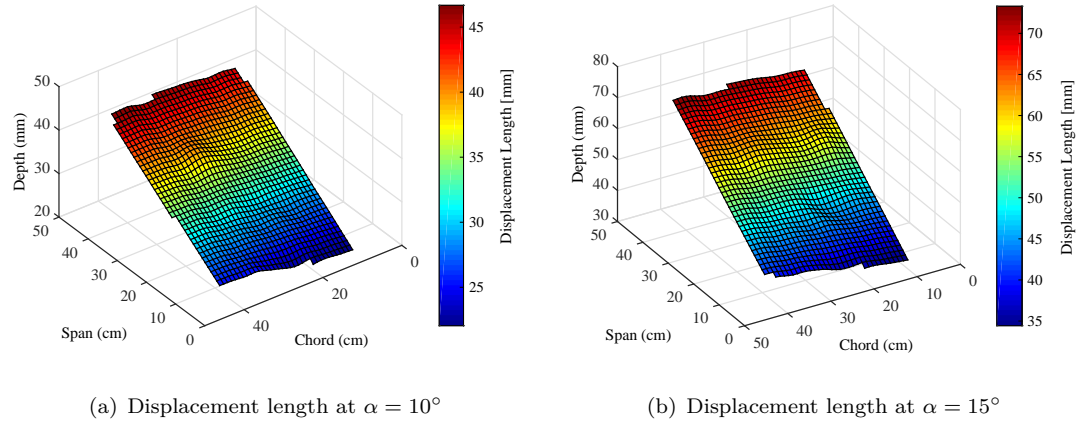


FIGURE 5.3: *Displacement length for two different angles of attack at $V_S = 25 \text{ ms}^{-1}$.*

Figure 5.4 shows the images captured from the two high-speed cameras as well as the mapped image with the displacement, measured at $\alpha = 15^\circ$ and $V_S = 25 \text{ ms}^{-1}$, overlaid. Moreover, the histogram of the two images (i.e. assessing the speckle pattern quality) is shown in Figure 5.4(d). From the images it can be seen clearly how the aerofoil covers a large part of the field of view. The possibility of rotating the aerofoil using only one calibration led to the positioning of the cameras in a location where they were capable of detecting the whole aerofoil in the field of view at all the investigated angles of attack, while still maintaining a stereo angle of 41° to maximise the in-plane and out-of-plane accuracy. The position of camera 2 allows the aerofoil to cover the field of view almost entirely. This is reflected when investigating the histogram (Figure 5.4(d)), as the one from camera two presents lower values of black, indicating fewer background points, and higher values of white range, since the image almost completely represents the speckle pattern.

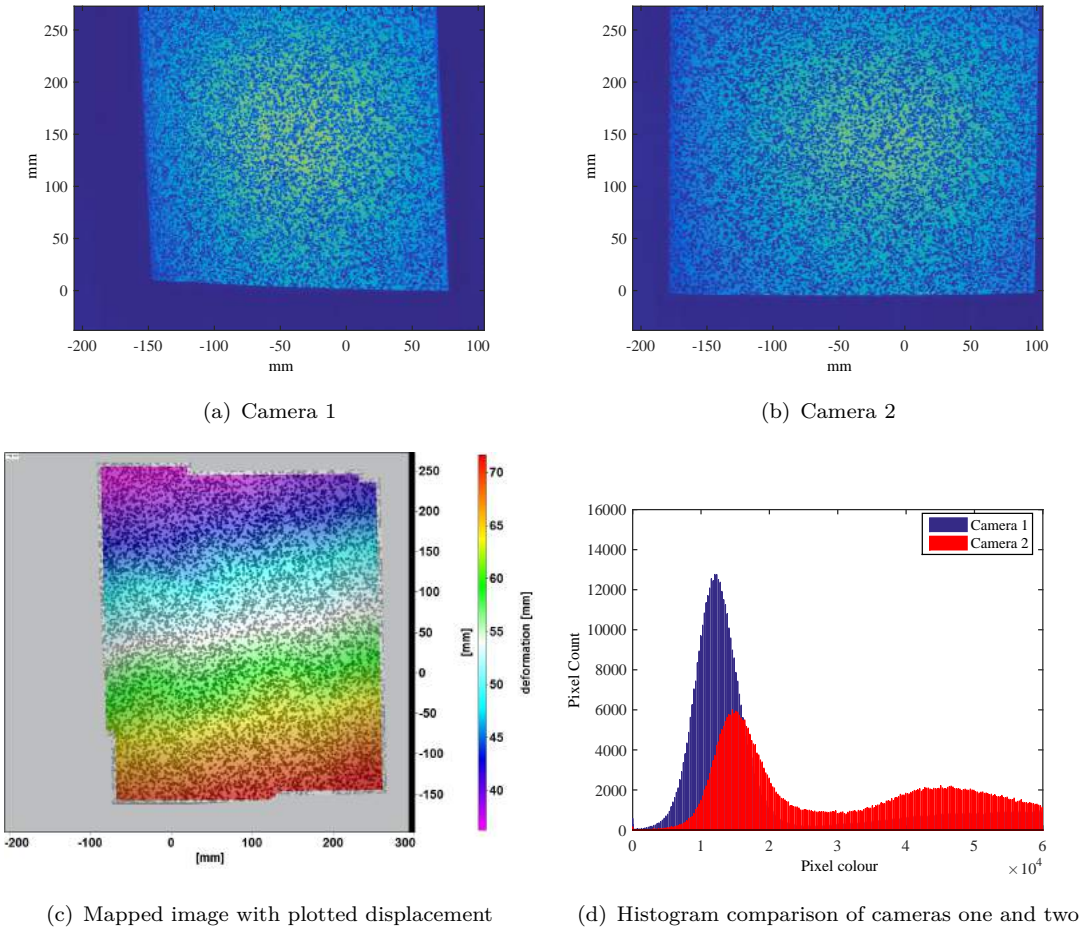


FIGURE 5.4: *Images from the two high-speed DIC cameras, mapped image deriving from the calibration procedure and histogram comparison of the images coming from the two cameras for $\alpha = 15^\circ$ and $V_S = 25 \text{ ms}^{-1}$.*

Figure 5.5 presents the conventions used when analysing the DIC measure results to extract the tip displacement as well as the lines where the twist angle is investigated.

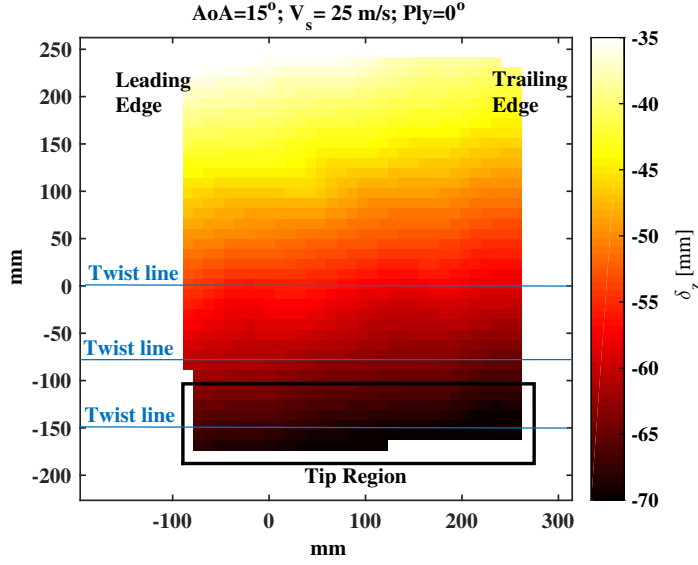


FIGURE 5.5: *DIC tip region and twist line conventions.*

During the wind tunnel experiments, three different sandwich beams were tested: one with no bend-twist coupling (i.e. $\phi = 0^\circ$) and two Passive Adaptive Composite beams, of which one would resist the twist and one would enhance it (i.e. $\phi = -30^\circ$ and $\phi = 2 \times 30^\circ$ respectively). As discussed in Section 4.2.1 the highest level of influence of the passive adaptive plies was found to be at $\phi = 30^\circ$. Therefore, a ply angle of 30° was chosen over other ply angles to assess the influence of large induced-twist values on the aerodynamic response of the aerofoil. Figure 5.6(a) presents the ply angle convention within the wind tunnel. Figure 5.6(b) shows the position of the plies with respect to the aerofoil plan form.

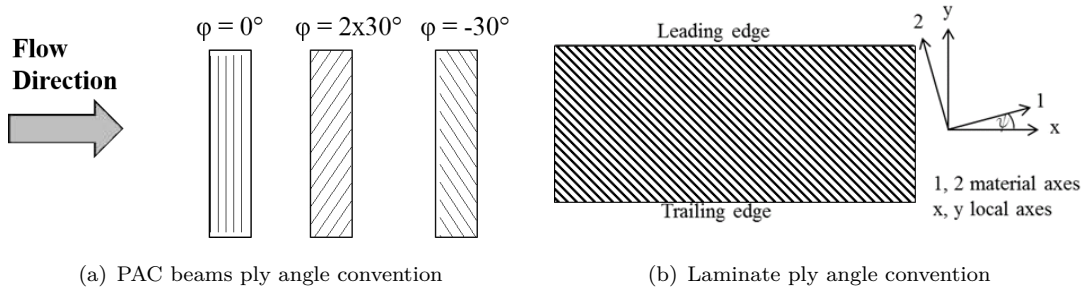


FIGURE 5.6: *Angle conventions for the structural specimens.*

All the presented results for DIC are averaged over a large number of images varying from 100 to 3000, as stated in Section 3.4. The standard deviation of the deflection and twist is presented as error bars in the following graphs.

Having set the parameters used for DIC, structural response the most relevant results are discussed in the following sections, particularly focusing on the results measured

when the PIV was running simultaneously to DIC and when the load-carrying beam was changed.

5.3 Experimental Coupled Systems

Having coupled three different acquisition systems together, it is possible to compare the results for the structural (from DIC), aerodynamic (from forces and moments balance) and fluid (from PIV) responses. In this section the results for the zero ply angle (i.e. $\phi = 0^\circ$) are analysed, comparing the three systems.

Figure 5.7 presents the frequency history of both the DIC tip deflection and the aerodynamic side force responses for $\alpha = 25^\circ$ and $V_S = 25$ m/s. The acquisition frequency of both systems was set to 1 kHz to investigate not only the first mode frequency but also the mechanical frequencies deriving from the dynamometer. The time-history data was passed through a Fast Fourier transform (FFT) which identified a peak frequency of 4.44 Hz. In addition, the higher frequency noise in the side force data shown in the figure is identified as a frequency of 40 Hz, corresponding to the first natural frequency of the Nuntem forces and moments balance, as tested with an impact test. The other peaks can be related to the secondary modes of the structure, as described later in Section 5.5.1.

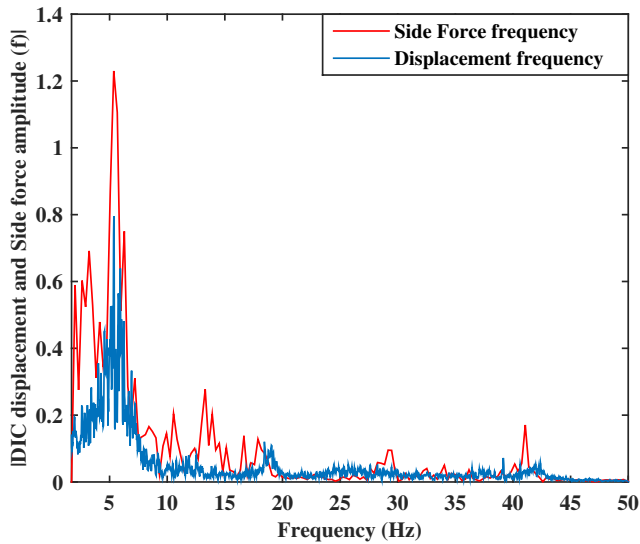


FIGURE 5.7: Frequency response for structural and aerodynamic data.

In order to correctly assess the influence of the coupling between the two non-contact measuring techniques, a steady test case was chosen, due to the lower acquisition frequency of the PIV system. An angle of attack (α) of 15° for a range of wind speeds

($V_S=0, 10, 15, 20, 25$ m/s) was investigated. In this condition the flow is still attached to the foil and stall does not occur, even at the higher wind speeds.

Figure 5.8(a) presents the structural response of the tip of the aerofoil captured in two different data sets, one where only the DIC system was acquiring (with white-light) and one where the two systems were coupled together (with the addition of the magenta filters). The DIC-PIV deflection result is averaged over 3000 images, whereas each DIC-only result is averaged over 130 images. The results show a very good agreement for all the investigated wind speeds, with differences of less than 5% for wind speeds of 10 m/s and less than 2% for wind speeds greater than 10 m/s. The standard deviation for all the runs is less than 0.3 mm, recorded at the highest wind speed. The aerodynamic forces normal to the aerofoil are also presented in the Figure. From the figure it is possible to see how the deflection increases linearly with the force normal to the aerofoil surface.

Figure 5.8(b) presents the relative displacement measured from a base wind speed of 10 m/s for both the tip deflection and the averaged position of the vortex core. The vortex structure and the location of its centre is found by means of the basic VORTFIND algorithm, developed by Pemberton *et al.* (2002). The algorithm is applied to a transverse vector field on a plane perpendicular to the vortex direction, the laser plane. Each vector is assigned to a velocity direction sector of the flow field based on the angle between the vector and the reference axis. The vortex centre is detected as is surrounded by vectors from each direction sectors as the flow rotates about that point. Therefore, ranking all the vectors by their proximity to the different sectors, it is possible to determine their position with respect to the vortex centre. This allows also to describe the tangential and radial velocities away from the vortices.

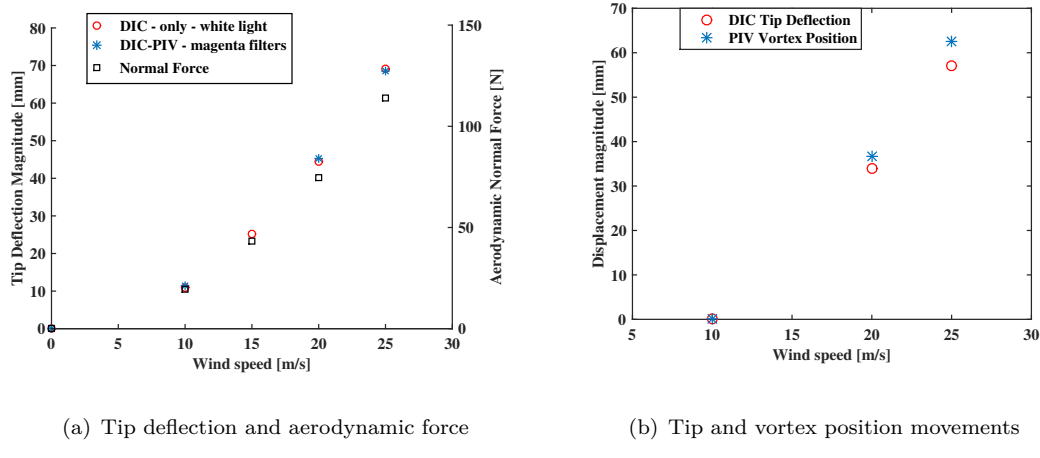


FIGURE 5.8: Comparison of structural tip displacement between one set of DIC-only data and coupled DIC-PIV data and aerodynamic loads for $\alpha = 15$ degrees and a range of wind speeds. Differences between tip displacement and vortex position.

Considering the highest wind speed of 25 m/s, the vortex core is displaced by 62.5 mm. The error associated with this measurement will be a combination of the in-plane PIV

accuracy (2.7%) and error associated with the VORTFIND algorithm which should be no more than the PIV vector spacing (≈ 1.2 mm) (Pashias, 2005). The out-of-plane tip displacement measured by DIC in Figure 5.8 is 58 ± 0.87 mm, where the accuracy is 1.5% as measured by means of the translation stage (as shown in Figure 3.5). From these results it is possible to see the close interaction between tip deflection and developed flow features. It is also apparent that the relative displacements of the tip deflection and the vortex core position do not exactly match, demonstrating the complexity involved in aero-elastic problems, and the need to understand the interactions more fully. For instance, the change in blade twist due to structural deformation, and the changes in vortex formation due to Reynolds number effect, will all affect how the fluid and structure interact.

Figure 5.9 presents the change in angle of attack with increasing wind speed due to a difference in the centre of pressure and shear centre of the structure. The Figure shows the comparison between the averaged results for two sets of DIC measurements (white-light) and the coupled PIV-DIC run (magenta filters). The maximum standard deviation between the two sets of DIC only data was 0.23 mm in tip motion and 0.07° in twist change. This demonstrates the high repeatability of the technique. The angle of attack decreases with increasing aerodynamic loading reaching a maximum twist deformation of 0.6° . The measured twist angles show similar trends at all span-wise locations. This indicates that the aerodynamic centre of pressure is behind the structural shear centre, decreasing the effective angle of attack, and enabling the aerofoil to delay its stall point as the wind speed increases.

It should be noted that the decrease in the foil angle of attack due to structural deformation has the impact of increasing the y displacement of the trailing edge compared to the leading edge. This change in local angle of attack will have the effect of shifting the tip vortex to the right hand side in Figure 5.10 (i.e. increasing the y position). This helps to explain why the average tip deflection is lower than the tip vortex displacement, as seen in Figure 5.8(b).

The comparison of the DIC only and coupled data shows a similar trend to the error assessment with the introduction of the magenta filters. The response of the board is very similar, but the results are shifted, especially in twist. The error comparison between the different runs is less than 20% and the standard deviation of all the measurements is less than 0.02° .

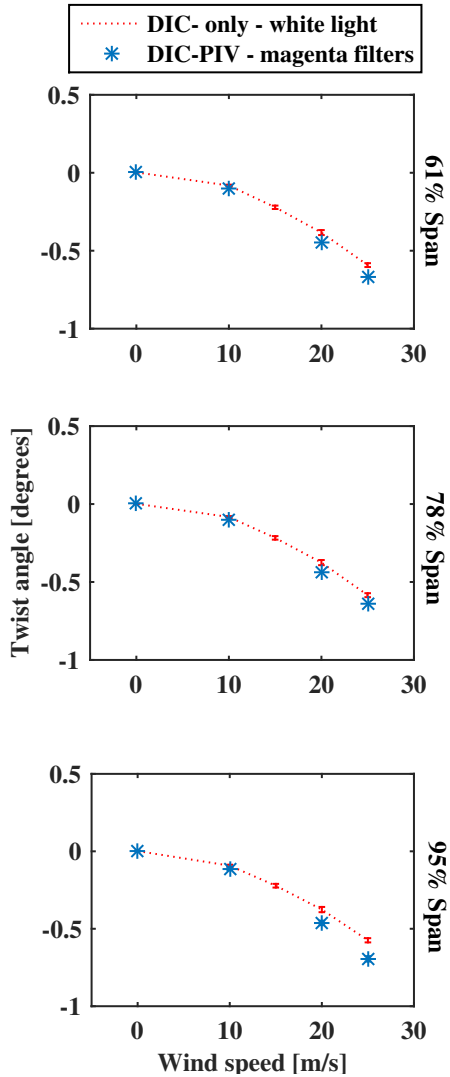


FIGURE 5.9: *Structural response comparison for the change in angle of attack between DIC only data and coupled DIC-PIV data. The Figure shows the change in twist angle for a range of wind speeds at three different locations in the span-wise direction for $\alpha = 15$ degrees.*

The results presented in Figure 5.8 and Figure 5.9 show again the repeatability of the technique and the robustness of the measurement methodology, which is able to capture the structural response under fluid load with very small standard deviations.

Figure 5.10 presents the time-averaged axial velocity distribution relative to the free-stream velocities at different wind speeds. The time-averaged in-plane velocity vectors are displayed, and used to locate the position of the vortex centre, highlighted in white. From the figure, it is possible to see that the vortex core position shifts to the right as the wind speed is increased causing greater structural deformation.

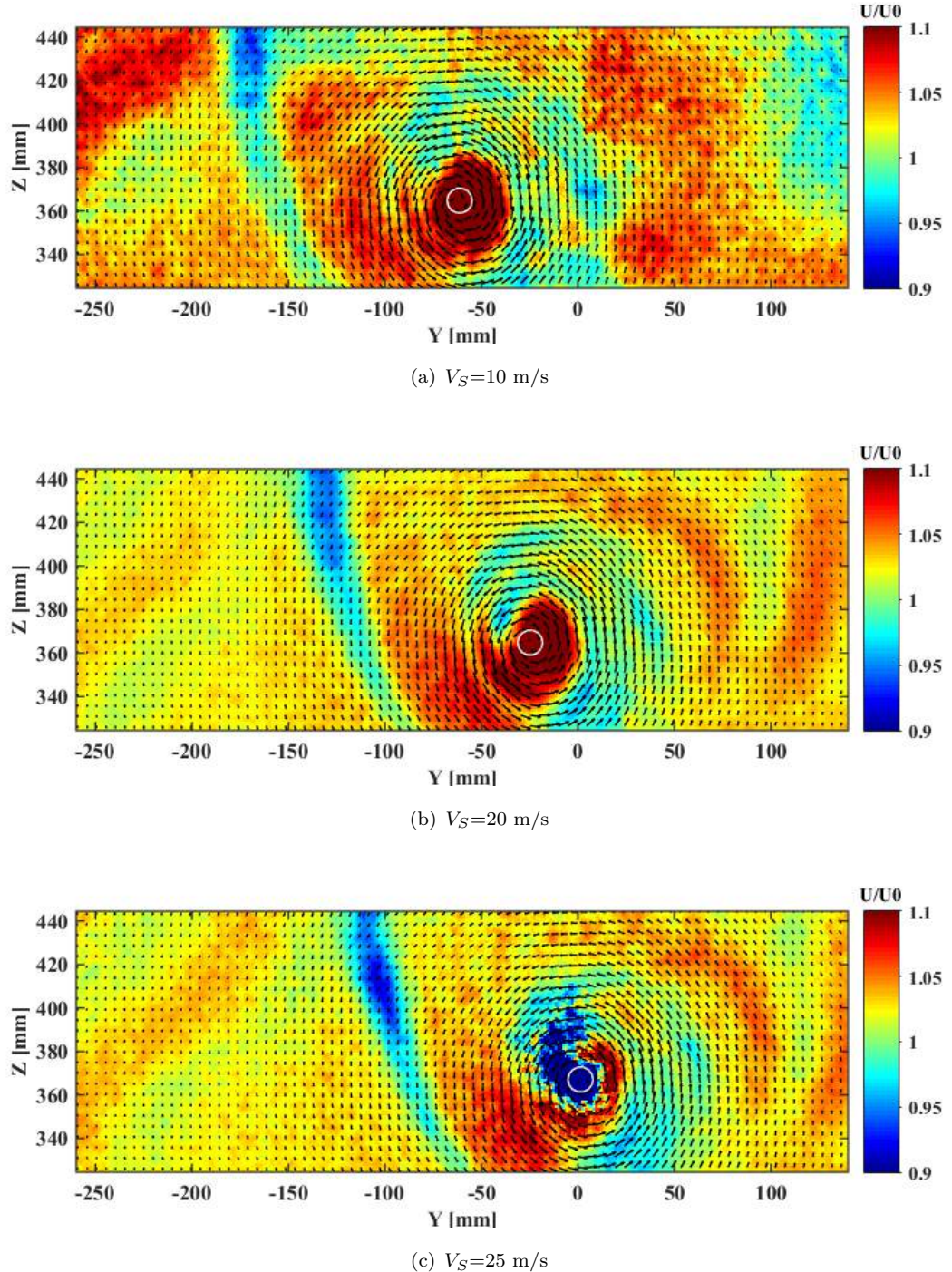


FIGURE 5.10: Time-averaged axial velocity distribution relative to the free stream velocities. The in-plane velocity field is represented as vectors. The vortex centre calculated from the mean velocity field is represented by a white circle.

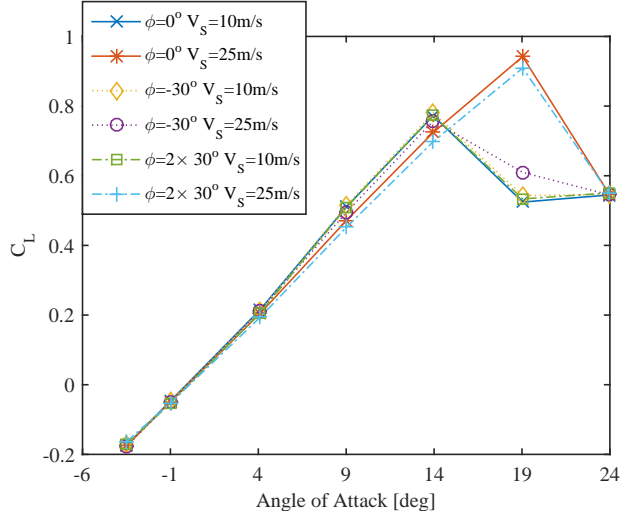
The vortex position and the wake wrap-up are presented on a transverse plane one-chord downstream of the aerofoil trailing edge. Figure 5.10 shows that the vortex core is well formed for $V_S=10 \text{ m/s}$ and $V_S=20 \text{ m/s}$ ($R_e=320000$ and 640000), however, at the higher

flow velocity of $V_S=25$ m/s ($R_e = 800000$) the increased inertial effect moves the wrap-up location further downstream. This increase in Reynolds number with a fixed laser position results in the PIV plane capturing more of the wake features than a fully formed vortex core. It should also be noted that the tested velocity range passes through the critical Reynolds number, resulting in the potential for significant flow regime changes as transition from laminar to turbulent flow occurs. The maximum tangential velocity is found at the same distance from the vortex centre for each wind speed.

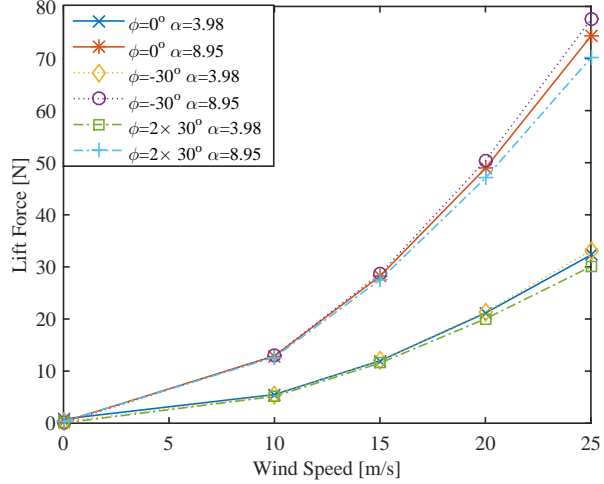
5.4 Ply Angle Investigation

In this section the results from the three different beams are presented, and the effect of changing the ply orientation angle is discussed.

In Figure 5.11 it is possible to see the consequences of changing the ply angle on the aerodynamic forces. The effects of twist angle (shown in Figure 5.13) in the higher wind speed delay the stall point for the quasi-isotropic and the PAC beam twisting toward feather, Figure 5.11(a). It is extremely interesting to assess the lift over velocity plot to understand the non-linear influence of the passive adaptive plies on the aerodynamic response. As can be seen in Figure 5.11(b) the positive ply angle, which twists the aerofoil toward feather, presents the same lift as the other configurations at low speeds, and a decrease in lift at higher wind speeds. The possibility of designing an aerofoil to reach a desired lift force can therefore be assessed.



(a) Lift coefficient over angle of attack



(b) Lift force over wind speed

FIGURE 5.11: Aerodynamic forces acting on the flexible aerofoil for the three different internal structures. Full line: $\phi = 0^\circ$, dotted line: $\phi = -30^\circ$ and dot-dash line: $\phi = 2 \times 30^\circ$.

Figure 5.12 presents the tip displacement comparison between the three investigated beams. The tip deflection values are averaged over two runs for each beam, and each value is averaged over 500-2000 images taken at 0.1 Hz. From the figure it can clearly be seen how increasing the ply angle allows a higher deflection in the aerofoil. Moreover, the $\phi = -30^\circ$ PAC beam presents the highest deflections in general, however, it can be seen that the stall point is not well captured, as it is expected to stall between $\alpha = 13.7^\circ$ and $\alpha = 18.3^\circ$ because, as the PAC resists the twist (twisting toward stall), the stall point is expected to occur earlier. This phenomenon can also be seen in Figure 5.11(a). The highest standard deviation variation is therefore seen at $\alpha = 18.3^\circ$ for $\phi = -30^\circ$ due to the unsteadiness of the aerofoil caused by the early-stall condition.

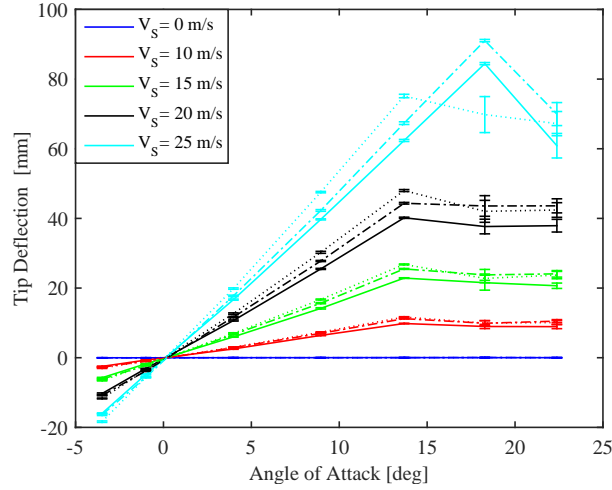


FIGURE 5.12: *Tip displacement comparison for the three PAC beams at a range of wind speeds and angles of attack. Full line: $\phi = 0^\circ$, dotted line: $\phi = -30^\circ$ and dot-dash line: $\phi = 2 \times 30^\circ$.*

From Figure 5.12 it can be observed that the same deflection trend is seen for the three different beams, even though the magnitude of the displacement varies.

Figure 5.13 shows the change in angle of attack for the three beams at different wind speeds and angles of attack, measured at three span-wise locations, 80%, 88% and 97% of the span. The standard deviation is provided in the plot, to show the increase in board motions at higher wind speeds and angles of attack. Looking at Figure 5.13 it is possible to see quite clearly how the PAC beam with $\phi = -30^\circ$ configuration tries to resist the twist.

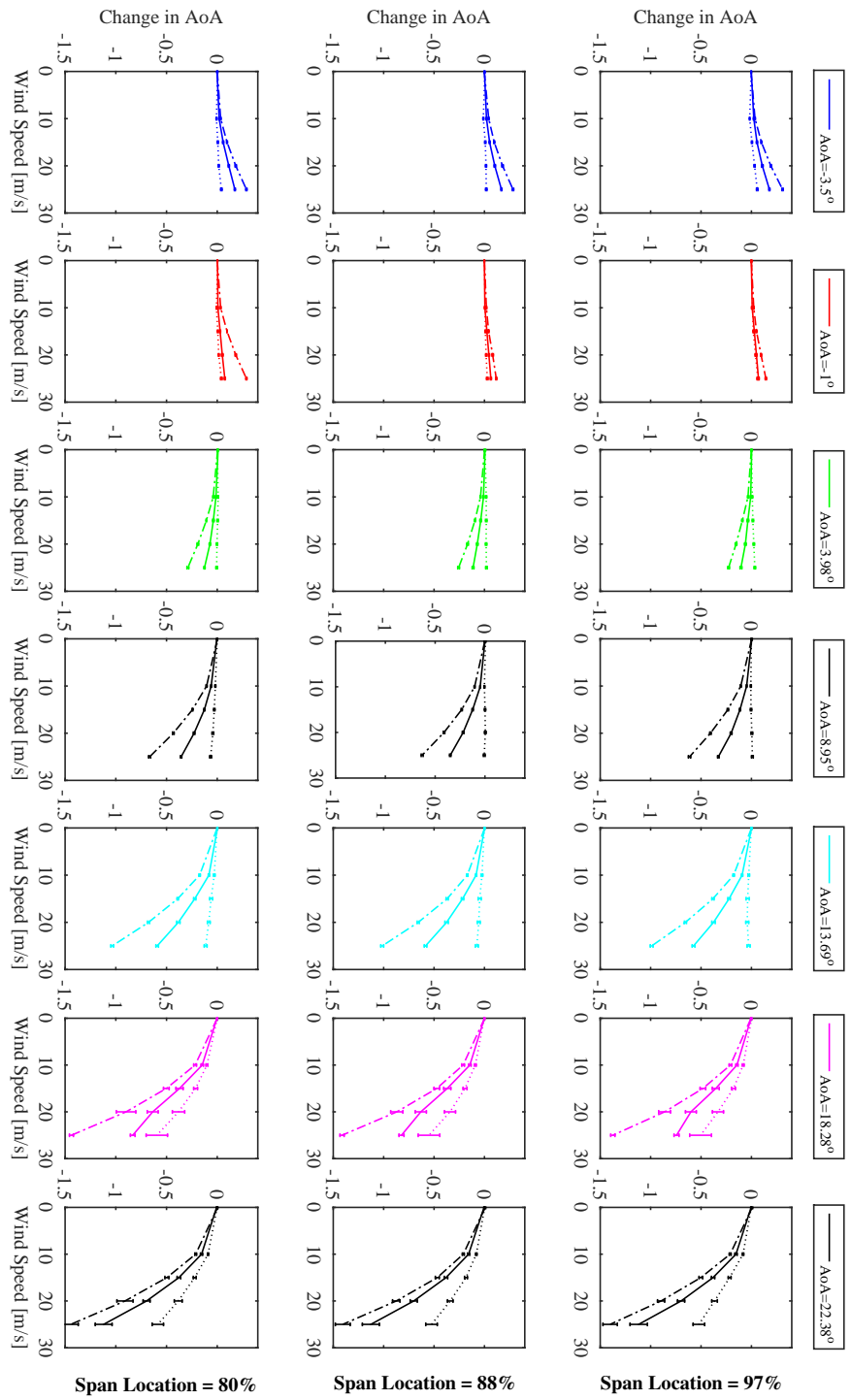


FIGURE 5.13: *Twist angle comparison for the three PAC beams at a range of wind speeds and angles of attack. Full line: $\phi = 0^\circ$, dotted line: $\phi = -30^\circ$ and dot-dash line: $\phi = 2 \times 30^\circ$.*

From the figure, therefore, the PAC behaviour of the beams is represented. The beam with $\phi = 2 \times 30^\circ$ configuration enhances the change in angle of attack toward feather, delaying the stall point. From a design point of view, the maximum twist for a minimum deflection is obtained in the $\phi = 2 \times 30^\circ$ beam, where $\frac{\text{twist}}{\text{deflection}} = 0.6^\circ/\text{mm}$. This configuration not only enhances the change in angle of attack in all the investigated conditions, but also the influence of the composite skins positioned further apart from the neutral axis allows the beam to twist even further. The highest change in angle of attack between the non-PAC beam and the $\phi = 2 \times 30^\circ$ beam occurs at $\alpha = 18.3^\circ$, therefore, the stall point is expected to occur at $\alpha \approx 20^\circ$ if more data points were investigated, further delaying the stall.

In order to compare the response of different structures, it is possible to investigate the non-dimensional displacement and the non-dimensional twist, δ' and θ' respectively. These values, initially presented by Zarruk *et al.* (2014), permit the comparison of different structures, taking into consideration the material properties, the dimensions and the forces applied to the specimens, following equations (5.1-5.2).

$$\delta' = \frac{\delta EI}{F_N a^3} \quad (5.1)$$

$$\theta' = \frac{\theta GJ}{M_Y a} \quad (5.2)$$

In these equations the stiffness E , the second moment of area I , the force normal to the chord line F_N , the distance to the point load a , the shear modulus G , the torsional constant J and the yaw moment M_Y are taken into consideration to allow a comparison between differing structures. The results for the non-dimensional displacement and twist are presented in Figure 6.24.

From Figures 5.14(a) and 5.14(b) it is possible to see that the introduction of the ply angle increases the deflection, as discussed for Figure 5.12. It is interesting to note how the influence of the passive adaptivity is more effective at small angles of attack at the highest speed, as can be seen in Figure 5.14(c). The amount of twist experienced in all the conditions is due to the large design distance between the shear centre and the centre of pressure. In order to design a structure that can tailor its response to a given load it is important therefore to thoroughly understand the influence of both the position of the oriented plies with respect to the neutral axis, and the position of the shear centre compared to the centre of pressure.

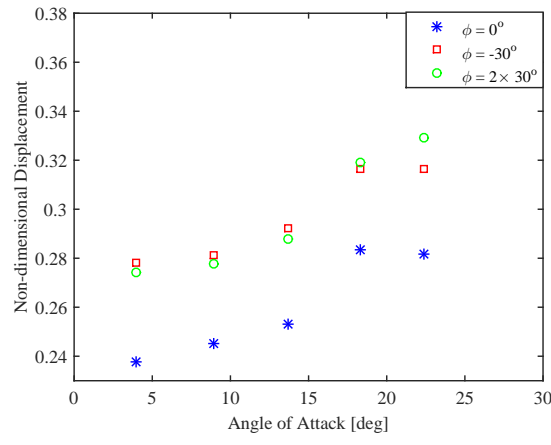
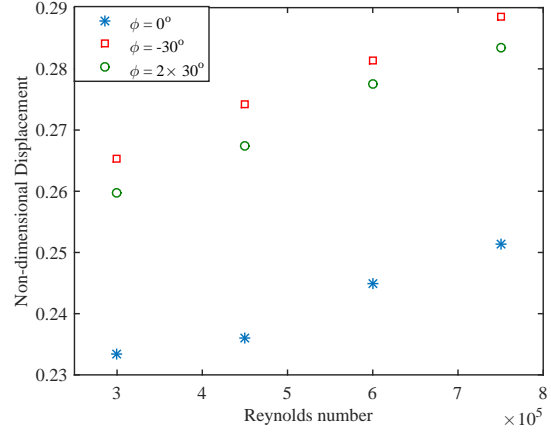
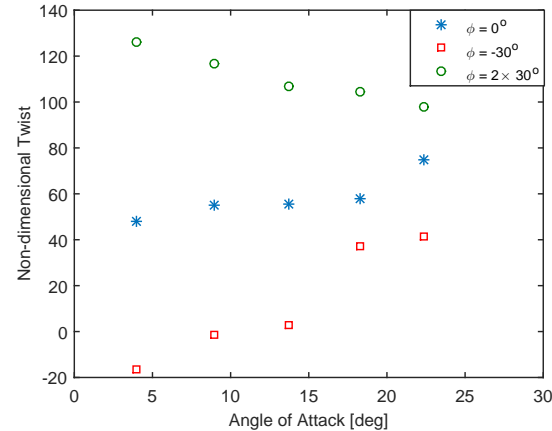
(a) $V_S=20$ m/s(b) $\alpha=10.02^\circ$ (c) $V_S=25$ m/s

FIGURE 5.14: Non-dimensional displacement and twist for the three different internal structures.

5.5 Numerical Results

Having analysed the results from the wind tunnel experiments, it was possible to compare the test measurements with the numerical simulation results. The experimental results are compared to the numerical analysis both for static and dynamic simulations. The initial results presented compare a FEA model with a static load applied at the centre of pressure. The forces applied represent the forces measured in the wind tunnel. The FEA model is also compared to the impact test developed on the aerofoil to assess the modal frequencies discrepancies between the simulated and the real model.

The CFD model was initially validated in Section 4.4. The flow-field data are herein presented to compare the CFD against the PIV measures. The full FSI numerical model is also presented. In this case the time-history response of the numerical model is compared to the measured one.

5.5.1 Finite Element Analysis Results

The complexity of the numerical simulations was improved starting from a static load applied at the centre of pressure location in the three directions. The results from these simulations can be seen in Figure 5.15 and Figure 5.16.

The FEA deflections and twists are compared to the data measured in the wind tunnel, as can be seen in Figure 5.15 and Figure 5.16 respectively. From both figures it is possible to see that the results lie within the standard deviation error of the DIC measurements for steady cases (i.e. when the angle of attack - α - is less than 13.7 degrees). For both deflection and twist, the standard deviation of the DIC measurement in the steady case is extremely small (i.e. <0.5 mm for deflection and $<0.02^\circ$ for twist). In unsteady (stalled) conditions ($\alpha > 13.7^\circ$) the FEA results follow the same trend as the DIC measures, but differ from them since only a static load is applied to the centre of pressure; therefore the unsteady condition is not reproduced in the numerical model.

The deflection curve follows the force measurements, as after stall the lift force produced by the aerofoil drastically decreases and the drag force increases, but the total force magnitude on the aerofoil decreases, leading to a smaller deflection.

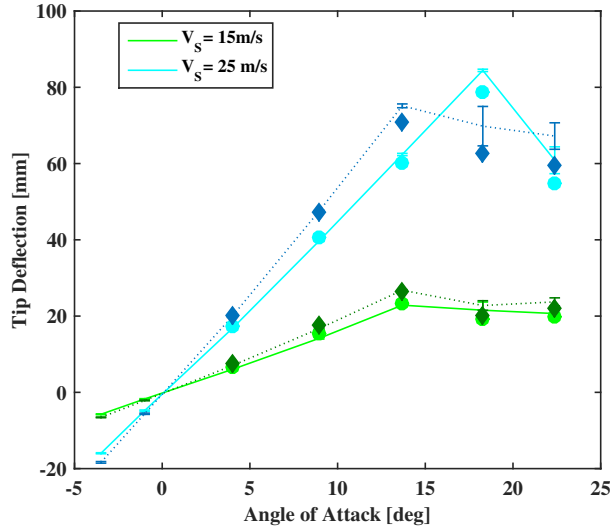


FIGURE 5.15: *Tip deflection magnitude over angle of attack for two different wind speeds. The solid lines represent $\phi = 0^\circ$ and the dotted lines represent $\phi = -30^\circ$ measured in the experiments. The markers represent the FEA results for both $\phi = 0^\circ$ (light-colours) and $\phi = -30^\circ$ (dark colours).*

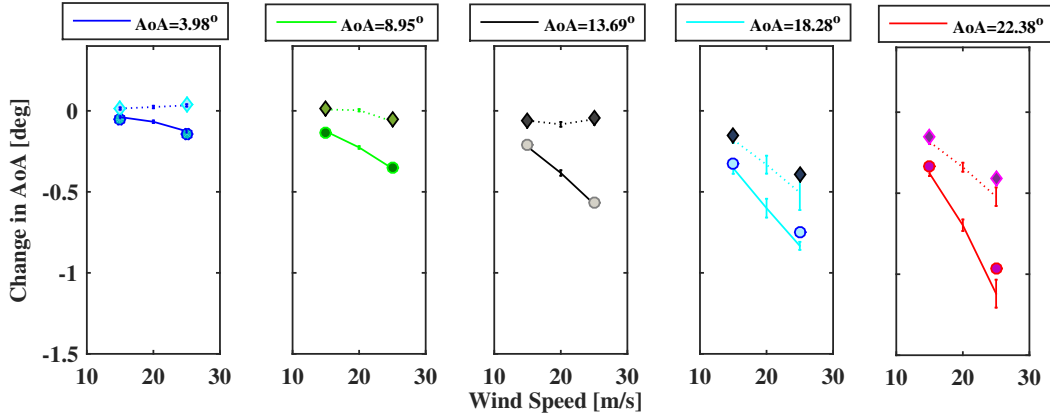


FIGURE 5.16: *Change in angle of attack for different wind speeds and set-angles of attack. The solid lines represent $\phi = 0^\circ$ and the dotted lines represent $\phi = -30^\circ$ measured in the experiments. The markers represent the FEA results for both $\phi = 0^\circ$ and $\phi = -30^\circ$.*

It is important to note how the FEA model is able to accurately predict the structural response when a fibre angle of $\phi = -30^\circ$ is introduced, capturing the higher deflection and the change in angle of attack.

Knowing the material properties of the various components, it was possible to assess the natural frequencies obtained with the numerical simulations, and compare them with the experimental results. The first five natural frequencies can be seen in Figure 5.17. The first mode natural frequency corresponds to $\omega = 4.20 \text{ Hz}$. The first natural frequency from the experimental results is $\omega = 4.44 \text{ Hz}$, as analysed with an impact test on the

wind tunnel, and the limited difference of 5% between the two values can be explained by the small variations of the numerical and the experimental models.

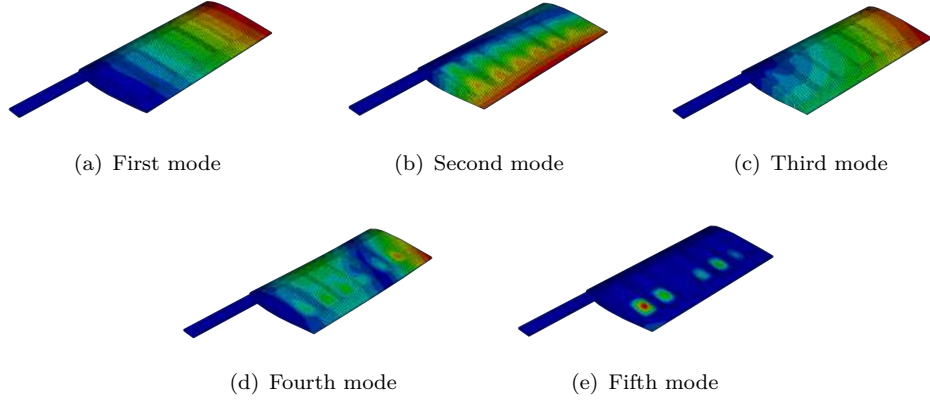


FIGURE 5.17: *First five mode frequencies of the flexible aerofoil. Scale factor 10.*

Table 5.1 presents a summary of the first five mode natural frequencies from the experimental and numerical results. The experimental results are evaluated by means of an impact test on the aerofoil structure and analysing the force response in the y -direction in the frequency domain.

TABLE 5.1: First five mode natural frequencies of the flexible aerofoil in wind tunnel and numerical analyses.

Mode number	Numerical	Experimental
1	4.20 Hz	4.44 Hz
2	15.21 Hz	15 Hz
3	30.03 Hz	24.99 Hz
4	34.18 Hz	35 Hz
5	41.74 Hz	45 Hz

From Table 5.1 it can be seen that the FEA model values agree particularly well with the experimental values, especially looking at the first two modes. Being able to inspect the aerofoil natural frequency is extremely important in the design process in order to be able to minimise the effects of divergence and flutter, i.e. the bending and twisting modes of fixed wings respectively.

5.5.2 Computational Fluid Dynamics Results

In order to compare the CFD results with the experimental aerodynamic data, not only the forces and moments were taken into consideration, as previously presented in Section 4.4, but also the PIV flow field was compared to the numerical simulations.

In the CFD domain it was possible to extract the data at a plane section one-chord downstream of the aerofoil trailing edge, where the laser sheet was positioned during the experiments. Figure 5.18 presents the contour plot of the axial velocity distribution relative to the free-stream velocity. The in-plane vectors are shown and are used to locate the position of the vortex centre. The differences in vector density and spacing that can be seen in the figure, especially away from the wake wrap-up and the vortex position, are due to the mesh density. The mesh in the CFD domain presents areas of refinements near the vortex region and in the wake area. Comparing Figure 5.18 with 5.10(c) it is possible to see that the vortex in the numerical environment is well captured and represented. The axial velocity relative to the free-stream velocity is slightly smaller in the numerical environment. This can be attributed mainly to the use of integer values for the free-stream velocities in the PIV measures, instead of the averaged free-stream velocity values over time.

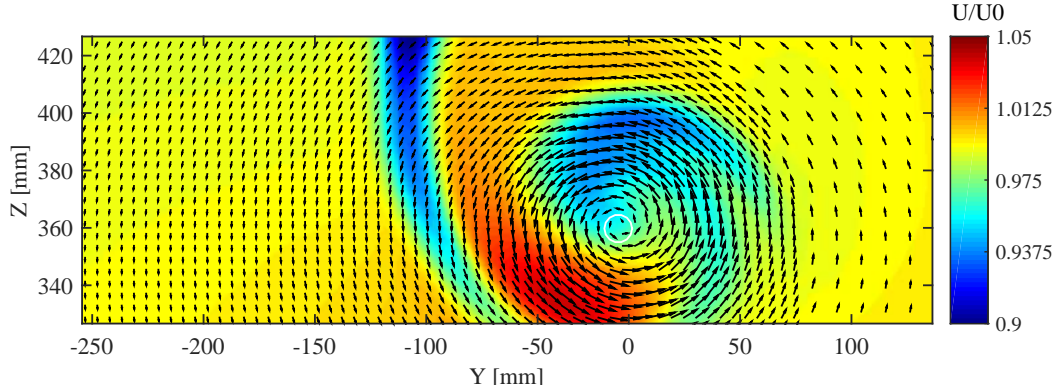


FIGURE 5.18: *Axial velocity distribution relative to the free stream velocity of 25 m/s in wind tunnel axis system. The in-plane velocity field is represented as vectors. The vortex centre detected by the VORTFIND algorithm is represented by a white circle.*

Having assessed the differences between the numerical and experimental flow-data in a quasi-qualitative fashion, it was possible to compare the tangential velocity and its decay away from the vortex centre (Figure 5.19). From the figure it is possible to see how both the maximum tangential velocity peak and its position are well represented by the CFD simulations. In order to represent entirely the flow-features that can be detected by the high-resolution PIV, the grid spacing in the CFD domain should match the PIV spatial resolution, leading to an extremely large mesh, not reproducible for FSI simulation. The level of refinement and the accuracy achieved with the chosen mesh and settings of the CFD domain ensured that it was possible to correctly represent both the position of the vortex centre, the wake wrap-up and the strength of the tip vortex.

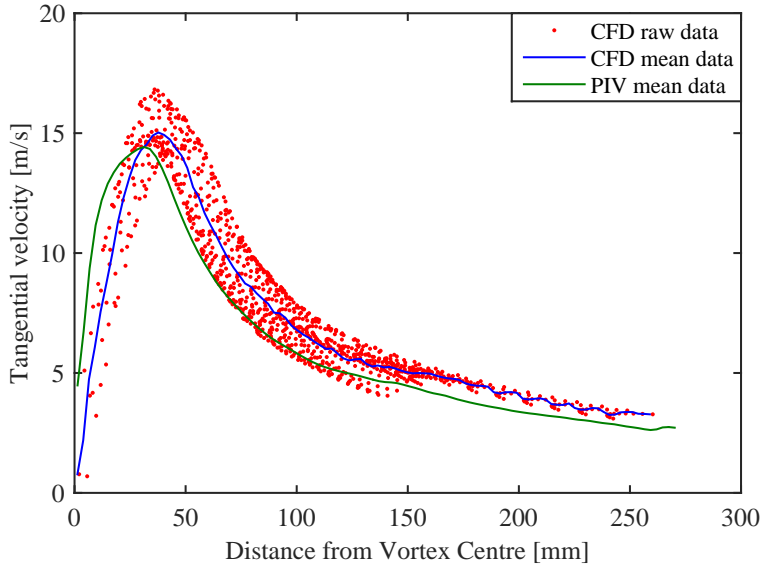


FIGURE 5.19: *Tangential velocity for CFD numerical model and PIV measures for $\alpha = 15^\circ$ and $V_S = 25 \text{ m/s}$.*

5.5.3 Fluid Structure Interaction Results

Having assessed the validity of the FEA and CFD numerical models, it was possible to couple them in order to assess the response of the aerofoil over time. As described in Section 4.3.2, both simulations are set as dynamic implicit, as the highly flexible model needs to be represented by a strongly coupled simulation in order to capture the small changes in deflections over time. In a time-accurate response, the pressure and shear are exported from the CFD to the FEA analysis and the displacement and deformation are imported to the CFD from the FEA. A common physical interface surface is established in the two software: the aerofoil external shape plus the 50 mm of beam exposed to the wind. In this surface the pressures and shears are read in the CFD domain at the mesh-cell centre and the deflections are read in the FEA domain at the mesh-nodes. Therefore, a mapping between the two meshes is developed within the CSE (Co-Simulation Engine) to correctly apply the loads to the structure and the deformation in the fluid domain.

The cases presented correspond to a wind speed $V_S = 14.95 \text{ m/s}$ and angle of attack $\alpha = 9.97^\circ$. Two internal spars are investigated, namely $\phi = 0^\circ$ and $\phi = -30^\circ$. Figure 5.20 presents the FSI results for the side force and the deflections for both the numerical and experimental data. It has to be noted that the CFD domain is initiated to develop the flow around the aerofoil with the fixed geometry. Moreover, the aerofoil is released and becomes free to move, leading to an initial overshoot in the deflection response. The experimental data recording always began when the flow, and consequently the aerofoil, reached a steady condition. Therefore the results are compared for $t > 2.3 \text{ s}$, when the numerical simulations approach a steady condition. Both the side forces and the

deflections show a good agreement between the experiments and the numerical simulations. The numerical simulations present a deflection and a side-force 3.5% smaller than the experimental value for $\phi = 0^\circ$ and 4.6% smaller than the experimental value for $\phi = -30^\circ$.

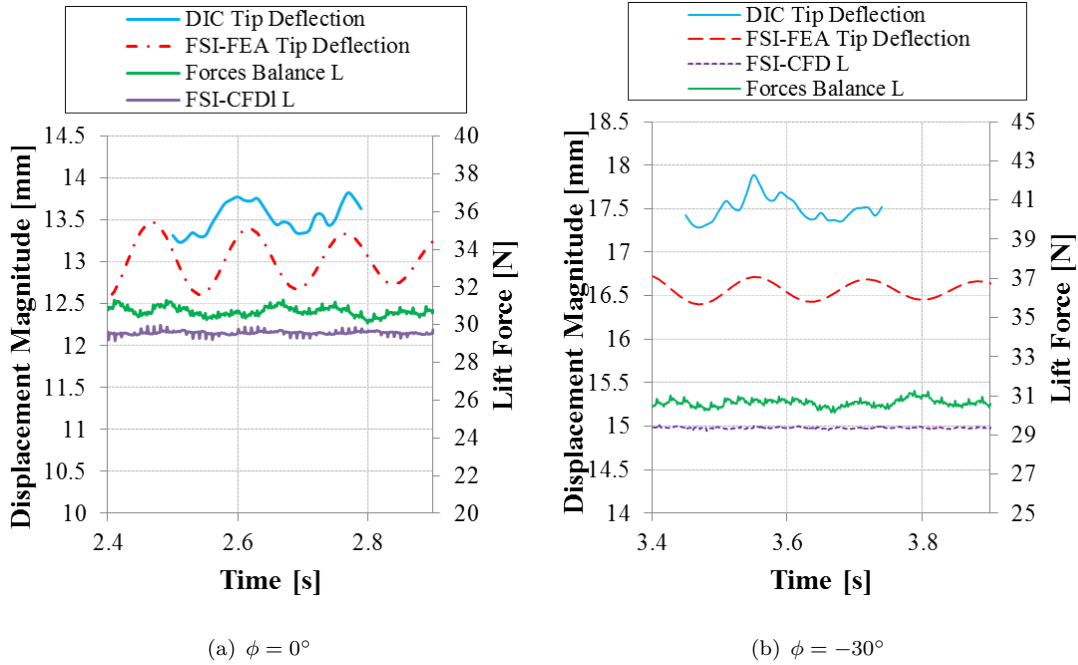
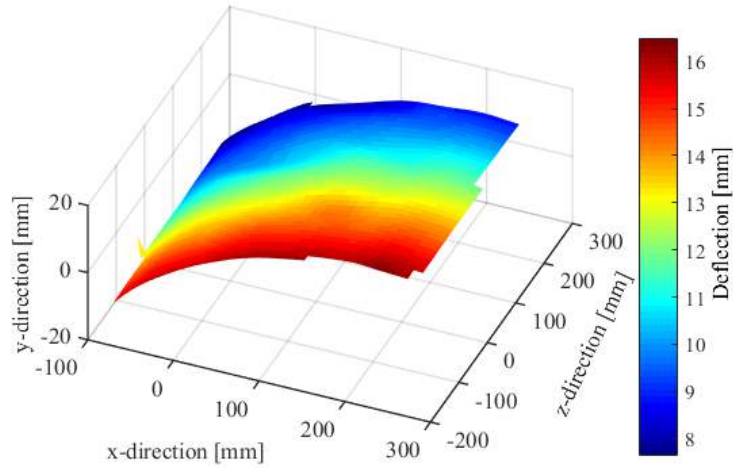


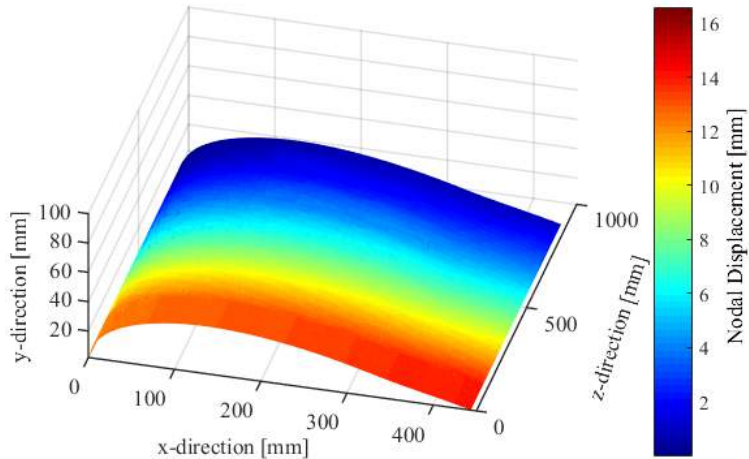
FIGURE 5.20: *Deflection and lift force (L) over time for wind tunnel measurements (i.e. deflection measured with DIC and lift by the forces balance) and FSI numerical simulations.*

It is possible to see from the figure how the structural response is well represented by the numerical simulation not only in amplitude but also in period, leading to small oscillations at approximately 6.6 Hz, as recorded in the wind tunnel. This frequency differs from the first mode natural frequency values, as it is enforced by the increase in wind speed. As discussed in Section 4.4 the discrepancies detected between the experimental and numerical results can derive from the error of $\pm 1^\circ$ associated with the experimental set angle of attack.

DIC and PIV are capable of recording the data necessary to describe the surface's structural behaviour or the flow surrounding an object without modifying the nature of the structure or of the flow itself. It is therefore possible to assess the structural deformation of the aerofoil as recorded in the wind tunnel experiments, Figure 5.21(a), and as modelled in the numerical FSI analysis, Figure 5.21(b), over the investigated aerofoil surface.



(a) Experimental aerofoil: DIC speckle pattern dimensions 450×450 mm, DIC coordinate system



(b) Numerical aerofoil Mylar surface: structural (FEA) response to fluid (CFD) pressure load, aerofoil coordinate system

FIGURE 5.21: Aerofoil deflection as measured with DIC and as simulated in the numerical environment for $V_S = 14.95$ m/s, $\alpha = 9.97^\circ$ and $\phi = 0^\circ$.

Figure 5.22 shows the comparison of twist angles at three different span-wise locations as measured with DIC, and as modelled in the FSI simulation. It is possible to see that the FSI solution closely represents the DIC measures, and the change in angle of attack experienced by the numerical aerofoil falls within the standard deviation of the DIC measurements apart from the top location of $\phi = -30^\circ$. In that location the Mylar on the wind tunnel model presents a wrinkle that slightly affects the reading of the results. From both Figures 5.20 and 5.22 it is possible to see how the coupled FSI represents

correctly the increase in displacement and the decrease in angle of attack experienced with the oriented ply.

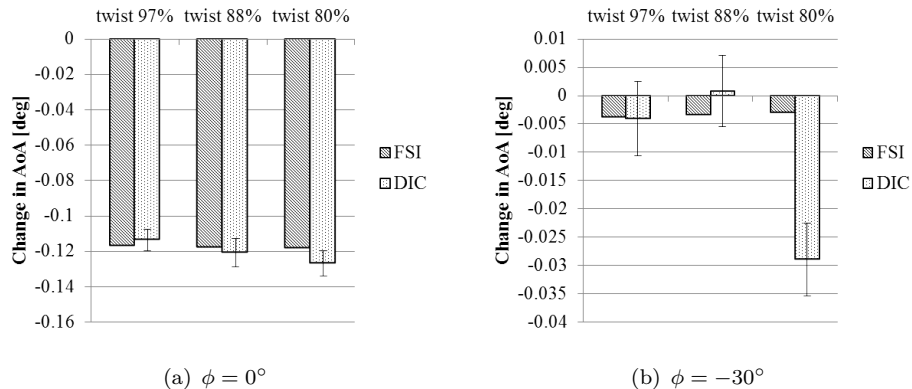


FIGURE 5.22: *Twist angle comparison between DIC and FSI numerical simulations at three different span-wise locations.*

In order to correctly evaluate the change in twist along the span, the numerical displacements at the leading and trailing edges were compared to the values measured in the wind tunnel, as can be seen in Figure 5.23. From the figure it is possible to see the initial non-linear twist occurring at the root of the aerofoil, where the displacement is zero. The linear increase in displacement is well represented in the tip area, as can be seen by comparing the numerical and experimental values.

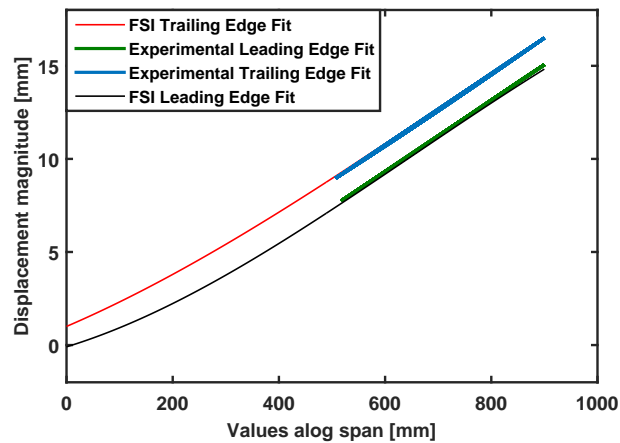


FIGURE 5.23: Displacement magnitude along the aerofoil span at the leading and trailing edges. Wind speed $V_S = 14.95 \text{ m/s}$ and angle of attack $\alpha = 9.97^\circ$

Figure 5.24 presents the numerical wind tunnel section in which the streamlines are represented together with the nodal displacement. In the figure, the wind tunnel reference system is also represented about which the moments acting on the aerofoil are measured.

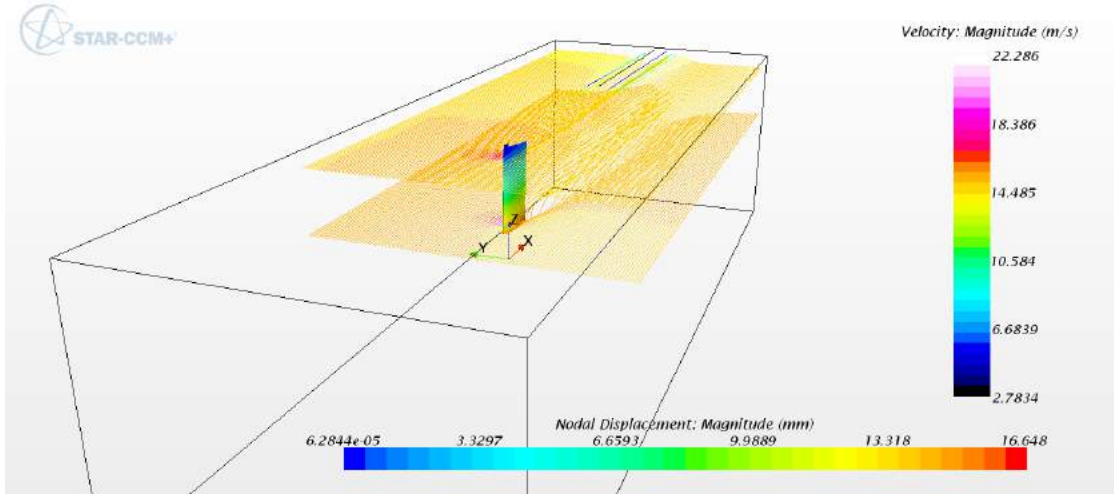


FIGURE 5.24: Velocity streamlines and nodal deflection shown in the numerical wind tunnel working section. Wind speed $V_S = 14.95 \text{ m/s}$ and angle of attack $\alpha = 9.97^\circ$

5.6 Summary of the Chapter

In this chapter the results for the flexible aerofoil were presented. The chapter was subdivided into two main areas: one where the experimental results were analysed and discussed, and one where the numerical simulations were compared to the experimental measurements. In order to clarify the position of the ply orientation and its influence on the structural response, the conventions of the angles with respect to the flow direction and the aerofoil plan form were presented. The orientation of the plies indeed determines whether the aerofoil would twist toward feather or toward stall, therefore it is extremely important to implement the ply angle in the desired direction.

The results deriving from coupling the three different systems were described for a quasi-isotropic beam in a steady condition. The repeatability of the system was demonstrated both with and without filters, showing the robustness of the experimental set-up, which is able to capture not only the forces but also the flow features and the structural response of a specimen under real load.

The influence of the ply orientation and its position with respect to the neutral axis was discussed when analysing the response measured in the wind tunnel. Moreover, the non-dimensional displacement and twist, which take into account the material properties of the aerofoil, were introduced. These parameters allowed the comparison of different specimens in order to achieve an optimal tailored design. Understanding the influence of the oriented plies in the aerodynamic and structural response of a structure is important for designing new structures tailored to a given load.

Finally, the numerical results were presented, and compared to the experimental values. The FEA, the CFD and the full FSI models showed that it was possible to represent

an anisotropic structure and its response in a numerical environment correctly. The complex FEA model was solved coupled with the CFD domain, so that the dynamic and inertia effects could be described under a realistic wind load. This approach showed that the forces and deflection experienced in the wind tunnel differed by 3.5% and 4.5% from the ones simulated (respectively for the $\phi = 0^\circ$ and for the $\phi = -30^\circ$ beams) and that the simulated twist lies within the standard deviation of the DIC measuring system. Furthermore, the same change in deflection frequency was seen in both the experimental and numerical model.

6

Design & Test

6.1 Introduction

The bend-twist coupling deriving from the oriented plies in the laminate makes it possible to achieve tailored designs for an expected load, inducing a twist on an aerofoil-shaped section. An ideal hydrofoil lift over velocity profile achieves a level of twist that is capable of reaching a constant lift (ideally equal to the weight of the sailing boat) after a design take-off speed, as seen in Figure 6.1. In the figure, the case of a high-performance foiling boat is taken into consideration. In the new era of foiling boats it is necessary to reach the take-off speed in order to reduce the drag associated with hull resistance. Having reached the take off speed, ideally the lift curve should reach a constant value to achieve a stable flight. The reduction in lift for higher boat speeds is beneficial also for a reduction in induced drag, which decreases proportionally with angle of attack.

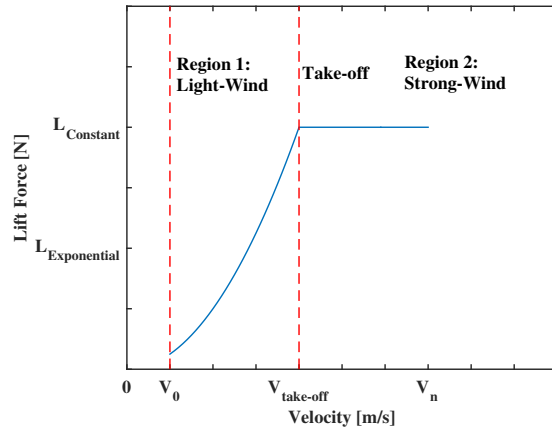


FIGURE 6.1: *Ideal lift over velocity profile for a hydrofoil section.*

Figure 6.2 shows the transverse and longitudinal views of a foiling catamaran. In order to achieve a stable flight, it is necessary to control the pitch angle by adjusting the rake. In the design process presented, the change in angle of attack (twist angle) represents a means of controlling the pitch angle passively, adapting the internal structure to a given load.

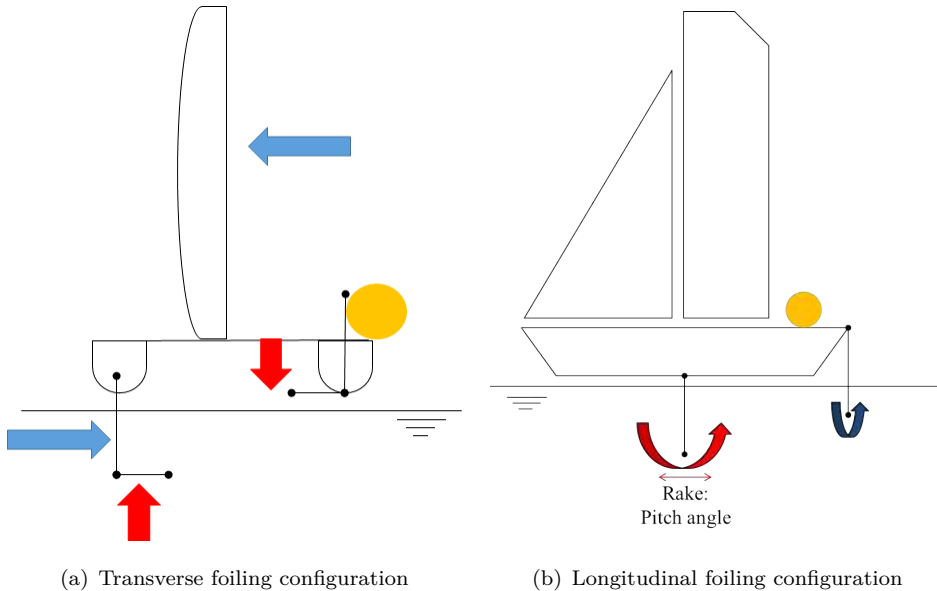


FIGURE 6.2: *Foiling catamaran configuration. In the transverse plane it is possible to change the cant-angle, and in the longitudinal plane the rake, which adjusts the pitch angle.*

Achieving a constant lift curve once the boat is foiling is possible when taking into consideration the lift equation

$$L = \frac{1}{2} \rho A V^2 C_L \quad (6.1)$$

and the proportionality between the lift coefficient C_L and the angle of attack α , where α is formed of $(\alpha_0 \pm \frac{\partial\alpha}{\partial L}L)$. In this case α_0 is the set angle of attack and $\frac{\partial\alpha}{\partial L}$ is the level of twist achievable with the bend-twist coupling. The positive or negative sign of $\frac{\partial\alpha}{\partial L}$ depends on the orientation of the passive-adaptive plies, i.e. if it changes the angle of attack toward feather or toward stall. Therefore, rearranging the lift Equation (6.1) it is possible to obtain the lift force as a function of the bend-twist coupling value. For:

$$C_L = K \left(\alpha_0 \pm \frac{\partial\alpha}{\partial L} L \right) + C, \quad (6.2)$$

the lift force can be calculated as:

$$L = \frac{\frac{1}{2}\rho AV^2 K \alpha_0 + C}{1 \pm \frac{1}{2}\rho AV^2 K \frac{\partial\alpha}{\partial L}} \quad (6.3)$$

where ρ is the fluid density, A is the aerofoil surface area, V is the flow speed, K is a constant defined from the shape of the aerofoil and is derived from the lift coefficient over angle of attack ratio, and C is constant for asymmetric aerofoils. In order to achieve a constant lift force at a certain speed, it is necessary to correctly understand the amount of bend-twist coupling needed. Given a real structure, it is not possible to achieve a constant lift force value without exceeding the ultimate strength of the structure. Therefore, the design goal was set as being able to achieve a linear increase in lift force and a constant decrease in C_L with wind speed. This configuration in high performance sailing allows to reach a correct pitch angle with a passive adaptive hydrofoil and to adjust the rake value for fine-tunings needed once the boat is foiling.

This chapter will describe the design process developed to achieve an aerofoil that could decrease its lift-increase rate with an increase in speed. The manufacturing and wind tunnel tests will be described and the results presented.

6.2 Design Development

The initial design, hereafter called Design 0 (Figure 3.1), was initially developed to achieve a substantial change in angle of attack, due to the large distance between the shear centre and the centre of pressure. At the design stage, the aerofoil was developed to present a simple 3-dimensional test case that can be easily reproduced in numerical and experimental assessments. In order to design a structure tailored to a certain load, it was necessary to understand the influence on the change in twist given by the longitudinal position of the spar and the position of the oriented plies with respect to the neutral axis. Therefore, a number of different designs, shown in Figure 6.3, were simulated using the FEA numerical tools, and their responses were analysed.

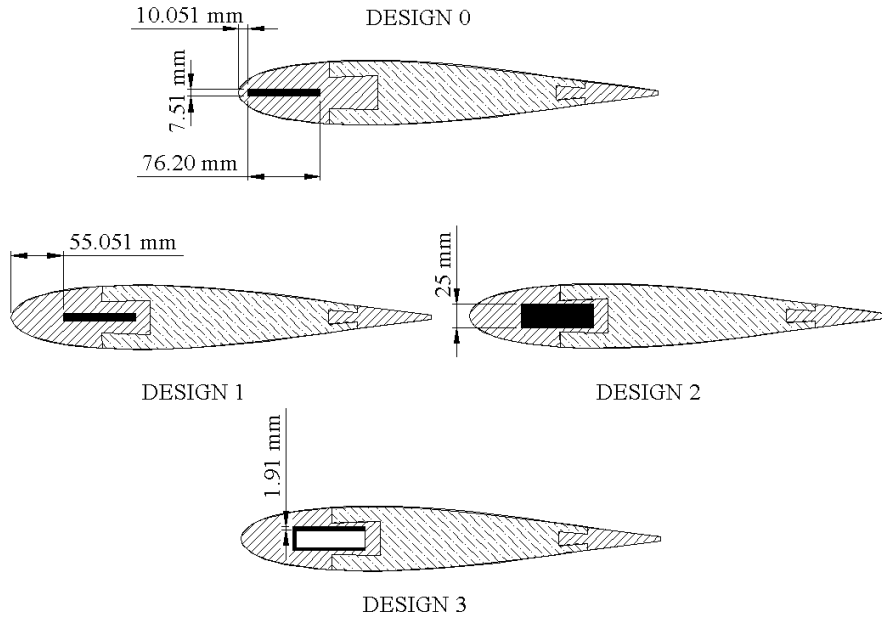


FIGURE 6.3: *Change in aerofoil internal design. Design 1 shear centre location moved 10% toward the trailing edge. Design 2 oriented plies moved 30% away from the neutral axis. The internal spar of Design 3 is a C-beam, which presents a shear centre location forward of the one of Designs 1 and 2 and maximum distance between the oriented plies and the neutral axis.*

In developing the new design, two bent-twist techniques are brought together: the bend-twist coupling due to the orientation of the plies utilising Passive Adaptive Composites (extensively discussed in Section 2) and the bend-twist coupling due to stiffness variation along the aerofoil chord utilising Differential Stiffness Bend-Twist (DSBT). DSBT has been introduced initially by Raither *et al.* (2012) with a conceptual investigation of a beam-like structure and its response to flexural load with different web-stiffness, as presented in Figure 6.4. By stiffening one side of the web more than the other, it is possible to induce twist to the structure. This concept is particularly important in aerofoil structures and their aero-elastic behaviour. Indeed, by stiffening the leading edge of a wing, the shear centre is moved forward, away from the centre of pressure, and the torsional stiffness is therefore increased resulting in a structure twisting toward feather under bending load.

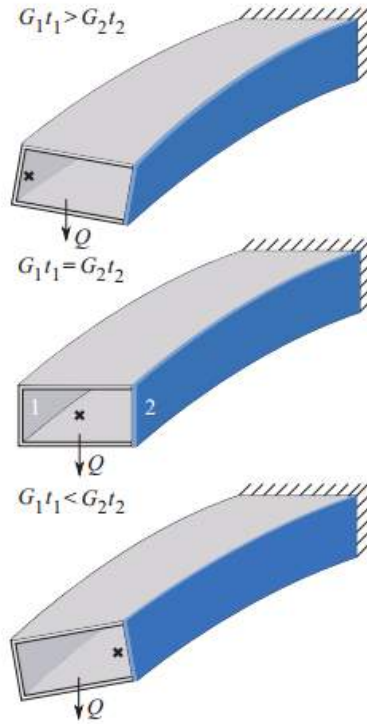


FIGURE 6.4: *Differential Stiffness Bend-Twist coupling for a closed box-beam section with different stiffness of the webs as presented by Raither et al. (2012).*

Changing the stiffness along the aerofoil chord to modify the shear centre position with respect to the centre of pressure is further analysed by Herath *et al.* (2015) as a way of load alleviation in wind turbine blades. Therefore, in the development of the new design it was important to understand the influence of both stiffness and passive adaptivity.

Design 1 and Design 2 were then analysed. These two designs have their shear centre as close as possible to the centre of pressure, as presented in Figure 6.5. This position minimises the effects of induced twist. Design 2 was developed to have a maximum second moment of area, leading to a large separation between the oriented plies and the neutral axis. The sandwich core of Design 2 was changed to give the same laminate rigidity for the increased second moment of area. This was achieved using a foam core (Core Cell M100 (Gurit, 2015)) rather than the aluminium one.

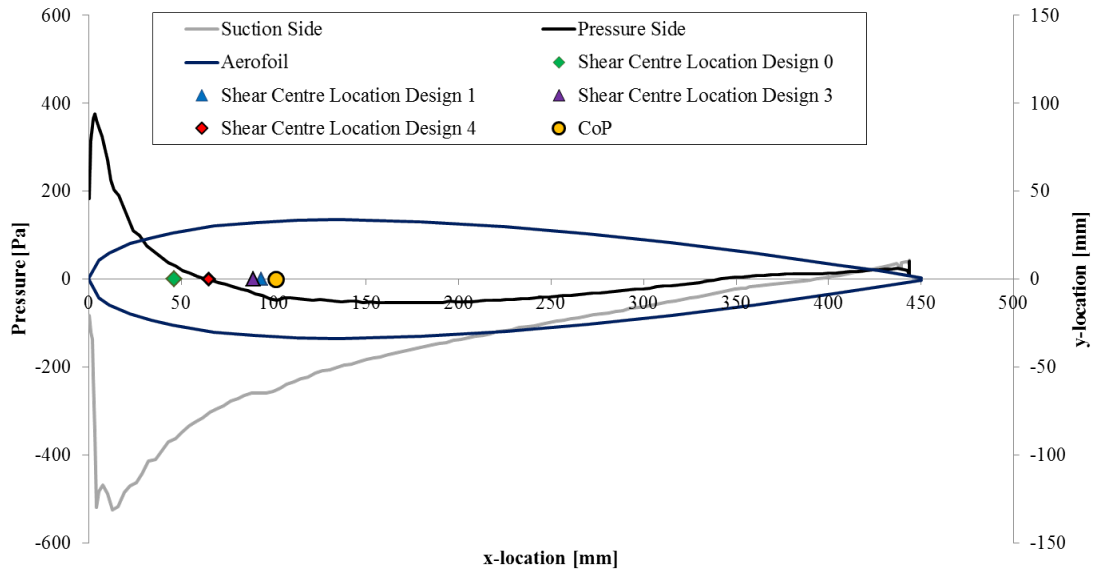


FIGURE 6.5: *CFD pressure and position of shear centres and centre of pressure (CoP) on aerofoil section for Design 0 and Designs 1, 2, 3 and 4.*

The FEA analysis on the different designs was initially performed with a static Computational Fluid Dynamics (CFD) pressure load corresponding to a wind speed $V_S=25$ m/s and an angle of attack $\alpha=8.93^\circ$. This allows the assessment of the structural response change for a constant pressure, where the only changes in response are given by the changes in the internal spar. In the CFD simulation the transition model is used to better represent the transition from laminar to turbulent boundary layer occurring near the leading edge of the aerofoil. The flow regime transition is shown in the suction side (grey line in Figure 6.5) just downstream of the trailing edge. In this region the intermittency (γ) transitions from zero to one, following equation (6.4), and the wall shear stress is higher than in the fully turbulent flow developed further downstream.

$$\gamma = \frac{t_{turb}}{t_{lam} + t_{turb}}. \quad (6.4)$$

For laminar flows the intermittency value is zero and for turbulent flows is one. The time scale (t) is defined by Menter *et al.* (2006) as:

$$t = \frac{500\mu}{\rho U^2}.$$

The results from the numerical investigations of Designs 1,2 and 3 are compared to the experimental values of Design 0 as measured in the wind tunnel and presented in Section 5.4. Setting a constant pressure value to the investigated designs allows to understand the bend-twist coupling effects on the structural response.

Moving the shear centre closer to the centre of pressure position and keeping a closed section with the same second moment of area (Design 1) drastically reduces the passive

adaptivity of the aerofoil, as can be seen from Figure 6.6(a). The relative effect of the oriented plies is still visible, with an increase in twist of 10% between the $\phi = 0^\circ$ beam and the $\phi = 2 \times 30^\circ$ beams and a decrease in twist of 2% between the $\phi = 0^\circ$ beam and the $\phi = -30^\circ$ beams. With the shear centre almost aligned with the centre of pressure position, the torsional stiffness of the structure is increased compared Design 0. The relationship between bending and twist is therefore reduced and a decrease in deflection of 15% is measured between Design 1 and Design 0. This behaviour shows how the position of the internal spar affects the passive adaptive response of the structure.

In order to overcome the decrease in twist, and more importantly the decrease of passive adaptivity, shown in Design 1, the second moment of area of the structure is maximised in Design 2. From Figure 6.6(a) it is possible to see that the increase in distance between the oriented ply and the neutral axis is more effective than the longitudinal position of the spar, as the Design 2 beams with passive adaptivity allow a larger magnitude in change of angle of attack than the ones from Design 0.

The internal spar of Design 3 brings together the knowledge of the response acquired in the previous iterations. The C-beam allows a natural increase in twist due to the low torsional rigidity of the open section, placing the shear centre away from the centre of pressure. The oriented plies are also separated from the neutral axis. In order to achieve a balanced response, the C-beam has been designed with four unidirectional laminae (oriented as quasi-isotropic [0/45/-45/0]) and one/two oriented plies bonded to the top and bottom faces of the beam. Design 3 is stiffer than Designs 0-2 (by $\approx 70\%$) due to the transverse laminae and the higher number of carbon layers present in the spar. The increased stiffness still allows a substantial amount of twist to be created under the static pressure load, as can be seen in Figure 6.6(a). In this configuration the increase in twist of the $\phi = 2 \times 30^\circ$ spar compared to the $\phi = 0^\circ$ is 5% and for the beam resisting the angle change there is a decrease in twist of $\approx 2\%$.

The increase in stiffness given by the transverse carbon plies enhances the twist/displacement ratio compared to the other designs, as shown in Figure 6.6(b). Achieving a large amount of twist compared to the deflection allows an aerofoil to withstand different loading conditions, allowing a real structure to perform, for example, under gust loads or a wider range of operating speeds.

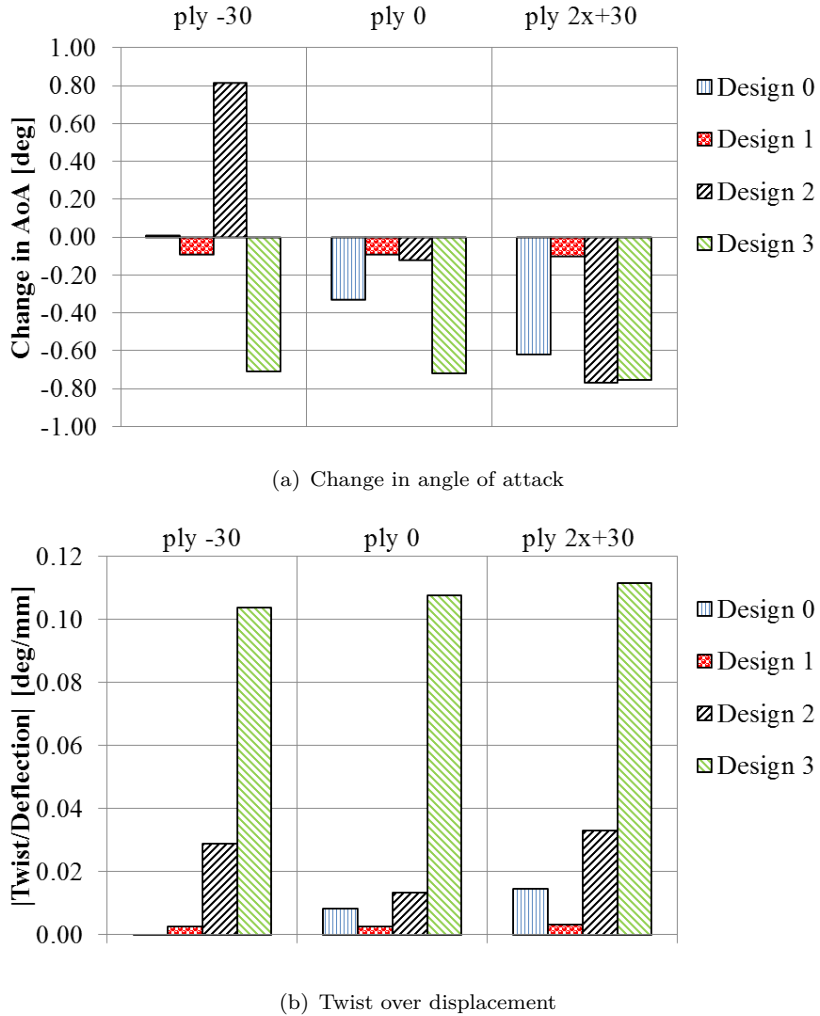


FIGURE 6.6: Comparison of twist levels between the four different designs.

6.3 Optimised Design For Bend-Twist Coupling

The design iterations developed to better understand the passive adaptivity from Design 0 to Design 3, showed that in order to achieve a level of twist high enough to reduce the rate of change of lift with speed, it is necessary to maximise the distance between the shear centre and the centre of pressure, and that the PAC plies should lie as far apart as possible from the neutral axis. When the bending and torsional stiffness are increased, a reduction in coupling effects is seen.

Considering equation (6.3) and analysing the wind tunnel results from Design 0, it was possible to create an analytical model that could calculate the rate of change in lift for the change in twist angle over wind speed. Figure 6.7 presents the twist achieved at different angles of attack and wind speeds as calculated with the analytical model, taking into consideration $\frac{\partial \alpha}{\partial L}$. The results presented in the figure show the twist angle for the quasi-isotropic Design 0 model, with a NACA0015 shape.

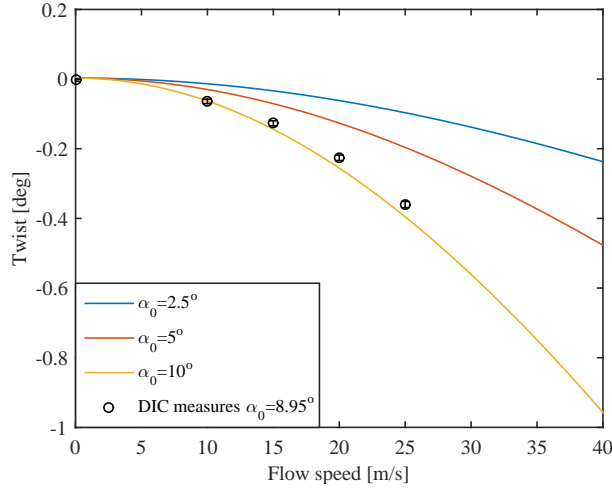


FIGURE 6.7: *Change in twist angle with wind speed for a range of angles of attack, as calculated by the analytical model and as measured in the wind tunnel.*

The level of twist achieved with Design 0 allows a decrease in the lift force at increased speed. However, the lift force, even if it is decreased for the $\phi = 2 \times 30$ case compared to the quasi-isotropic structure, still increases with the wind speed squared, as presented in Figure 5.11(b).

In order to achieve higher levels of lift at low wind/boat speeds, to be able to reach the take-off speed faster, it is necessary to consider a cambered aerofoil section. The section shape of a daggerboard tip from the America's cup team Land Rover Ben Ainslie Racing was assessed and the shape was compared to a NACA 2412, as can be seen from Figure 6.8.

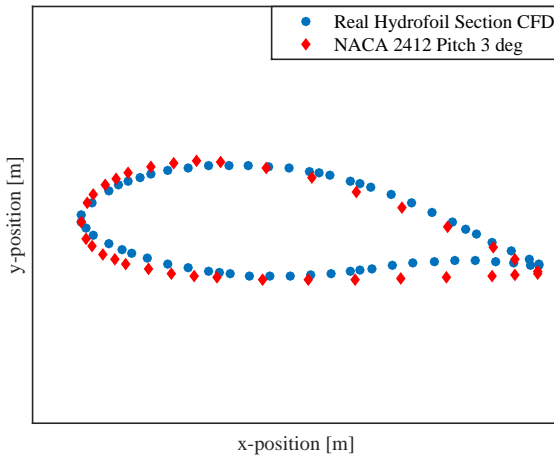


FIGURE 6.8: *Section shape of a real hydrofoil tip and of a NACA 2412 aerofoil.*

The NACA 2412 shape presents a very similar shape and camber to the daggerboard tip section. Therefore, in order to create a design that can be reproduced, the NACA

section was chosen. It has to be noted that in order to reach the take-off speed in a foiling boat a pitch angle of $\approx 3^\circ$ is often set. This configuration, compared to Design 0, is not only able to achieve a higher lift at lower wind speeds, but is more characteristic of a real structure.

Moving the C-beam spar as close to the leading edge as possible increases again the distance between the shear centre and the centre of pressure (Figure 6.5), increasing the influence of passive adaptivity on the response. However, a large twist angle during tests on a cambered aerofoil fixed at one end could create inverse loading conditions, which would result in failure of the structure. Therefore, an initial pre-twist is introduced along the span of the aerofoil. Furthermore, as the amount of twist increases from the root to the tip, a section shape with no-camber is chosen at the root (i.e. NACA0015) to create a small amount of lift in the root area. At half-span a NACA1412 section is introduced with a pre-twist angle of 1.5 degrees. This section shape is introduced to allow a smooth transition between a NACA 0015 and a NACA 2412, especially considering the glueing process of the Mylar sheet. Finally, at the tip, a NACA2412 is chosen with a pre-twist of 3 degrees, as presented in Figure 6.9.

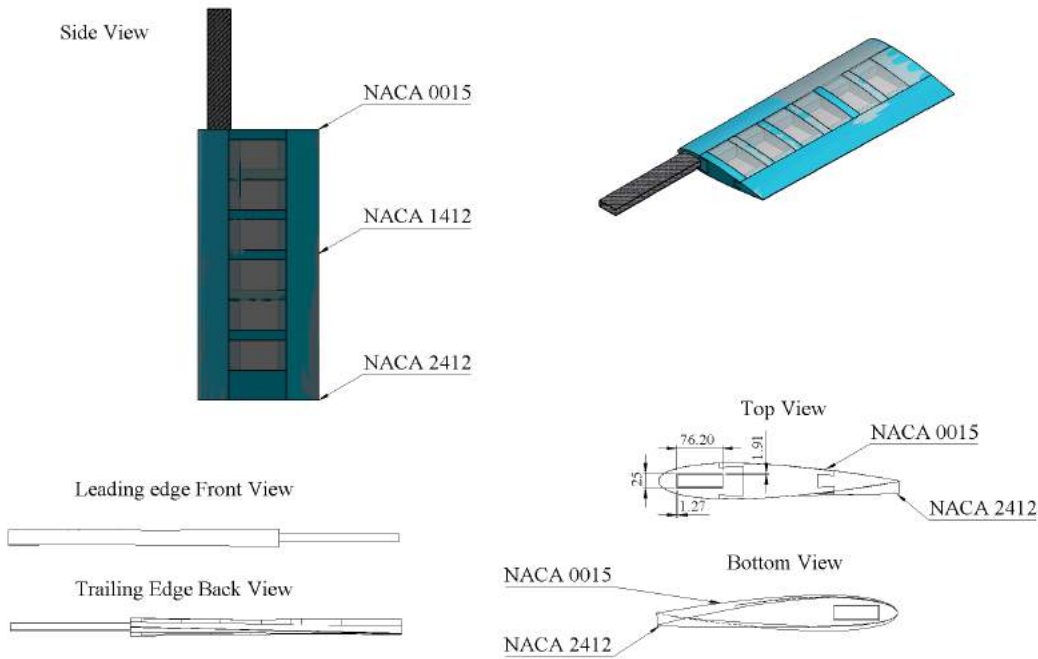


FIGURE 6.9: *Design 4 technical drawing showing the different section shapes and the principal dimensions. All the dimensions shown are in millimetres.*

From the top, bottom and trailing edge views, the increase in pre-twist and the transition between a non-cambered to a cambered section are clearly visible. This configuration, when analysed on the analytical model, shows that it is possible to achieve a decrease in

lift-increase rate for a range of wind speeds, as can be seen in Figure 6.10. The proposed Design 4 response takes into consideration a section-shape-constant (K) averaged for the three NACA sections. A study on the level of the passive adaptivity necessary, showed that the twist values should be almost doubled with respect to the ones achieved in Design 0. Therefore, it was possible to calculate the $\frac{\partial\alpha}{\partial L}$ value needed to be able to achieve a lift aiming at a constant value. The passive adaptivity value represents the rate of change of twist with lift force.

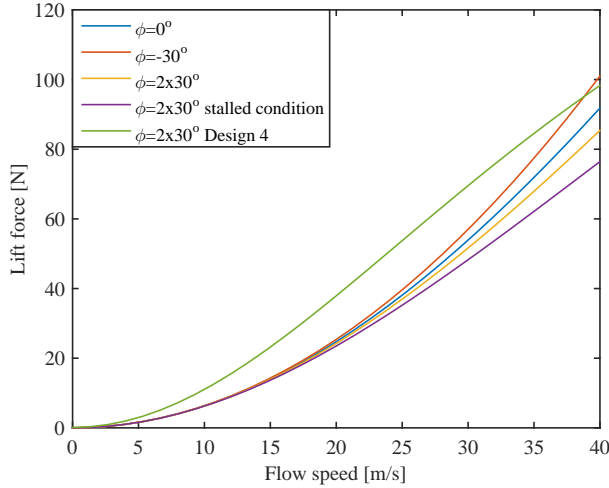


FIGURE 6.10: Lift over velocity profile for Design 0 and Design 4 at $\alpha = 5^\circ$.

The different responses for the Design 0 case represent the different influences of the passive adaptivity value ($\frac{\partial\alpha}{\partial L}$). The $\phi = 2 \times 30^\circ$ stalled case takes into consideration the $\frac{\partial\alpha}{\partial L}$ value in stalled condition, therefore when the centre of pressure moves toward the trailing edge, i.e. the centre of pressure is further away from the shear centre when the aerofoil stalls compared to a non-stalled condition. The maximum speed represented is 40 m/s, corresponding to the higher wind speed achievable in the R. J. Mitchell wind tunnel. From Figure 6.10 it is possible to see how for speeds > 15 m/s the lift response is changing from varying with square of the velocity to linear, and for speeds > 25 m/s the lift response is inverting its trend toward a constant value. If the same analytical model is run with the density of the water, it is possible to see that the lift reaches a constant value at 3 m/s. The presented model is too flexible to be tested in water, therefore a more stiff design, with the same level of passive adaptivity, should be tested in a towing tank.

Having analysed analytically the proposed design it was necessary to numerically simulate the wind tunnel environment and the structural response of the aerofoil under aerodynamic loading. Given the high costs involved in experimental campaigns, it was necessary to achieve enough confidence in the response of the aerofoil prior to entering the wind tunnel. Therefore, the numerical tools, that in the case of Design 0 were

validated against experimental values, for Design 4 were used as design and developing tools to ensure a tailored response to load.

As discussed previously an ideal lift profile aims to achieve a constant level of lift at a chosen take-off speed. Given the structural constraints of the specimen and the geometric and performance constraints of the wind tunnel, being able to achieve a linear increase in lift force with wind speed and a decrease in C_L was chosen as a realistic design goal for Design 4. In order to achieve a constant lift-curve, not only should the angle of attack change substantially but also the shape of the aerofoil, so as to decrease C_L linearly over V^2 . The blue arrow in Figure 6.11 represents a way in which the hydrofoil could achieve a constant lift value. Figure 6.11 shows two typical lift coefficient curves for a cambered and a symmetric section. Using passive adaptivity it is possible to change the angle of attack, decreasing the C_L value in increasing speed. This leads to a linear variation of lift with velocity. Decreasing the lift coefficient with speed at high angles of attack allows the delay of the stall angle, twisting the aerofoil toward feather. The ability to reduce the lift coefficient with increased flow speed allows to reduce also the induced drag, as the induced drag decreases proportionally to a decrease in angle of attack. For a daggerboard design the effectiveness of passive adaptivity at low angles of attack (pitch angles) is important, as the rake has a limited range of angles adjustments.

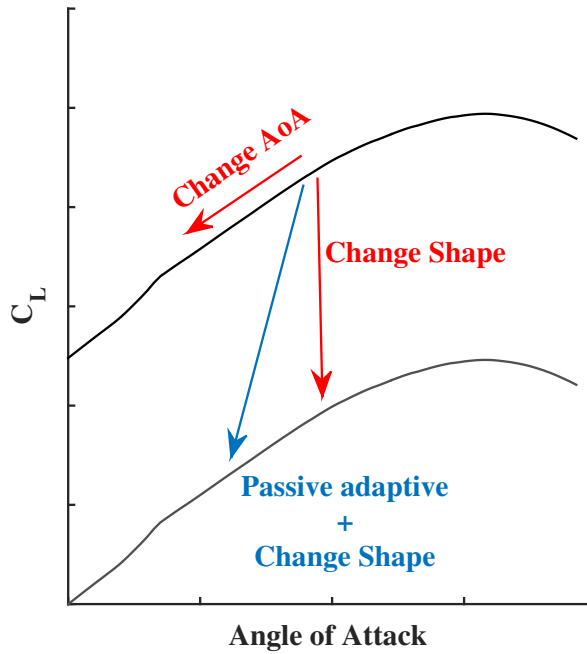


FIGURE 6.11: *Lift coefficient curves for cambered and symmetric sections. The arrows show the influence of using PAC composites that change the angle of attack, and the change in section shape that can be achieved with multi-elements foils or flaps.*

The aerofoil shown in Figure 6.9 was modelled in the numerical environment creating a

FEA model in Abaqus 6.14 and a CFD model in Star-CCM+ 11.02. The numerical set up described in Chapter 4 was applied to the Design 4 structure. In order to correctly represent the passive adaptivity of the aerofoil, the ply angles reference system described in section 5.2 was used, and the $\phi = 0^\circ$ orientation is shown in Figure 6.12. The C-beam was laminated with 4 plies as quasi-isotropic in the three surfaces [$\phi = 0/45/-45/0$] and two bend-twist coupling plies on the top and bottom surfaces [$\phi = 30/30$]. So the top surface laminate was modelled as [$\phi = 0/45/-45/0/30/30$] from bottom to top.

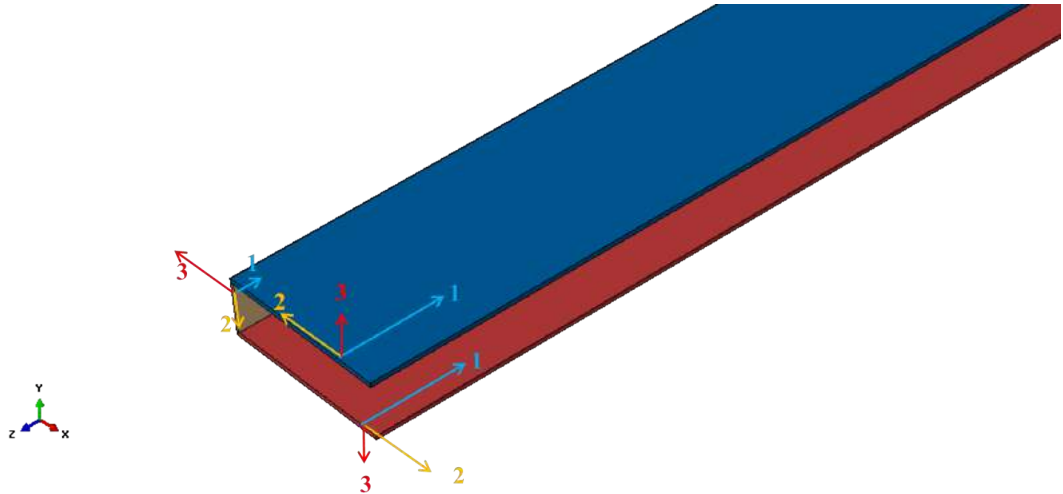


FIGURE 6.12: *Plies orientation reference systems for the C-beam internal spar. The plies are oriented around axis 1 and stacked along axis 3.*

For the CFD domain it was important to represent correctly the boundary layer mesh and the transition along the span from the symmetric aerofoil section to the asymmetric one. Figure 6.13 shows the mesh around the aerofoil in the tip region. The CFD mesh was approximately formed of 2.5 million cells and the FEA mesh of 50,000 elements.

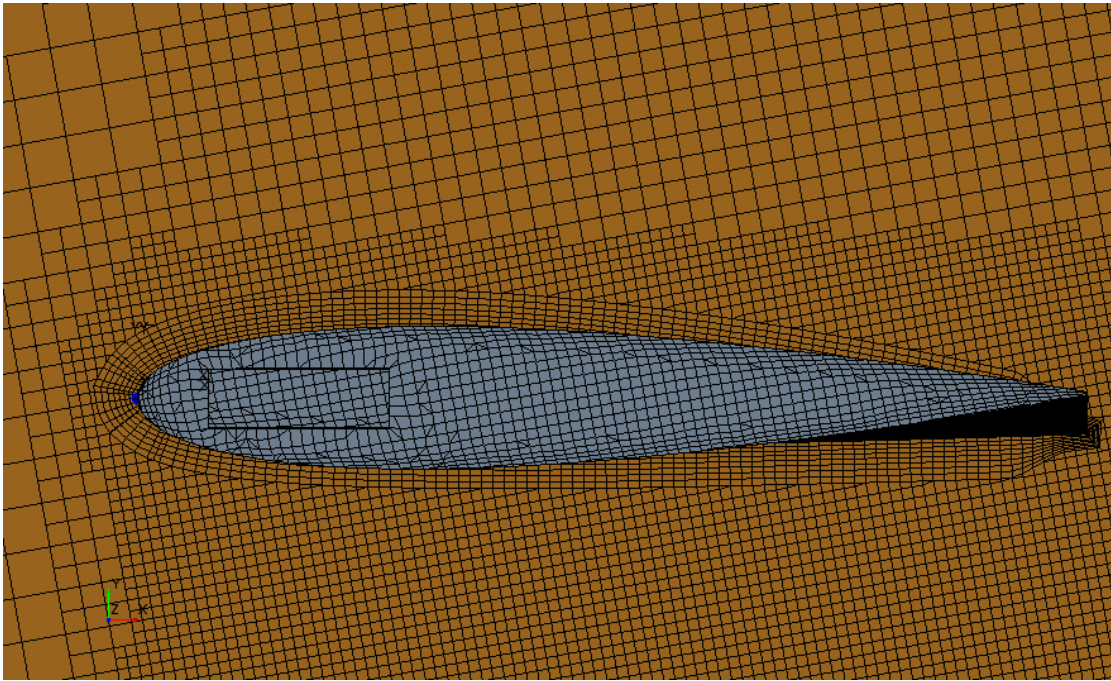


FIGURE 6.13: *CFD boundary layer mesh at the tip of Design 4.*

An initial sweep of simulations was performed with the CFD solver without the coupling of the FEA. This process was necessary to ensure that the settings and the mesh were appropriate to simulate the new geometry. The CFD simulations were run for a wind speed $V_S=15$ m/s at different angles of attack. The results of these simulations can be seen in Figure 6.14. The CFD results are compared to the measures obtained at a later stage in the wind tunnel. The differences between the two responses, especially at high angles of attack, can be associated with the lack of the full-FSI loop. In the CFD-only case, the effects of deflection and twist are not taken into consideration. The responses, however, are similar. The CFD settings used were the same validated in the simulations of Design 0 and the mesh was adjusted to correctly represent the change in shape. A complete fluid-structure interaction simulation was then carried out.

In dynamic simulations the Courant number was controlled to be always <5 and the y^+ to be >30 and <100 , therefore in the turbulent region. The $\gamma R_e \theta$ transition model was used to accurately capture the transition region from laminar to turbulent flow.

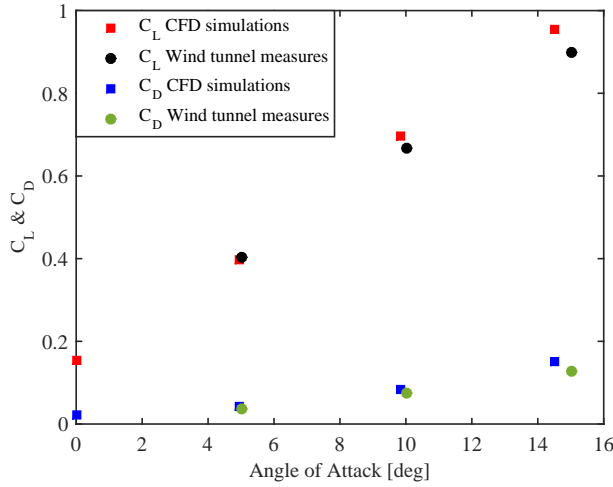


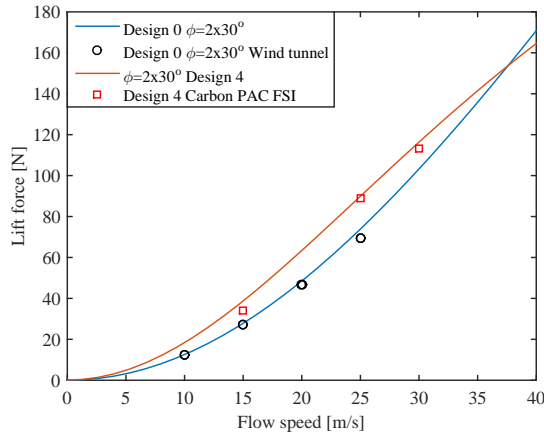
FIGURE 6.14: *Lift and drag coefficients over a range of angles of attack for $V_S=15$ m/s.*

FSI coupled simulations were performed to assess the response of Design 4 to aerodynamic load. Both the structural and the aerodynamic response of the new design can be seen in Figure 6.15. The FSI simulations were performed for $\alpha = 10.02^\circ$ and three different wind speeds. Figure 6.15(a) shows the differences in lift force achieved with Design 0 and Design 4. From the Figure it is possible to see that the FSI lift-force is slightly lower than the one predicted by the analytical model. For Design 0 the shape constant (K) was derived directly from the wind tunnel results. For Design 4 instead, K and C were derived from x-foil two-dimensional simulations. The constant values K and C are averaged for the three section shapes characteristic of Design 4. In order to achieve a 2-D response able to represent a finite-span wing, the effects of an elliptical lift distribution were modelled, as stated in the incompressible theory (Molland and Turnock, 2007). In the case of a PAC 3-D symmetric aerofoil the lift coefficient at an incidence α is obtained as:

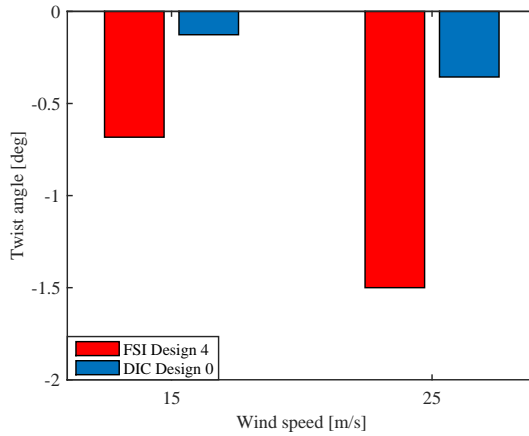
$$C_L = K \left(\alpha - \epsilon - \frac{\partial \alpha}{\partial L} L \right) \quad (6.5)$$

where K is the lift curve slope, ϵ is the effective angle of attack on a three-dimensional aerofoil and $\frac{\partial \alpha}{\partial L}$ is the amount of twist achievable with the bend-twist coupling, which further decreases the lift coefficient for a given angle of attack. Therefore, for a three-dimensional PAC beam that twists toward feather, the lift force can be calculated as:

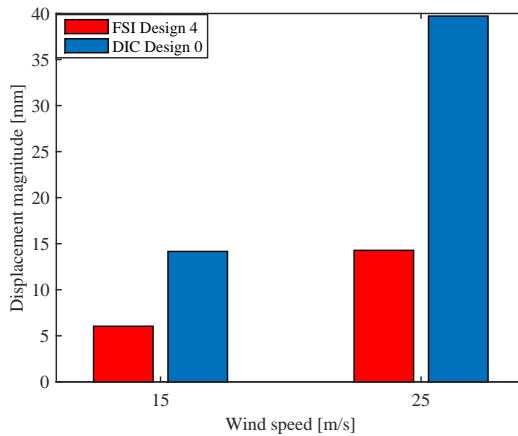
$$L = \frac{\frac{1}{2}\rho AV^2 K(\alpha - \epsilon) + C}{1 + \frac{1}{2}\rho AV^2 K \frac{\partial \alpha}{\partial L}}. \quad (6.6)$$



(a) Lift force response for analytical and FSI simulations on Design 4, and analytical and wind tunnel results on Design 0



(b) Twist response



(c) Deflection magnitude

FIGURE 6.15: Fluid-structure interaction response of Design 4 compared to Design 0.

The losses in side-force due to the aerofoil deflection are not taken into consideration in the analytical case. Therefore, as expected, the three-dimensional FSI response is lower

than the ideal 2-D case. The response of the lift force is well captured and the numerical results can then be compared to the wind tunnel measurements.

From Figure 6.15(b) it is possible to see the twist response occurring on the aerofoil. Those values, if compared to the ones from Design 0 presented in section 5.4, are increased by almost 200%.

Figure 6.15(c) shows the decrease in deflection of Design 4 compared to Design 0. The C-beam, given its large second moment of area and the strength of the carbon, is much stiffer than the rectangular cross-section used in Design 0. The stiffer structure is able to withstand higher loads induced by the cambered shape (Figure 6.15(a)) and to achieve a very large twist over displacement ratio, which is controlled and driven by the bend-twist coupling layup.

The response of Design 4, modelled in the analytical and numerical environment, ensured that the level of passive adaptivity was sufficient to allow a linear decrease of C_L in increased wind speed, thus meeting the design goal set. It was therefore necessary to manufacture and build the model and to test it in the wind tunnel with similar settings as those presented in Chapter 3.

6.4 Manufacture & Test

To be able to achieve the predicted structural response it was necessary to closely represent the structure modelled in the FSI simulations. The tests were performed to verify the possibility of using numerical simulations as design tools in complex composite structures.

The aerofoil was manufactured, built and tested at the University of Southampton. Two internal spars were produced to be aid understanding the influence of passive adaptivity in different materials. One C-beam was made only of pre-preg unidirectional carbon plies (Gurit, 2012a): in top and bottom faces $\phi=[0/45/-45/0/30/30]_C$. The second beam was manufactured with pre-preg unidirectional quasi-isotropic E-Glass plies (PRF Composite Materials, 2015) and carbon PAC plies: in top and bottom faces $\phi=[0/45/-45/0]_G+[30/30]_C$.

Figure 6.16 shows the two beam structures. The composite fibres were layered on top of a rectangular foam structure. This layering process ensured that the C-beam, once cured, maintained straight faces that could easily slide inside the aerodynamic foam structure.

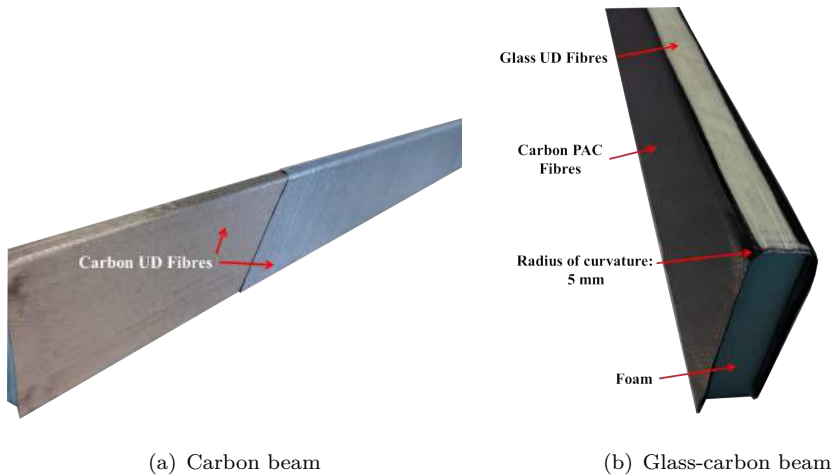


FIGURE 6.16: *Design 4 C-beam internal spars composite lay-up process.*

During the manufacturing of the beams, the composite plies were layered, ensuring that the angle conventions were the same as the modelled ones. It was also important to avoid overlaps between the PAC plies and the leading edge of the C-beam.

The foam was manufactured using the same hotwire technique as for the Design 0 specimen. The aerodynamic foam was joined together with two-component epoxy glue. The same glue was used to glue the Mylar to the exterior surface of the foam-ribbed structure. The finished structure can be seen in Figure 6.17.

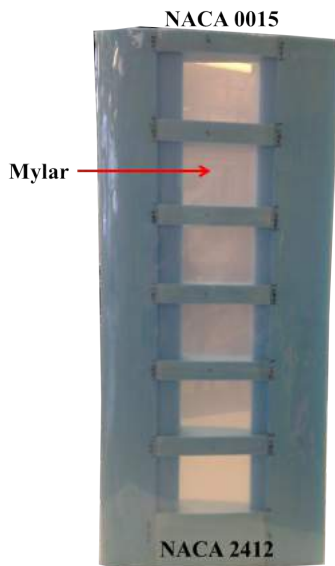


FIGURE 6.17: *Design 4 aerodynamic structure made of foam and Mylar.*

The structure was tested in the R. J. Mitchell closed circuit wind tunnel. The internal spar was fixed to the dynamometer via the Rexroth ® frame.

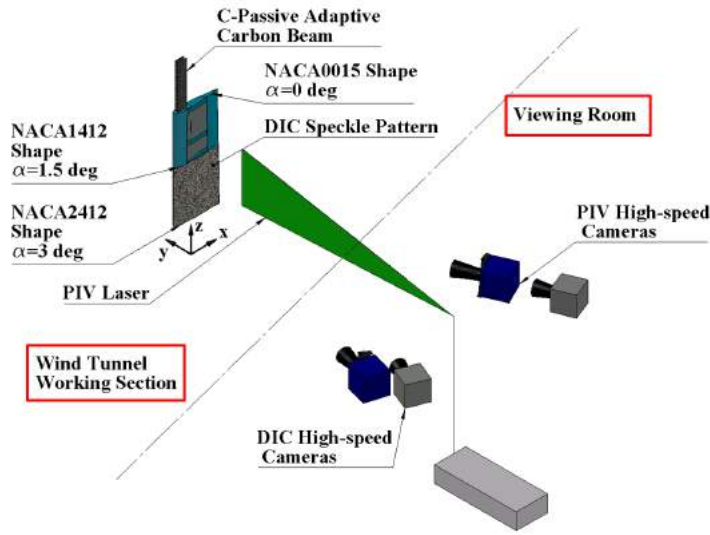
For the tests on design 4, both DIC and PIV were high-speed systems. All four cameras and the laser were positioned in the viewing room, as can be seen in Figure 6.18. The same DIC set up used for Design 0 (and described in section 3.4) was used in the Design 4 tests. The high-speed stereo PIV equipment is detailed in Table 6.1. The depth of field was calculated again with equation 3.2 as both the stand-off distance and the lens focal length were increased by moving the cameras into the viewing room.

TABLE 6.1: PIV performance table showing the equipment and the setting used.

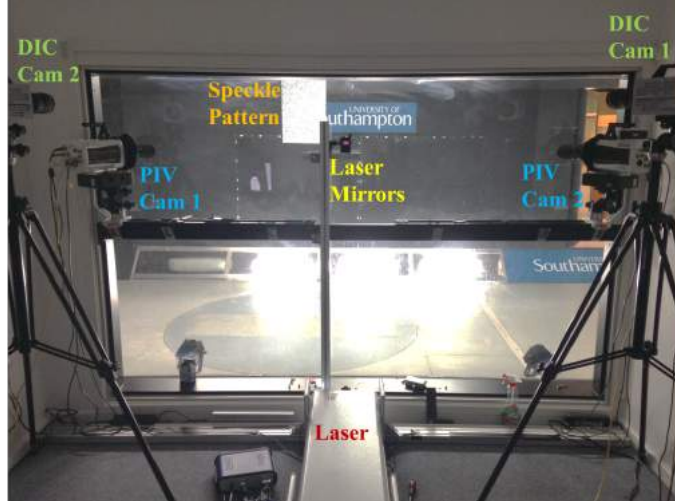
Equipment	Set-up
Camera	2 Phantom v xx1 Sensor size: 25.6×16 mm Pixel size: $10 \mu\text{m}$ Resolution (max): 2560×1600 pixels Exposure time: $2498 \mu\text{s}$ Frame rate: 0.2-0.4 kHz Stereo angle: ≈ 39.5 deg. $\Delta t = 60-40-30-25-20 \mu\text{s}$ for $V_S = 10-15-20-25-30 \text{ m/s}$
Lens	Nikon 200 mm f4 Aperture: $f-4$ Depth of field: 16 mm
Laser	LD75-G PIV High repetition rate DPSS Nd:YAG Wavelength: 532 nm Output energy: 7.5 mJ at 10kHz

Figure 6.18(a) shows a schematic drawing of the equipment in the wind tunnel. The high-speed laser was positioned in the viewing room and the laser beam was deviated through two mirrors angled at 45° to obtain a focused sheet positioned $1/3$ of chord downstream of the trailing edge. The laser thickness was measured with burn paper to be ≈ 2 mm at 75% of the power and at the centre of the field of view.

The two PIV cameras were positioned and focused on the two sides of the laser sheet. The calibration was therefore performed calibrating the left-hand camera (Cam1) with the front of the calibration plate and the right-hand camera (Cam2) with the back of the calibration plate.



(a) Wind tunnel set up drawing



(b) Viewing room set-up

FIGURE 6.18: Wind tunnel and equipment set-up.

Having set the laser in the viewing room together with the DIC cameras, in order to ensure optical isolation between the two systems it was necessary to apply a filter on the DIC cameras with transmittance of 0% in the green-wavelength region. The R-60 filter by Edmund Optics (2016) was installed on the DIC cameras and its transmittance can be seen in Figure 6.19.

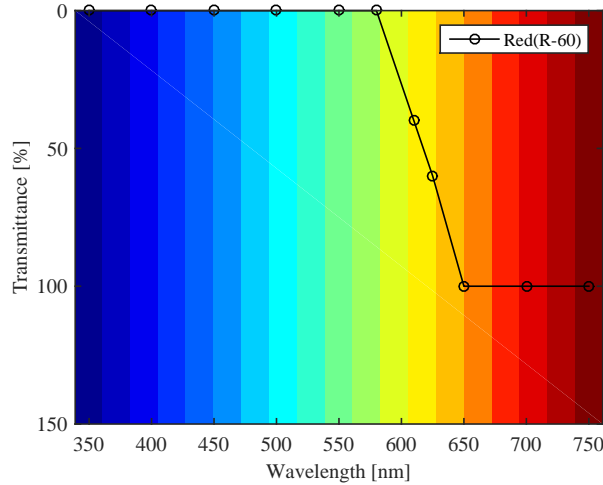


FIGURE 6.19: *Transmission of red filters on DIC high-speed cameras.*

These filters decrease the amount of light on the white-light DIC images. Therefore, the *f-number* is decreased from $f - 16$ to $f - 11$ to obtain a larger lens aperture. This process was done ensuring that the depth of field was still long enough to allow the aerofoil to deflect without losing focus on the speckles ($\text{DoF} \approx 430 \text{ mm}$).

The two optical measuring systems were synchronised through the LaVision high-speed controller. The trigger signal from the PIV and DIC cameras was then connected to the six-components Nuntem balance to synchronise the structural dynamics with the aerodynamic loads.

6.5 Wind Tunnel Results

The wind tunnel measurements could then be compared to the analytical and numerical FSI predictions. After having presented a comparison of the lift force between the three approaches, the discussion of the results is then divided in two sections, the first investigates the change in response for the two internal spars in quasi-static tests. The second section focuses on the dynamic response to aerodynamic loading.

Figure 6.20 presents the lift force response for $\alpha = 10.02^\circ$ and a range of wind speeds. The two internal structures are compared. It is possible to see that the glass-carbon C-beam, being more flexible and prone to twist, allows a larger reduction in lift over velocity slope. This response is possible due to the larger bend-twist coupling effects occurring in the structure with less bending and torsional stiffness.

Both the numerical and wind tunnel data show that it is possible to design a structure tailored to a design goal controlling the level of bend-twist coupling. All the presented responses aim toward a constant lift value, ensuring that is possible to use numerical

FSI methods to aid the design of tailored structures. Due to the structural constraints of the aerofoil, and the flow-speed constraints of the wind tunnel, the aerofoil could not be tested for wind speeds >30 m/s.

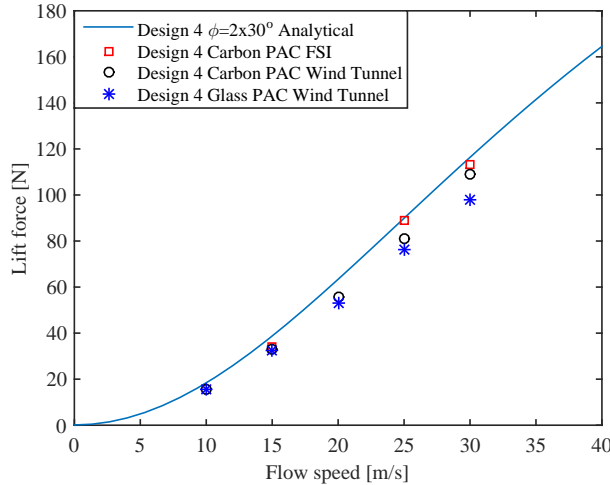


FIGURE 6.20: *Lift force over wind speed for $\alpha = 10.02^\circ$: analytical, numerical FSI and wind tunnel results.*

6.5.1 Quasi-Static Results

In this section the structural response of the two internal spars is presented and the changes deriving from the differences in strength are discussed. Figure 6.21 shows the change in lift with wind speed. As seen in Figure 6.20, the glass-carbon beam approaches a constant increase of lift with wind speed earlier than the carbon spar. The passive adaptivity of the internal spars is more effective at low set-angles of attack. This is particularly important if considering a high-performance catamaran hydrofoil, as it is necessary to change the lift response at low pitch (rake) angles. From the Design 0 response for $\phi=2\times 30^\circ$, where the lift was increasing with $V^{1.95}$ for $\alpha=3.98^\circ$, the lift response of Design 4 with the glass-carbon spar is now increasing with $V^{1.65}$ for $\alpha=5.1^\circ$. This decrease of the power value proves that Design 4 was designed to achieve a goal that was then met.

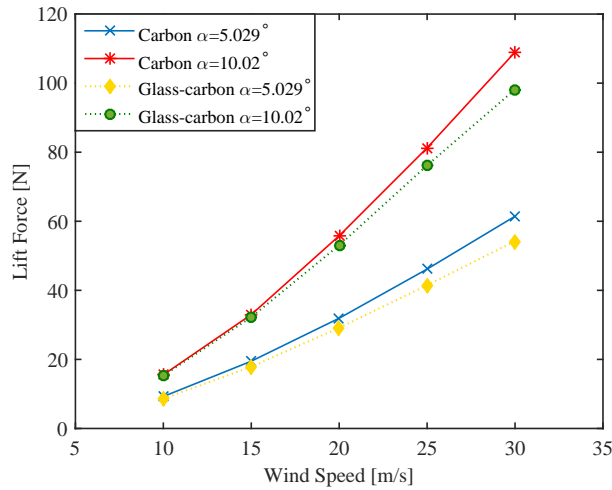


FIGURE 6.21: Aerodynamic lift force acting on the flexible aerofoil over wind speed for the two different internal structures. Solid line: carbon spar, dotted line: glass-carbon spar.

The influence of both the deflection and the twist affect the aerodynamic response and vice-versa. For this reason it is important to understand and accurately measure the interactions between the flow features and the structure. The two tested structures are identical aside from the quasi-isotropic piles in the internal spar. Changing the material in those plies enhances or decreases the passive adaptivity of the structure. Figure 6.22 presents the change in tip deflection for the two beams. From the figure it is possible to see how the glass-carbon spar is more flexible than the carbon one. This behaviour is reflected also in a lower torsional rigidity of the glass fibres and therefore an increase in twist values (Figure 6.23). From both figures it is possible to see how the FSI numerical model correctly captures the deflection and the twist of the aerofoil with a carbon spar. The FSI numerical model present a slightly higher bending stiffness (maximum deflection error at $V_S = 25$ m/s of 14%) and torsional stiffness (maximum twist error at $V_S = 25$ m/s of 7%) due to the discrepancies in the internal spar dimensions and the fillet of the C-spar edges manufactured to easily slide the spar in the foam leading edge.

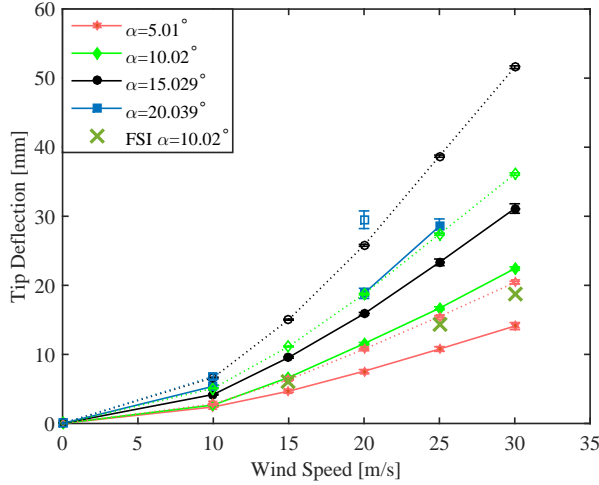


FIGURE 6.22: *Tip displacement comparison for the two internal structures at a range of wind speeds and angles of attack. Solid line full markers: carbon spar, dotted line open markers: glass-carbon spar and X: FSI response of the carbon spar as modelled numerically.*

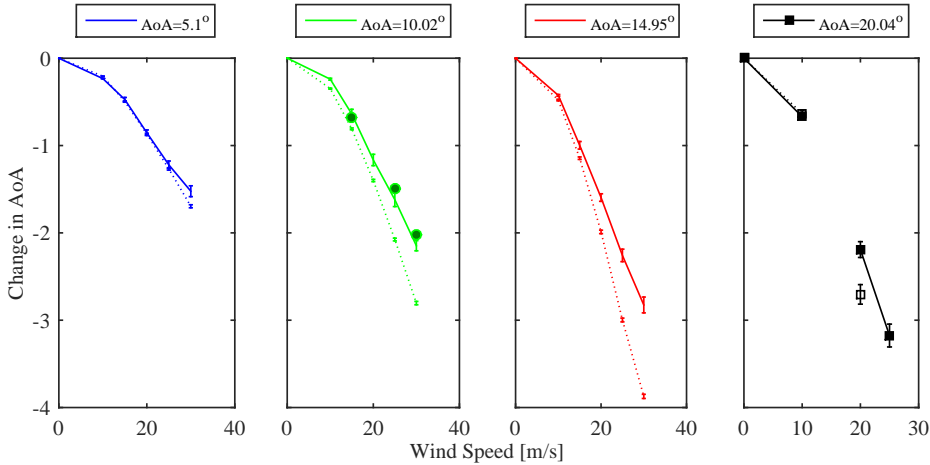


FIGURE 6.23: *Change in angle of attack for different wind speeds and set-angles of attack at 90% of aerofoil span. The solid lines represent the carbon spar and the dotted lines represent the glass-carbon spar as measured in the wind tunnel. For $\alpha = 20.04^\circ$ the closed marker indicates the carbon beam and the open marker the glass-carbon beam. The green markers presented for $\alpha = 10.02^\circ$ show the FSI twist for the modelled aerofoil with a carbon spar.*

From Figures 6.22 and 6.23 it is clear that the lower stiffness of the quasi-isotropic glass fibres enhances the influence of the carbon PAC oriented plies, allowing a large change in angle of attack. This helps to reduce the C_L value for a given speed and angle of attack.

When comparing the non-dimensional displacement and twist values, calculated following equations (5.1-5.2), and taking into consideration the strength of the structure, as shown in Figures 6.24(a) and 6.24(b), it is possible to see that the aerofoil responds as

shown in the dimensional results (i.e. with a higher deflection and a higher twist for the glass-carbon spar). Comparing the non-dimensional results with those from Design 0, it is possible to see that the twist increases substantially when designing a structure able to change its lift response to load. This achievement was possible because, as discussed in section 6.2, prior to designing a structure tailored for a given response, it was necessary to understand the influence of passive adaptive plies when located in different parts of the structure.

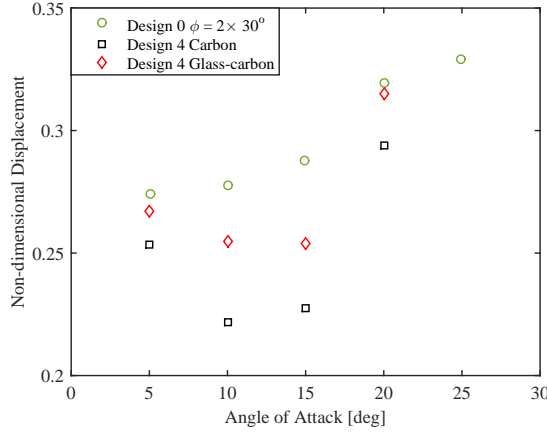
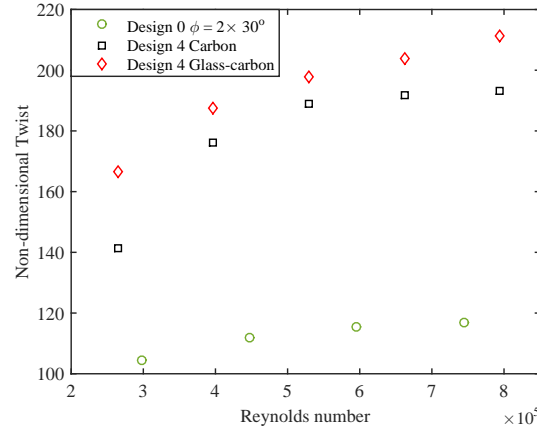
(a) $V_S=20$ m/s(b) $\alpha=10.02^\circ$

FIGURE 6.24: *Non-dimensional displacement and twist for the two internal structures materials compared to the Design 0 $\phi = 2 \times 30^\circ$.*

From the non-dimensional figures it is possible to see that Design 4 not only presents higher twist values but results in being stiffer and in deflecting less than Design 0. In order to design a new hydrofoil able to change its pitch angle with increased boat-wind speed, it is therefore necessary to understand the loading encountered in a sailing condition and then design a structure with similar bend-twist properties to Design 4.

6.5.2 Dynamic Results

The aerofoil was tested not only in steady conditions: its unsteady response was also assessed. At high angles of attack and wind speeds it was possible to inspect flutter motions. This is reflected in the high standard deviation values encountered in those tests conditions when measuring only one wind speed and angle of attack per test (Figures 6.22 and 6.23). It is particularly interesting to test the unsteady response of the aerofoil to be able to correctly capture the flow features around the specimen and inspect the dynamic response of the structure. For this reason the acquisition frame rate was increased to 0.4 kHz.

Figure 6.25 shows the dynamic lift coefficient response for different angles of attack at two wind speeds for the glass-carbon internal spar. The aerofoil was tested after having achieved a constant wind speed at $\alpha = 10.02^\circ$. The acquisition was then started and the angle of attack was increased from $\alpha = 10.02^\circ$ to $\alpha = 28^\circ$. The same approach was used for both wind speeds. The Figure shows that the lift coefficient for higher wind speeds is lower in the linear region (by $\approx 13\%$). Reducing the C_L allows the stall point to be delayed by $\approx 3^\circ$. This effect is enhanced by the passive adaptivity of the aerofoil. As presented in Figure 6.23 for a set angle of attack $\alpha=20.02^\circ$ and two different wind speeds $V_S=10-20$ m/s, the twist changes by $d\theta=2.07^\circ$. The stall point is further delayed by the influence of the increased deflection in the structure. When compared to the static lift coefficient, the dynamic stall is greatly delayed due to the ramp-up motion. The dynamic lift results in being substantially greater than the static lift especially at angles greater than the static stall angle (Shen and Fuhs, 1999). This behaviour is explained by Theodorsen's theory on dynamic lift, and it applies also in a case of low reduced frequency.

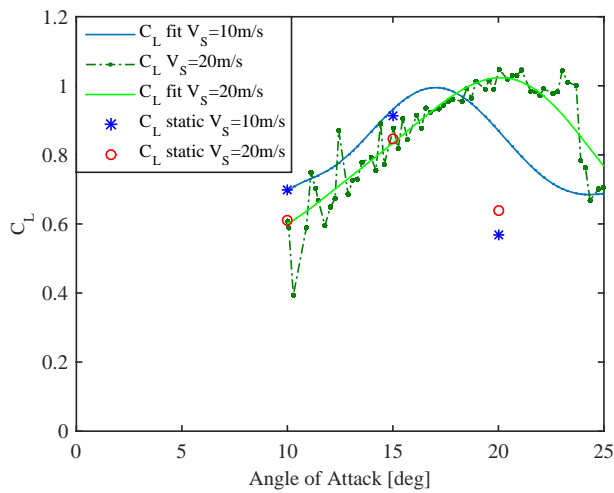


FIGURE 6.25: *Lift coefficient over angle of attack for two different wind speeds - Glass PAC.*

Figure 6.26 presents the same dynamic response as Figure 6.25 but it shows the change in angle of attack as measured with DIC. The reference image is taken at $\alpha = 10.02^\circ$, therefore the values are presented as a change in angle starting from zero.

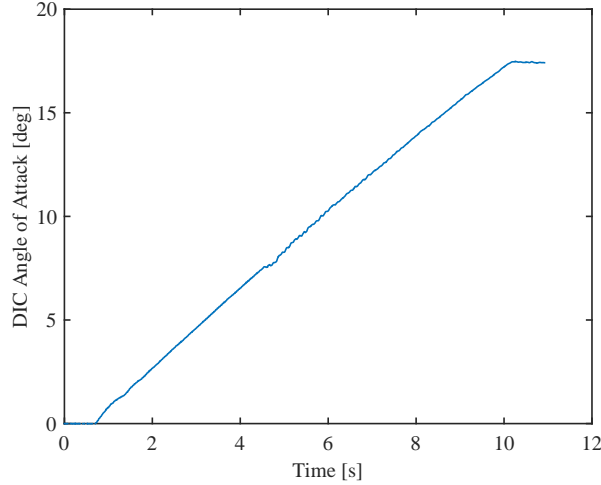


FIGURE 6.26: *Change in angle of attack in a dynamic run from $\alpha = 10.02^\circ$ to $\alpha = 28^\circ$ as measured with DIC for $V_s=10$ m/s.*

The Figure shows that the acquisition was started when the angle was steady at $\alpha = 10.02^\circ$, then a linear change in angle was measured until the maximum angle of attack was reached. Having assessed the validity and the accuracy of the DIC measurements both in translation and rotation for static and dynamic cases (as presented in section 3.3.1), Figure 6.26 shows the ability to correctly capture a change in angle of attack under wind loading in unsteady conditions.

Figure 6.27 presents the lift force, the displacement magnitude and the relative change in tip vortex position over time. The acquisition of the three synchronised systems was started when the wind speed in the wind tunnel was settled at $V_s=10$ m/s. The maximum wind speed achieved was $V_s \approx 27$ m/s. The acquisition of the DIC and PIV was started 3.314 s after the forces acquisition. The maximum deflection of the aerofoil was achieved at $V_s \approx 27$ m/s and corresponded to $\delta = 26.5$ mm if considering a zero displacement at $V_s=10$ m/s, similarly the tip vortex displaced by $\delta_{vortex} = 27.6$ mm from a zero position at $V_s=10$ m/s. From these results the close interaction between the tip deflection and the developed flow features can be appreciated. It is also apparent that the relative displacements of each do not match exactly, demonstrating again the complexity involved in aero-elastic problems and the need to understand the interactions occurring.

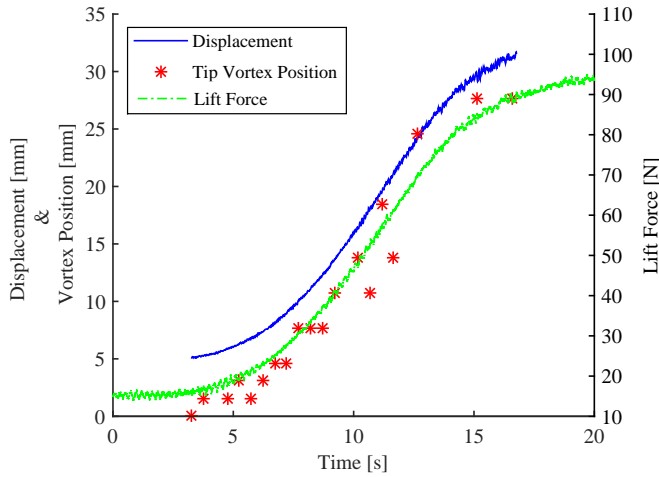


FIGURE 6.27: *Lift force, displacement magnitude and relative tip vortex movement over recording time for $\alpha = 10.02^\circ$.*

The increase in speed in the wind tunnel is not linear, therefore the lift, aerofoil deflection and tip vortex displacement responses present an initial slow increase rate. Moreover, the wind speed increases rapidly until when the target wind speed of $V_S=30$ m/s is approached.

Finally, the structures' natural frequencies were measured by means of an impact test, with the two different spars clamped to the dynamometer. Their responses can be seen in Figure 6.28. As expected, the more flexible structure (glass-carbon) presents a lower first natural frequency value ($\omega_n=17$ Hz) compared to the carbon beam ($\omega_n=21.8$ Hz). Both responses correctly capture the forces and moments balance natural frequency, which occurs at $\omega \approx 40$ Hz, as seen previously in Figure 5.7.

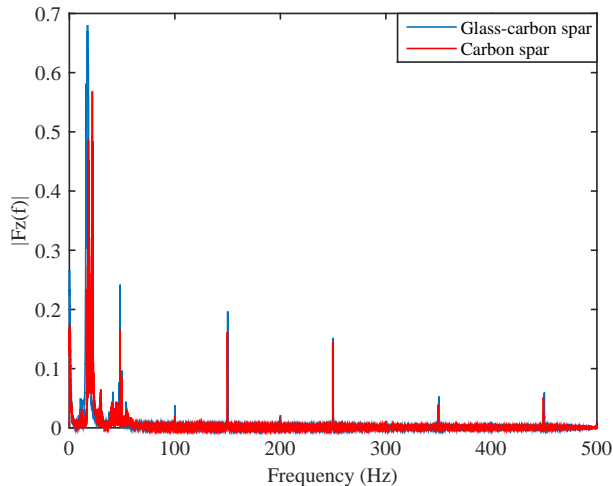


FIGURE 6.28: *Natural frequency response of both internal spars as measured in an impact test.*

6.6 Summary of the Chapter

In this chapter the design challenge was explained. What is necessary in a foiling boat is to reach the take-off speed and then passively adapt the pitch angle of the horizontal part of the foil to stabilise the flight height to the weight of the boat. This can be achieved reaching a constant lift value. In order to achieve a constant lift value it is necessary to change the effective angle of attack of the foil (in this case with passive adaptivity) and the shape of the foil (with multi-element foils or flaps for example). To be able to design a new structure that could passively twist by a desired amount the influence of oriented plies on their position with respect to the centre of pressure and the neutral axis was initially assessed.

Once the effects of passive adaptivity were understood, it was possible to model and then manufacture and test a new design (Design 4). Initially an analytical model capable of calculating the lift force for a given level of twist was developed. The numerical methodology described in Chapter 4 was then used as a design tool. The conditions of the wind tunnel were replicated in a numerical environment, modelling the structure and the flow features as presented in the experiments. Due to structural constraints of the specimen, and the geometric and performance constraints of the wind tunnel, it was not possible to achieve a constant level of lift with increased velocity (corresponding to boat or wind speed in a real environment). However, it was possible to achieve a decrease in lift coefficient with an increase in wind. This response was encountered for both internal spars, but a larger decrease in lift coefficient and angle of attack is seen for the aerofoil with the glass-carbon beam. The lower strength of the glass quasi-isotropic laminae allows a greater influence of the passive adaptive carbon plies, enhancing the level of twist of the structure. This is reflected also when inspecting the non-dimensional displacement and twist values, where the bending and torsional stiffness of the structure are taken into consideration.

After having assessed both internal structures and the influence of the passive adaptivity in their responses, some results for dynamic tests were presented. These tests are particularly interesting when analysing the flow features around the object. Moreover, while assessing the structure dynamically a better understanding of the outcomes of effective angle of attack on the stall point of the aerofoil becomes possible. For the glass-carbon beam the stall angle is delayed by $\approx 3^\circ$ thanks to the level of twist achieved by the structure.

7

Conclusions

This thesis has presented a detailed study of the Passive Adaptive Composites (PAC) and the influence of adding bend-twist coupling oriented plies to aerofoil sections. The possibility of tailoring a design to a certain load is extremely important in aerofoil sections, especially when investigating high-performance foiling catamarans, which have to fly at a stable height above the water in order to reduce the drag associated with the immersed hull.

A review of background theory and literature has shown that the possibility of using PAC in industrial applications was initially investigated in 1988 by Karaolis *et al.* (1988). However, there was a lack of experimental tests for tailored composite structures on the literature to date. Therefore, it was necessary to give to the scientific community a full-field FSI experimental validation model. The advantages, disadvantages and applications of full-field measuring techniques were investigated.

Chapter 3 gives a detailed description of a new experimental technique that can be used to assess the structural response as well as the fluid behaviour and the aerodynamic response of a PAC flexible aerofoil simultaneously under fluid loading. The experiments are described in all their aspects, from the manufacturing of the PAC beams to the coupling techniques used in the wind tunnel. A large part of the experimental set-up chapter describes the accuracy of the full-field non-contact measurement techniques, focusing especially on the errors introduced while coupling the two systems together. It was proven that the accuracy of the DIC system was not significantly affected by the addition of the PIV seeding particles and laser light to the methodology. Vice-versa the addition of

magenta-lights do not affect the PIV measures. Being able to assess the uncertainty values of the two measurement techniques and the robustness of the synchronised systems allows the presented experimental methodology to investigate the influence of changing the internal design of a structure tailored to improve its performances in varying loading conditions.

A numerical FSI methodology was then described in Chapter 4. In order to be able to correctly capture the differences in response between a quasi-isotropic and a passive adaptive structure, a finite-element model that could reliably capture those changes was developed. This was achieved by particularly paying attention to the element formulation for composite beam-bending problems. Following this, the whole model tested in the wind tunnel was reproduced numerically, coupling the FEA with the CFD in a full fluid-structure interaction solution. The possibility of designing a structure that passively adapts to a load needs to be described in time, as the inertia effects of the varying load, affected by the deflection and vice-versa, need to be accounted for. Therefore, the different coupling techniques were described and their main advantages and drawbacks were outlined. The approach used in systematically setting up both the FEA and the CFD simulations independently ensured that the FSI simulations could achieve a high level of fidelity compared to the experimental measures.

The experimental and numerical results were then presented and discussed. Chapter 5 focused on explaining the effects of different ply lay-ups on the structural response of the aerofoil. Three different internal spars were tested and modelled: one that presents a quasi-isotropic behaviour, one that would twist toward feather and one that would twist toward stall. The angular conventions chosen were described in detail. Analysing the results of both experimental and numerical methods, it is important to note the major outcomes:

- Repeatability and robustness of the experimental technique involving the use of DIC, PIV and forces and moments balance. The designed experimental set-up is able to capture not only the forces but also the flow features and the structural response of an aerofoil under wind load.
- Possibility of designing a structure that is able to change its angle of attack in a range of loading conditions. This configuration not only affects the structural deformation and twist, but also and more importantly, the load response of the structure, changing the slope of the lift over velocity profile and the stall point of the aerofoil.
- Describing the deflection and twist measures as non-dimensional values, taking into consideration the bending and torsional strength of the aerofoil, allows a comparison of different structures.

- Precision in measurement of the material properties of all the components used in the experiments enabled accurate representation of the response over time of an anisotropic structure in a numerical environment with errors smaller than 5%.

Having proven that it was possible to model a complex flow-structure interaction problem numerically, this numerical method was used as a design tool enabling achievement of the ultimate goal of the research. In Chapter 6 the design challenge of building a hydrofoil that could adapt its pitch angle to reach a constant value of lift (equal to the weight of the catamaran) was described. In order to design a new structure that could passively twist a desired amount, it was necessary to understand the influence of the bend-twist oriented plies on their position with respect both to the centre of pressure and the neutral axis. Therefore, a number of different designs were developed and their responses were modelled numerically. Considering the real angle of attack that a three-dimensional aerofoil faces (formed of the set-angle of attack, the effective angle of attack of a 3-D aerofoil and the amount of twist achievable by the PAC structure) it is possible to substantially decrease the lift coefficient value with increased wind speed. This response allows the structure to reach an almost linear increase in lift with velocity. If comparing the new design response with a quasi-isotropic structure that increases its lift with the flow-velocity squared, it is possible to see how the design goal is achieved. The decrease in C_L with speed was encountered modelling the new design numerically and then when testing the aerofoil in the wind tunnel. The experimental methodology described in Chapter 3 was used again with Design 4. In this last set of experiments both systems used were high speed, so the unsteady flow and structure responses could be analysed. Two internal structures were tested and it was possible to prove that the lower strength of the glass-carbon spar allows a larger impact of the bend-twist coupling plies, enhancing the level of twist on the structural response.

7.1 Contributions

The results found in literature confirmed that a flexible composite foil-structure can be more efficient, especially in off-design loads, compared to the metallic counterparts. However, a systematic design methodology and an experimental validation case for 3-dimensional structures were still lacking. The main contributions and the novelty of this research to the possibility of adopting passive adaptive composite in foil-shape structures are herein presented.

7.1.1 Fluid Structure Interaction Experimental Methodology

This research focused on identifying a simple design test case that was reproducible with numerical simulations, and in conducting a repeatable and robust experimental

methodology. The contribution and novelty of this part of the research to this field can be summarised in the following key-points:

- the developed experimental methodology is not only capable of describing the structural response of a full-scale aerofoil under wind load, but also the flow features that are affected by the deformation and twist of the aerofoil;
- the set-up was developed to minimise the measurement error while synchronising the two full-field measurement techniques. The uncertainty levels of both DIC and PIV systems (separately and synchronised) were measured and the error values were stated. The possibility of knowing the uncertainty associated with experimental measures enables an accurate comparison of a numerical model with experimental data.

The findings of the test methodology are therefore able to counteract the deficiencies discussed in section 2.3.2.

7.1.2 Design Development of a Passive Adaptive Structure

To design a new aerofoil capable of twisting a desired amount, it was initially necessary to comprehend the effects of passive adaptivity on a given structure. The innovation associated with the design of the new structure was connected to the understanding of the changes required in the original hydrofoil design. Having acquired the knowledge of flow-structure interactions of bend-twist coupling foils during the current research, it was possible to:

- describe the effects of passive adaptive oriented plies in changing their position inside a structure;
- utilise the validated numerical methodology as a design tool to achieve the proposed goal of reaching a constant change of lift force with speed;
- better understand the effects of tailoring the angle of attack of an aerofoil on the dynamic forces responses.

The newly-proposed design increases by almost 200% the amount of twist achievable compared to the initial design. This improvement allows an increase of 3° in the stall angle of the aerofoil section under increased aerodynamic loading. These findings therefore allow the possibility of creating and subsequently building a real hydrofoil that could passively adapt its pitch angle to achieve a stable flight.

7.2 Project Achievements

- The experimental methodology proposed enables an accurate assessment of the effects of aerodynamic loading on a structure.
- The level of uncertainty associated with the experimental error can be quantified.
- The numerical set-up used permitted an accurate description of the effects of bend-twist coupling on a fluid-structure interaction problem.
- The effects of coupling techniques in FSI problems were outlined and the major advantages and drawbacks explained.
- Particular care was taken when describing the ply-angles orientation convention used, to explain the effects of positive or negative ply angles on the response of a structure.
- The synchronisation of the three acquisition systems ensured a robust methodology that can be compared with numerical simulations.
- The numerical methodology was used as a design tool to avoid initial excessive costs of long experimental test campaigns.
- The design process brought the new structure to linearly decrease the lift coefficient in increased wind speed.

All the above achievements proved that it is possible to improve the performance of an aerofoil by merely changing its internal structure.

7.3 Further Work

Having completed three years of work on fluid-structure interaction problems the research field is still extremely large, and there are a number of different projects that could be successfully exploited in future years. Narrowing down the list there would seem to be two main areas for future work.

7.3.1 Future Projects in Experimental FSI

Regarding the experimental methodology, future work will focus on developing an experimental set-up able to measure the structural deformation and flow features in a towing tank. Being able to describe the structural response in water allows stiff structures to be tested (as in water the forces experienced by the specimen are five times greater than in air). This methodology would therefore be suitable to test a real hydrofoil structure.

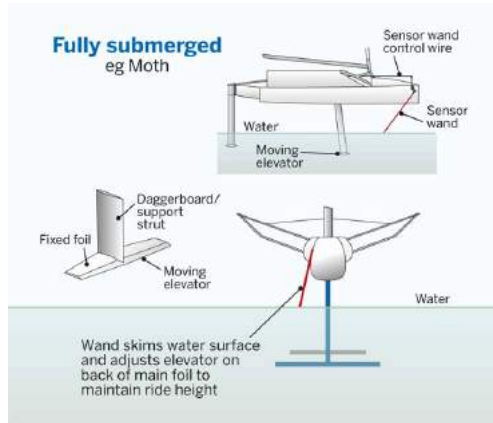
In order to be able to correctly capture the flow features and the structural deformation, underwater Particle Image Velocimetry and Digital Image Correlation will need to be developed and used. The main set-up problems will be caused by the vibration induced by the moving carriage, by the image deformation due to the refraction level of the water and by the amount of light propagating in the water.

7.3.2 Design of Real Hydrofoil Structure

In what concerns the FSI field, it would be extremely interesting to apply a passive-adaptive internal structure to a hydrofoil that is able to change its shape (with multi-element foils or flaps). This configuration will allow the structure to achieve a constant lift force with speeds higher than the design take-off speed. An immediate application of this newly developed structure could be the foiling moth class, shown in Figure 7.1. The International Moth is a single-handed development class boat, and it follows open class rules. Therefore, the designer and builder have full liberty to develop and produce the fastest boat (International Moth Class, 2013).



(a) Foiling International Moth



(b) The Moth hydrofoils configuration

FIGURE 7.1: *The International Moth class shown when sailed and its hydrofoil configurations (Sheahan, M., 2015).*

In the configuration shown in Figure 7.1(b) the fixed foil upstream of the moving elevator can be created with passive adaptive composite plies. The structure, if designed toward feather, would allow a lower range of angles of attack to be controlled by the sensor wand (and the elevator) at high speeds, allowing to foil more easily in extreme weather-waves conditions.

The same configuration could be used in America's Cup foils design and its design will be investigated in the near future.

References

- ABAQUS Simulia (2013), ABAQUS Analysis User's Guide. *Tech. rep.*
- Ahmed, M. (2012), Blade sections for wind turbine and tidal current turbine applications - current status and future challenges. *International Journal of Energy Research*, **36**: pp. 829–844.
- Albertani, R., Stanford, B., Hubner, J.P. and Ifju, P.G. (2007), Aerodynamic coefficients and deformation measurements on flexible micro air vehicle wings. *Experimental Mechanics*, **47**(5): pp. 625–635.
- Arafath, A.R.A., Vaziri, R. and Poursartip, A. (2007), Modelling process-induced deformations in composite structures using higher order elements. In: *16th International Conference on Composite Materials*.
- Ashby, F. (1992), *Materials Selection in Mechanical Design. No. pt. 1 in Materials Selection in Mechanical Design*. Elsevier Science & Technology Books.
- ASTM International (2003), ASTM D 1623 Standard test for tensile and tensile adhesion properties of rigid cellular plastics.
- (2004), ASTM D621 Standard test method for compressive properties of rigid cellular plastics. *Tech. rep.*
- (2007), ASTM D273 Standard properties of sandwich core materials. *Tech. rep.*
- Barbero, E.J. (2008), *Finite Element Analysis of Composite Materials*. CRC Press.
- Ben Ainslie Racing (2015). URL http://ben-ainslie-racing.americascup.com/en/news/143_A-New-Era.html.
- Benra, F.K., Dohmen, H.J., Pei, J., Schuster, S. and Wan, B. (2011), A comparison of one-way and two-way coupling methods for numerical analysis of fluid-strcuture interactions. *Journal of Applied Mathematics*.
- Blachut, J. and Stainer, D. (2012), Elastic Buckling of Conical Shells under the Combined Loading of Axial Compression and External Pressure. In: *Proceedings of the 11th International Conference on Computational Structures Technology*.

- Byrd, A.W. (2012), *Fluid-Structure Interaction Simulations of a Flapping Wing Micro Air Vehicle*. Master's thesis, Wright State University, US.
- Capponnetto, M. (2014). URL <http://www.deskeng.com/de/cfd-provides-the-winning-edge/>.
- Castro, I.P. (2001), Calibration tests in the working section of the R J Mitchell Wind Tunnel. *Tech. rep.*, University of Southampton.
- Chattopaghyay, A. and Jha, R. (1996), Development of a composite tailoring technique for airplane wing. *Tech. rep.*, NASA-CR-205326.
- Chen, F., Chen, X., Xie, X., Feng, X. and Yang, L. (2013), Full-field 3D measurement using multi-camera digital image correlation system. *Optics and Lasers in Engineering*, **51**(9): pp. 1044–1052.
- Clyne, T. (2014), Material sciences: composite materials. University of Cambridge.
- Corbet, D. and Morgan, C. (1992), Report on the passive control of horizontal axis wind turbine. *Tech. rep.*, Garrad Hassan and Partners.
- Crammond, G., Boyd, S. and Dulieu-Barton, J. (2013), Speckle pattern quality assessment for digital image correlation. *Optics and Lasers in Engineering*, **51**(12): pp. 1368–1378.
- de Borst, R., Nithiarasu, P., Tezduyar, T., Yagawa, G. and Zohdi, T. (2013), *Computational Fluid-Structure Interaction*. John Wiley & Sons, Ltd., Publication, ISBN 9780470978771.
- De Goeij, W.C., Van Tooren, M.J.L. and Beukers, A. (1999), Implementation of bending-torsion coupling in the design of a wind-turbine rotor-blade. *Applied Energy*, **63**(3): pp. 191–207.
- Donea, J., Giuliani, S. and Halleux, J.P. (1982), An Arbitrary-Lagrangian-Eulerian finite element method for transient dynamic fluid-structure interaction. *Computer Methods in Applied Mechanics and Engineering*, **33**: pp. 689–723.
- Ducouin, A. and Young, Y.L. (2013), Hydroelastic response and stability of a hydrofoil in viscous flow. *Journal of Fluids and Structures*, **38**: pp. 40–57.
- Ducouin, A., André Astolfi, J. and Sigrist, J.F. (2012a), An experimental analysis of fluid structure interaction on a flexible hydrofoil in various flow regimes including cavitating flow. *European Journal of Mechanics, B/Fluids*, **36**: pp. 63–74.
- (2012b), An experimental analysis of fluid structure interaction on a flexible hydrofoil in various flow regimes including cavitating flow. *European Journal of Mechanics, B/Fluids*, **36**: pp. 63–74, doi:10.1016/j.euromechflu.2012.03.009.

- Edmund Optics (2016). URL <http://www.edmundoptics.co.uk/optics/optical-filters/color-dichroic-filters/mounted-color-filters/49797/>.
- Eric Greene Associates (1999), *Marine Composites*. Eric Greene Associates.
- Fedorov, V. (2012), *Bend-Twist Coupling Effects in Wind Turbine Blades*. Ph.D. thesis, Technical University of Denmark.
- Fedorov, V.A., Dimitrov, N., Berggreen, C., Krenk, S., Branner, K. and Berring, P. (2009), Investigation of structural behaviour due to bend-twist couplings in wind turbine. In: *17th International Conference on Composite Materials*.
- Findlay, M. and Turnock, S. (2008), Investigation of the effects of hydrofoil set-up on the performance of an international moth dinghy using a dynamic vpp. In: *Innovation in High Performance Sailing Yachts*.
- Friedmann, P.P., Glaz, B. and Palacios, R. (2009), A moderate deflection composite helicopter rotor blade model with an improved cross-sectional analysis. *International Journal of Solids and Structures*, **46**(10): pp. 2186–2200.
- Funatani, S., Fujisawa, N. and Ikeda, H. (2004), Simultaneous measurement of temperature and velocity using two-colour LIFT combined with PIV with a colour CCD camera and its application to the turbulent buoyant plume. *Measurement Science and Technology*, **15**: pp. 983–990.
- Ganguli, R. and Chopra, I. (1995), Aeroelastic Optimization of a Helicopter Rotor with Composite Coupling. *Journal of Aircraft*, **32**(6): pp. 1326–1334.
- Gibson, L. and Michael, F. (1988), *Cellular Solids: structure and properties*.
- Giuni, M. (2013), *Formation and early development of wingtip vortices*. Ph.D. thesis, University of Glasgow.
- Grant, B.M.B., Stone, H.J., Withers, P.J. and Preuss, M. (2009), High-temperature strain field measurement using digital image correlation. *Strain Analysis*, **44**(6): pp. 263–271.
- Grediac, M. and Hild, F. (2012), *Full-Field Measurements and Identification in Solid Mechanics*. John Wiley & Sons.
- Guo, S. (2007), Aeroelastic optimization of an aerobatic aircraft wing structure. *Aerospace Science and Technology*, **11**(5): pp. 396–404.
- Guo, X., Liang, J., Tang, Z., Cao, B. and Yu, M. (2014), High-temperature digital image correlation method for full-field deformation measurement captured with filters at 2600°C using spraying to form speckle patterns. *Optical Engineering*, **53**(6).
- Gurit (2012a), SE 84 LV Low temperature cure epoxy prepreg. *Tech. rep.*, URL <http://www.gurit.com/files/documents/se-84lvv16pdf.pdf>.

- (2012b), SA 80 Toughened epoxi adhesive film. *Tech. rep.*, URL <http://www.gurit.com/files/documents/sa-80v11pdf.pdf>.
- (2012c), Guide to composites. *Tech. rep.*, Gurit.
- (2015), Gurit Corecell M, The Marine Foam. *Tech. rep.*
- Haghigat, S., Martins, J. and Liu, H. (2012), Aerostervoelastic design optimisaion of a flexible wing. *Journal of Aircraft*, **49**(2).
- Helm, J., McNeill, S. and Sutton, M. (1996), Improved three-dimensional image correlation for surface displacement measurement. *Optical Engineering*: pp. 1911–1920.
- Herath, M.T., Lee, A.K.L. and Gangadhara Prusty, B. (2015), Design of shape-adaptive wind turbine blades using Differential Stiffness Bend-Twist coupling. *Ocean Engineering*, **95**: pp. 157–165.
- Hong, C.H. and Chopra, I. (1985), Aeroelastic stability analysis of a composite rotor blade. *Journal of the American Helicopter Society*, **30**(2).
- (1986), Aeroelastic stability analysis of a composite bearingless rotor blade. *Journal of the American Helicopter Society*, **31**: pp. 29–35.
- Hou, G., Wang, J. and Layton, A. (2012), Numerical Methods for Fluid-Structure Interaction - A Review. *Communications in Computational Physics*, **12**(2): pp. 337–377, doi:10.4208/cicp.291210.290411s.
- Hu, H., Tamai, M. and Murphy, J.T. (2008), Flexible-Membrane Airfoils at Low Reynolds Numbers. *Journal of Aircraft*, **45**(5): pp. 1767–1778.
- International Moth Class (2013), International Moth Class Rules. *Tech. rep.*
- Jacobson, R.E., Ray, S.F., Attridge, G.G. and Axford, N.R. (2000), *The manual of Photography: photographic and digital imaging*. Focal Press.
- Jones, G.S., Lin, J.C., Allan, B.G., Milholen, W.E., Rumsey, C.L. and Swanson, R.C. (2008), Overview of CFD Validation Experiments for Circulation Control Applications at NASA. In: *International Powered Lift Conference*, pp. 1–16.
- Jung, S., Kim, K.T. and Kim, S. (2002), Aeroelastic stability analysis of hingeless rotor blades with composite flexures. *KSME International Journal*, **16**(4).
- Karaolis, N., Mussgrove, P. and Jeronimidis, G. (1988), Active and passive aeroelastic power control using asymmetric fiber reinforced laminates for wind turbine blades. In: *10th British Wind Energy Conference*.
- Ke, X.D., Sutton, S. and Wang, Y. (2011), Error assessment in stereo-based deformation measurements. *Experimental Mechanics*, **51**: pp. 423–441.

- Kennedy, G.J., Hansen, J.S. and Martins, J.R.R.a. (2011), A Timoshenko beam theory with pressure corrections for layered orthotropic beams. *International Journal of Solids and Structures*, **48**(16-17): pp. 2373–2382.
- Kenway, G. and Martins, J. (2008), Aerostructural Shape Optimization of Wind Turbine Blades Considering Site-Specific Winds. *12th AIAA/ISSMO Multidisciplinary Analysis and Optimization Conference*: pp. 1–12.
- Khan, A., Adams, D., Dayal, V. and Vogel, J. (2000), Effects of bend-twist coupling on composite propeller performance. *Mechanics of Composite Materials and Structures*, **7**: pp. 383–401.
- Kootsookos, A. (2001), Comparison of the seawater durability of carbon and glass polymer composites. In: *International Committee on Composite Materials*.
- LaVision (2012), Strain master. *Tech. rep.*, LaVision product-manual for Davis 8.1.
- (2016), Flow master. *Tech. rep.*, LaVision product-manual for Davis 8.2.
- Lawson, N. and Wu, J. (1997), Three-dimensional particle image velocimetry: error analysis of stereoscopic techniques. *Measurements science and technology*, **8**: pp. 894–900.
- Lee, Y.J. and Lin, C.C. (2004), Optimized Design of Composite Propeller. *Mechanics of Advanced Materials and Structures*, **11**(1): pp. 17–30.
- Lee, Y.J., Jhan, Y.T. and Chung, C.H. (2012), Fluid-structure interaction of FRP wind turbine blades under aerodynamic effect. *Composites Part B: Engineering*, **43**(5): pp. 2180–2191.
- Lin, C.C., Lee, Y.J. and Hung, C.S. (2009), Optimization and experiment of composite marine propellers. *Composite Structures*, **89**(2): pp. 206–215, doi:10.1016/j.compstruct.2008.07.020.
- Lin, H.J. and Lai, W.M. (2010), A Study of Elastic Coupling to the Wind Turbine Blade by Combined Analytical and Finite Element Beam Model. *Journal of Composite Materials*, **44**(23): pp. 2643–2665, doi:10.1177/0021998310369578.
- Lobitz, D. and Veers, P. (1997), Aeroelastic behavior of twist-coupled HAWT blades. *AIAA*.
- Lothode, C., Durand, M., Roux, Y., Leroyer, A., Visonneau, M. and Dorez, L. (June 2013), Dynamic fluid structure interaction of a foil. In: *The Third International Conference on Innovation in High Performance Sailing Yachts*.
- Madenci, E. and Guven, I. (2006), *The Finite Element Method and Applications in Engineering Using ANSYS*. Springer.

- Maheri, A. and Isikveren, A.T. (2009), Design of wind turbine passive smart blades. In: *European Wind Energy Conference*.
- Maheri, A., Noroozi, S. and Vinney, J. (2007), Combined analytical/FEA-based coupled aero structure simulation of a wind turbine with bend-twist adaptive blades. *Renewable Energy*, **32**(6): pp. 916–930, doi:10.1016/j.renene.2006.04.007.
- Malan, P. (2009), Calibrating the $\gamma - Re_\theta$ Transition Model for Commercial CFD. In: *47th AIAA Aerospace Sciences Meeting*.
- Malijaarsl, P.J. and Kaminski, M.L. (2015), Hydro-elastic Analysis of Flexible Propellers: an overview. In: *Fourth International Symposium on Marine Propulsors*, Austin, ISBN 9780996459440.
- Marimon Giovannetti, L., Banks, J., Turnock, S.R. and Boyd, S.W. (2016), Uncertainty assessment of coupled Digital Image Correlation and Particle Image Velocimetry during wind tunnel experiments. *Journal of Fluids and Structures*, **68**: pp. 125–140.
- Mccormick, N. (2012), Digital image correlation for structural measurements. *Proceedings of the Institution of Civil Engineers*, **165**: pp. 185–190.
- Menter, F., Langtry, R. and Volker, S. (2006), Transition modelling for general purpose CFD codes. *Flow Turbulence Combust*, **77**: pp. 277–303.
- Miao, J.M. and Ho, M.H. (2006), Effect of flexure on aerodynamic propulsive efficiency of flapping flexible airfoil. *Journal of Fluids and Structures*, **22**(3): pp. 401–419, doi:10.1016/j.jfluidstructs.2005.11.004.
- Molland, A.F. and Turnock, S.R. (2007), *Marine Rudders and Control Surfaces*. Butterworth-Heinemann.
- Moth International (2014). URL http://www.yachtingaustralia.com.au/site/yachting/rycv/downloads/OTB/Coaching/2012_03_04/1020International20Moth.pdf.
- Mottelet, S., de Saint Germain, L. and Mondin, O. (2012), Smart depth of field optimisation applied to a robotised view camera. *Journal of Mathematical Imaging and Vision*, **44**: pp. 1–18.
- Murugan, S., Ganguli, R. and Harursampath, D. (2008), Aeroelastic Response of Composite Helicopter Rotor with Random Material Properties. *Journal of Aircraft*, **45**(1): pp. 306–322, doi:10.2514/1.30180.
- NACRA International (2014), NACRA 17 Class Rules. *Tech. rep.*
- Nicholls-Lee, R., Boyd, S.W. and Turnock, S.R. (2009), Development of high performance composite bend-twist coupled blades for a horizontal axis tidal turbine. In: *17th International Conference on Composite Materials*.

- Nicholls-Lee, R.F. (2011), *Adaptive Composite Blades for Horizontal Axis Tidal Turbines*. Phd thesis, University of Southampton.
- Nicholson, M. (2015), Investigation into the application of bistable composites to marine control surfaces. University of Southampton.
- Note, P.J. (2014), *Developement of a twist sensitive daggerboard for wind tunnel testing*. Master's thesis, University of Southampton, UK.
- Pan, B., Xie, H., Wang, Z., Qian, K. and Wang, Z. (2008), Study on subset size selection in digital image correlation for speckle patterns. *Optics express*, **16**(10): pp. 7037–7048.
- Pan, B., Wu, D. and Yu, L. (2012), Optimization of a three-dimensional digital image correlation system for deformation measurements in extreme environments. *Applied optics*, **51**(19): pp. 4409–19, doi:10.1364/AO.51.004409.
- Park, I.J., Dhadwal, M.K., Jung, S.N. and Kim, D.H. (2011), Experimental Validation of Cross-Sectional Analysis for Composite Rotor Blades. In: *18th International Conference on Composite Materials*.
- Pashias, C. (2005), *Propeller tip vortex simulations using adaptive grid refinement based on flow feature identification*. Ph.d thesis, University of Southampton.
- Patil, M.J. (1998), Aeroelastic Tailoring of Composite Box Beams. *21st Congress of International Council of the Aeronautical Sciences, Melbourne, Australia, September 1998*.
- Pemberton, R., Turnock, S.R., Dodd, T. and Rogers, E. (2002), A novel method for identifying vortical structures. *International Journal for Numerical Methods in Fluids*, **16**(23): pp. 1051–1057.
- Post, M.E., Trump, D.D., Goss, L.P. and Hancock, R.D. (1994), Two-color particle-image velocimetry using a single argon-ion laser. *Experiments in Fluids*, **16**: pp. 263–272.
- Potes, F.C. (2012), *General Comceptual Design Problems of a Parabolic Solar Sail Structure*. Master's thesis, Universidade da Beira Interior.
- Prasad, A. and Jensen, K. (1995), Scheimpflug stereocamera for particle image velocimetry in liquid flows. *Applied Optics*, **34**(30): pp. 7092–7099.
- Prasad, A.K. (2000), Stereoscopic particle image velocimetry. *Experiments in Fluids*, **29**(February): pp. 103–116, doi:10.1007/s003480000143.
- PRF Composite Materials (2015), Toughened Epoxy Prepreg System RP-528: low-medium temperature cure 85-120 deg C. *Tech. rep.*

- Raffel, M., Willert, C. and Wereley, S. (2007), *Particle Image Velocimetry - A Practical Guide.*
- Raither, W., Bergamini, A. and Ermanni, P. (2012), Profile beams with adaptive bending-twist coupling by adjustable shear centre location. *Journal of Intelligent Material Systems and Structures*, **24**: pp. 334–346.
- Rastogi, P. and Hack, E. (2012), *Optical Methods for Solid Mechanics: A Full-Field Approach.*
- Reddy, J.N. (2003), *Mechanics of laminated composite plates and shells.* CRC Press.
- Reu, P. (2012), Stereo-Rig Design : Creating the Stereo-Rig Layout: Part 1. *Experimental techniques*, **36**(Dic): pp. 3–4.
- (2013), Stereo-rig Design : Stereo angle selection - Part 4. *Experimental techniques*, **37**: pp. 1–2.
- Reu, P. and Miller, T. (2008), The application of High-Speed Digital Image Correlation. *Journal of Strain Analysis*, **43**.
- Rocket, T. and Rose, V. (1987), The causes of boat hull blisters. *Tech. rep.*, University of Rhode Island.
- Schmidt, T., Tyson, J., Galanulis, K. and Revilock, D. (2004), Full-filed dynamic deformation and strain measurements using high-speed digital cameras. In: *Proceedings of the SPIE 26th International Congress on High-Speed photography and photonics*.
- Schreier, H., Orteu, J.J. and Sutton, M.a. (2009), *Image Correlation for Shape, Motion and Deformation Measurements.* Boston, MA: Springer US, ISBN 978-0-387-78746-6, doi:10.1007/978-0-387-78747-3.
- Sciacchitano, A., Neal, D.R., Smith, B.L., Warner, S.O., Vlachos, P.P., Wieneke, B. and Scarano, F. (2015), Collaborative framework for piv uncertainty quantification: comparative assessment of methods. *Measurement Science and Technology*, **26**(7): p. 074,004.
- Selzer, R. and Friedrich, K. (1997), Mechanical properties and failure behaviour of carbon fibre-reinforced polymer composites under the influence of moisture. *Composites Part A*, **28**: pp. 595–604.
- Sheahan, M. (2015). URL <http://www.yachtingworld.com/features/the-foiling-phenomenon-66269>.
- Shen, Y.T. and Fuhs, D. (1999), Dynamic effects on propeller blade section lift, drag and pitching moment coefficients. *Tech. rep.*
- Shirk, M.H., Hertz, T.J. and Weisshaar, T.A. (1985), Aeroelastic Tailoring: Theory, Practice, and Promise. *Journal of Aircraft*, **23**(1).

- Siddiqui, M.Z. (2014), 2D-DIC for the quantitative validation of FE simulations and non-destructive inspection of aft end debonds in solid propellant grains. *Aerospace Science and Technology*, **39**: pp. 128–136, doi:10.1016/j.ast.2014.08.015.
- Sieber, G. (2002), *Numerical simulation of fluid-structure interaction using loose couple methods*. Phd thesis, Technischen Universitat Darmstadt.
- Sigrist, J.F. (2015), *Fluid-Structure Interaction an introduction to finite element coupling*. Wiley.
- Smith, E. and Chopra, I. (July 1993), Aeroelastic response, loads, and stability of a composite rotor in forward flight. *AIAA Journal*, **31**(7).
- Soubeyran, X. (2013), *Deformation Measurement of Multihull Daggerboard under Realistic Sailing Loads*. Master's thesis, University of Southampton.
- Star-ccm+ (2015), Star-ccm+ user guide. *Tech. rep.*
- Sutton, M., Orteu, J. and Schreier, H. (2009), *Image Correlation for Shape Motion and Deformation Measurements: Basic Concepts, Theory and Applications*. Springer.
- Sutton, M.A. (2009), Parameter choice for optimized digital image correlation. *Optics and Lasers in Engineering*: pp. 728–737.
- Svard, L. (2012), *Composite failure modelling and optimisation of a spring orthosis*. Master's thesis, Chalmers University of Technology, Sweden.
- Tamai, M., Murphy, J.T. and Hu, H. (2008), An Experimental Study of Flexible Membrane Airfoils at Low Reynolds Numbers. *46th AIAA Aerospace Sciences Meeting and Exhibit*: pp. 1–12.
- Tang, Z., Liang, J., Xiao, Z. and Guo, C. (2012), Large deformation measurement scheme for 3D digital image correlation method. *Optics and Lasers in Engineering*, **50**(2): pp. 122–130, doi:10.1016/j.optlaseng.2011.09.018.
- Tessler, A., Sleight, D.W. and Wang, J.T. (2003), Nonlinear shell modelling of thin membrane with emphasis on structural wrinkling. In: *44th AIAA/ASME/ASCE/AHS Structures, Structural Dynamics and Materials Conference*, American Institute of Aeronautics and Astronautics.
- The Foiling Week (2015). URL <http://www.foilingweek.com/tag/nacra-20-fcs/>.
- Thuwis, G.a.a., De Breuker, R., Abdalla, M.M. and Gürdal, Z. (2009), Aeroelastic tailoring using lamination parameters. *Structural and Multidisciplinary Optimization*, **41**(4): pp. 637–646, doi:10.1007/s00158-009-0437-6.
- Trebuna, F. and Hagara, M. (2014), Experimental modal analysis performed by high-speed digital image correlation system. *Measurement*, **50**: pp. 78–85.

- Tsenoglou, C., Pavlidou, S. and Papaspyrides, C. (2006), Evaluation of interfacial relaxation due to water absorption in fibre-polymer composites. *Composites Science and Technology*, **66**: pp. 2855–2864.
- Turner, M.J., W., C.R., Martin, H.C. and Topp, L.J. (1956), Stiffness and deflection analysis of complex structures. *Journal of the Aeronautical Sciences*, **23**(9): pp. 805–823.
- Turnock, S.R. and Wright, a.M. (2000), Directly coupled fluid structural model of a ship rudder behind a propeller. *Marine Structures*, **13**: pp. 53–72, doi:10.1016/S0951-8339(00)00009-5.
- Vaassen, J.M., De Vincenzo, P., Hirsch, C. and Leonard, B. (2010), Strong coupling algorithm to solve fluid-structure-interaction problems with a staggered approach. In: *11th International WS on Simulation & EGSE Facilities for Space Programmes*.
- Veers, P., Laboratories, S.N., Bir, G., Renewable, N., Wind, N. and Lobitz, D. (1998), Aeroelastic Tailoring in Wind-Turbine Blade Applications. *Wind Energy*.
- Wang, S. and Chung, D. (2012), Effect of moisture on the interlaminar interface of carbon fiber polymer-matrix composite, studied by contact electrical resistivity measurement. *Composite Interfaces*, **9**: pp. 453–458.
- Wang, Y.Q., Sutton, M.a., Ke, X.D., Schreier, H.W., Reu, P.L. and Miller, T.J. (2011), On Error Assessment in Stereo-based Deformation Measurements. *Experimental Mechanics*, **51**(4): pp. 405–422, doi:10.1007/s11340-010-9450-3.
- Wieneke, B. (2014), Generic a-posteriori uncertainty quantification for PIV vector fields by correlation statistics. In: *17th International Symposium on Applications of Laser Techniques to Fluid Mechanics*, pp. 7–10.
- (2015), Piv uncertainty quantification from correlation statistics. *Measurement Science and Technology*, **26**(7): p. 074,002.
- Young, Y.L. (2008), Fluid-structure interaction analysis of flexible composite marine propellers. *Journal of Fluids and Structures*, **24**: pp. 799–818.
- Young, Y.L. and Motley, M.R. (2011), Influence of Material and Loading Uncertainties on the Hydroelastic Performance of Advanced Material Propellers. In: *Second International Symposium on Marine Propulsors*.
- Zarruk, G.A., Brandner, P.A., Pearce, B.W. and Phillisa, A.W. (2014), Experimental study of the steady fluid-structure interaction of flexible hydrofoils. *Journal of Fluids and Structures*, **51**: pp. 326–343.
- Zhang, W., Markfort, C.D. and Porté-Agel, F. (2012), Near-wake flow structure downwind of a wind turbine in a turbulent boundary layer. *Experiments in Fluids*, **52**: pp. 1219–1235.